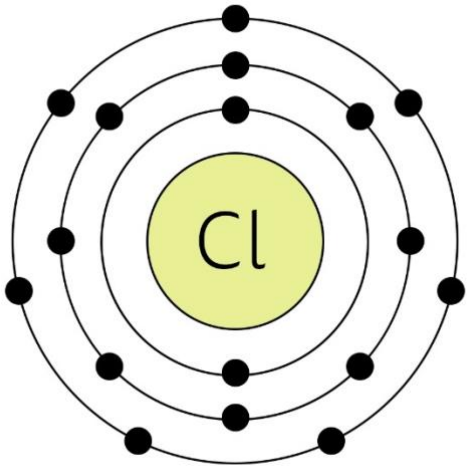
Experimental investigations into the thermodynamic properties of halogens in silicate melts

Richard W Thomas

A thesis submitted to the University of Oxford

for the degree of Doctor of Philosophy



Department of Earth Sciences

and Worcester College

February 2022

Supervised by Professor Bernard J Wood,

Dr Andrew K Matzen, and Dr Kate Kiseeva

Funded by the Natural Environmental Research Council (NE/L002612/1), and the Oxford Doctoral Training Partnership in Environmental Research

Declaration of originality

The contents of this thesis are all my own work, except where otherwise stated. The views and opinions expressed herein are mine and not necessarily those of any other person or body unless so attributed.



Signature

11/02/2022

Date

Citation: Richard W Thomas (2022), Experimental investigations into the thermodynamic properties of halogens in silicate melts, D.Phil. Thesis, University of Oxford, Department of Earth Sciences, Oxford, UK.

Acknowledgements

First and foremost, I would like to thank Professor Bernard Wood for his supervision and mentorship over the past four years. Bernie took me under his wing and helped me grow as a scientist. Most importantly, he has taught me how to think about a problem. If I have gained even a tenth of his wisdom, I would consider myself to be very lucky.

Dr Andrew Matzen has been there for me since day one and has taught me how to be a careful experimentalist and analyst. Andrew also welcomed me into his family, repeatedly fixed my bike and has been a great friend to me.

Sincere thanks are also owed to Professor Jon Wade, who not only came to help me throughout my trip to the Diamond synchrotron but also helped me understand the intricacies of XAFS. Jon's ability to understand a problem and create ideas are inspiring.

A big thank you to Dr Kate Kiseeva, who brought me to Oxford and helped me secure funding to explore halogen partition between sulphides and silicates. It was only when we started this project that we realised we did not know the fundamentals of halogen behaviour, which sparked the idea for this thesis.

I would also like to thank the Ex-Pet group past and present, including Dr Duane Smythe, Dr Anke Wohlers, Dr Michael Cassidy, Dr Edward Baker, Dr Julien Boulliung, Dr Elena Melekhova and my fellow student, Aart Van Der Waal. Thank you all for making the lab such a fun and friendly environment.

I would not have been able to complete any of my lab work without the help of the workshop team: Jamie Long, James King, and David Pinchin. Their precision and skill in manufacturing the items needed for an experimental project such as this are invaluable.

A further thank you to Dr Phillip Goupon, who taught me how to use the electron probe that was vital for the data acquisition of this project. Also, to Dr Konstantin Ignatyev, the beam scientist who helped collect the data that made up chapter 4 of this thesis. Without their help, I would not have any data.

These last four years in Oxford have been some of the best in my life so far. Although, the work involved in writing this thesis has not always been easy. It is thanks to my friends and family who have supported me throughout. Including the inhabitants of office 20.16 past and present, and of course Anya Bond and Atlas.

I would also like to thank my thesis examiners, Professor Jon Blundy of the University of Oxford, and Professeur Bruno Scaillet of the Institut des Sciences de la Terre d'Orléans, for taking time out of their schedules to read and review this thesis. I truly appreciate it.

Finally, thank you to the Natural Environmental Research Council (NE/L002612/1) and the Oxford Doctoral Training Partnership for funding me, and continuing to do so throughout a pandemic.

Abstract

The aim of this thesis is to understand the chemical behaviour of halogens in silicate melts by experimentally determining their thermodynamic activities. This includes defining how halogens become incorporated into a melt and what influences chlorine's solubility and bonding behaviour in silicate melts.

A halogen buffer has been developed using Ag/AgCl, in which Ag (as oxide) is virtually insoluble in silicate melt under the conditions of the experiment. The buffer controls the fugacity of chlorine. Experiments were performed at 5-20 kbar and 1200-1500 °C in a piston-cylinder apparatus. The effect of oxygen fugacity on Cl solubility was determined using Re-ReO_2 and C-CO_2 oxygen buffers. Experiments show (1) that chlorine solubility in haplobasalt at 15 kbar/1400 °C can reach 5 wt%, even at Cl_2 fugacities as low as 0.0035 bar. 2) Cl concentration increases linearly with the square root of chlorine fugacity at fixed $f(O_2)$, obeying Henry's Law up to ~3% Cl in the melt of a haplobasalt. 3) Cl solubility decreases with the fourth root of oxygen fugacity at fixed $\sqrt{f(Cl_2)}$. This implies that Cl^- replaces O^{2-} in the silicate framework as follows:

$$Cl_{2(gas)} + [O^{2-}]_{(melt)} = 2[Cl^-]_{(melt)} + \tfrac{1}{2}O_{2(gas)} \qquad [i]$$

This relationship is used to correct for the effect of oxygen and chlorine fugacity on pressure and temperature, to determine more accurately how chlorine solubility changes with these intensive variables. Results show that Cl increases with temperature and decreases with pressure at fixed conditions.

The chlorine buffering method was then applied to 44 chemically different compositions, all performed at 1400 °C, 15 kbar, and a fixed oxygen and chlorine fugacity. Results show that

chlorine solubility increases with Ca and Fe and decreases with Si content. Knowing the compositional effects at fixed conditions allowed for the quantification of a chloride capacity (C_{Cl}), defined as:

$$C_{Cl} = \frac{Cl\ (wt\%)}{\sqrt{f(Cl_2)}} \times \sqrt[4]{f(O_2)} \qquad \text{[ii]}$$

The chlorine capacity allows for the comparison of literature data (including those performed with water) if the temperature, pressure, oxygen fugacity and chemical composition are known. Literature data were combined with the 44 experiments performed across a wide compositional range and the pressure and temperature series of experiments. Cl content in wt% can then be expressed as a function of the different variables as:

$$logC_{Cl} = 0.571 + (4873X_{Ca} - 3803X_{Si} + 2724X_{Fe} + 1891\text{-}\ 943\text{P})/\text{T} \qquad \text{[iii]}$$

Water was found to be insignificant in controlling chlorine solubility at concentrations less than 4.3 wt%. [iii] can then be used to determine the conditions that HCl would degas. Results indicate that, at fixed Cl_2 fugacity, pressure, and temperature that most HCl loss occurs at pressures below 2 MPa. Additionally, the fraction lost as the surface is approached varies dramatically with composition as rhyolite>dacite>andesite>basalt. Constraining the thermodynamic activities also allows for determining the conditions under which Cl rich minerals such as sodalite would form and when brines would begin to segregate from the melt.

The bonding behaviour of chlorine in silicate melts was investigated by X-ray absorption fine structure. Results indicate that Cl predominantly bonds with 2^+ cations (Ca, Mg and Fe) but can also covalently bond with Si in melts that exhibit low 2^+ cation contents.

Contents

Declaration of originality....i
Acknowledgements.... ii
Abstract....iv
List of tables....ix
List of figures....x
Chapter 1 An introduction to halogen chemistry....1
1.1 The chemical properties of the halogens....2
1.2 Halogen abundances and distributions....3
1.3 Implications of chlorine on geological processes....7
1.4 Previous experimental work....10
1.5 Aims of the thesis....12
1.6 Method development....13
1.7 Thermodynamic concepts....17
1.8 Structure and contributions of this thesis....24
1.9 References....25
Chapter 2 The chemical behaviour of chlorine in silicate melts....35
2.1 Abstract....36
2.2 Introduction....38
2.2.1 Chlorine dissolution in silicate melt....39
2.3 Experimental methodology....41
2.3.1 Control of chlorine fugacity....41
2.3.2 Control of oxygen fugacity....45
2.3.3 Analytical techniques....47
2.4 Results....48
2.4.1 Attainment of equilibrium....51
2.4.2 Calculation of chlorine fugacity $f(Cl_2)$ under experimental conditions....51
2.4.3 Chlorine solubility as a function of chlorine fugacity, $f(Cl_2)$....54
2.4.4 Oxygen fugacity $f(O_2)$....57
2.4.5 The effects of pressure and temperature on chlorine solubility....58
2.5 Discussion....61
2.5.1 Chlorine fugacity and gas composition on the basalt liquidus....61
2.5.2 HCl solubility in basaltic melts....69
2.5.3 Hydrous melts in equilibrium with Cl-bearing fluids....70
2.5.4 Stability of Sodalite in trachytes and phonolites....72
2.6 Conclusions....77
2.7 Acknowledgements....79

2.8 Supplementary material 80
2.9 References 80
Chapter 3 The effect of composition on chlorine solubility and behaviour in silicate melts 89
3.1 Abstract 90
3.2 Introduction 91
3.2.1 Chlorine dissolution in silicate melts 94
3.3 Experimental methodology 97
3.3.1 Starting compositions 97
3.3.2 Controlling chlorine and oxygen fugacity 100
3.3.3 Analytical techniques 102
3.4 Results 103
3.4.1 Henry's Law and melt composition 106
3.4.2 Correlation of empirical compositional parameters with chloride capacity 107
3.5 Discussion 111
3.5.1 The effects of H_2O on chloride capacity 111
3.6 Implications 114
3.6.1 H_2O and HCl degassing 114
3.6.2 Controls on chlorine partitioning 118
3.6.3 NaCl activities in Cl-containing silicate melts 121
3.7 Conclusions 125
3.8 Acknowledgements 127
3.9 Supplementary material 127
3.10 References 128
Chapter 4 The bonding behaviour of chlorine in silicate melts 141
4.1 Abstract 142
4.2 Introduction 144
4.2.1 Chlorine incorporation in silicate glasses 144
4.3 Methodology 150
4.3.1 Starting compositions and experimental conditions 150
4.3.2 Analytical measurement 155
4.3.3 XAF measurements 155
4.3.4 Post-run analysis and interpretation 157
4.4 Results and discussion 160
4.4.1 Interpreting salt standard spectra 164
4.4.2 Determining the effect of chemical composition on chlorine bonding 166
4.4.3 The effect of temperature, pressure, chlorine fugacity ($f(Cl_2)$) and water content on the bonding environment of Cl 179
4.5 Conclusions 181

4.6 Acknowledgements....183
4.7 References....183
Chapter 5 Conclusions and future directions....189
5.1 Conclusions....190
5.2 Future directions....193
5.2.1 Composition, temperature, and pressure effects on Cl solubility in silicate melts....194
5.2.2 Chlorine fugacities and the properties of fluids and brines....195
5.2.3 Determining the NaCl activity of silicate melts by chlorine solubility....197
5.2.4 Determining the fugacities of F, Br and I using the AgX/Ag buffer approach....198
5.3 References....199
Appendix A....205
A.1 Piston cylinder apparatus....205
A.2 Choice of capsule material....206
A.3 Pressure calibration....208
A.4 Improving the quench rate of an experiment....212
A.5 Further details for calculating chlorine fugacity ($f(Cl_2)$)....212
A.6 Reducing $f(Cl_2)$....215
A.7 Mass balancing for low $f(Cl_2)$ – Keeping enough glass to analyse....216
A.8 Derivations for calculating HCl degassing....218
A.9 Attainment of equilibrium....220
A.10 Fundamentals of X-Ray Absorption Spectroscopy (XAFS)....221
A.11 References....223
Appendix B....225
Appendix C....227

List of tables

Table 1.1	The stable halogens: a summary of their fundamental properties	3
Table 1.2	Estimates of halogen contents in terrestrial reservoirs	5
Table 1.3	Attempts at retaining the starting composition with a buffered assembly	15
Table 2.1	Silicate melt compositions used for measuring chlorine solubility.	43
Table 2.2	Experimental conditions and compositions	49
Table 3.1	Normalised silicate melt compositions used for measuring chlorine solubility	98
Table 3.2	Experimental conditions and compositions	104
Table 3.3	Normalised silicate melt compositions at water saturation	115
Table 4.1	Silicate melt compositions measured by EPMA	152
Table 4.2	Experimental conditions and measured XAF parameters	161
Table S1	Compositions of silicate glass in wt% measured by EPMA, which accompanies chapter 2	225
Table S2	Compositions of silicate glass in wt% measured by EPMA, which accompanies chapter 3	227

List of figures

Figure 1.1	CaO loss with increasing available Cl content (buffer added)…	17
Figure 1.2	Schematic graph demonstrating Raoult's law. Total vapour pressure and..	22
Figure 1.3	Schematic graph demonstrating Henry's law and Raoult's law…	23
Figure 2.1	Capsule assemblies i) CCO buffered experiments…	44
Figure 2.2	A) Composite SEM image of a typical experimental product…	45
Figure 2.3	Chlorine concentration in $An_{50}Di_{28}Fo_{22}$ melt as a function of time…	51
Figure 2.4	log*f*(Cl2) as a function of A) temperature, and B) pressure…	53
Figure 2.5	Chlorine concentration in the melt at 1400 °C and 1.5 GPa...	55
Figure 2.6	log(Cl wt% melt) as a function of oxygen fugacity, log($f(O_2)$)…	58
Figure 2.7	Plot of logK for the reaction : $0.5Cl_2 + 0.5[O^{2-}]_{melt} = [Cl^-]_{melt} + 0.25O_2$ as a function of pressure…	60
Figure 2.8	Plot of logK for the reaction : $0.5Cl_2 + 0.5[O^{2-}]_{melt} = [Cl^-]_{melt} + 0.25O_2$ versus 1/T…	61
Figure 2.9	Shows calculated HCl contents (mole fraction) of gases emitted by basalt…	66
Figure 2.10	Shows relationships between Cl_2 fugacity, O_2 fugacity and gas composition...	68
Figure 2.11	Plot of Cl contents of hydrous basalts in equilibrium with excess fluid…	72
Figure 2.11	Calculated stability of sodalite relative to nepheline as a function of Cl_2 and O_2 fugacities…	76
Figure 3.1	A schematic showing the form of the relationship between Cl content and Cl_2 fugacity…	96
Figure 3.2	This figure illustrates the minimum lengths of the Henry's Law…	106
Figure 3.3	Shows our chloride capacity data at 1.5GPa/1400^{o}C…	108
Figure 3.4	Shows the expected losses of chlorine as HCl from ascending magmas…	116
Figure 3.5	Shows the calculated $D^{f^{l/m}}$ of the same 4 compositions as in Fig 3.4 as a function of pressure (A)...	120
Figure 3.6	Shows the calculated Cl contents of the same 4 compositions as in Fig 3.4…	124

Figure 4.1 X-ray absorption fine structure (XAFS)… 159

Figure 4.2 Stacked, normalised X-ray absorption fine structure (XAFS) of compressed salt standards… 165

Figure 4.3 XAF spectra, covering a range of compositions from granite to basalt… 167

Figure 4.4 XAF Spectra showing a series of experiments with the addition of CaO (A), MgO (B)… 168

Figure 4.5 Pre-edge centroid positions shift towards higher eV with increasing 2^+ cation concentration… 170

Figure 4.6 Experimental spectra plotting in E_0 vs E_{Max} space… 172

Figure 4.7 E_{Max} increasing with A) cation and B) chloride capacity (C_{Cl})… 175

Figure 4.8 Bonding distances (Å) with the addition of… 177

Figure 4.9 Compiled XAFS measurements of a series of experiments... 180

Chapter 1

An introduction to halogen chemistry

1.1 The chemical properties of the halogens

The term 'halogen' was coined in 1842, by Swedish chemist Baron Jöns Jakob Berzelius, from the Greek words *hálas* meaning 'salt' and *genos* meaning 'come to be' to describe the elements that produce a salt with a metal. The halogens are non-metallic, highly volatile, lithophile elements (McDonough and Sun, 1995) that makeup Group 17 (in the IUPAC convention; formerly VII, VIIA) of the periodic table and include four stable elements: fluorine (F), chlorine (Cl), bromine (Br), and iodine (I) (Table 1.1); a fifth, highly unstable halogen, astatine (At), a radioactive element whose most stable isotope only has a half-life of approximately 8.1 hours (Harlov and Aranovich, 2018); and *potentially*, a sixth, artificially created halogen, element 117, Tennessine (Ts). As At is one of the rarest elements in the earth's crust due to its short half-life, and Ts is synthetically made, they have little importance geologically. They, therefore, are not considered further in the following discussions.

In their elemental form, halogens exist as diatomic molecules. However, these are relatively unstable due to their highly electronegative affinity due to a one-electron deficiency in their outer p shell (Table 1.1). Consequently, the halogens are reactive and rarely found in nature in their free elemental states and are more typically combined as halide ions (X^-) in salts, solutions and gases (Pyle and Mather, 2009). Their relative reactivities decrease with decreasing electronegativities and electron affinities from fluorine to iodine (Aiuppa et al., (2009); Table 1.1).

The halogens can form a range of chemical bonds and form purely ionic to nearly wholly covalent. The bonding becomes increasingly covalent with the increasing atomic mass of the halogen involved (i.e., Br and I; Table 1.1). Halogens can also form oxy-halogen compounds with oxygen binary compounds with hydrogen (e.g., chlorates (ClO_3^-) and HCl, respectively).

Table 1.1 The stable halogens: a summary of their fundamental properties

Halogen (Ion)	F (F^{-1})	Cl (Cl^{-1})	Br (Br^{-1})	I (I^{-1})
Atomic number	9	17	35	53
Atomic mass	18.998	35.453	79.904	126.905
Ionic radii (Å)	1.33	1.81	1.96	2.2
Electronic configuration	$(He)2s^2 2p^5$	$(Ne)3s^2 3p^5$	$(Ar)3d^{10}4s^2 4p^5$	$(Kr)4d^{10}5s^2 5p^5$
Electro-negativity	4	3	2.8	2.5
Electron affinity (kJ/mol)	-328	-349	-324.6	-295.2
Melting point / Boiling point (°C)	-219.7/-188.1	-101/34.6	7.2/58.8	113.7/184.4
50% Nebular condensation temperature (T(K) at 10 Pa)	674	472	420	-
Stable isotopes*	^{19}F (100%)	^{35}Cl (*75.78%*) ^{37}Cl (*24.22%*)	^{79}Br (*50.69%*) ^{81}Br (*49.31%*)	^{127}I (*100%*)

Data compiled by Pyle and Mather, (2009) and Hanley and Koga, (2018) using references therein, and condensation temperatures from Wood et al., (2019)
*Isotope mass and % natural abundances

1.2 Halogen abundances and distributions

Carbonaceous Ivuna (CI)-type chondrites provide a reference for the initial abundance of elements in the solar system. The halogen contents of CI chondrites (Table 1.2) decrease in the order Cl>F>Br>I (Palme and Jones, 2003; Clay et al., 2017). In the earth, however, they are typically in low concentrations, at ppm to ppb levels (Table 1.2). As shown in Table 1.2, there remain significant uncertainties in constraining the global budgets of volatile species. This is

especially true for the heavier, larger ionic radii halogens (Table 1.1), Br and I, which are typically found in ppb concentrations. This uncertainty reflects, in part, their low nebular condensation temperatures (420–674 K; Table 1.1; (Wood et al., 2019)). However, despite the uncertainties, it is notable that the halogens are concentrated within the earth's differentiated crust (Table 1.2). Fluorine is by far the most abundant halogen in all crustal and mantle reservoirs investigated, found to be 2-9 times more abundant than the second most abundant halogen, chlorine (in the bulk crust and depleted mantle, respectively). Chlorine (and to a lesser extent, Br) predominantly reside within the oceans, where Cl is the most abundant element in seawater after hydrogen and oxygen. Oceans are predicted to hold up to 73% and 51% of all terrestrial Cl and Br concentrations, respectively (Kramers, 2003). This highlights how strongly both Cl (and Br) partition into an aqueous phase, and so may also be classified as 'hydrophile' elements (Sharp et al., 2010). Less is known about I (potentially due to its low concentrations); however, it is most abundant within the upper crust (Table 1.2), potentially bound to organic materials within seabed sediments or terrestrial soils (Harvey, 1980). Some suggest that low concentrations of I in terrestrial environments might indicate partitioning into the earth's core (Jephcoat et al., 2008; Armytage et al., 2013).

Table 1.2 Estimates of halogen contents in terrestrial reservoirs

Reservoir	F (ppm)	Cl (ppm)	Br (ppb)	I (ppb)	Ref
CI chondrite	58.2 (*15%*)[a]	115 (*31%*)	189 (*38%*)	57 (*12%*)	a,b
Bulk crust	553	244	880	700	c
Upper crust	557 (*10%*)	370 (*100%*)	1600	1500 (*50%*)	c
Primitive mantle	18 (*33%*)	26 (*30%*)	76 (*33%*)	7 (*58%*)	d
Depleted mantle	11-65	0.5-7.3	20	-	c
Seawater	1.3	19,350	67,300	58	d
Volcanic-arc flux (Tg/Yr)	0.15	0.30	0.0001	0.00004	e,f
Volcanic non-arc flux (Tg/Yr)	0.58	5.50	0.0160	0.0017	e,f

Bracketed numbers in italics indicate the estimated percentage error in the value, if given by the original source

References: a- (Palme and Jones, 2003), b- (Clay et al., 2017), c - (Pyle and Mather, 2009), d - (Kendrick, 2018), e - (Gerlach, 2004), f - (Aiuppa et al., 2009) and references therein.

In natural silicate melts, the halogens are only the fourth most abundant volatile, after water, carbon dioxide, and sulphur (Symonds et al., 1994). The solubility of F, Cl, Br, and I in a silicate melt decreases with the progressive mismatch of the ionic radii of the halide ions (Table 1.1) and that of the oxygen ions, which dominate the melt structure (Bureau et al., 2000a). This mechanism means that F (1.33 Å), being very close to O and hydroxyl radii (1.40 and 1.37 Å respectively, (Shannon, 1976)) can readily substitute for O^{2-} in the silicate framework, promoting solubility in the melt; whereas, the larger I (2.20 Å) is restricted to the interstitial or network-modifier sites, impeding its solubility in the melt (Dolejš and Zajacz, 2018). This reflects what is shown in Table 1.2, with halogen concentrations decreasing with ionic radii in silicate material. It is, therefore, possible that all halogen ions join a silicate framework via

substitutions with O^{2-}. However, general observations of the differences in viscosity caused by the addition of F to silicate melts (Dingwell and Scarfe, 1985) as opposed to those induced by the addition of Cl (Dingwell and Hess, 1998; Hess et al., 2004) indicate that the substitution mechanism controlling halogen incorporation in silicate melts may vary, at least for F than Cl, and so requires further study.

Despite typically being found in low concentrations, because the halogens behave as highly incompatible elements (Edmonds et al., 2009; Pyle and Mather, 2009), they can become concentrated in the melts during igneous differentiation until incorporated into a quenched glass and minor crystalline phases such as apatite or sodalite (Sharp and Draper, 2013), or lost in a gas, or to a brine or fluid phase (discussed below).

Halogens released by volcanic emissions are thought to predominantly take the form of halogen acids (HF, HCl, HBr, and HI; Gerlach, (2004); Martin et al., (2006)). Typical volcanic gases comprise > 90% H_2O + CO_2, with < 10% SO_2 plus HCl and HF and trace amounts of H_2S, H_2, CO, HBr and HI (Pyle and Mather, 2009; Martin et al., 2012). Estimates of halogen fluxes (Table 1.2) show that low, predominantly sub-ppm levels are released from arc and non-arc volcanism. These observations are taken as evidence that the halogens are less volatile (relative to S) in volcanic systems, and of the halogens, that Cl is most likely to be expelled from a melt during degassing (Aiuppa, 2009). It is also clear that Cl is the most abundant of the volcanic halogens, followed by F, which is on average a factor ~5 times less abundant in volcanic gas (Aiuppa et al., 2009), and so remains strongly lithophile, displaying no apparent H_2O dependence in volcanic gases.

1.3 Implications of chlorine on geological processes

Despite their relatively low abundances in nature (typically < 5000 ppm (Aiuppa et al., 2009)), chlorine has been repeatedly shown to exert significant controls over a variety of geochemical processes. To demonstrate its apparent versatility, let us consider a magma ascending through a magmatic system.

Within the mantle, chlorine has been shown to influence magma genesis. For example, Filiberto and Treiman, (2009) found that on a molar basis, Cl is twice as effective as H_2O in depressing the liquidus temperatures of basalts. The mechanism in which Cl reduces the liquidus is proposed to be due to Cl-complexation with network-modifying cations (particularly, Fe, Mg and Ca), reducing the activities of these cations, whilst increasing the relative activity of SiO2 in the melt, causing depolymerisation, which results in a decrease of the liquidus. This finding was confirmed by Farcy et al., (2016), who also found that the addition of Cl to the Martian mantle lowered the crystallisation temperature, concluding that Cl is vital for the petrogenesis of Martian magmas. Although significantly less abundant in terrestrial magmas, it can be presumed that a similar process may occur here on earth within a relatively dry, lower crust and upper mantle.

As chlorine behaves incompatibly with most common minerals (Yardley et al., 2003), it is likely to remain in a melt phase during igneous differentiation throughout its ascent through the crust (Edmonds et al., 2009; Pyle and Mather, 2009). Upon interaction with a fluid phase, chlorine, which is highly soluble in aqueous and aqueous carbonic fluids (Webster et al., 2018), will begin to partition into the aqueous phase (as shown experimentally by Mathez and Webster, 2005; Stelling et al., 2008; Alletti et al., 2009; Baker and Alletti, 2012; Beermann et al., 2015). Pure H_2O has little metal transport capability; however, the addition of chloride salts

provides negatively-charged ligands that form complexes with the positively-charged metal ions (Lecumberri-Sanchez and Bodnar, 2018), and so, can sequester elements from crystallising silicate melts, forming stable neutral complexes with alkali, alkaline earth and heavy metals in aqueous solutions at magmatic temperatures and pressures (Kilinc and Burnham, 1972; Zajacz et al., 2008; Boomeri et al., 2009; Edmonds and Woods, 2018). During ascent, this process will be continuously repeated, with the exsolved volatiles depleting, or enriching the magma reservoir and country rocks, depending on the physiochemical conditions changes along their migration path (Zajacz et al., 2008).

This has the potential to result in large-scale implications, for example:

1) The addition of halide salts to H_2O modifies the Pressure-Volume-Temperature-Composition (PVTX) properties of the hydrothermal fluids, altering mineralisation processes and potentially enlarging the PT field of fluid immiscibility relative to pure H_2O (Lecumberri-Sanchez and Bodnar, 2018).

2) Selective removal of elements from a magma will also modify the polymerisation and cation activities of the melt, in turn altering the phase relations in the magma (Filiberto and Treiman, 2009b), changing the density, viscosity, and buoyancy of the melt (Dingwell and Hess, 1998; Zimova and Webb, 2006; Filiberto and Treiman, 2009a; Baasner et al., 2013).

3) Chlorine acting as a ligand with economically important metals such as Cu and Au, will promote the migration of valuable metals to the upper reaches of the magma reservoir system (Blundy et al., 2015), where it can form metal-rich hypersaline liquid reservoirs beneath active volcanoes (Blundy et al., 2021). This ability appears to be quite unique to chlorine, with some stating that the efficacy of a volatile phase to carry metals is ultimately defined by its chlorinity (Halter and Webster, 2004; Edmonds and Woods, 2018). This is supported by the

thermodynamic models of Reed and Palandri, (2006), who showed that chloride species of Fe, Zn and Pb are more stable at higher temperatures, which means that sulphides are more likely to precipitate from lower temperature hydrothermal fluids (~200°C), and the observations of Yardley and Bodnar, (2014) who suggest that chlorine is 1 to 3 orders of magnitude more abundant than all other halogens in metal-laden fluids recorded from different ore-forming environments.

4) Exsolved metals can degas into the atmosphere more efficiently when in the form of stable chloride complexes (Colson, 1992; Symonds et al., 1992; Scholtysik and Canil, 2021) as catalysts for the destruction of stratospheric ozone (von Glasow et al., 2009), and the continues degradation of the hydrosphere (Bobrowski et al., 2007).

Extending beyond the geological realm, understanding the chemical behaviour of halogens in silica-bearing melts has become important for the nuclear waste and glass/ceramics industry, where halogens are used in pyrochemical reprocessing of spent nuclear fuels, leading to the generation of halide-containing wastes (Tan and Hand, 2018a). Anionic species such as chlorides and bromides play a crucial role in melting, fining, and homogenising high-quality borosilicate glasses. At the same time, these anions are generally abundant in the nuclear wastes destined for confinement in multi-oxide borosilicate glass (the most widely employed glass for radioactive waste immobilisation). A limiting factor for these industries is the difficulty of dissolving high concentrations of chlorine into borosilicate melts which means that the volume of waste is increased to facilitate Cl dissolution. Understanding the chemical controls on halogen solubility in melts will allow for the optimisation of Cl dissolution, which is of the utmost importance for these industries.

1.4 Previous experimental work

Given their environmental, geochemical and materials importance, the need to understand how halogens dissolve in and exsolve from silicate melts has gained growing interest. Current knowledge is primarily derived experimentally and, to a lesser extent, by thermodynamic and empirical modelling, within the literature of various disciplines, from geology to glass technology, ceramics, archaeology and nuclear waste (a thorough review can be found in Webster et al., 2018).

Chlorine concentrations in the fluids of dynamic magma sources are primarily controlled by their partitioning behaviour between fluids and silicate melts (Webster et al., 2018). As such, there have been a considerable number of studies of the partitioning of Cl and other elements between silicate melts and aqueous fluids at moderate pressures and temperatures (e.g. Shinohara et al., 1989; Métrich and Rutherford, 1992; Webster, 1992; Kravchuk and Keppler, 1994; Webster and Rebbert, 1998; Bureau et al., 2000; Signorelli and Carroll, 2000; Signorelli and Carroll, 2002; Botcharnikov et al., 2007; Chevychelov et al., 2008; Stelling et al., 2008; Alletti et al., 2009; Webster et al., 2009; Zajacz et al., 2012; Alletti et al., 2014; Beermann et al., 2015; Botcharnikov et al., 2015; Webster et al., 2015). In evolving magmatic systems, Cl concentration within a silicate melt will also depend on its partitioning behaviour with minerals that interact with or crystallise from the melt. The partitioning behaviour of chlorine has also been extensively investigated, including minerals such as apatite, wadsleyite, ringwoodite, forsterite, enstatite mica and olivine (Brenan, 1993; Mathez and Webster, 2005; Chevychelov et al., 2008; Fabbrizio et al., 2013; Joachim et al., 2017; Roberge et al., 2017). The key findings of these studies show that the partitioning behaviour of Cl, and its dissolution into silicate melts is complex, as it varies with both the composition of the melt and the fluid, but also with temperature and pressure.

There is a general consensus in the literature that Cl solubility in silicate melts increases with decreasing concentrations of network-forming ions, such as Si and Al (Iwasaki and Katsura, 1967; Carroll and Webster, 1994; Webster et al., 1999; Signorelli and Carroll, 2000; Webster and De Vivo, 2002). Decreasing concentrations of network-forming ions typically correlate with increasing activities of network-modifying cations such as the alkali and alkaline earth elements. Currently, the only available model that supports the calculation of Cl solubility in silicate melts is provided by Webster et al., (2015), building from the original model from Webster and De Vivo (2002). Their empirical model applies to Cl dissolution in melts of most silicate magmas at depths of <25 km and indicates that Cl content, at fixed temperature and pressure increases with CaO, MgO and alkali contents of the coexisting silicate melts. Currently, however, these previous studies depend on the presence of an aqueous fluid or hydrosaline liquid to control the activity of Cl_2 in the silicate melt. Typically, this is done by adding chloride salts such as NaCl, KCl, $PtCl_2$, $PtCl_4$, $CaCl_2$, $MgCl_2$ and $FeCl_2$ to the silicate and determining the chlorine contents of the melts at saturation in a hydrosaline liquid with or without vapour (Webster et al., 2015). In such cases, changes in Cl solubility depend not only on the changing composition, pressure, or temperature of the silicate melt but also on the changing, variable composition of the coexisting fluid or liquid. The lack of an adequate description of Cl_2 fugacity (or activity) in either phase is the principal difficulty in comparing different data sets, except in an empirical fashion.

Despite being the focus of many studies, the chemical behaviour of chlorine in silicate melts is still not well understood. For example, the mechanism by which Cl^- dissolves into a silicate melt (the focus of chapter 2) or how Cl^- bonds within a silicate melt (the focus of chapter 4) is still not clear. This project aims to fill these gaps in our understanding.

1.5 Aims of the thesis

The influence of a volatile on a volcanic process is ultimately controlled by how much can be dissolved in the melt phase (Holloway and Wood, 1988). Therefore, to truly understand, and predict the physical and chemical properties of silicate melts, the fluids they exsolve and the glasses they form, detailed knowledge of the underlying thermodynamic processes, solubility, and speciation of halogens in silicate melts at relevant conditions are essential. The activity of any component is the ratio of the fugacity of the component to that in its standard state: $a_i^j = f_i/f_i^0$ (with component *i*, in phase *j*; Wood and Fraser, (1977)). Therefore, to calculate the thermodynamic activity of volatile elements in a melt, it is crucial to consider the fugacity of the volatile of interest. Additionally, many authors have explored the effect of oxygen fugacity ($f(O_2)$) on natural processes and have shown that prevailing redox conditions exert strong controls on magmatic phase equilibria, liquidus temperature and speciation of volatiles (Bell and Simon, (2011), and references therein). Although changes in $f(O_2)$ have been shown to have important effects on volatile exsolution, few attempts have been made to assess (or even control) the influence of oxygen fugacity on halogen solubility and partitioning in silicate melts (Webster et al., 2015; Webster et al., 2018; Webster et al., 2020) and so are often difficult to interpret.

The aims of this project are, therefore:

1) To develop an experimental methodology that will buffer both the oxygen and Cl fugacities in a silicate melt at high pressure and temperature.
2) To utilise this methodology to determine i) the dissolution mechanism of chlorine in silicate melts and ii) the effect of oxygen and chlorine fugacity, pressure, temperature, and melt composition on chlorine solubility in silicate melts.

3) To derive an equation that will allow calculation of the chlorine fugacity (and activity) in a silicate melt at a given temperature, pressure, composition, and oxygen fugacity. This will allow for Cl solubility experiments (performed at known conditions) currently in the literature to be compared to one another more accurately.
4) To use the data obtained at known conditions (temperature, pressure, and chlorine, and oxygen fugacity) to determine the conditions under which Cl degasses and forms mineral and brines in silicate melts.
5) To investigate the bonding environment of chlorine in silicate glasses over a wide range of geological relevant compositions, temperatures, and pressures.

1.6 Method development

To achieve any of the aims discussed above relies on the development of a robust experimental methodology that 1) allows for the addition of Cl at a known, and buffered chlorine and oxygen fugacity, and 2) does not change the starting silicate melt composition as the composition is likely the greatest control over chlorine solubility (as discussed above). This will allow for the effects of single independent variables on Cl solubility to be explored whilst all others remain constant. As such, much of my time spent during my PhD project has been devoted to method development. The complete method is outlined in detail in chapter 2. However, as it was written as a paper article, it did not include all the trials and tribulations that made up most of my time here. So, here is a section on what not to try. A continued discussion of methodology and method development is presented in Appendix A.

To control the fugacity of chlorine, trials began by using incompatible and noble metal chloride buffers, Ag-AgCl, Pd-$PdCl_2$, Re-$ReCl_3$ and Cu-CuCl, to produce a range of Cl fugacities whilst preventing significant amounts of the metal from joining the silicate melt under the conditions

tested. In practice, all four potential buffers control the chlorine fugacity at high values that are far too high for the basalt-like compositions used in this project. This became apparent by i) chlorine concentrations were much higher than is seen in nature, dissolving up to 9 wt% in the silicate melt (Table 1.3); ii) the generation of immiscible chloride *'blobs'* rich in Ca and Mg during the experiment with concomitant decreases in the CaO and MgO contents of the coexisting silicate melt (Table 1.3; Figure 1.1 and 2.2b). This Cl-complexation decreases the Ca and Mg-(and other potential cations) activity in the melt and increases the melt's overall Si and Al activity, polymerising the melt, altering the melt structure, and therefore the solubility of Cl at the same time.

Table 1.3 Attempts at retaining the starting composition with a buffered assembly

Experiment ID	Duration (mins)	Mass fraction buffer added	Average Cl_{glass} (wt%)	Normalised CaO (wt%)	Measured/expected CaO content
Ag+AgCl					
AgCl-001	60	5	1.07 (0.40)	16.4 (0.27)	0.95
AgCl-002	60	15	0.99 (0.70)	9.17 (0.38)	0.53
AgCl-004	60	66.66	2.06 (0.12)	3.71 (0.15)	0.21
AgCl-005	7	25	3.42 (0.72)	16.33 (0.2)	0.94
Pd+$PdCl_2$					
Pd/$PdCl_2$-001	60	5	1.27 (0.04)	15.94 (0.48)	0.92
Pd/$PdCl_2$-003	60	10	3.685 (0.05)	14.92 (0.11)	0.86
Pd/$PdCl_2$-006	60	20	3.27 (0.27)	9.95 (0.10)	0.57
Pd/$PdCl_2$-002	60	35	8.71 (5.20)	8.39 (0.50)	0.48
$PdCl_2$/CMAS-001	60	50	4.15 (0.35)	8.18 (0.10)	0.47
Re+$ReCl_3$					
Re/$ReCl_3$-001	60	20	5.082 (0.98)	14.45 (1.00)	0.83
Re/$ReCl_3$-004	60	50	4.94 (0.33)	10.98 (0.1)	0.63
Cu+CuCl					
CuCl-001	60	20	4.63 (0.64)	15.05 (1.48)	0.87
CuCl2-003	60	50	3.10 (0.15)	10.72 (0.18)	0.62
Ag+AgBr+AgCl					
AgBr/Cl-001	60	20	1.63 (0.03)	17.17 (0.14)	0.99
AgBr/Cl-003	60	50	2.79 (0.61)	16.12 (0.30)	0.93
AgBr/Cl-004	60	50	2.64 (0.09)	16.16 (0.20)	0.93
AgBr/Cl-005	60	75	2.65 (0.12)	15.00 (0.14)	0.87
Pd+PdBr+$PdCl_2$					
PdBrCl-001	60	50	2.75 (0.22)	9.45 (0.28)	0.55
Ag+AgI+AgCl					
AgI/Cl-000	60	50	2.96 (0.02)	17.4 (0.18)	1.00
AgI/Cl-005	60	75	2.55 (0.04)	17.22 (0.19)	0.99
AgI/Cl-008	60	90	1.02 (0.03)	16.9 (0.27)	0.98
Ag+AgI+AgCl - Time series					
AgI/Cl-007	5	75	2.24 (0.05)	17.10 (0.34)	0.99
AgI/Cl-002	30	75	2.74 (0.14)	17.00 (0.15)	0.98
AgI/Cl-005	60	75	2.55 (0.04)	17.22 (0.19)	0.99
AgI/Cl-006	120	75	2.56 (0.07)	17.01 (0.25)	0.99

() are errors of 2 Stdev

To suppress the formation of the chloride blobs, the chlorine fugacity had to be reduced to levels lower than these metal chlorides could provide. Therefore, we began by diluting the Cl

fugacity by incorporation of bromine in the form of Pd+PdBr+PdCl and Ag+AgBr+AgCl (Table 1.3). It was hoped that this could allow for the exploration of both Br and Cl solubility simultaneously. But, as can be seen from Figure 1.1, the addition of PdBr, only slightly suppressed the exsolution of CaO; and the addition of AgBr to the buffer retained 99% of the CaO content in starting silicate melt at low buffer fractions. Increasing the fraction of the buffer reduced the CaO retention to approximately 87% and dissolved up to 1.35 wt% Br into the silicate melt at conditions tested. Considering that halogen solubility is predicted to decrease with increasing ionic radii (Bureau et al., 2000a) and that Ag provided the most promising results when combined with Br, we finally settled on mixed ratios of AgI:AgCl. Using this buffering mixture ensures that the starting composition remains unchanged (within the uncertainties of the analysis) with >98% CaO (and >99% MgO) retained, and also the solubility of I was found to be negligible, of order 0.1 wt% and did not vary over the buffer fractions tested. Finally, as can be seen from Figure 1.1 and Table 1.3, the loss of Ca (and Mg) was found to vary with time; with an experiment performed for approximately 7 minutes using the Ag+AgCl buffer retaining 94% of its CaO, significantly more than that of a similar buffer mixture that ran for an hour. This suggests that this buffer had not reached equilibrium within the melt. Therefore, as a final test, using the AgI+AgCl buffer, we performed a time series of experiments that are outlined in chapter 2. This showed that by using the buffer AgI+AgCl, there was no change in the silicate composition at all experimental durations tested (5 to 120 minutes). We can, therefore, confidently vary the chlorine fugacity by mixing AgCl, AgI and Ag at various ratios, forming a “sliding” chlorine buffer. At the temperature of the experiment,

both melt to form -two additional liquids (metal and halide), both of which are immiscible with one another and with the silicate melt (Figure 2.2).

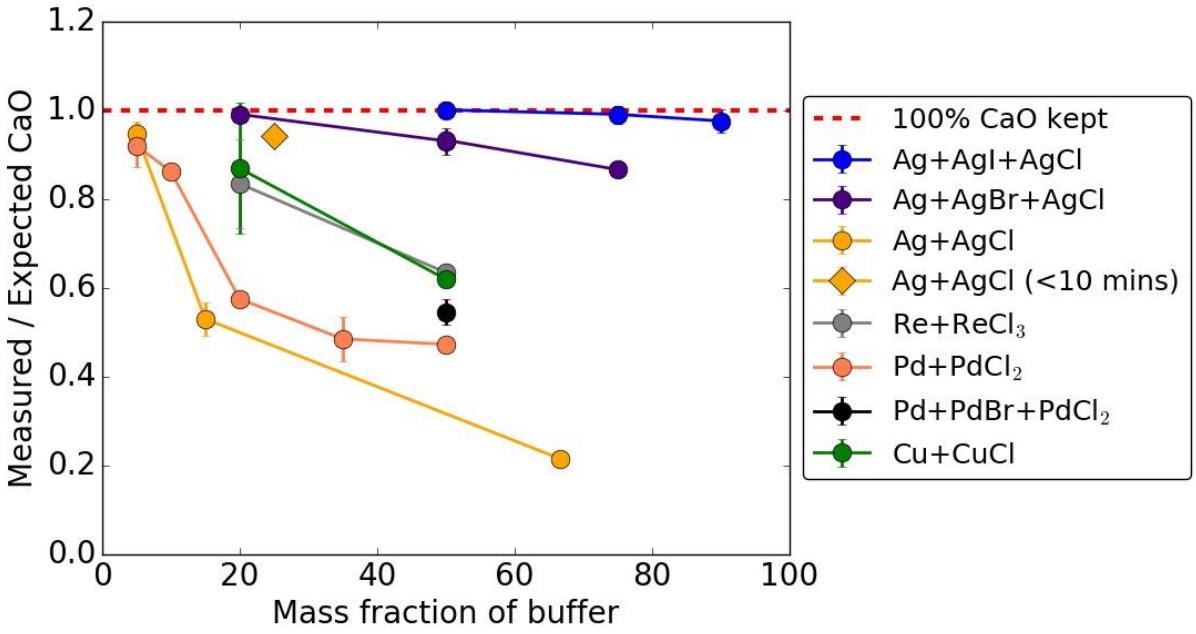


Figure 1.1 CaO loss with increasing available Cl content (buffer added). All experiments were performed for 1 hour at 1400 °C, 1.5GPa and held at the C-CO2 buffer. There is a marked decrease in alkaline earth elemental loss by diluting Cl fugacity with Br (Purple) and I (Blue). 1 experiment was run for <10 minutes using the Ag+AgCl buffer (orange diamond).

1.7 Thermodynamic concepts

This thesis includes a lot of thermodynamic definitions and calculations. Therefore, I feel it constructive to include a section detailing the meanings of the key parameters used throughout this thesis.

System: This is a loosely defined term, which covers whatever we wish to consider our system, the boundary of the system can be fixed at will. This can be homogeneous (e.g., a single phase), or heterogenous, (e.g., a rock).

Phase: Physically homogenous substance, this is an idealisation which some substances closely approach, such as water or air. This is a macroscopic concept that presupposes a limit to scale homogeneity. A zoned tourmaline for example would not represent a single phase.

Intensive properties: The value of the whole is the same for any of its parts, and is thus independent of amount present, for example temperature, density, colour.

Extensive properties: The value of the whole is the sum of the value of the parts. For example, mass, and volume.

Equilibrium: Is an idealised concept, whereby something is in equilibrium if physical properties do not change during the period of observation. In other words, chemical equilibrium is the state that indicates that the concentrations of reactants and products no longer change in a reaction.

Equilibrium constant: is the ratio of the concentration of products to the concentration of reactants for a reaction that is in chemical equilibrium. This is used to quantitatively analyse the equilibrium state of a given reaction. For example:

$$aA + bB \leftrightarrow cC + dD$$

The equilibrium constant (K) is defined as

$$K = \frac{[C]^c[D]^d}{[A]^a[B]^b}$$

Where the square brackets indicate the concentration of the species, and the exponent is the stoichiometric factor. The derivation and use of the equilibrium constant relies on two assumptions: i) it is assumed that all solids behave as pure solids, i.e. [A] = 1, thus eliminating them from the equations. Only reactants and products in the gas phase or solutions appear in the expression; and ii) it assumes that all gases behave ideally, meaning that their concentration

is equal to the partial pressure which is equal to the fugacity: $[A] = P_A = f_A$. The thermodynamic definition of the equilibrium constant is:

$$K = exp\left(-\frac{\Delta G_f^0}{RT}\right)$$

Where ΔG_f^0 is the Guvvs energy of formation at a given T_0 (298.15 K), R is the gas constant, and T is temperature (in K). The equilibrium constant of a given reaction can be determined by thermodynamic databases, by:

$$log(K_{Reaction}) = \sum log(K_{Products}) - \sum log(K_{Reactants})$$

Fugacity: Unfortunately, in chemistry, real gases deviate from their *'ideal'* properties, especially at high pressures. Fugacity is an empirically derived parameter that adjusts for this deviation from ideality. It measures the effective pressure of a gas for a given pressure or partial pressure of that gas, in equilibrium terms of the other variables of the ideal gas law.

An ideal gas is defined by the gas law:

$$PV = nRT$$

Where P is the pressure in Pascals (Pa), V is the volume (m^3), n is the number of moles, R is the gas constant (8.3145 J/mol K), and T is the temperature in K. As the fugacity of a real gas is an effective partial pressure which replaces the mechanical partial pressure of an ideal gas; then fugacity is equal to the pressure of an ideal gas which has the same temperature and molar Gibbs free energy as the real gas.

The Gibbs free energy, G, is the maximum reversible work that may be performed by a thermodynamic system at a constant temperature and pressure:

$$\Delta G = -S\Delta T + V\Delta P$$

Where S is entropy, and V is volume (m^3) and P is pressure (Pa).

$$\Delta G = V\Delta P$$

$$G(P) - G(P^0) = \int_{P^0}^{P} V\Delta P = nRT \int_{P_0}^{P} \frac{1}{P}\Delta P G(P) = G(P^0) + nRT\ ln\left(\frac{P}{P^0}\right)$$

$$\mu = \mu_i + RT\ ln\left(\frac{P}{P^0}\right)$$

No gas is ideal, so we make a correction, and replace the "P's" with "f's"

$$\mu = \mu_i + RT\ ln\left(\frac{f}{f_0}\right)$$

Where μ_i is the chemical potential of component *i* at P, T and X_i . Fugacity (*f*) is essentially a corrected pressure, and therefore is closely related to activity (*a*), which defines a corrected concentration.

$$f = \gamma_i P_i$$

Where γ_i is the activity coefficient of component *i* in a given phase.

$$a_i = \gamma_i X_i$$

Where a_i is the activity of component i, and X_i is the mol fraction of *i*.

Partial molar volume: This is the change in volume of a mixture per mole of a given substance added to a mixture of large volume.

Solubility: This is simply the degree to which a given element can dissolve into a solvent to make a solution, typically expressed as wt% (Weight percent) or ppm (parts per million). In this thesis, the chlorine solubility defines the maximum content of chlorine that can be dissolved in a silicate melt that is in equilibrium with a gas mixture (Cl_2 gas), at a given temperature and pressure. If a substance is dissolved into a solution to an extent in which no more solute can be dissolved, at a given temperature, pressure, oxygen fugacity and composition, it is said to be *saturated*.

Capacity: This is essentially a correction on solubility, which varies as a function of temperature (T), pressure (P), fugacities of both the element of interest and oxygen, and melt composition. Chloride capacity of the melt, as described in this thesis (3.5) may also be thought of as analogous to the equilibrium constant for reaction (2.17).

Partitioning: Elements that are typically found in low concentrations, and unable to build their own minerals, can instead enter a mineral structure or other phase; with some elements becoming incorporated into a phase preferentially over another. This process is known as partitioning, which can be described by the partition coefficient, D:

$$D = \frac{C_a}{C_b}$$

The partition coefficient is therefore the concentration (C) ratio of an element between two phases (a and b in this example). It asserts that each component of an ideal mixture of liquids has a partial pressure equal to the vapour pressure of the pure component (liquid or solid) multiplied by its mole fraction in the mixture.

Raoult's Law: The ratio of the partial vapour pressure of each component (P_i) is equal to the vapour pressure of a pure liquid, $\frac{P_i}{P_i^\circ}$, multiplied by the mole fraction of a given element (X_i) in the liquid mixture:

$$P_i = X_i P_i^\circ$$

Mixtures that obey the law throughout a compositional range from pure *a* to pure b are denoted as *'ideal solutions'*, this is shown graphically in figure 1.2:

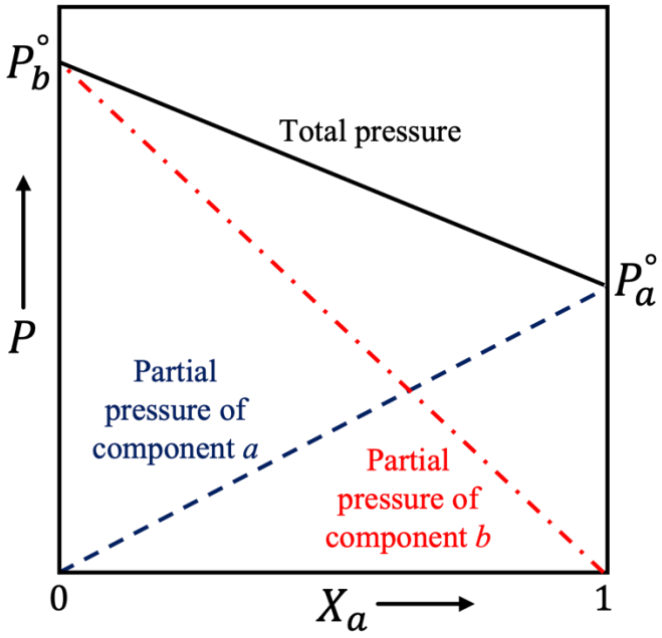


Figure 1.2 Schematic graph demonstrating Raoult's law. Total vapour pressure and the two partial vapour pressures of an ideal mixture are proportional to the mole fractions of the components (Figure adapted from Atkins and De Paula, (2017)).

Henrys Law: Is a gas a law that states that the solubility of a gas in a liquid is directly proportional to the partial pressure of the gas above the liquid:

$$X_i = P_i K_i$$

Where X_i is the mol fraction of the solute, P_i is the partial pressure of the gas (Pa or units of atm) and K_i is an empirical constant, which represents the mixtures in which the solute obeys Henry's law, and the solvent obeys Raoul's law are defined as *'ideal-dilute solutions'*.

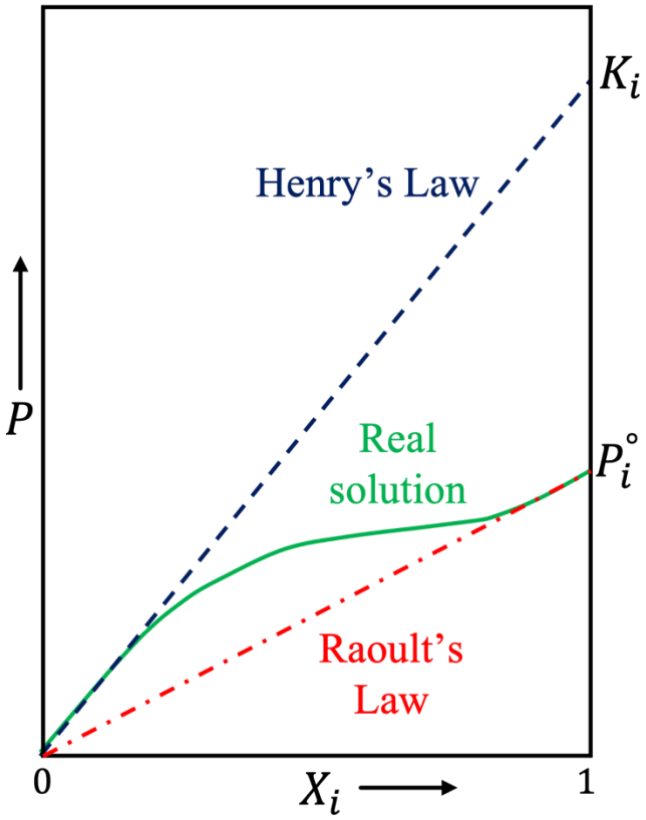


Figure 1.3 Schematic graph demonstrating Henry's law and Raoult's law. When a component is nearly pure (the solvent), its vapour pressure is proportional to its molar volume with slope P_i° (Raoult's law), when it's a minor component (the solute) its vapour pressure is still proportional to the mole fraction, but the constant of proportionality is now K_i (Henry's law). (Figure adapted from Atkins and De Paula, (2017)).

1.8 Structure and contributions of this thesis

This thesis is presented in an integrated format. As such, each data chapter has been written as an individual and stand-alone article, with their own introductions, methodologies, results, and discussions. In this regard, I have attempted to resolve my above aims as follows:

Chapter 2: *The chemical behaviour of chlorine in silicate melts* outlines the development of a new methodology in which both Cl and O fugacity are controlled and varied at geologically relevant conditions. Results- indicated that Cl joins the melt by the reaction: $Cl_2 + [O^{2-}] = 2[Cl^-] + 0.5O_2$. To accurately determine the effects of pressure and temperature on Cl solubility, their effects on the Cl and oxygen buffer required correcting. This was achieved by correcting the Cl concentration in the melt to a constant ratio of $f(Cl_2)^{0.5}$:$f(O_2)^{0.25}$. The corrected data set was then used to determine the conditions under which Cl degasses from basaltic melts and the conditions under which sodalite is likely to form.

This chapter has been published as: Thomas R. W. and Wood B. J. (2021) The chemical behaviour of chlorine in silicate melts. *Geochim. Cosmochim. Acta* **294**, 28–42.

Chapter 3: *The effect of composition on chlorine solubility and behaviour in silicate melts* utilises the methodology outlined in Chapter 2 to accurately determine how Cl solubility changes as a function of composition, covering a range of compositions from granitic to basaltic, at a constant temperature, pressure, and oxygen fugacity, using identical Cl buffer mixtures. The results were used to define a chloride capacity (C_{Cl}) for each melt at the pressure and temperature of the experiment: $C_{Cl} = \frac{Cl\ (wt\%)}{\sqrt{f(Cl_2)}} \times \sqrt[4]{f(O_2)}$. This allows for data sets from the literature to be treated in a consistent way and was subsequently used to derive an equation to determine chlorine capacity at a given pressure, temperature, Cl and O fugacity, and

composition, including water. This allowed for calculation of the degassing path of Cl from a range of compositionally different melts, building on what was done in chapter 2.

This chapter is currently under review as: Thomas R. W. and Wood B. J. (In review) The effect of composition on chlorine solubility and behaviour in silicate melts. *Am. Mineral.*

Chapter 4: *The bonding behaviour of chlorine in silicate melts,* analysed the experiments performed and outlined in chapters 2 and 3 by X-ray absorption spectroscopy, to explore the bonding environment of Cl in the silicate melt, and to determine how bonding changes as a function of temperature, pressure, and composition. Results indicate that chlorine predominantly bonds with 2^+ cations but can form strong covalent bonds with Si, in 2^+ cation poor compositions such as granites and rhyolites.

This chapter is currently in preparation for submission to Chemical Geology as: Thomas R. W., Wade J., Matzen, A K., and Wood B. J. (In prep) The bonding behaviour of chlorine in silicate melts by X-ray absorption spectroscopy.

Chapter 5: *Conclusions, and further work,* provides a summation of this project's key findings and outlines future directions that can be taken.

1.9 References

Aiuppa A. (2009) Degassing of halogens from basaltic volcanism: Insights from volcanic gas observations. *Chem. Geol.* **263**, 99–109.

Aiuppa A., Baker D. R. and Webster J. D. (2009) Halogens in volcanic systems. *Chem. Geol.* **263**, 1–18.

Alletti M., Baker D. R., Scaillet B., Aiuppa A., Moretti R. and Ottolini L. (2009) Chlorine

partitioning between a basaltic melt and H 2 O–CO 2 fluids at Mount Etna. *Chem. Geol.* **263**, 37–50.

Alletti M., Burgisser A., Scaillet B. and Oppenheimer C. (2014) Chloride partitioning and solubility in hydrous phonolites from Erebus volcano: A contribution towards a multi-component degassing model. *GeoResJ* **3**–**4**, 27–45.

Armytage R. M. G., Jephcoat A. P., Bouhifd M. A. and Porcelli D. (2013) Metal–silicate partitioning of iodine at high pressures and temperatures: Implications for the Earth's core and 129*Xe budgets. *Earth Planet. Sci. Lett.* **373**, 140–149.

Atkins P. and De Paula J. (2017) Atkin's physical chemistry. **9th ed**., *Oxford University Press*, Oxford.

Baasner A., Schmidt B. C. and Webb S. L. (2013) The effect of chlorine, fluorine and water on the viscosity of aluminosilicate melts. *Chem. Geol.* **357**, 134–149.

Baker D. R. and Alletti M. (2012) Fluid saturation and volatile partitioning between melts and hydrous fluids in crustal magmatic systems: The contribution of experimental measurements and solubility models. *Earth-Science Rev.* **114**, 298–324.

Beermann O., Botcharnikov R. E. and Nowak M. (2015) Partitioning of sulfur and chlorine between aqueous fluid and basaltic melt at 1050°C, 100 and 200 MPa. *Chem. Geol.* **418**, 132–157.

Bell A. S. and Simon A. (2011) Experimental evidence for the alteration of the Fe3+/ΣFe of silicate melt caused by the degassing of chlorine-bearing aqueous volatiles. *Geology* **39**, 499–502.

Blundy J., Afanasyev A., Tattitch B., Sparks S., Melnik O., Utkin I. and Rust A. (2021) The economic potential of metalliferous sub-volcanic brines. *R. Soc. Open Sci.* **8**.

Blundy J., Mavrogenes J., Tattitch B., Sparks S. and Gilmer A. (2015) Generation of porphyry copper deposits by gas-brine reaction in volcanic arcs. *Nat. Geosci.* **8**, 235–240.

Bobrowski N., von Glasow R., Aiuppa A., Inguaggiato S., Louban I., Ibrahim O. W. and Platt U. (2007) Reactive halogen chemistry in volcanic plumes. *J. Geophys. Res.* **112**, 1–17.

Boomeri M., Nakashima K. and Lentz D. R. (2009) The Miduk porphyry Cu deposit, Kerman, Iran: A geochemical analysis of the potassic zone including halogen element systematics related to Cu mineralization processes. *J. Geochemical Explor.* **103**, 17–29.

Botcharnikov R. E., Holtz F. and Beherens H. (2007) The effect of CO2 on the solubility of H2O-Cl fluids in andesitic melt. *Eur. J. Mineral.* **19**, 671–680.

Botcharnikov R. E., Holtz F. and Behrens H. (2015) Solubility and fluid–melt partitioning of H2O and Cl in andesitic magmas as a function of pressure between 50 and 500 MPa. *Chem. Geol.* **418**, 117–131.

Brenan J. M. (1993) Partitioning of fluorine and chlorine between apatite and aqueous fluids at high pressure and temperature: implications for the F and Cl content of high P-T fluids. *Earth Planet. Sci. Lett.* **117**, 251–263.

Bureau H., Keppler H. and Métrich N. (2000) Volcanic degassing of bromine and iodine: experimental fluid/melt partitioning data and applications to stratospheric chemistry. *Earth Planet. Lett.* **189**, 51–60.

Carroll M. R. and Webster J. D. (1994) Solubilities of sulfur, noble gases, nitrogen, chlorine, and fluorine in magmas. *Mineral. Soc. Am. Rev. Mineral.* **30**, 231 –279.

Chevychelov V. Y., Bocharnikov R. E. and Holtz F. (2008) Experimental study of chlorine and fluorine partitioning between fluid and subalkaline basaltic melt. *Dokl. Earth Sci.* **422**, 1089–1092.

Clay P. L., Burgess R., Busemann H., Ruzié-Hamilton L., Joachim B., Day J. M. D. and Ballentine C. J. (2017) Halogens in chondritic meteorites and terrestrial accretion. *Nat. Publ. Gr.* **551**, 614–618.

Colson R. O. (1992) Mineralization on the Moon?: Theoretical considerations of Apollo 16

"rusty rocks", sulfide replacement in 67016, and surface-correlated volatiles on lunar volcanic glass. *Proc. Lunar Planet. Sci.* **22**, 427–436.

Dingwell D. B. and Hess K. U. (1998) Melt viscosities in the system Na-Fe-Si-O-F-Cl: Contrasting effects of F and Cl in alkaline melts. *Am. Mineral.* **83**, 1016–1021.

Dingwell D. B. and Scarfe C. M. (1985) Chemical diffusion of fluorine in melts in the system Na2O-Al2O3-SiO2. *Earth Planet. Sci. Lett.* **73**, 377–384.

Dolejš D. and Zajacz Z. (2018) Chapter 7 Halogens in Silicic Magmas and Their Hydrothermal Systems. In *The Role of Halogens in Terrestrial and Extraterrestrial Geochemical Processes* pp. 431–543.

Edmonds M., Gerlach T. M. and Herd R. A. (2009) Halogen degassing during ascent and eruption of water-poor basaltic magma. *Chem. Geol.* **263**, 122–130.

Edmonds M. and Woods A. W. (2018) Exsolved volatiles in magma reservoirs. *J. Volcanol. Geotherm. Res.* **368**, 13–30.

Evans K. A., Mavrogenes J. A., O'Neill H. S., Keller N. S. and Jang L. Y. (2008) A preliminary investigation of chlorine XANES in silicate glasses. *Geochemistry, Geophys. Geosystems* **9**, 1–15.

Fabbrizio A., Stalder R., Hametner K. and Günther D. (2013) Experimental chlorine partitioning between forsterite, enstatite and aqueous fluid at upper mantle conditions. *Geochim. Cosmochim. Acta* **121**, 684–700.

Farcy B. J., Gross J., Carpenter P., Hicks J. and Filiberto J. (2016) Effect of chlorine on near-liquidus crystallization of olivine-phyric shergottite NWA 6234 at 1 GPa: Implication for volatile-induced melting of the Martian mantle. *Meteorit. Planet. Sci.* **51**, 1–12.

Filiberto J. and Treiman A. H. (2009a) Martian magmas contained abundant chlorine, but little water. *Geology* **37**, 1087–1090.

Filiberto J. and Treiman A. H. (2009b) The effect of chlorine on the liquidus of basalt: First

results and implications for basalt genesis on Mars and Earth. *Chem. Geol.* **263**, 60–68.

Gerlach T. M. (2004) Volcanic sources of tropospheric ozone-depleting trace gases. *Geochemistry, Geophys. Geosystems* **5**, 1–16.

von Glasow R., Bobrowski N. and Kern C. (2009) The effects of volcanic eruptions on atmospheric chemistry. *Chem. Geol.* **263**, 131–142.

Halter W. E. and Webster J. D. (2004) The magmatic to hydrothermal transition and its bearing on ore-forming systems. *Chem. Geol.* **210**, 1–6.

Hanley J. J. and Koga K. T. (2018) Halogens in Terrestrial and Cosmic Geochemical Systems : Abundances, Geochemical Behaviors, and Analytical Methods. In *The Role of Halogens in Terrestrial and Extraterrestrial Geochemical Processes* (eds. D. E. Harlov and L. Aranovich). Springer Geochemistry. pp. 21–121.

Harlov D. E. and Aranovich L. (2018) The Role of Halogens in Terrestrial and Extraterrestrial Geochemical Processes: Surface, Crust, and Mantle. In *The Role of Halogens in Terrestrial and Extraterrestrial Geochemical Processes* (eds. D. E. Harlov and L. Aranovich). Springer Geochemistry. pp. 1–19.

Harvey G. R. (1980) A Study of the chemistry of iodine and bromine in marine sediments. *Mar. Chem.* **8**, 327–332.

Hess K. U., Dingwell D. B., Potuzak M. and Courtial P. (2004) The effect of halogens (F, Cl, Br, I) on the viscosity-temperature behaviour of a silicate melt. In *Lithos* p. S50.

Holloway J. R. and Wood B. J. (1988) *Simulating the Earth: Experimental Geochemistry*.,

Iwasaki B. and Katsura T. (1967) The solubility of hydrogen chloride in volcanic rock melts at a total pressure of one atmosphere and at temperatures of 1200°C and 1290°C under anhydrous conditions. *Bull. Chem. Soc. Jpn.* **40**, 554–561.

Jephcoat A. P., Ali Bouhifd M. and Porcelli D. (2008) Partitioning experiments in the laser-heated diamond anvil cell: volatile content in the Earth's core. *Philos. Trans. R. Soc.* **366**,

4295–4314.

Joachim B., Stechern A., Ludwig T., Konzett J., Pawley A., Ruzié-Hamilton L., Clay P. L., Burgess R. and Ballentine C. J. (2017) Effect of water on the fluorine and chlorine partitioning behavior between olivine and silicate melt. *Contrib. to Mineral. Petrol.* **172**, 1–15.

Kendrick M. A. (2018) Halogens in Seawater, Marine Sediments and the Altered Oceanic Lithosphere. In *The Role of Halogens in Terrestrial and Extraterrestrial Geochemical Processes* (eds. D. E. Harlov and L. Aranovich). Springer Geochemistry. pp. 591–648.

Kilinc I. A. and Burnham C. W. (1972) Partitioning of chloride between a silicate melt and coexisting aqueous phase from 2 to 8 kilobars 1. *Econ. Geol.* **67**, 231–235.

Kramers J. D. (2003) Volatile element abundance patterns and an early liquid water ocean on Earth. *Precambrian Res.* **126**, 379–394.

Kravchuk I. F. and Keppler H. (1994) Distribution of chloride between aqueous fluids and felsic melts at 2 kbar and 800°C. *Eur. J. Mineral.* **6**, 913–923.

Lecumberri-Sanchez P. and Bodnar R. J. (2018) Halogen geochemistry of ore deposits: Contributions towards understanding sources and processes. In *The Role of Halogens in Terrestrial and Extraterrestrial Geochemical Processes* (eds. D. E. Harlov and L. Aranovich). Springer Geochemistry. pp. 261–305.

Martin R. S., Mather T. A. and Pyle D. M. (2006) High-temperature mixtures of magmatic and atmospheric gases. *Geochemistry, Geophys. Geosystems* **7**, 1–14.

Martin R. S., Wheeler J. C., Ilyinskaya E., Braban C. F. and Oppenheimer C. (2012) The uptake of halogen (HF, HCl, HBr and HI) and nitric (HNO3) acids into acidic sulphate particles in quiescent volcanic plumes. *Chem. Geol.* **296**–**297**, 19–25.

Mathez E. A. and Webster J. D. (2005) Partitioning behavior of chlorine and fluorine in the system apatite-silicate melt-fluid.

McDonough W. F. and Sun S. s (1995) The composition of the Earth. *Chem. Geol.* **120**, 223–253.

Métrich N. and Rutherford M. J. (1992) Experimental study of chlorine behavior in hydrous silicic melts. *Geochemica Cosmochim. Acta* **56**, 607–616.

Palme H. and Jones A. (2003) Solar system abundances of the elements. *Treatise on Geochemistry* **1**, 41–61.

Pyle D. M. and Mather T. A. (2009) Halogens in igneous processes and their fluxes to the atmosphere and oceans from volcanic activity: A review. *Chem. Geol.* **263**, 110–121.

Reed M. H. and Palandri J. (2006) Sulfide Mineral Precipitation from Hydrothermal Fluids. *Rev. Mineral. Geochemistry* **61**, 609–631.

Roberge M., Bureau H., Bolfan-Casanova N., Raepsaet C., Surble S., Khodja H., Auzende A.-L., Cordier P. and Fiquet G. (2017) Chlorine in wadsleyite and ringwoodite: An experimental study. *Earth Planet. Sci. Lett.* **467**, 99–107.

Scholtysik R. and Canil D. (2021) The effects of S , Cl and oxygen fugacity on the sublimation of volatile trace metals degassed from silicate melts with implications for volcanic emissions. *Geochim. Cosmochim. Acta* **In Press**.

Shannon R. D. (1976) Revised effective ionic radii and systematic studies of interatomie distances in halides and chaleogenides. *Acta Crystallogr.* **32**, 751–767.

Sharp Z. D., Barnes J. D., Fischer T. P. and Halick M. (2010) An experimental determination of chlorine isotope fractionation in acid systems and applications to volcanic fumaroles. *Geochim. Cosmochim. Acta* **74**, 264–273.

Sharp Z. D. and Draper D. S. (2013) The chlorine abundance of Earth: Implications for a habitable planet. *Earth Planet. Sci. Lett.* **369**–**370**, 71–77.

Shinohara H., Iiyama J. T. and Matsuo S. (1989) Partition of chlorine compounds between silicate melt and hydrothermal solutions: I. Partition of NaCl-KCl. *Geochim. Cosmochim.*

Acta **53**, 2617–2630.

Signorelli S. and Carroll M. R. (2002) Experimental study of Cl solubility in hydrous alkaline melts: constraints on the theoretical maximum amount of Cl in trachytic and phonolitic melts. *Contrib. to Miner. Petrol.* **143**, 209–218.

Signorelli S. and Carroll M. R. (2000) Solubility and fluid-melt partitioning of Cl in hydrous phonolitic melts. *Geochim. Cosmochim. Acta* **64**, 2851–2862.

Stelling J., Botcharnikov R. E., Beermann O. and Nowak M. (2008) Solubility of H2O-and chlorine-bearing fluids in basaltic melt of Mount Etna at T = 1050–1250 °C and P = 200 MPa. *Chem. Geol.* **256**, 102–110.

Symonds R. B., Reed M. H. and Rose W. I. (1992) Origin, speciation, and fluxes of trace-element gases at Augustine volcano, Alaska: insights into magma degassing and fumarolic processes. *Geochim. Cosmochim. Acta* **56**, 633–657.

Symonds R. B., Rose W. I., Bluth G. J. S. and Gerlach T. M. (1994) Volcanic-gas studies: methods, results and applications. In *Reviews in Mineralogy and Geochemistry* (eds. M. R. Carroll and J. R. Holloway). pp. 1–66.

Tan S. and Hand R. J. (2018) Incorporation and phase separation of Cl in alkaline earth aluminosilicate glasses. *J. Nucl. Mater.* **507**, 135–144.

Webster J. D. (1992) Fluid-melt interactions involving Cl-rich granites: Experimental study from 2 to 8 kbar. *Geochim. Cosmochim. Acta* **56**, 659–678.

Webster J. D., Baker D. R. and Aiuppa A. (2018) Halogens in Mafic and Intermediate-Silica Content Magmas. In *The Role of Halogens in Terrestrial and Extraterrestrial Geochemical Processes* (eds. D. E. Harlov and L. Aranovich). Springer Geochemistry. pp. 307–430.

Webster J. D., Iveson A. A., Rowe M. C. and Webster P. M. (2019) Chlorine and felsic magma evolution: Modeling the behavior of an under-appreciated volatile component. *Geochim.*

Cosmochim. Acta, 248–288.

Webster J. D., Kinzler R. J. and Mathez E. A. (1999) Chloride and water solubility in basalt and andesite melts and implications for magmatic degassing. *Geochim. Cosmochim. Acta* **63**, 729–738.

Webster J. D. and Rebbert C. R. (1998) Experimental investigation of H2O and Cl- solubilities in F-enriched silicate liquids; implications for volatile saturation of topaz rhyolite magmas. *Contrib. to Mineral. Petrol.* **132**, 198–207.

Webster J. D., Sintoni M. F. and De Vivo B. (2009) The partitioning behavior of Cl, S, and H2O in aqueous vapor- ±saline-liquid saturated phonolitic and trachytic melts at 200 MPa. *Chem. Geol.* **263**, 19–36.

Webster J. D., Vetere F., Botcharnikov R. E., Goldoff B., McBirney A. and Doherty A. L. (2015) Experimental and modeled chlorine solubilities in aluminosilicate melts at 1 to 7000 bars and 700 to 1250 °c: Applications to magmas of Augustine Volcano, Alaska. *Am. Mineral.* **100**, 522–535.

Webster J. D. and De Vivo B. (2002) Experimental and modeled solubilities of chlorine in aluminosilicate melts, consequences of magma evolution, and implications for exsolution of hydrous chloride melt at Mt. Somma-Vesuvius. *Am. Mineral.* **87**, 1046–1061.

Wood B. J. and Fraser D. G. (1977) *Elementary thermodynamics for geologists*., Oxford University Press, Oxford.

Wood B. J., Smythe D. J. and Harrison T. (2019) The condensation temperatures of the elements: A reappraisal. *Am. Mineral.* **104**, 844–856.

Yardley B., Bennett A. and Banks D. (2003) Controls on the chemical composition of crustal brines. *J. Geochemical Explor.* **78**–**79**, 133–135.

Yardley B. W. D. and Bodnar R. J. (2014) Fluids in the continental crust. *Geochemical Perspect.* **3**, 1–127.

Zajacz Z., Candela P. A., Piccoli P. M. and Sanchez-Valle C. (2012) The partitioning of sulfur and chlorine between andesite melts and magmatic volatiles and the exchange coefficients of major cations. *Geochim. Cosmochim. Acta* **89**, 81–101.

Zajacz Z., Halter W. E., Pettke T. and Guillong M. (2008) Determination of fluid/melt partition coefficients by LA-ICPMS analysis of co-existing fluid and silicate melt inclusions: Controls on element partitioning. *Geochim. Cosmochim. Acta* **72**, 2169–2197.

Zimova M. and Webb S. (2006) The effect of chlorine on the viscosity of Na2O-Fe2O3-Al2O3-SiO2 melts. *Am. Mineral.* **91**, 344–352.

Chapter 2

The chemical behaviour of chlorine in silicate melts

This chapter has been published as the following:

Thomas R. W. and Wood B. J. (2021) The chemical behaviour of chlorine in silicate melts. *Geochimica et Cosmochimica Acta.* **294**, 28–42.

2.1 Abstract

We have performed experiments at 0.5-2GPa and 1200-1500 ˚C to investigate the dissolution behaviour of chlorine in silicate melts. The experiments were performed with chlorine fugacities controlled by mixtures of Ag, AgCl and AgI and oxygen fugacity buffered at C-CO-CO_2 (CCO) and Re-ReO_2. The results demonstrate that the initial chlorine dissolution mechanism involves the replacement of O^{2-} in the silicate melt by two dissociated Cl^- ions according to the reaction:

$$Cl_2 + [O^{2-}]_{melt} = 2[Cl^-]_{melt} + 0.5O_2$$

The same dissolution mechanism applies to hydrous, fluid-saturated basalt at 100-200 MPa/1050ºC. Experiments using both an Fe-free haplobasaltic composition ($An_{50}Di_{28}Fo_{22}$) and an Icelandic basalt followed the predicted dependence of Cl concentration on $f(Cl_2)^{0.5}$ and $f(O_2)^{0.25}$. This Henrian behaviour extends from 0 to at least 2.6 wt% Cl dissolved in the haplobasaltic composition, 1.6 wt% Cl in anhydrous basalt and ~1.5 wt% Cl in fluid-saturated basalt. Deviations from Henry's Law behaviour at higher concentrations are consistent with progressive association of Cl^- ions. In the Henry's Law region Cl concentration in the $An_{50}Di_{28}Fo_{22}$ composition is given by (wt%):

$$logCl_{melt} = 1.206(32) - \frac{940(40)\mathrm{P}}{\mathrm{T}} - 0.25log\left(f(O_2)\right) + 0.5log\left(f(Cl_2)\right)$$

P is in GPa, T in kelvin, values in brackets are 1 standard error, and $f(Cl_2)$ and $f(O_2)$ refer to standard states of pure gas at 0.1MPa and the temperature of interest. For the natural anhydrous basalt, we obtain:

$$logCl_{melt} = 0.984(64) - \frac{930(70)\mathrm{P}}{\mathrm{T}} - 0.25log\left(f(O_2)\right) + 0.5log\left(f(Cl_2)\right)$$

By considering the P-T dependences of the Cl contents of melts we find that the concentrations observed in nature are extremely stable in basalt to very low pressures. Basalts containing the typical concentration range of 0.05-0.5 wt% Cl should, for example, only begin to degas their chlorine significantly, as HCl, at pressures in the range 0-5MPa. Data on hydrous, fluid-saturated basalt at 100-200 MPa are, when corrected for dissolution of Ca, Na and K in the fluid, broadly consistent with our results for anhydrous basalt.

Finally, we use recently evaluated thermodynamic data for sodalite ($Na_4Al_3Si_3O_{12}Cl$) to calculate the conditions under which this phase would stabilise in trachytes and phonolites. We find that the appearance of sodalite as a liquidus phase reflects a combination of low liquidus temperature and high Na_2O activity rather than unusually high chlorine fugacity.

2.2 Introduction

Chlorine is an important volatile component in magmas, exerting significant controls on the properties of silicate melts including diffusion, density, viscosity and phase equilibria (Dingwell and Hess, 1998; Zimova and Webb, 2006; Filiberto and Treiman, 2009a; Baasner et al., 2013). Filiberto and Treiman, (2009b) have, for example demonstrated that addition of chlorine to model Martian basalt suppresses the liquidus temperature by amounts comparable, on a weight basis, to those of H_2O. On a molar basis, this means that chlorine has twice as great an effect on liquidus temperature as water. In addition to these effects on melt properties, chlorine is an important ligand in high-temperature hydrothermal fluids, forming soluble complexes with economically important metals such as Cu and Au (Blundy et al., 2015). Volcanogenic chlorine, degassed principally as HCl (Gerlach, 2004) also impacts the atmosphere and hydrosphere, perturbing tropospheric and stratospheric ozone budgets (Bobrowski et al., 2007; Aiuppa et al., 2009), contributing to the development of acid rain, air pollution and the acidification of surficial soils and waters (Aiuppa et al., 2004).

Given its environmental, geochemical and materials importance, the properties and distribution of Cl in natural and experimentally-produced silicate melts and coexisting fluid and vapour phases have been extensively investigated (Webster et al., 2018). In a ground-breaking study, Webster et al., (2015) determined the solubility of Cl in melts ranging from basalt to rhyolite at pressures of 1 to 7000 bars and 700 to 1250 °C. This was done by adding chloride salts NaCl, KCl, $PtCl_2$, $PtCl_4$, $CaCl_2$, $MgCl_2$ and $FeCl_2$ to the silicate and determining the chlorine contents of the melts at saturation in a hydrosaline liquid with or without vapour (Webster et al., 2015). The data confirm a strong compositional dependence of Cl solubility such that there is a decline of more than an order of magnitude in Cl content as melts evolve from basalt to rhyolite. This study also confirmed earlier results indicating that Cl solubility increases with increasing

peralkalinity (Carroll and Webster, 1994; Signorelli and Carroll, 2002; and Evans et al., 2008) and showed strong positive dependences on CaO, MgO and FeO contents. Measured pressure and temperature dependences of Cl solubility appear to depend on the experimental approach taken. In experiments saturated in vapour or high salinity fluid, some data indicate an increase in Cl solubility with decreasing pressure (Shinohara et al., 1989; Métrich and Rutherford, 1992; Signorelli and Carroll, 2002;Carroll, 2005) while others observe an increase in solubility with increasing pressure (Webster, 1992; Webster et al., 1999; Webster et al., 2015). Webster et al., (2015) found increases in Cl solubility in equilibrium with hydrosaline liquid with both increasing pressure and increasing temperature. Other authors find a negligible effect of temperature on the solubility of chlorine (Chevychelov et al., 2008; Balcone-Boissard et al., 2016). All of these previous studies depend, however, on the presence of an aqueous fluid or hydrosaline liquid to control the activity of Cl_2 in the silicate melt. In such cases changes in Cl solubility depend not only on the changing composition of the silicate melt, but also on the changing, variable composition of the coexisting fluid or liquid. Our aim here was to avoid this dependence on the nature of the coexisting phase and to buffer Cl contents by an assemblage of known Cl_2 fugacity. In that way we are able to more accurately define the compositional, pressure and temperature dependences of chlorine concentration in silicate melts.

2.2.1 Chlorine dissolution in silicate melt

Given the negative charge and the ionic radius of Cl^- (0.181 nm) it seems likely that this ion substitutes for O^{2-} (ionic radius 0.140 nm, Shannon, 1976) in the silicate framework. This hypothesis was supported experimentally by Bureau et al., (2000) who showed that halogen solubility decreases with the progressive mismatch of the ionic radii of the halide ions

(solubility of F>Cl>Br>I), and that of the oxygen ions which dominate the melt structure. The hypothesis of replacement of O^{2-} by Cl^{-} leads to two end-member substitution mechanisms:

$Cl_2 + [O^{2-}] = [Cl_2^{2-}] + 0.5O_2$ (A)

$Cl_2 + [O^{2-}] = 2[Cl^{-}] + 0.5O_2$ (B)

In equilibria (A) and (B) the nominally charged melt components are represented by brackets [] while the activities of O_2 and Cl_2 are unbracketed. Note that, in both these simplified cases, the solubility of Cl should depend on *both* the fugacity of Cl_2 and the fugacity of O_2. In equilibrium (A) the Cl^{-} ions are assumed to be associated in the melt structure while in equilibrium (B) they are effectively dissociated. Inspection of the equilibrium constants indicates that, in the Henry's Law region, dominance of mechanism (A) should lead to chlorine content of the silicate melt increasing linearly with the fugacity of Cl_2 and decreasing with the square root of oxygen fugacity. In the case of dissociation of the Cl^{-} ions (mechanism B), the Cl content of the silicate melt should increase with the square root of the chlorine fugacity and decrease with the fourth root of oxygen fugacity.

Other suggested halogen dissolution mechanisms (e.g. Joachim et al., (2015)) include replacement of an $[SiO_4]^{4-}$ tetrahedron by a $[halide]^{4-}$ quadruplet, and Cl^{-} substitution into the O^{2-} site charge-balanced by the substitution of Al^{3+} for Si^{4+} (Dalou et al., 2012). In both cases the appropriate charge-balanced equilibria involve both chlorine and oxygen, as well as SiO_2 and Al_2O_3, so that control of both Cl_2 and O_2 fugacities are essential to any experimental test of the proposed mechanism.

It is clear from the preceding discussion that in order to understand the basic chemistry of chlorine dissolution in silicate melt, we need to perform experiments under controlled fugacities of chlorine and oxygen. That was the initial aim of this work.

2.3 Experimental methodology

2.3.1 Control of chlorine fugacity

We began by following Frantz and Eugster, (1973) who developed a chlorine fugacity buffer based on the equilibrium between Ag and AgCl:

$$2AgCl_{(liquid)} \leftrightarrow 2Ag_{(liquid)} + Cl_{2\,(gas)} \quad (2.1)$$

Under the conditions of our experiments at 1200-1500ºC and 0.5-2 GPa, we may add metallic Ag and AgCl directly to our silicate melts because Ag_2O is virtually insoluble in the melt. Note that both Ag metal and AgCl are molten during the high-pressure experiment and that our initial experiments were performed with a silicate melt composition in the system anorthite-diopside-forsterite (Table 2.1). For equilibrium (2.1) the fugacity of chlorine is fixed by the equilibrium constant if the Ag metal and AgCl remain pure:

$$f(Cl_2) = \left(K_{AgCl}\right)_{P,T} \quad (2.2)$$

Thus, we can, in principle, determine the Cl content of the silicate melt at fixed and known chlorine fugacity. We knew from the work of Filiberto and Treiman, (2009b) that the Ag/AgCl buffer would release several weight % of Cl into the melt at high pressure and temperature making analysis straightforward with the electron microprobe. In order to investigate the dependence of Cl content on Cl fugacity, we initially expanded the range of Cl fugacities by using other potential buffers Pd-$PdCl_2$, Re-$ReCl_3$ and Cu-CuCl. In practice, we find that all 4 of the potential buffers control the chlorine fugacity at too high values for the basalt-like compositions we have used. The evidence for this statement is the generation of immiscible chloride *'blobs'* rich in Ca and Mg during the experiment with concomitant decreases in the

CaO and MgO contents of the coexisting silicate melt (Figure 2.2b) and Cl contents of the latter of up to 9 wt%.

In order to suppress the formation of chloride blobs, we reduced the chlorine fugacity by mixing the AgCl with either AgBr or AgI. We found that high ratios of AgI:AgCl was the best option because the solubility of I (<0.1 wt%) in melts is much lower than that of Br, which dissolved in the melt as much as 1.65 wt%. This finding is as predicted from the findings Cadoux et al., (2018), who explored Br partitioning between fluids and melts and found it has a great propensity to remain within a silicate melt. During the experiment the Ag and AgCl/AgI mixtures both melt to form 2 additional liquids (metal and halide) both of which are immiscible with one another and with the silicate melt.

Most experiments used an anorthite–diopside–forsterite ($An_{50}Di_{28}Fo_{22}$) mixture, which is close to the 1.5 GPa eutectic in the system $CaO\text{-}MgO\text{-}Al_2O_3\text{-}SiO_2$ (Presnall et al., 1978) and is hence an Fe-free model of a low degree mantle melt. The starting composition was prepared from a mixture of analytical grade oxide powders and $CaCO_3$. The mixture was decarbonated by heating overnight from 500-1100^{o}C. A second series of experiments was performed using a crushed and powdered natural basalt from Reykjanes Ridge, Iceland (Norris and Wood, 2017; Table 2.1). Finally, because the experiments on the natural basalt experienced, for reasons which are as yet unclear, various degrees of Fe loss to the Pt capsule, we examined the effects of FeO concentration by performing three experiments in which various amounts (3, 7 and 10 wt%) of synthetic $Fe_{1-x}O$ were intimately mixed with our buffer- $An_{50}Di_{28}Fo_{22}$ mixes.

Table 2.1 Silicate melt compositions used for measuring chlorine solubility.

Composition	CMAS ($An_{50}Di_{28}Fo_{22}$) [a]	Icelandic basalt[b]
SiO_2	46.53	50.59
TiO_2	-	1.02
Al_2O_3	18.33	15.27
FeO	-	9.58
MgO	17.82	9.16
K_2O	-	0.03
MnO	-	0.12
CaO	17.33	12.22
Na_2O	-	2.00

[a]1.5 GPa approximate eutectic composition, (Presnall et al., 1978)
[b]Natural Icelandic Basalt (Norris and Wood, 2017)

Experiments were performed with anhydrous silicates (Table 2.1) in an end-loaded 'Boyd and England'-type ½ inch piston-cylinder apparatus (Boyd and England, 1960) at the University of Oxford. Starting compositions of intimate mixtures of silicate and chlorine buffer were loaded into capsules, the configuration of which depended on the required oxygen fugacity (Figure 2.1). The Pt outer capsules were welded shut and weighed prior to the experiment.

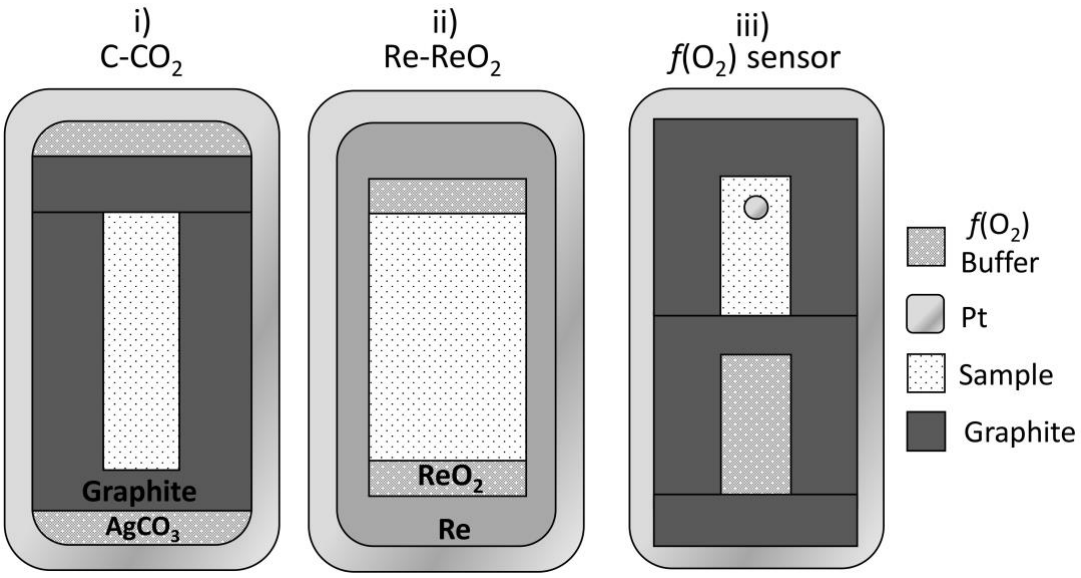


Figure 2.1 Capsule assemblies i) CCO buffered experiments. Mixtures of chlorine buffer (Ag/AgCl/AgI) plus silicate were packed into 2.5mm O.D, 1 mm I.D. graphite capsules encapsulated in a Pt capsule of 2.5mm I.D and 3.0mm O.D. Ag2CO¬3 (source of CO2) added above and below the graphite capsule and Pt outer capsule welded shut. ii) Re-ReO2 buffered experiments. ReO2 powder packed above and below the silicate-chlorine buffer mixture inside 2.5 mm (O.D) Re foil capsule within a welded outer Pt capsule. iii) Assembly to check f(O2). Lower graphite capsule with a CO_2 source and upper with iron-bearing sample (IB, Table 2.1) and a small Pt bead.

The experiments employed a 32 mm long, 12.5 mm outside diameter, 8 mm inside diameter calcium fluoride cylinder as the principal pressure medium. Inside this cylinder was an 8mm O.D., 6mm .I.D graphite cylinder which acts as the furnace. The 3 mm outside diameter capsule (Figure 2.1) was placed in the centre of the graphite furnace with crushable MgO pieces above, below and around the capsule. The temperature was measured and controlled using an alumina-sheathed C-type ($W_{95}Re_5$–$W_{74}Re_{26}$) thermocouple, introduced through a hole in the upper MgO piece and separated from the capsule by a 0.5 mm thick alumina disc. Experiments were performed at 1200-1500°C and 0.5-2.0 GPa (Table 2.1) using the *'hot piston-in'* method and the pressure calibrations of McDade et al., (2002) for ≥1.0 GPa, and Vlach et al., (2019) for <1.0GPa. Experimental durations, mostly 1 hour, were based on a time-series performed to test

for the approach to equilibrium (see below; Figure 2.3). All experiments were quenched by cutting the power to the graphite furnace (cooling at ≈110°C/s). Once extracted, the recovered capsule was cleaned, weighed, and compared to pre-experimental measurements to ensure no mass was lost or gained during the experiment.

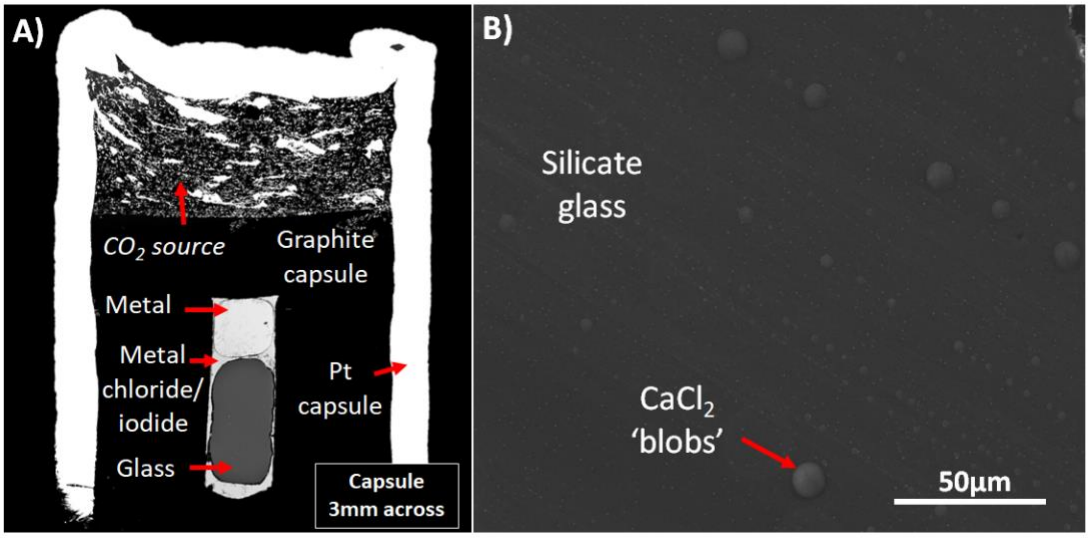


Figure 2.2 A) Composite SEM image of a typical experimental product, displaying 1) CO2 source and 2) Separate and distinct phases of silicate glass, metal chloride, and metal. B) SEM image of silicate glass displaying immiscible chloride 'blobs' rich in Ca and Mg which exsolve from the silicate melt at high chlorine fugacities. SEM images were taken on the FEI Quanta 650 at the University of Oxford's Department of Earth Sciences.

2.3.2 Control of oxygen fugacity

We tested our ability to control oxygen fugacity at the CCO buffer using the $f(O_2)$ sensor model of Kessel et al., (2001) at 1350°C and 1.5GPa. This model uses activity-composition relations of Pt-Fe alloys in conjunction with silicate activities as follows:

$$log\ f(O_2) = log\left\{exp\left[lna^{liq}_{Fe_2SiO_4} - lna^{liq}_{SiO_2} - 2lna^{alloy}_{Fe} - \left(\frac{-\Delta G^0_T}{RT}\right)\right]\right\} \qquad (2.3)$$

Where ΔG_r^0 is the standard state free energy change for the reaction $2Fe^{alloy} + O_2^{gas} + SiO_2^{liq} = Fe_2SiO_4^{liq}$

The model employs the MELTS supplementary calculator (Ghiorso and Sack, 1995) to calculate the activities of SiO_2 and Fe_2SiO_4 components in the complex liquid. The accuracy of the MELTS program at producing activities was tested against known experimental values, which is discussed further in section 2.5.4.

An experimental assembly was created using two graphite capsules within the outer Pt capsule. In the upper capsule, the powdered Icelandic basalt (Table 2.1) was added with a small Pt bead. In the bottom capsule, Ag_2CO_3 and graphite powder were added to form the C-CO-CO_2 (CCO) buffer (Figure 2.1), given, as follows from Jakobsson and Oskarsson, (1994):

$$logf(O_2)\ (CCO) = 4.325 - \left(\frac{21803}{T}\right) + 0.171\left(\frac{(P-1)}{T}\right) \qquad (2.4)$$

Analysis of the bead after the experiment yielded a mol fraction of 0.31 Fe (11.34 wt%) in the Pt and 5.22 wt% FeO in the silicate melt which indicates an oxygen fugacity 1.79 log units below the FMQ buffer. Taking the latter from Frost, (1991):

$$logf(O_2)\ (FMQ) = \left(\frac{-25096.3}{T}\right) + 8.735 + 0.11\left(\frac{(P-1)}{T}\right) \qquad (2.5)$$

This is within 0.03 of the expected value, of 1.82 log units and so we can be confident that our oxygen fugacity is fixed at CCO. Fe was lost from the silicate melt (from 9.61 to 5.22 wt%) to the Pt. However, the Fe concentration near the edge of the bead, and 15-20 μm within the bead was homogenous and so assumed to be in local equilibrium.

In order to determine the effect of oxygen fugacity on the Cl content of the silicate melt, we performed additional experiments using the Re-ReO_2 (RRO) oxygen buffer. We lined the Pt

capsule with Re foil and added ReO_2 in layers on the top and bottom of the charge (Figure 2.1). The oxygen fugacity is given by Pownceby and O'Neill, (1994):

$$logf(O_2)\ (RRO) = \frac{(-451020+297.595T-14.6585\,T\ln T)}{RT2.303} + \left(\frac{0.9917\,P}{\mathrm{R}\,T2.303}\right) \quad (2.6)$$

Note that pressure in equations (2.4), (2.5) and (2.6) is in bars, and temperature is in Kelvin.

Attempts to use additional anhydrous oxygen buffers have so far proven unsuccessful. A Mo-MoO_2 mixture released too much Mo into the silicate (~36 wt%), and pure oxygen (from PtO_2) oxidised the Ag buffer which dissolved ~ 24 wt% Ag_2O into the melt.

2.3.3 Analytical techniques

During the experiment, the buffer-silicate mixture segregated into a homogeneous translucent glass, a metal chloride/iodide phase, and an Ag-rich metal alloy (Figure 2.2a). The capsules were mounted in epoxy, ground to expose the charge, and polished with diamond powder using toluene or mineral oil as a lubricant to prevent any Cl loss to water-based lubricants. From a check on the potential for Cl-loss, however, we found, in agreement with Mungall and Brenan, (2003) that two samples re-polished with water-based lubricant showed no measurable loss of Cl.

Product silicate glasses and chlorine fugacity buffers were analysed on the CAMECA SX-Five-FE at the University of Oxford's Department of Earth Sciences and the JEOL-8600 electron microprobe in the University of Oxford's Archaeology department. The results obtained from each instrument were used to check for inconsistencies and levels of precision and accuracy. A 20 nA beam current, 15 kV accelerating potential and a defocused 10μm beam diameter was used for the glass analysis. To minimise the potential for element migration during analysis,

Cl, Na, and Si were analysed first with the 10 μm defocused beam. Standards used for silicate glass analysis were natural albite (Si, Al, Na), andradite (Ca, Fe), Titanium dioxide (Ti) Thallium-bromide-iodide (Br, I), synthetic NaCl crystals (Cl), periclase (Mg) and pure metals of Pt, Re, and Ag. Counting times were a minimum of 30 s peak and 15 s background for all elements except for Cl for which 80s peak and 40 s background were used to obtain a detection limit of 120 ppm. Replicate analysis on the same spots of glass revealed that Cl counts were stable and consistent at these conditions; with over 40 points on each silicate portion of the charge, and 10-20 points within the remaining buffer and resultant metal phases. Results remained consistent with low (<0.2 wt%) standard deviations (Table 2.2); secondary standards including Durango and Bamble apatite, containing known concentrations of Cl of 0.41 wt% (Kusebauch et al., 2015a) and 7.09 wt% (Kusebauch et al., 2015b) respectively were used to ensure accurate Cl analysis. In the case of Durango apatite (0.41 wt% Cl) we obtained an average of 0.415 wt% Cl with standard deviation of 0.015% for 98 analyses performed over the duration of the study.

2.4 Results

All experimental run conditions, the concentrations of chlorine in the resultant glass phases and calculated chlorine fugacities are given in Table 2.2. Complete analyses of the silicate glass products are presented in supplementary Table S1 (Appendix B).

Table 2.2 Experimental conditions and compositions

Experiment	Silicate composition	Time (mins)	Temperature (°C)	Pressure (GPa)	$f(O_2)$ buffer	log $f(O_2)$	Measured Cl^{glass} wt%	FeO wt% in melt	Buffer/Silicate by mass	Initial weight ratio *Cl/(Cl+I)*	Final Molar *Cl/(Cl+I)*	Molar *Ag/(Ag+Pt)*	$f(Cl_2)$
Time series													
AgI/Cl-007	CMAS	5	1400	1.5	CCO	-7.17	2.24 (0.05)	-	75/25	0.353	0.220	0.924	3.37E-04
AgI/Cl-002	CMAS	30	1400	1.5	CCO	-7.17	2.74 (0.14)	-	75/25	0.353	0.183	0.837	2.82E-04
AgI/Cl-005	CMAS	60	1400	1.5	CCO	-7.17	2.55 (0.04)	-	75/25	0.353	0.198	0.844	3.24E-04
AgI/Cl-006	CMAS	120	1400	1.5	CCO	-7.17	2.56 (0.07)	-	75/25	0.353	0.198	0.861	3.11E-04
***f*(Cl₂) series**													
AgI/Cl-018	CMAS	60	1400	1.5	CCO	-7.17	0.18 (0.01)	-	65/35	0.032	0.014	0.856	1.66E-06
AgI/Cl-010	CMAS	60	1400	1.5	CCO	-7.17	0.21 (0.01)	-	90/10	0.032	0.017	0.864	2.29E-06
AgI/Cl-009	CMAS	60	1400	1.5	CCO	-7.17	0.50 (0.03)	-	90/10	0.079	0.045	0.869	1.59E-05
AgI/Cl-008	CMAS	60	1400	1.5	CCO	-7.17	1.02 (0.03)	-	80/20	0.154	0.082	0.851	5.43E-05
AgI/Cl-005	CMAS	60	1400	1.5	CCO	-7.17	2.55 (0.04)	-	75/25	0.353	0.198	0.844	3.24E-04
AgI/Cl-013	CMAS	60	1400	1.5	CCO	-7.17	3.59 (0.09)	-	50/50	0.621	0.407	0.843	1.38E-03
AgI/Cl-027	ICB	60	1400	1.5	CCO	-7.17	1.60 (0.03)	0.5 (0.13)	50/50	0.353	0.209	0.778	4.24E-04
AgI/Cl-023	ICB	60	1400	1.5	CCO	-7.17	0.77 (0.06)	3.24 (0.89)	80/20	0.154	0.100	0.799	9.32E-05
AgI/Cl-037	ICB	60	1400	1.5	CCO	-7.17	0.41 (0.09)	1.67 (0.17)	90/10	0.079	0.052	0.823	2.31E-05
AgI/Cl-039	ICB	60	1400	1.5	CCO	-7.17	0.32 (0.01)	2.6 (0.18)	60/40	0.079	0.038	0.793	1.36E-05
***f*(O₂) series**													
AgI/Cl-029	CMAS	60	1400	1.5	RRO	-3.75	0.69 (0.04)	-	75/25	0.353	0.317	0.742	1.08E-03
AgI/Cl-031	ICB	60	1400	1.5	RRO	-3.75	0.33 (0.02)	3.48 (0.1)	50/50	0.353	0.329	0.823	9.45E-04
Temperature series													
AgI/Cl-028	CMAS	60	1500	1.5	CCO	-6.52	2.66 (0.07)	-	75/25	0.353	0.189	0.786	6.72E-04
AgI/Cl-005	CMAS	60	1400	1.5	CCO	-7.17	2.55 (0.04)	-	75/25	0.353	0.198	0.844	3.24E-04
AgI/Cl-020	CMAS	420	1300	1.5	CCO	-7.9	2.41 (0.16)	-	75/25	0.353	0.208	0.931	1.38E-04
AgI/Cl-043	ICB	60	1500	1.5	CCO	-6.52	1.77 (0.09)	8.52 (0.13)	50/50	0.353	0.189	0.702	8.44E-04
AgI/Cl-027	ICB	60	1400	1.5	CCO	-7.17	1.60 (0.03)	0.5 (0.13)	50/50	0.353	0.209	0.778	4.24E-04
AgI/Cl-044	ICB	300	1300	1.5	CCO	-7.90	1.52 (0.02)	1.15 (0.08)	50/50	0.353	0.217	0.814	1.97E-04
AgI/Cl-045	ICB	310	1200	1.5	CCO	-8.73	1.48 (0.17)	8.19 (0.36)	50/50	0.353	0.222	0.832	8.30E-05
Pressure series													
AgI/Cl-032	CMAS	60	1400	0.5	CCO	-8.2	3.39 (0.04)	-	75/25	0.353	0.128	0.909	1.09E-05
AgI/Cl-019	CMAS	60	1400	1	CCO	-7.68	2.93 (0.04)	-	75/25	0.353	0.169	0.858	7.46E-05
AgI/Cl-005	CMAS	60	1400	1.5	CCO	-7.17	2.55 (0.4)	-	75/25	0.353	0.198	0.844	3.24E-04
AgI/Cl-021	CMAS	60	1400	2	CCO	-6.66	2.12 (0.03)	-	75/25	0.353	0.229	0.830	1.20E-03
AgI/Cl-051	CMAS	60	1400	1	CCO	-7.68	1.23 (0.03)	-	80/20	0.154	0.065	0.865	1.07E-05
AgI/Cl-008	CMAS	60	1400	1.5	CCO	-7.17	1.02 (0.03)	-	80/20	0.154	0.082	0.851	5.43E-05
AgI/Cl-052	CMAS	120	1400	2	CCO	-6.66	0.81 (0.02)	-	80/20	0.154	0.097	0.852	2.05E-04
AgI/Cl-050	ICB	60	1400	0.5	CCO	-8.2	2.19 (0.11)	8.24 (0.15)	50/50	0.353	0.140	0.879	1.37E-05
AgI/Cl-048	ICB	60	1400	1	CCO	-7.68	2.05 (0.12)	7.57 (0.17)	50/50	0.353	0.156	0.821	6.95E-05

AgI/Cl-027	ICB	60	1400	1.5	CCO	-7.17	1.60 (0.03)	0.5 (0.13)	50/50	0.353	0.209	0.778	4.24E-04
AgI/Cl-049	ICB	150	1400	2	CCO	-6.66	1.62 (0.14)	8.22 (0.19)	50/50	0.353	0.206	0.657	1.55E-03
Fe-bearing CMAS													
AgI/Cl-024	CMAS	60	1400	1.5	CCO	-7.17	2.54 (0.06)	8.68 (0.19)	75/25	0.353	0.198	0.887	2.96E-04
AgI/Cl-025	CMAS	60	1400	1.5	CCO	-7.17	2.7 (0.19)	15.69 (0.46)	75/25	0.353	0.184	0.864	2.46E-04
AgI/Cl-026	CMAS	60	1400	1.5	CCO	-7.17	3.49 (0.28)	20.88 (0.49)	75/25	0.353	0.120	0.903	1.04E-04
Cl% error in () is 2 stdev													

2.4.1 Attainment of equilibrium

We performed a time series from 5 minutes to 2 hours at 1400°C/1.5GPa with oxygen fugacity fixed at the CCO buffer and chlorine fugacity provided by an initial AgI:AgCl ratio of 75:25 by weight. The concentration of Cl in the glass rose and levelled off after 5 minutes, with within-error variation between experiments performed at 0.5-2hours, and negligible difference between 1 and 2 hours (2.55 and 2.56 wt% Cl respectively; Table 2.2; Figure 2.3. Most further experiments were therefore performed for 1 hour (Table 2.2).

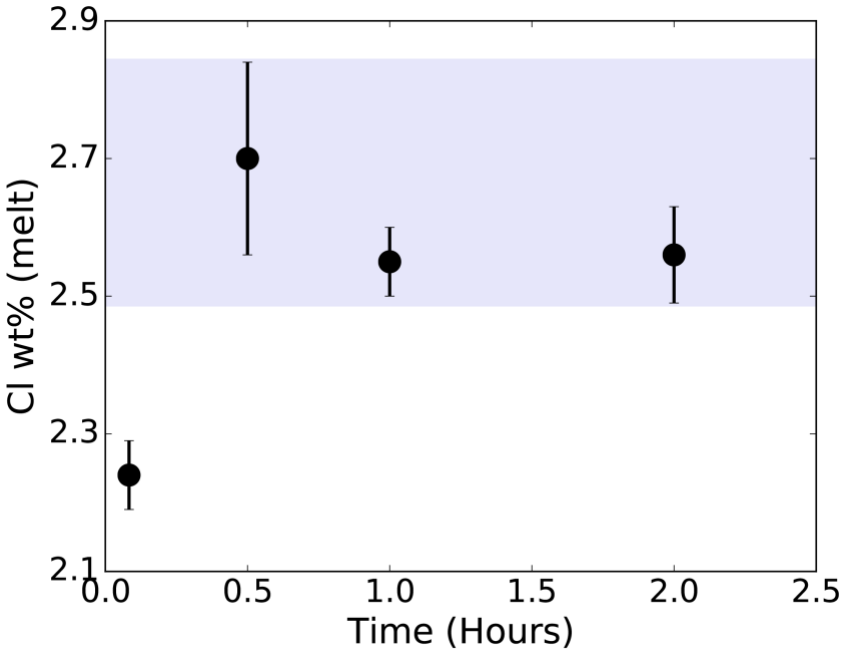


Figure 2.3 Chlorine concentration in $An_{50}Di_{28}Fo_{22}$ melt as a function of time at 1400 °C, 1.5 GPa and at the CCO oxygen buffer. Buffer contained AgI:AgCl of 75:25 (Table 2.2)

2.4.2 Calculation of chlorine fugacity $f(Cl_2)$ under experimental conditions

With both Ag metal and AgCl present as liquids in equilibrium, the fugacity of chlorine is calculated from the equilibrium constant (K) for reaction (2.1). The equilibrium constant was obtained at one bar from thermodynamic data of Barin et al., (1989):

$\log (K)_{1bar} = 11440/T - 2.961$ (1000-1800K) (2.7)

which yields if both Ag and AgCl are pure:

$\log f(Cl_2) = -11440/T + 2.961$ (2.8)

We use a 0.1 MPa standard state for Cl_2 and standard states for Ag and AgCl as the pure liquids at the pressure and temperature of interest. This means we need to integrate ΔVdP for the metal and chloride liquids from 1 bar to the pressure of interest. The volume of AgCl liquid is known to about 1123K (31.95 cc/mol), so we chose to integrate at this temperature. To a good approximation, we can express molar volume (V; cc/mol) as a function of pressure (P; GPa^{-1}) by:

$$V_{PT} = V_{1T}(1 - bP) \quad (2.9)$$

where *b* is the isothermal compressibility, of 0.101per GPa^{-1}at 801 K (Marcus, 2013). Taking account of the temperature dependence of the adiabatic compressibility from Takeda et al., (2007) implies isothermal compressibility of approximately 0.13/ GPa^{-1} at 1123 K.

For Ag liquid, the volume at the 1-atmosphere melting point of 1233 K is 11.49 cc/mol. Taking thermal expansion, volume and compressibility from Tsu et al., (1982) yields a volume of 11.37 cc/mol, and *b* of 0.0146/ GPa^{-1}at 1123 K by metastable extrapolation. Integrating between 0.1 MPa and P and adding in the VdP terms leads to:

$\log f(Cl_2) = -11440/T + 2.961 + 2150P/T - 208P^2/T$ (2.10)

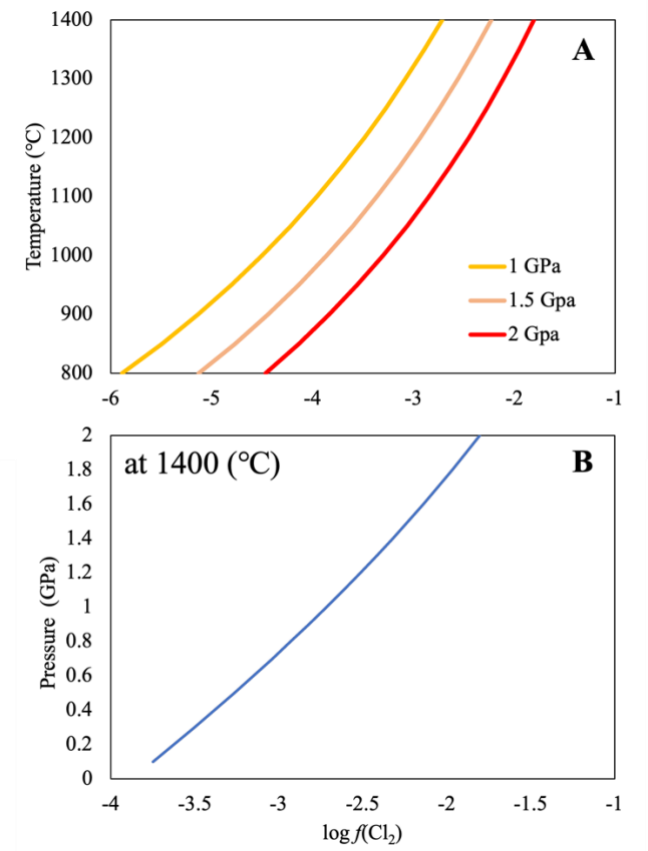


Figure 2.4 log$f(Cl_2)$ as a function of A) temperature, and B) pressure, calculated from equation 2.10.

In equation (2.10; shown graphically in figure 2.4) P is in GPa and, as before, the fugacity of chlorine refers to the value for pure Ag in equilibrium with pure AgCl and is relative to a standard state of pure chlorine at 0.1 MPa and the temperature of interest.

As discussed earlier, we found that use of the Ag/AgCl buffer with pure AgCl led to exsolution of a separate chloride phase rich in Ca and Mg (Figure 2.2b) and a corresponding change in major element composition of the silicate melt. In order to suppress this effect, we diluted the AgCl with, initially AgBr and then with AgI until there was no separate Ca-Mg chloride phase and no measurable reduction in the ratios of Ca and Mg to Si in the product silicate glass. We then reduced the AgCl/AgI ratio further to develop a range of chlorine fugacities at fixed pressure, temperature, and oxygen fugacity. In adopting this procedure, we adjusted the ratios

of chlorine buffer to silicate to ensure that the amount of Cl remaining in the buffer could be accurately calculated by mass-balance.

By diluting the liquid AgCl with AgI (or AgBr), we decrease chlorine fugacity by an amount approximately proportional to the square of the ratio Cl/(Cl+I). Additionally, we found that there was some Ag-Pt exchange between the metal of the capsule and that of the buffer. From the Ag-Pt phase diagram (Hart et al., 2017) we anticipate a mole fraction of Ag in the Ag-rich alloy of ~0.75-0.85 and values close to this were observed in all experiments (Table 2.2). No Iodine was observed within the melt blobs at the conditions tested, I remained within a AgI phase. In the absence of thermochemical mixing data for metal and halide liquids, we corrected for the effects of impurities by assuming ideal solution in both AgCl-AgI and Ag-Pt liquids. This yields:

$$logf(Cl_2) = logf\left(Cl_2^{Pure\ AgCl}\right) + 2log(X_{Cl}) - 2log\left(X_{Ag}\right) \qquad (2.11)$$

In equation (2.11) X_{Cl} refers to Cl/(Cl+I) in the halide liquid and X_{Ag} to Ag/(Ag+Pt) in the metal liquid on a molar basis (Table 2.2).

2.4.3 Chlorine solubility as a function of chlorine fugacity, *f*(Cl_2)

7 experiments were conducted on our CMAS composition at 1.5 GPa, 1400°C, using the CCO oxygen buffer (Figure 2.1). To examine the effects of variable FeO concentration, we also performed experiments in which 3, 7 and 10 wt% $Fe_{1-x}O$ were added to the starting mix of buffer plus CMAS. A similar series of 5 experiments were performed under identical conditions using the natural basalt as a starting composition. By adjusting the ratios of AgI to AgCl, and of buffer to silicate melt we were able to vary the fugacity of chlorine over the range

from 0 to 1.38x10^{-3} bar (Table 2.2 and Figure 2.4). Chlorine fugacities in Table 2.2 were calculated from the final Cl/(Cl+I) of the buffer mixture, which was determined by mass-balancing Cl concentration in the silicate glass with Cl content of the initial mixture. We assumed an initial weighing uncertainty of ±2% to generate the error bars of Figure 2.4. Analysis of the chloride buffer was also performed by EPMA and used as a check against the calculated value by mass-balance. However, the salt phase is very soft, and therefore difficult to polish, making an accurate and consistent analysis challenging. Additionally, no secondary standards for Ag and I were available, and so it was considered to not be as accurate as calculated mass balances. It was therefore only used as a check to ensure the mass balance was correct.

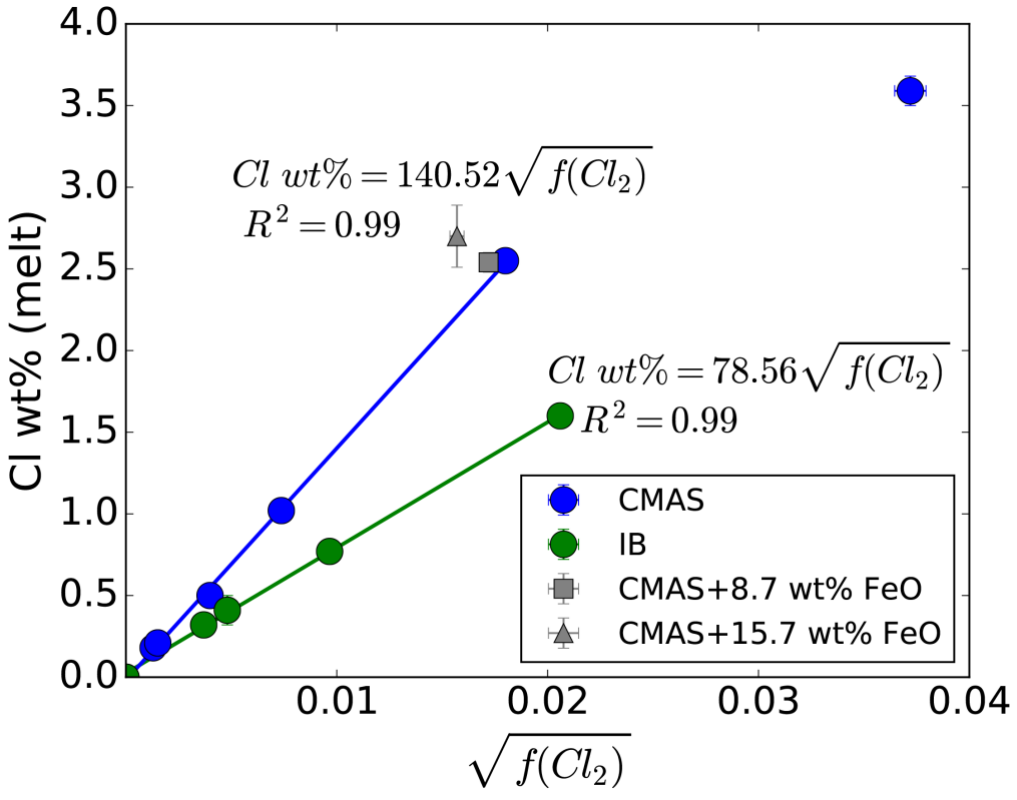


Figure 2.5 Chlorine concentration in the melt at 1400 °C and 1.5 GPa plotted as a function of the square root of chlorine fugacity with oxygen fugacity buffered at CCO. CMAS refers to $An_{50}Di_{28}Fo_{22}$ composition and IB to Icelandic basalt. Experiments performed with CMAS+FeO are denoted in grey, and 8.68 wt% FeO and 15.69 wt% FeO refer to wt% FeO in the product glasses.

In figure 2.5 we plot the Cl contents of the two melts versus the square root of chlorine fugacity. Figure 2.5 demonstrates clearly that the Cl contents of the melts are linear functions of $f(Cl_2)^{0.5}$ to concentrations of >2.6 wt% Cl. This constitutes Henry's Law behaviour of constant activity coefficient. Above a point in the range 2.6-3.6 wt% Cl behaviour becomes non-Henrian but the Henrian region is extensive. The clear linear dependence of Cl content on $f(Cl_2)^{0.5}$ in the region 0-2.6% Cl indicates that Cl dissolves according to reaction (B), with two dissociated Cl^- ions replacing O^{2-}. At higher concentrations the observed deviation (Figure 2.4) would be consistent with progressive association of Cl^- ions. It is also worth noting that addition of 8.7 wt% FeO to the CMAS composition produces a negligible change in Cl content and that the Cl concentration of melt with 15.7 wt% FeO added changes from 2.55 wt% (FeO-free) to 2.7 wt% (Figure 2.5). The observed $f(Cl_2)$-dependence means that we can exclude the proposed halogen dissolution mechanism in which an $[SiO_4]^{4-}$ tetrahedron is replaced by a $[halide]^{4-}$ quadruplet since this would lead to a dependence of Cl concentration on $f(Cl_2)^2$.

Both compositions tested obey a Henrian relationship with increasing $\sqrt{(f(Cl_2)}$. However, Cl solubility in Icelandic basalt is lower at fixed Cl_2 fugacity than in the haplobasalt indicating a significant compositional dependence of the Henry's Law constant. This compositional dependence is clearly not due to variable FeO content in the range 0-10 wt% (Figure 2.5). Since, in addition to FeO, the largest compositional differences between our 2 compositions are in their CaO and MgO contents we believe that these 2 components are largely responsible for the enhanced Cl content of the CMAS composition. This suggestion is consistent with the Cl solubility model of Webster et al., (2015) which is based on lower pressure experiments saturated in hydrosaline liquids and which indicates strong positive dependences of Cl solubility on CaO and MgO contents of the melt. In order to test our model of replacement of

O^{2-} by 2 dissociated Cl^- ions, we turned to the dependence of chlorine solubility on oxygen fugacity.

2.4.4 Oxygen fugacity *f*(O_2)

We explored the effect of oxygen fugacity on chlorine solubility using *f*(O_2) buffers CCO and Re-ReO_2, in both natural Icelandic basalt and haplobasaltic compositions (Table 2.1).

In order to quantify the effect of oxygen fugacity on Cl solubility, we need to correct the data to a constant chlorine fugacity. We did this by extrapolating the linear Henry's Law region determined from the experiments at the CCO buffer in each composition (Figure 2.4) to the point where the chlorine fugacity was the same as in our experiments at the Re-ReO_2 buffer. Once corrected in this way, it is apparent that chlorine solubility decreases, from 2.41 wt% to 0.33 wt%; and 4.61 wt% to 0.69 wt% (for ICB and CMAS compositions respectively) with increasing oxygen fugacity (Figure 2.6). The change in log *f*(O_2) from RRO (-3.75) to CCO (-7.17) at 15000 bars and 1400°C is -3.42. If Cl dissolution follows reaction (B), chlorine concentration should decrease with the fourth root of *f*(O_2). This means that the concentration at Re-ReO_2 should be 0.14 times the concentration at CCO. Our observed values are 0.15 times and 0.135 times for CMAS and ICB compositions, respectively. This consistency between predicted and observed *f*(O_2)-dependences leads us to conclude that reaction (B) represents the principal mechanism by which chlorine (and presumably other halogens) dissolves in silicate melts. We will, therefore, continue our treatment on this basis.

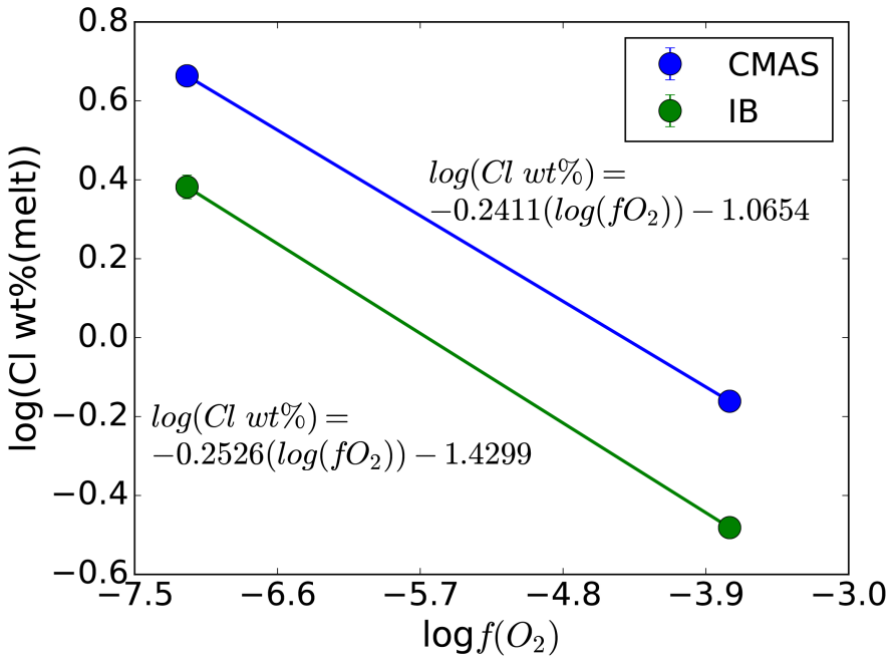


Figure 2.6 log(Cl wt% melt) as a function of oxygen fugacity, log(f(O_2)) at 1400 °C and 1.5GPa. Chlorine concentrations were corrected to a fixed f(Cl_2) by extrapolation from the Henrian region (Figure 2.4). Chlorine concentration should decrease with the fourth root of f(O_2) between CCO (-7.17) and Re-ReO_2 (-3.75) oxygen buffers if 2 Cl^- ions replace O^{2-} in the melt.

2.4.5 The effects of pressure and temperature on chlorine solubility

Experiments were conducted over a pressure range from 0.5 to 2 GPa, at a constant temperature of 1400°C, and held at the CCO buffer, using both CMAS and Icelandic basalt compositions with similar Cl/(Cl+I) contents of the buffer (25:75 AgCl to AgI by weight). Although raw results indicate a decrease in Cl concentration in the melt with increasing pressure, we need to correct out the pressure effects on the Cl and oxygen buffers in order to determine the true pressure effect. This was done by correcting the Cl concentration in the melt to a constant ratio of $f(Cl_2)^{0.5}$:$f(O_2)^{0.25}$ following the stoichiometry of reaction (B). Correcting this way allows us to express the pressure effect as (Figure 2.7):

$$\frac{\partial logK}{\partial P} = \frac{-\Delta V^0}{2.303RT} \qquad (2.12)$$

Where ΔV^0 is the volume change of reaction, R is the gas constant (8.3145 J K^{-1} mol^{-1}), T is the temperature in Kelvin, P is pressure and the equilibrium constant, K is given by:

$$logK_{(P,T)} = log(Cl^-) + 0.25log\big(f(O_2)\big) - 0.5log\big(f(Cl_2)\big) \qquad (2.13)$$

In equation (2.13), (Cl^-) is the concentration of chlorine in the silicate melt in weight %. Once these corrections are applied, similar negative correlations of logK with pressure are observed for both compositions at 1400 °C (Figure 2.7). The slope yields for ΔV^0 in the CMAS composition:

$$\Delta V^0 = -(-5.61 \times 10^{-5} * 2.303\mathrm{RT}) = 17.8\, cm^3.(gm.atom)^{-1} \quad (2.14)$$

The basalt composition yields ΔV^0 of 17.3 cm^3 per gm atom This volume change corresponds to the difference between the effective volumes of $1Cl^-$ and $0.5O^{2-}$ in the melt and would be expected to approximate half the volume difference between, for example, $CaCl_2$ and CaO (17.03 cm^3/mol) or $MgCl_2$ and MgO (14.78cm^3/mol) (Robie et al., 1979). The agreement provides further support for our dissolution model.

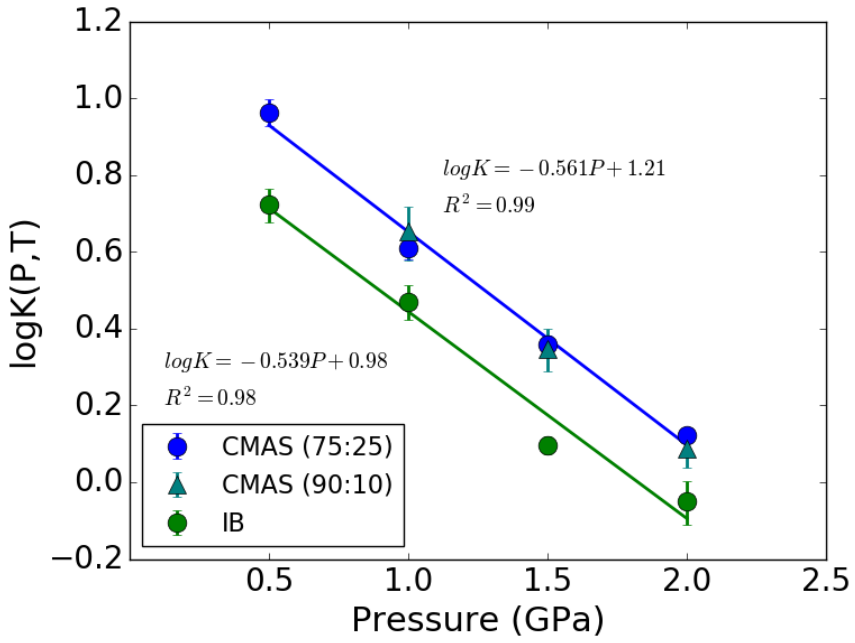


Figure 2.7 Plot of logK for the reaction : $0.5Cl_2 + 0.5[O^{2-}]_{melt} = [Cl^-]_{melt} + 0.25O_2$ as a function of pressure at 1400 °C. Experiments performed with oxygen fugacity at CCO. CMAS refers to $An_{50}Di_{28}Fo_{22}$ composition and (75:25) and (90:10) refer to weight percentages of AgI and AgCl in the buffer. IB refers to the Icelandic basalt of Table 2.1.

We performed experiments at 100 °C intervals between 1300 and 1500 °C for the CMAS composition and 1200-1500 °C for the basalt composition, in both cases at 1.5 GPa with oxygen fugacity buffered at CCO, and similar Cl/(Cl+I) contents of the buffer (25:75 AgCl to AgI by weight). We fitted the results for each composition by stepwise regression using the multiple linear regression tool of the SPSS statistical package. The appropriate fit equation is:

$$logK_{(P,T)} = log(Cl^-) + 0.25log\big(f(O_2)\big) - 0.5log\big(f(Cl_2)\big) = \text{A-B/T-CP/T} \qquad (2.15)$$

We found, however, that the B/T term in equation (2.15) does not pass the F-test at the normal level (α=0.05) requiring α of 0.2 in the CMAS composition and 0.9 in the basalt. This term was therefore excluded from the fit with the following result for the CMAS composition:

$$logK_{P,T}^{CMAS} = log(Cl^-) + 0.25log\big(f(O_2)\big) - 0.5log\big(f(Cl_2)\big) = 1.206(32) - 940(40)P/T \qquad (2.16)$$

and for the basalt:

$$logK_{P,T}^{basalt} = log(Cl^{-}) + 0.25log\big(f(O_2)\big) - 0.5log\big(f(Cl_2)\big)\text{=0.984(64)-930(70)P/T} \qquad (2.17)$$

In equations (2.16) and (2.17) P is in GPa, T in kelvin, *(Cl^-)* is the Cl content of the melt in weight% and the numbers in brackets are the standard errors in the 2 fit parameters. The standard errors of the fits are 0.030 and 0.053 in logK respectively.

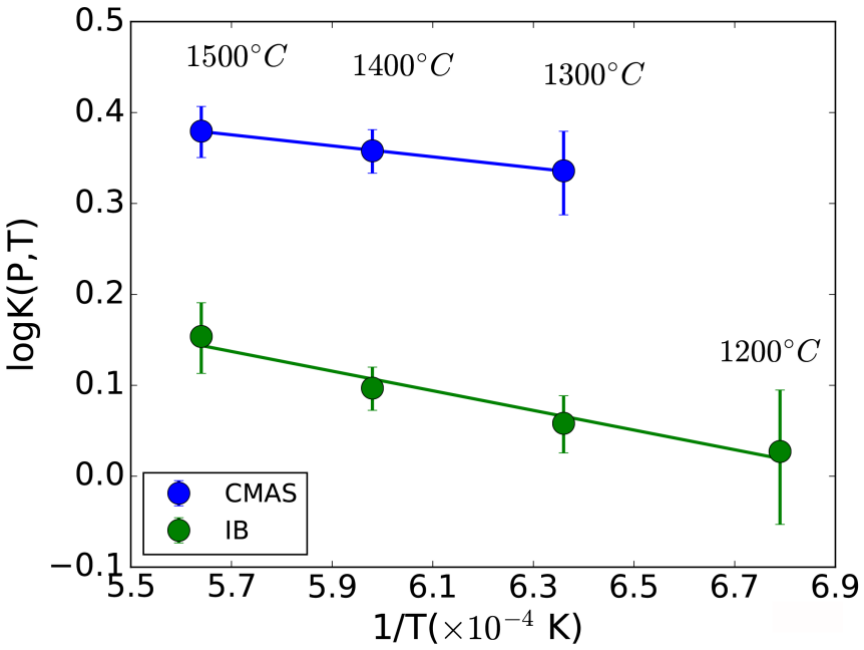


Figure 2.8 Plot of logK for the reaction : $0.5Cl_2 + 0.5[O^{2-}]_{melt} = [Cl^-]_{melt} + 0.25O_2$ versus 1/T at 1.5 GPa. Symbols as in Figure 2.7.

2.5 Discussion

2.5.1 Chlorine fugacity and gas composition on the basalt liquidus

The range of Cl concentrations in basalt glasses from the Mid-Ocean-Ridges and Back-Arc Basins typically extends from ~0.01 to 0.5 wt% with occasional values above the latter figure (Webster et al., 2018). In order to illustrate the implications of these concentrations for chlorine

fugacity and evolved gas composition, we started by assuming oxygen fugacities at FMQ (Cottrell and Kelley, 2011) and calculated chlorine fugacities from equation (2.17) for Cl contents of 0.05, 0.2 and 0.5 wt% . We assumed temperatures at the MORB liquidus of Médard and Grove, (2008):

$$T(°C) = 1267 + 65 \times P(GPa) \qquad (2.18)$$

We then calculated the composition of C-O-H-S-Cl gases which would be evolved from basalt at its liquidus temperature at shallow levels in the crust (Figure 2.9). For illustration, we assumed 5 mol% each of C and S species with the remainder H_2, H_2O and HCl. Thermodynamic data for the gas species were taken from Barin et al., (1989). Oxygen fugacity was fixed at FMQ with chlorine fugacity obtained from the fixed Cl content of the melt as described above. We used the 2-parameter Modified Redlich Kwong (MRK) equation of state with parameters for CO_2, H_2O, CO, H_2 and CH_4 from Holloway, (1977), as modified by Flowers, (1979). Data for HCl, H_2S and SO_2 were taken from Prausnitz et al., (1999). It should be noted, however, that because temperatures are high and pressures low, fugacity coefficients are close enough to 1 in the illustrated range for a perfect gas assumption to have given reasonable results. It is also important to note that the results of Figure 2.9 are actually *independent of oxygen fugacity* in the region where HCl is the dominant form of Cl in the gas phase. This is because, in an H_2O-rich fluid, the reaction controlling the HCl fugacity is:

$$0.5Cl_{2\,gas} + 0.5\,H_2O_{gas} = HCl_{gas} + 0.25O_{2\,gas} \qquad (2.19)$$

Inspection of reaction (2.19) shows that, at fixed H_2O fugacity, the HCl fugacity depends on the ratio of $f(Cl_2)^{0.5}$:$f(O_2)^{0.25}$. Since this is exactly the same dependence on the ratio of chlorine to oxygen fugacity as the Cl content of the melt (equilibrium B), any change in oxygen fugacity, at fixed Cl content of the melt, is cancelled-out by a corresponding change in chlorine fugacity.

To take this a step further and calculate the H_2O to HCl ratio in the fluid, we start by finding the equilibrium constant of reaction 2.19.

$$logK_{(2.19)} = logf(HCl) + \frac{1}{4}logf(O_2) - \frac{1}{2}logf(Cl_2) - \frac{1}{2}logf(H_2O) \qquad (2.20)$$

Next, we replace the ratio of $f(Cl_2)^{0.5}$ to $f(O_2)^{0.25}$ in equation 2.19 with the Cl content of the melt as derived from Eq. 2.17. Taking 2.17 from 2.20 yields:

$$logK^{Basalt}_{(P,T\ (2.17))} - logK_{(2.19)} = log(Cl^-) + \frac{1}{2}logf(H_2O) - logf(HCl) = 0.984 - \frac{930P}{T} - logK_{(2.19)} \qquad (2.21)$$

Where, as before, P is pressure, in GPa, T is in Kelvin, and (Cl^-) is the Cl content of the melt in wt%. The equilibrium constant of equation 2.20 can be calculated from the thermodynamic tables of Barin et al., (1989):

$$logK_{(2.19)} = \frac{-1551.3}{T} + 1.7875 \qquad (2.22)$$

And so, adding this to (2.21), provides:

$$\log(Cl^-) + \frac{1}{2}logf(H_2O) - logf(HCl) = 0.984 - \frac{930P}{T} + \frac{1551.3}{T} - 1.7875 \qquad (2.23)$$

$$\text{Therefore, } log\frac{f(H_2O)^{1/2}}{f(HCl)} = -\log(Cl^-) + 0.984 - \frac{930P}{T} + \frac{1551.3}{T} - 1.7875 \qquad (2.24)$$

This provides a means of calculating the ratio of H_2O and HCl in the fluid, at a given Cl content, temperature, and pressure.

As can be seen from Figure 2.9, Cl is calculated to degas significantly from basaltic melts and presumably from most other melts only at very shallow depths. Even for melts containing 0.5 wt% Cl, a C-O-H-S-Cl fluid evolved at 40 MPa would only contain an HCl mole fraction of

0.016. At 1 MPa the HCl mole fraction would be 0.10 and at 0.1 MPa 0.28. Thus, we would predict that HCl would degas only in the very uppermost parts of a volcanic edifice or during an eruption. This is consistent with the observations of Edmonds et al., (2009) who found that S degases at Kilauea at a greater depth than HCl and that the latter only degases at depths of 35 meters or less, pressures below 1MPa. Similarly, at Soufrière Hills, Montserrat, Edmonds et al., (2001) and Christopher et al., (2015) found that hydrous andesitic melts degas HCl at low pressures within the upper parts of the conduit system and during an eruption. Aiuppa, (2009) found that halogens only appreciably degassed during syn-eruptive, or late-stage degassing of residual magmas from Etna and Stromboli.

As a further illustration of the retention of Cl by the melt, even at very low pressure, we considered an H_2O- saturated basalt at 1269 °C and 40 MPa and calculated, using HCl concentrations in the evolved gas, the total amount of Cl lost during ascent to the surface from this pressure. The water-saturated basalt initially has 2 weight % H_2O and the degassing path was calculated using VolatileCalc2.0 (Newman and Lowenstern, 2002). As can be seen in Figure 2.9, the total fraction of the Cl degassed at pressures >5MPa is extremely small for all 3 concentrations of Cl considered. Eruption at the surface, with all H_2O lost, would lead to 98% of the original Cl remaining in the liquid if it had contained 0.05 wt% Cl initially, 93% if it originally contained 0.2 wt% Cl and 84% if it initially contained 0.5 wt % Cl i.e., 0.42 wt% Cl would remain in the liquid at 0.1MPa.

Chlorine is often cited as forming ligands with precious metals and playing a crucial role in the formation of ore deposits (e.g., Blundy et al., 2015; Blundy et al., 2021). Ore deposits however typically form at pressures of approximately 100 MPa (e.g., Frank et al., 2011). The observation that Cl predominantly degases at <5MPa appears contradictory to the theory of Cl assisted ore formation. However, a similar finding was presented by Lesne et al., (2011), who found that 99% of the initial chlorine remained dissolved in a silicate melt from 500-0 MPa,

also indicating that Cl only degasses at lower pressures. However, their experiments incorporated both Cl and S, and found a dramatic fractionation of the S/Cl ratio in the melt at approximately 100 MPa and concluded that Cl becomes strongly fractionated from sulphur at degassing pressures below 100 MPa, this might explain this conundrum.

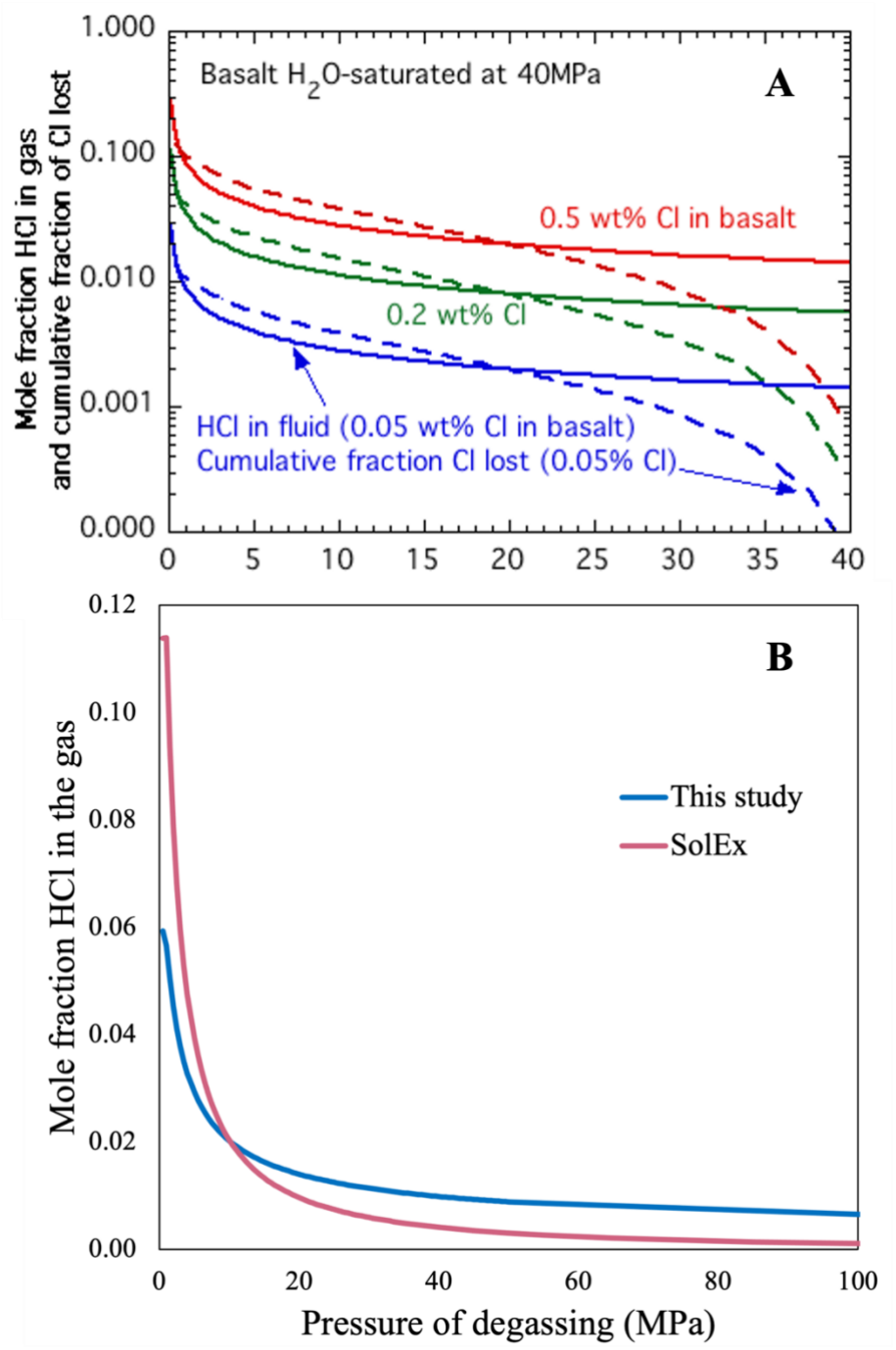


Figure 2.9 A) Shows calculated HCl contents (mole fraction) of gases emitted by basalt at its liquidus temperature as a function of pressure of degassing (solid lines). Curves refer to different Cl contents (wt %) of the basalt. Gas was assumed to contain 5% each of C and S species with the balance H_2, H_2O and HCl. Also shown (dashed lines) are cumulative fractions of total Cl degassed from an H_2O-saturated basalt at 40 MPa (2 wt% H_2O) during ascent to the surface. All results are independent of oxygen fugacity (see text). B) A comparison of our model with SolEx (Witham et al., 2021) Calculated at NNO+1 assuming 0.2 wt% Cl in the melt (see text).

The reason that HCl degasses only at very low pressures, given the very high solubility of Cl in silicate melts can be seen from inspection of reaction (2.19). The equilibrium constant for the reaction (equation 2.20) depends on the ratio of fugacities f(HCl):$f(H_2O)^{0.5}$. Since fugacities at these pressures are virtually identical to partial pressure, we can replace them by pressure and mole fractions X_{HCl} and X_{H_2O}:

$$\frac{f(HCl)}{f_{H_2O}^{0.5}} = constant \cong \frac{P.X_{HCl}}{(P.X_{H_2O})^{0.5}} \qquad (2.25)$$

From equation (2.25) and the breakdown of the thermodynamics (2.20-2.24), we see that with increasing pressure, the ratio X_{HCl}:X_{H_2O} in the fluid, at fixed Cl content of the melt, decreases with the square root of pressure as observed in Figure 2.9.

To test our degassing model, we chose to compare our model with the degassing model of *SolEx* (Witham et al., 2012). *SolEx*, can only be used at oxygen fugacities of >NNO+0.5 and with basaltic compositions, containing <53 wt% SiO_2. Therefore, for a comparison we recalculated the HCl in fluid for a basalt, again using a Cl content of 2000 ppm in the melt, but at the NNO+1 buffer, and applied the same composition and conditions to the SolEx model, in 'open system degassing mode', and calculated the water solubility at 5000 bars (the starting conditions of SolEx) with a spreadsheet presented by Moore (1998), providing a water content of 10.05 wt%. SolEx calculates the mole fraction of Cl degassed with pressure, and so, assuming Cl is present predominantly as HCl, then we can shift their results only by the percentage of H in HCl (2.76 wt%). We find, in agreement with SolEx, that HCl degasses at low pressures (Figure 2.9B) depicting similar pressure dependencies of HCl degassing. However, SolEx predicts substantial degassing to begin at approximately 30 MPa, and to degass more than our model at lower pressures <10 MPa.

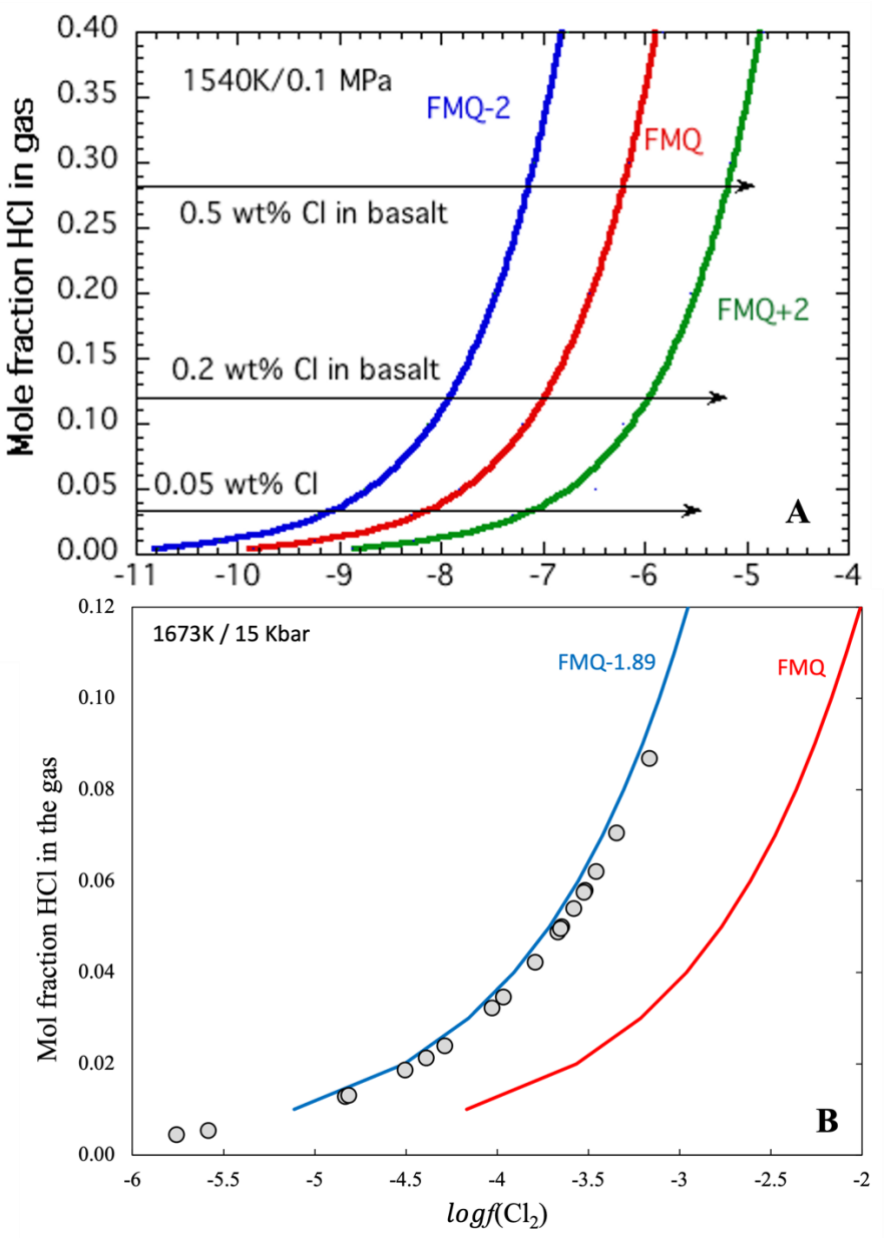


Figure 2.10 A Shows relationships between Cl_2 fugacity, O_2 fugacity and gas composition (mole fraction of HCl) for basalt at its liquidus temperature and a pressure of 0.1MPa. Note that for fixed Cl content of basalt (horizontal lines labelled in wt% Cl) the mole fraction of HCl is independent of Cl_2 and O_2 fugacities. HCl contents and Cl_2 fugacities covary along the lines labelled at oxygen fugacities relative to FMQ, the fayalite-magnetite-quartz buffer. B is replotted using the compositions and the conditions of the experiments presented in Table 2.2 and S1 conducted at 1673K and 1500 MPa.

In Figure 2.10, we present the calculated 0.1 MPa HCl contents of gases in equilibrium with basalt as functions of $f(O_2)$ and $f(Cl_2)$. As noted previously, the HCl concentrations depend only on the concentrations of Cl in the silicate melts, provided, as calculated from thermodynamic data, the HCl contents of the gases are very much greater than the Cl_2 concentrations. So, for example, a gas in equilibrium with basalt containing 0.5 weight% Cl has a mole fraction X_{HCl} of 0.28, independent of oxygen fugacity and chlorine fugacity. The concentration of 0.5 weight% Cl defines a line in $f(O_2)$- $f(Cl_2)$ space; however, as can be seen in figure 2.9. Thus, at FMQ, the log $f(Cl_2)$ associated with 0.5% Cl in the melt is -6.3, while a decrease or increase of $f(O_2)$ by 2 log units decreases or increases $f(Cl_2)$ by 1 log unit.

To explore how well the modelled curves of figure 2.9, describe our experimental data, we have calculated the mole fraction of HCl in the gas, using the experimental compositions presented in Table S1 at the conditions of the experiment (1673K and 15 kbar). As shown in figure 2.9B, the data closely plot along the FMQ-1.89 curve, calculated at 15 kbar and 1400°C.

2.5.2 HCl solubility in basaltic melts

In volcanic systems in which evolved gases are dominated by H_2O, the observed form of chlorine is HCl (Gerlach, 2004) and HCl is predicted, from thermodynamic data, to dominate over Cl_2 under all plausible conditions of H_2O content and oxygen fugacity, as shown by the equilibrium reaction presented in equation 2.20 where $f(HCl)>f(Cl_2)$, discussed further in Appendix A.8. Furthermore, Martin et al., (2006) modelled the gas speciation and mixing of magmatic gases using three commercially available gas mixing models. They found that the concentrations of HCl (and HF) were invariant with temperature (from 700-1300 °C) in pure magmatic gases and attributed this to the strong stability of HCl (and HF), and the relative

instability of all other Cl (and F) bearing species in magmatic gases. Given these observations and predictions, it is of interest to compare our results with the data of Iwasaki and Katsura, (1967) who measured the concentration of Cl in basalt (also andesite and rhyolite) equilibrated with mixtures of HCl and N_2 at 1-atmosphere pressure and temperatures of 1200-1290 °C. At 1290 °C, Iwasaki and Katsura found an HCl solubility of 1.06 wt% in basalt at 0.1 MPa of HCl pressure, 0.22 wt% at 0.01 MPa and 0.1 wt% at 0.003 MPa of HCl pressure. We used the saturation limit of 1.06 wt% HCl in the melt at 0.1 MPa of HCl pressure equation (2.16) to calculate the ratio $f(Cl_2):f(O_2)^{0.5}$ for a basalt containing 1.03 wt% Cl (equivalent to 1.06 wt% HCl). We then used (2.19) and (2.24), using the pHCl and pH_2O as the fugacities of each component (via 2.25), to calculate the composition of an HCl-H_2O gas which would be in equilibrium with this Cl content of basalt. We obtain a gas, at 0.1 MPa, which has an HCl partial pressure of 0.084 MPa effectively very close to the experimental value of 0.1 MPa. Alternatively, we can calculate the H_2 fugacity required to produce the measured Cl contents at known HCl fugacity. For all 3 measured HCl contents, we find that, if the HCl gas flowing through the furnace contained plausible H_2 contamination of less than 0.0001 (i.e., >0.9999 HCl, <0.0001 H_2) we can reproduce the measured HCl contents of the glasses from our solubility model. The agreement appears to us to be acceptable.

2.5.3 Hydrous melts in equilibrium with Cl-bearing fluids

Beermann et al., (2015) have determined the partitioning of Cl between hydrous basaltic melts and Cl-bearing aqueous fluids at 1050 °C and pressures of 100 and 200 MPa. The method used by these authors involved the addition of an H_2O-HCl liquid to a basalt glass starting material to which small amounts of sulphur had been added. The starting composition was calculated to contain about 5-6% excess fluid. Experiments in sealed gold capsules were performed in an internally heated pressure vessel under conditions where the H_2 fugacity was controlled by a

"Shaw"-membrane or measured using such a membrane. Glass composition was measured after the experiment and fluid composition reconstructed from the glass composition and the initial composition. The results indicate that Cl substitution in the hydrous melts follows Henry's Law, consistent with our proposed substitution mechanism (B) to concentrations of at least 1 wt% Cl in the melt. Of even greater interest is an estimate of how closely the Cl contents of these hydrous melts follow our anhydrous basalt model of equation (2.17).

We used the H_2 pressures and H_2O concentrations quoted by Beermann et al., (2015) to calculate O_2 fugacities from the equilibrium:

$$2H_2O = 2H_2 + O_2$$

We calculated H_2 and H_2O fugacities at the pressure and temperature of each experiment using the MRK equation of state as described above and used thermodynamic data of Barin et al., (1989) to calculate $f(O_2)$. Since Beermann et al observed appreciable dissolution of Ca, Na and K from the melt into the fluid we followed their Figure 10 and assumed that 25% of the Cl in the fluid was complexed as Ca, Na or K chlorides. The remaining Cl contents of the fluids were allocated to HCl and Cl_2 calculated from thermodynamic data (Barin et al., 1989) for the equilibrium:

$$2HCl = H_2 + Cl_2$$

As before, we used the MRK equation of state for H_2 and HCl and calculated chlorine fugacities relative to the 0.1MPa standard state. The calculated oxygen and chlorine fugacities were then inserted into equation (2.17) and the expected Cl contents of the melts calculated as if the melts were anhydrous. Results were not adjusted upwards to correct for the H_2O contents of the melts (2.7-7.5 wt%).

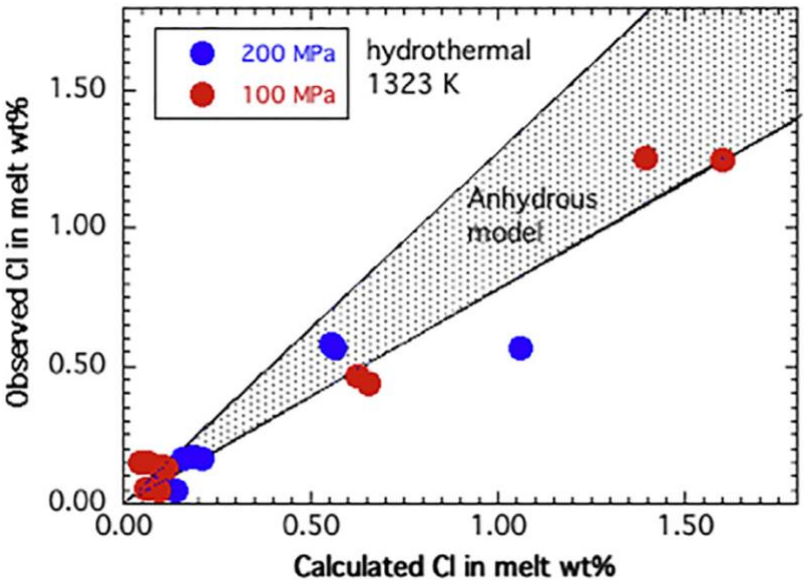


Figure 2.11 Plot of Cl contents of hydrous basalts in equilibrium with excess fluid at 100-200 MPa/1050°C (Beermann et al., 2015) versus values calculated from the compositions of the fluids using our anhydrous basalt model (equation 2.17). The field labelled "anhydrous model" covers ± 2 standard errors of the fit to our anhydrous data.

Figure 2.11 shows a comparison of calculated and measured Cl contents of the melts in the concentration range in which Henry's Law is closely obeyed (0-1.5 wt% Cl approx). As can be seen, when uncertainties in our results are considered, virtually all data are in agreement with the anhydrous model, which, given the potential errors and uncertainties is encouraging. It implies that hydrothermal and anhydrous results can be connected to one another in a relatively straightforward way.

2.5.4 Stability of Sodalite in trachytes and phonolites

Although Cl is a minor component of igneous apatite and amphibole, the principal phase in which it is a major component is sodalite, nominally $Na_4Al_3Si_3O_{12}Cl$ which is a primary

precipitating phase in some peralkaline trachytes and phonolites. We consider it instructive to calculate the chlorine fugacities required to stabilise sodalite in trachytes and compare them with the values we have obtained for basalts (Figure 2.10). Stormer and Carmichael, (1971) estimated the free energy of sodalite from the experiments of Wellman, (1969) and calculated the conditions under which sodalite would be stable relative to nepheline and other silicates. In order to calculate the chlorine fugacity required to stabilise sodalite, they used the equilibrium:

$$2NaFeSi_2O_6 + 6NaAlSiO_4 + Cl_2 = 2Na_4Al_3Si_3O_{12}Cl + 4SiO_2 + 0.667Fe_3O_4 + 0.667O_2 \quad (2.21)$$

clinopyroxene nepheline sodalite oxide

This was applied to a lava (W158) from Mt. Suswa, Kenya in which sodalite coexists with nepheline, plagioclase, olivine, clinopyroxene and oxide. Coexistence of nepheline and albitic plagioclase enables calculation of SiO_2 activity while the activities of Fe_3O_4, $NaFeSi_2O_6$ and $NaAlSiO_4$ together with oxygen fugacity were calculated from the compositions of oxide, olivine clinopyroxene and nepheline determined by Nash et al., (1969). The calculation presented by Stormer and Carmichael indicates that extremely low Cl_2 fugacities (~10^{-16} at 1300K/1bar) are required to stabilise sodalite in trachytic lavas. This value is about 7 orders of magnitude lower than the typical chlorine fugacities implied by the Cl contents of basaltic magmas at their liquidus temperatures (Figure 2.10). It is, however, based on experiments in which gas pressures over decomposing sodalite at 1 atm were measured (Wellman, 1969) and is based on the assumption of equilibrium between sodalite and its decomposition products nepheline and NaCl gas. Sharp et al., (1989) showed, however, that Wellman's experiments dramatically overestimate the stability of sodalite and therefore that the requisite chlorine fugacities for sodalite stability must be much higher than implied by the earlier data.

In a recent paper, Wood et al., (2019) used Sharp et al's (1989) high-pressure experimental reversals of the breakdown of sodalite to β-nepheline plus solid NaCl together with the heat

capacity and third law entropy measurements of Komada et al., (1995) to obtain the free energy of sodalite in the temperature range 300-1000K. We extended the temperature range of sodalite free energy data by taking account of the experimental reversals at 1073 K (0.78-0.80 GPa) and 1173 K (0.84-0.86GPa). These enable us to make calculations of chlorine fugacity in the 1-atmosphere liquidus-solidus interval of trachyte.

In order to calculate the chlorine fugacities necessary to stabilise sodalite in trachytes and phonolites we used the equilibrium:

$$3NaAlSiO_4 + 0.5Cl_2 + 0.5Na_2O = Na_4Al_3Si_3O_{12}Cl + 0.25O_2 \qquad (2.22)$$

nepheline gas solid sodalite gas

We took thermodynamic data from Barin et al., (1989) combined with our free energy of sodalite, to calculate the free energy change of (2.22). For the experimental temperature range of 800-1175 K and 0.1 MPa pressure we obtain, for equilibrium (2.22):

$$\log K_{22} = -0.526 + 10710/T \qquad R^2 = 0.9999 \qquad (2.23)$$

For comparison with earlier results, we have extrapolated the data slightly and perform the following calculations at 1300K.

At 1300K and 0.1 MPa pressure $\log K_{22}$ is 7.71. In order to calculate the ratio $f(Cl_2):f(O_2)^{0.5}$ required to stabilise sodalite, given nepheline saturation, we need to know the activity of Na_2O in the melt, relative to a standard state of pure solid Na_2O. We derived Na_2O activity from the MELTS thermodynamic model of Ghiorso and Sack, (1995). In order to do this, we used the MELTS supplemental calculator to calculate activities of Na_2SiO_3 and SiO_2 in the melts of interest. We then calculated the activity of Na_2O from the equilibrium:

$$Na_2SiO_3 = Na_2O + SiO_2 \qquad (2.24)$$

Melt solid melt

We tested the validity of this approach by using the MELTS supplementary calculator to calculate Na_2O activities in melts in the system Na_2O-Al_2O_3-SiO_2 studied by Itoh and Yokokawa, (1984) at 1400K. The latter authors measured Na_2O activities relative to the solid standard state we use in equilibrium (2.22). At 1400K, we obtain an Na_2O activity of $10^{-9.3}$ from MELTS for the composition $20Na_2O:80SiO_2$ (mole %) as compared to an experimental value of $10^{-9.5}$. For aluminous compositions $Na_2O:Al_2O_3:SiO_2$ of 20:10:70, 20:5:75 and 25:5:70 we obtain respectively, experimental values in parentheses- $10^{-9.2}$ ($10^{-9.0}$), $10^{-9.3}$ ($10^{-9.2}$) and $10^{-8..3}$ ($10^{-8.9}$). This demonstrates that the MELTS approach should yield reasonable values of Na_2O activity for mildly peralkaline silicate liquids.

We calculated the activity of Na_2O in 3 trachytes (W158 discussed above, W120 and W227) from Mt. Suswa, Kenya analysed by Nash et al., (1969). At 1300K, we obtained between $10^{-12.5}$ and $10^{-12.6}$ for all 3 liquids using the MELTS software. Note that we changed the standard state free energies of Na_2SiO_3 and SiO_2 liquids slightly to be consistent with Barin et al's., (1989) data but that this increases Na_2O activities only slightly, by about 0.1 log units.

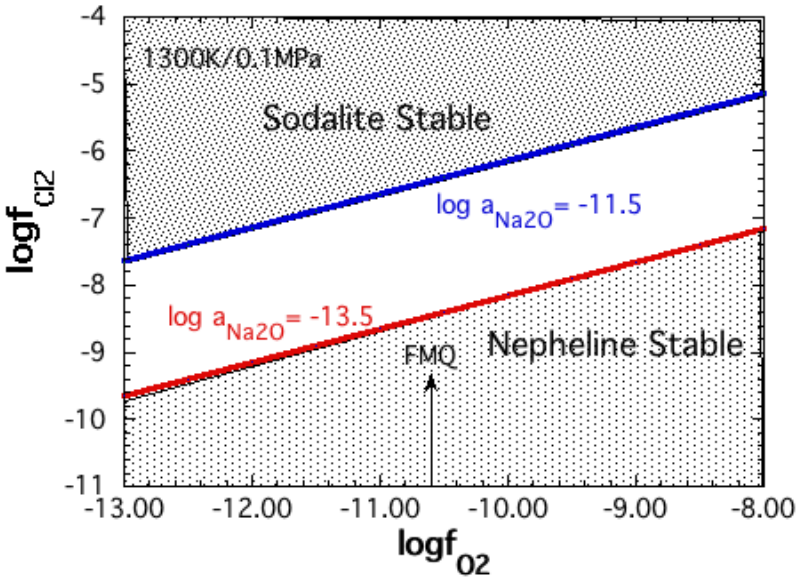


Figure 2.12 Calculated stability of sodalite relative to nepheline as a function of Cl_2 and O_2 fugacities at 1300K and 0.1 MPa. The calculated Na_2O activity in trachyte is ~$10^{-12.5}$ and the lines at $10^{-11.5}$ and $10^{-13.5}$ are intended to provide a reasonable estimate of uncertainty. FMQ=fayalite-magnetite-quartz oxygen buffer.

Given the calculated Na_2O activity in trachyte of about $10^{-12.5}$ at 1300K, we are able to apply equilibrium (2.22) to calculate the conditions under which sodalite would be stabilised in such a melt. We assumed, following Nash et al., (1969) that the typical nepheline would be about 75% $NaAlSiO_4$ and allowed it to be an ideal solution. We then constructed lines of equilibrium log$f$(Cl_2) versus log$f$(O_2) for equilibrium between sodalite and nepheline according to (2.22). Sodalite is stable at high f(Cl_2) and nepheline at low f(Cl_2), as shown in Figure 2.12. This figure shows that, as anticipated, the chlorine fugacity required to stabilise sodalite is much higher (~9 orders of magnitude) than that calculated by Stormer and Carmichael, (1971). For illustration, we allow a liberal uncertainty of +/- 1 log units in Na_2O activity since this is larger than the difference between any of the calculated values and the experiments discussed above and construct lines in log$f$(Cl_2):log$f$(O_2) space at Na_2O activities of $10^{-11.5}$ and $10^{-13.5}$ (Figure 2.11). As can be seen from Figure 2.12, the Cl_2 fugacities required to stabilise sodalite in

trachyte at FMQ/1300K are of the order of $10^{-6.8}$ to $10^{-8.8}$, almost exactly the same as those required to dissolve 0.05-0.5 wt% Cl in basalt at 1540 K (Figure 2.10). For comparison, Nash et al., (1969) note that the sodalite-bearing lavas of Mt. Suswa contain, in their centres 0.25-0.5 wt% Cl whereas glassy, sodalite-free lavas contain <0.25 wt% Cl. The implications are that the Cl_2 fugacities and the HCl contents of gases in equilibrium with basalt containing 0.5 wt% Cl are similar to those in equilibrium with trachyte containing 0.5% Cl. Whether this is coincidence or indicates a relatively small dependence of Cl content on melt composition in the range basalt-trachyte is as yet unknown. Furthermore, figure 2.12 could be used to develop an oxybarometer, which would be a useful tool in assessing the redox state of many phonolites and trachytes. This will be the focus of a further study.

2.6 Conclusions

Our experiments have demonstrated that chlorine initially dissolves in silicate melts by a mechanism in which one oxygen anion is replaced by 2 dissociated chloride, Cl^- ions. The same mechanism applies to both anhydrous and hydrous basaltic melts. We find that dissolution behaviour follows Henry's Law (constant ratio of concentration to $f(Cl_2)^{0.5}$) from zero to concentrations of at least 2.6 wt% Cl in a haplobasalt of composition $An_{50}Di_{28}Fo_{22}$ and at least 1.6 wt% Cl in an Icelandic basalt (Table 2.1, Figure 2.5) both at 1400 °C. At fixed temperature, pressure and fugacities of chlorine and oxygen, however, the Cl concentration in the FeO-free composition is 1.7 times that in the Icelandic basalt (Figure 2.5, equations 2.16, 2.17). In the case of hydrous basalt at 1050 °C Henry's Law is obeyed to ~1.5 wt% Cl and Cl contents are similar to values predicted from the anhydrous basalt data.

We performed experiments to determine whether the difference in Cl contents of our two anhydrous compositions is due to the presence of FeO in the natural basalt. Addition of 8.68 wt% FeO to the $An_{50}Di_{28}Fo_{22}$ composition melt made, however, negligible difference to the Cl content of 2.55 wt%. Even addition of 15.69 wt% FeO only raised the Cl content, under equivalent conditions of pressure, temperature and fugacities of chlorine and oxygen from 2.55 to 2.7 wt%. We conclude that variations in FeO content in the range 0-10 wt% should not generate measurable differences in equilibrium Cl content of a silicate melt.

At high Cl fugacities, generated by Ag/AgCl mixtures without AgI addition, we observed losses of CaO and MgO into immiscible chloride *'blobs'* (Figure 2.1). We, therefore, consider it probable that the major compositional factors controlling the differences in Cl dissolution between our two compositions are CaO and MgO concentrations, both of which act to increase the equilibrium Cl content. From the pressure dependence of Cl content at fixed fugacities of chlorine and oxygen, we find that the difference in volume between $1Cl^-$ ion and $0.5O^{2-}$ in silicate melt is 17.3-17.8 cm^3/mol. This compares well with half the volume difference between crystalline $CaCl_2$ and CaO of 17.03 cm^3/mol.

Our data enable us to calculate chlorine fugacities in basalt as a function of pressure, temperature, and composition. Given that Cl predominantly degasses from silicate melt as HCl, we used our equation for Cl content and Cl fugacity, (2.17), to calculate the HCl contents of gases released from basaltic melt as a function of pressure in the upper crust (Figure 2.9). This figure shows that basalts containing the typical concentration range of 0.05-0.5 wt% Cl degas little of their Cl at 25-30 MPa (800-900 meters depth) with chlorine being largely retained until pressures are below 5MPa. The strong pressure dependence of equilibrium HCl contents is due to the fact that when H_2O interacts with Cl in the melt 2 molecules of HCl are produced

for every molecule of H_2O consumed (equation 2.19). This results in a large increase in volume, an effect which causes HCl release to be reduced as pressure increases.

At FMQ and 0.1 MPa, the range of equilibrium chlorine fugacities implied by a basalt containing 0.5-0.05% Cl is $10^{-6.3}$ to $10^{-8.3}$ (Figure 2.10). This value increases by 1 log unit for every 2 log units increase in oxygen fugacity. We addressed the changes in Cl_2 fugacity likely to be observed in nature by calculating the conditions under which the Cl-rich phase sodalite would become stable near the liquidus in alkaline trachytes or phonolites. We calculate, based on thermodynamic data for sodalite, that this phase would be stable at 1300K/0.1MPa and oxygen fugacities at the FMQ buffer if chlorine fugacities were $10^{-6.8}$ to $10^{-8.8}$ (Figure 2.12). There appears, therefore, to be little difference in chlorine fugacities represented by alkaline trachytes at their liquidus and basalts at their liquidus. Appearance of sodalite as a liquidus phase is probably, therefore, due to a combination of low temperature and high Na_2O activity rather than unusually high chlorine fugacity.

2.7 Acknowledgements

RWT is grateful to the Natural Environmental Research Council, and the Oxford Doctoral Training Partnership in Environmental Research for studentship and funding (NE/L002612/1). BJW acknowledges funding from Science and Technology Facilities Council grant ST/R000999/1 and the NERC FAMOS project . We acknowledge the thorough reviews of 2 anonymous reviewers and Dr. Z, Zajacz.

2.8 Supplementary material

Supplementary data to this chapter can be found in Appendix B, or online at: https://doi.org/10.1016/j.gca.2020.11.018

2.9 References

Aiuppa A. (2009) Degassing of halogens from basaltic volcanism: Insights from volcanic gas observations. *Chem. Geol.* **263**, 99–109.

Aiuppa A., Baker D. R. and Webster J. D. (2009) Halogens in volcanic systems. *Chem. Geol.* **263**, 1–18.

Aiuppa A., Federico C., Giudice G., Gurrieri S., Paonita A. and Valenza M. (2004) Plume chemistry provides insights into mechanisms of sulfur and halogen degassing in basaltic volcanoes. *Earth Planet. Sci. Lett.* **222**, 469–483.

Baasner A., Schmidt B. C. and Webb S. L. (2013) The effect of chlorine, fluorine and water on the viscosity of aluminosilicate melts. *Chem. Geol.* **357**, 134–149.

Balcone-Boissard H., Boudon G., Cioni R., Webster J. D., Zdanowicz G., Orsi G. and Civetta L. (2016) Chlorine as a geobarometer for alkaline magmas: Evidence from a systematic study of the eruptions of Mount Somma-Vesuvius. *Sci. Rep.* **6**.

Barin I., Sauert F., Schultze-Rhonhof E. and Sheng W. S. (1989) *Thermochemical data of pure substances: Part II*., Weinheim, New York, Basel, Cambridge.

Beermann O., Botcharnikov R. E. and Nowak M. (2015) Partitioning of sulfur and chlorine between aqueous fluid and basaltic melt at 1050°C, 100 and 200 MPa. *Chem. Geol.* **418**, 132–157.

Blundy J., Afanasyev A., Tattitch B., Sparks S., Melnik O., Utkin I. and Rust A. (2021) The

economic potential of metalliferous sub-volcanic brines. *R. Soc. Open Sci.* **8**.

Blundy J., Mavrogenes J., Tattitch B., Sparks S. and Gilmer A. (2015) Generation of porphyry copper deposits by gas-brine reaction in volcanic arcs. *Nat. Geosci.* **8**, 235–240.

Bobrowski N., von Glasow R., Aiuppa A., Inguaggiato S., Louban I., Ibrahim O. W. and Platt U. (2007) Reactive halogen chemistry in volcanic plumes. *J. Geophys. Res.* **112**, 1–17.

Boyd F. R. and England J. L. (1960) Apparatus for phase-equilibrium measurements at pressures up to 50 kilobars and temperatures up to 1750°C. *J. Geophys. Res.* **65**, 741–748.

Bureau H., Keppler H. and Métrich N. (2000) Volcanic degassing of bromine and iodine: experimental fluid/melt partitioning data and applications to stratospheric chemistry. *Earth Planet. Lett.* **189**, 51–60.

Cadoux A., Iacono-Marziano G., Scaillet B., Aiuppa A., Mather T. A., Pyle D. M., Deloule E., Gennaro E. and Paonita A. (2018) The role of melt composition on aqueous fluid vs. silicate melt partitioning of bromine in magmas. *Earth Planet. Sci. Lett.* **498**, 450–463.

Carroll M. R. (2005) Chlorine solubility in evolved alkaline magmas. *Ann. Geophys.* **48**, 619–631.

Carroll M. R. and Webster J. D. (1994) Solubilities of sulfur, noble gases, nitrogen, chlorine, and fluorine in magmas. *Mineral. Soc. Am. Rev. Mineral.* **30**, 231 –279.

Chevychelov V., Bocharnikov R. E. and Holtz F. (2008) Experimental study of chlorine and fluorine partitioning between fluid and subalkaline basaltic melt. *Dokl. Earth Sci.* **422**, 93–97.

Christopher T. E., Blundy J., Cashman K., Cole P., Edmonds M., Smith P. J. and Sparks R. S. J. (2015) Crustal-scale degassing due to magma system destabilization and magma-gas

decoupling at Soufriére Hills Volcano, Montserrat. *Geochemistry Geophys. Geosystems* **16**, 267–300.

Cottrell E. and Kelley K. A. (2011) The oxidation state of Fe in MORB glasses and the oxygen fugacity of the upper mantle. *Earth Planet. Sci. Lett.* **305**, 270–282.

Dalou C., Koga K. T., Nobumichi S., Boulon J. and Devidal J.-L. (2012) Experimental determination of F and Cl partitioning between lherzolite and basaltic melt. *Contrib. to Mineral. Petrol.* **163**, 591–609.

Dingwell D. B. and Hess K. U. (1998) Melt viscosities in the system Na-Fe-Si-O-F-Cl: Contrasting effects of F and Cl in alkaline melts. *Am. Mineral.* **83**, 1016–1021.

Edmonds M., Gerlach T. M. and Herd R. A. (2009) Halogen degassing during ascent and eruption of water-poor basaltic magma. *Chem. Geol.* **263**, 122–130.

Edmonds M., Pyle D. and Oppenheimer C. (2001) A model for degassing at the Soufrière Hill Volcano, Montserrat, West Indies, based on geochemical data. *Earth Planet. Sci. Lett.* **186**, 159–173.

Evans K. A., Mavrogenes J. A., O'Neill H. S., Keller N. S. and Jang L. Y. (2008) A preliminary investigation of chlorine XANES in silicate glasses. *Geochemistry, Geophys. Geosystems* **9**, 1–15.

Filiberto J. and Treiman A. H. (2009a) Martian magmas contained abundant chlorine, but little water. *Geology* **37**, 1087–1090.

Filiberto J. and Treiman A. H. (2009b) The effect of chlorine on the liquidus of basalt: First results and implications for basalt genesis on Mars and Earth. *Chem. Geol.* **263**, 60–68.

Flowers G. C. (1979) Correction of Holloway's (1977) adaptation of the modified Redlich-Kwong equation of state for calculation of the fugacities of molecular species in

supercritical fluids of geologic interest. *Contrib. to Mineral. Petrol.* **69**, 315–318.

Frank, M.R., Simon, A.C., Pettke, T., Candela, P.A., and Piccoli, P.M. (2011) Gold and copper partitioning in magmatic-hydrothermal systems at 800°C and 100MPa. *Geochimica et Cosmochimica Acta*, **75**, 2470–2482.

Frantz J. D. and Eugster H. P. (1973) Acid-base buffers: Use of Ag + AgCl in the experimental control of solution equilibria at elevated pressures and temperatures. *Am. J. Sci.* **273**, 268–286.

Frost R. B. (1991) Introduction to oxygen fugacity and its petrologic importance. *Rev. Mineral. Geochemistry* **25**, 1–9.

Gerlach T. M. (2004) Volcanic sources of tropospheric ozone-depleting trace gases. *Geochemistry, Geophys. Geosystems* **5**, 1–16.

Ghiorso M. S. and Sack R. O. (1995) Chemical mass transfer in magmatic processes IV. A revised and internally consistent thermodynamic model for the interpolation and extrapolation of liquid-solid equilibria in magmatic systems at elevated temperatures and pressures. *Contrib. to Mineral. Petrol.* **119**, 197–212.

Hart G. L. W., Nelson L. J., Vanfleet R. R., Campbell B. J., Sluiter M. H. F., Neethling J. H., Olivier E. J., Allies S., Lang C. I., Meredig B. and Wolverton C. (2017) Revisiting the revised Ag-Pt phase diagram. *Acta Mater.* **124**, 325–332.

Holloway J. R. (1977) Fugacity and activity of molecular species in supercritical fluids. In *Thermodynamics in Geology* (ed. D. G. Fraser). D. Reidel Publishing Company, Dordrecht. pp. 161–181.

Itoh H. and Yokokawa T. (1984) Thermodynamic activity of Na2O in Na2O-SiO2-Al2O3 melt. *Trans. Japan Inst. Met.* **25**, 879–884.

Iwasaki B. and Katsura T. (1967) The solubility of hydrogen chloride in volcanic rock melts at a total pressure of one atmosphere and at temperatures of 1200°C and 1290°C under anhydrous conditions. *Bull. Chem. Soc. Jpn.* **40**, 554–561.

Jakobsson S. and Oskarsson N. (1994) The system C-O in equilibrium with graphite at high pressure and temperature: An experimental study. *Geochim. Cosmochim. Acta* **58**, 9–17.

Joachim B., Pawley A., Lyon I. C., Marquardt K., Henkel T., Clay P. L., Ruzié L., Burgess R. and Ballentine C. J. (2015) Experimental partitioning of F and Cl between olivine, orthopyroxene and silicate melt at Earth's mantle conditions. *Chem. Geol.* **416**, 65–78.

Kessel R., Beckett J. R. and Stolper E. M. (2001) Thermodynamic properties of the Pt-Fe system. *Am. Mineral.* **86**, 1003–1014.

Komada N., Westrum E. F., Hemingway B. S., Zolotov M. Y., Semenov Y. V, Khodakovsky I. L. and Anovitz L. M. (1995) Thermodynamic properties of sodalite at temperatures from 15 K to 1000 K. *J. Chem. Thermodyn.* **27**, 1119–1132.

Kusebauch C., John T., Whitehouse M. J., Klemme S. and Putnis A. (2015a) Distribution of halogens between fluid and apatite during fluid-mediated replacement processes. *Geochim. Cosmochim. Acta* **170**, 225–246.

Kusebauch C., Timm J., Whitehouse M. J. and Engvik A. K. (2015b) Apatite as probe for the halogen composition of metamorphic fluids (Bamble Sector, SE Norway). *Contrib. to Mineral. Petrol.* **170**.

Lesne P., Kohn S. C., Blundy J., Witham F., Botcharnikov R. E. and Behrens H. (2011) Experimental simulation of closed-system degassing in the system basalt-H2O-CO2-S-Cl. *J. Petrol.* **52**, 1737–1762.

Lowenstern J. B. (2000) A review of the constraining behaviour of two magmatic volatiles:

Chlorine and Carbon dioxide. *J. Geochemical Explor.* **69**–**70**, 287–290.

Malinin S. D., Kravchuk I. F. and Delbove F. (1989) Chloride distribution between phases in hydrated and dry chloride-aluminosilicate melt systems as a function of phase composition. *Geochemical Perspect. Lett.* **26**, 32–36.

Marcus Y. (2013) The compressibility of molten salts. *J. Chem. Thermodyn.* **61**, 7–10.

Martin R. S., Mather T. A. and Pyle D. M. (2006) High-temperature mixtures of magmatic and atmospheric gases. *Geochemistry, Geophys. Geosystems* **7**, 1–14.

McDade P., Wood B. J., Van Westrenen W., Brooker R., Gudmundsson G., Soulard H., Najorka J. and Blundy J. (2002) Pressure corrections for a selection of piston-cylinder cell assemblies. *Mineral. Mag.* **66**, 1021–1028.

Médard E. and Grove T. L. (2008) The effect of H2O on the olivine liquidus of basaltic melts: Experiments and thermodynamic models. *Contrib. to Mineral. Petrol.* **155**, 417–432.

Métrich N. and Rutherford M. J. (1992) Experimental study of chlorine behavior in hydrous silicic melts. *Geochemica Cosmochim. Acta* **56**, 607–616.

Mungall J. E. and Brenan J. M. (2003) Experimental evidence for the Chalcophile behavior of the halogens. *Can. Mineral.* **41**, 207–220.

Nash W. P., Carmichael I. S. E. and Johnson R. W. (1969) The mineralogy and petrology of Mount Suswa, Kenya. *Earth Sci. Rev.* **10**, 409–439.

Newman S. and Lowenstern J. B. (2002) VOLATILECALC: A silicate melt-H2O-CO2 solution model written in Visual Basic for excel. *Comput. Geosci.* **28**, 597–604.

Norris C. A. and Wood B. J. (2017) Earth's volatile contents established by melting and vaporization. *Nature* **549**, 507–510.

Pownceby M. I. and O'Neill H. S. C. (1994) Thermodynamic data from redox reactions at high temperatures. IV. Calibration of the Re-ReO2 oxygen buffer from EMF and NiO + Ni-Pd redox sensor measurements. *Contrib. to Mineral. Petrol.* **118**, 130–137.

Prausnitz J. M., Lichtenthaler R. N. and Gomes De Azevedo E. (1999) *Molecular thermodynamics of fluid-phase equilibria*. Third. ed. N. R. Amundson, Prentice Hall International series in the physical and chemical engineering sciences, New Jersey.

Presnall D. C., Dixon S. A., Dixon J. R., O'Donnell T. H., Brenner N. L., Schrock R. L. and Dycus D. W. (1978) Liquidus phase relations on the join Diopside-Forsterite-Anorthite from 1 atm to 20 kbar. Their bearing on the generation and crystallization of basaltic magma. *Contrib. to Mineral. Petrol.* **66**, 203–220.

Robie R. A., Hemingway B. S. and Fisher J. R. (1979) *Thermodynamic properties of minerals and related substances at 298.15 K and 1 bar (10^5 Pascals) pressure and at higher temperatures*., Washington.

Shannon R. D. (1976) Revised effective ionic radii and systematic studies of interatomie distances in halides and chaleogenides. *Acta Crystallogr.* **32**, 751–767.

Sharp Z. D., Helffrich G. R., Bohlen S. R. and Essene E. J. (1989) The stability of sodalite in the system NaAlSiO4-NaCl. *Geochim. Cosmochim. Acta* **53**, 1943–1954.

Shinohara H., Iiyama J. T. and Matsuo S. (1989) Partition of chlorine compounds between silicate melt and hydrothermal solutions: I. Partition of NaCl-KCl. *Geochim. Cosmochim. Acta* **53**, 2617–2630.

Signorelli S. and Carroll M. R. (2002) Experimental study of Cl solubility in hydrous alkaline melts: constraints on the theoretical maximum amount of Cl in trachytic and phonolitic melts. *Contrib. to Miner. Petrol.* **143**, 209–218.

Stelling J., Botcharnikov R. E., Beermann O. and Nowak M. (2008) Solubility of H2O-and chlorine-bearing fluids in basaltic melt of Mount Etna at T = 1050–1250 °C and P = 200 MPa. *Chem. Geol.* **256**, 102–110.

Stormer J. C. and Carmichael I. S. E. (1971) The free energy of soldalite and the behaivour of chloride, fluoride and sulfate in silicate magmas. *Am. Mineral.* **56**, 292–306.

Takeda S., Nagata Y. and Kawakita Y. (2007) Slow dynamic properties of molten silver halides. *J. Non. Cryst. Solids* **353**, 3169–3173.

Tsu Y., Suenaga H., Katsutoshi T. and Yutaka S. (1982) The velocity of ultrasound in molten bismuth, aluminium, silver and copper. *Trans. Japan Inst. Met.* **23**, 1–7.

Vlach S. R. F., Salazar-Naranjo A. F., Torres-Corredor J. S., De Carvalho P. R. and Mallmann G. (2019) Calibration of high-temperature furnace assemblies for experiments between 200 and 600 MPa with end-loaded piston-cylinder apparatuses. *Brazilian J. Geol.* **49**.

Witham F., Blundy J., Kohn S. C., Lesne P., Dixon J., Churakov S. V and Botcharnikov R. (2012) SolEx: A model for mixed COHSCl-volatile solubilities and exsolved gas compositions in basalt. *Comput. Geosci.* **45**, 87–97.

Webster J. D. (1992) Fluid-melt interactions involving Cl-rich granites: Experimental study from 2 to 8 kbar. *Geochim. Cosmochim. Acta* **56**, 659–678.

Webster J. D. (2004) The exsolution of magmatic hydrosaline chloride liquids. *Chem. Geol.* **210**, 33–48.

Webster J. D., Baker D. R. and Aiuppa A. (2018) Halogens in Mafic and Intermediate-Silica Content Magmas. In *The Role of Halogens in Terrestrial and Extraterrestrial Geochemical Processes* (eds. D. E. Harlov and L. Aranovich). Springer Geochemistry. pp. 307–430.

Webster J. D. and Holloway J. R. (1988) Experimental constraints on the partitioning of Cl between topaz rhyolite melt and H20 and H20 + CO2 fluids: New implications for granitic differentiation and ore deposition. *Geochim. Cosmochim. Acta* **51**, 2091–2105.

Webster J. D., Kinzler R. J. and Mathez E. A. (1999) Chloride and water solubility in basalt and andesite melts and implications for magmatic degassing. *Geochim. Cosmochim. Acta* **63**, 729–738.

Webster J. D., Vetere F., Botcharnikov R. E., Goldoff B., McBirney A. and Doherty A. L. (2015) Experimental and modeled chlorine solubilities in aluminosilicate melts at 1 to 7000 bars and 700 to 1250 °c: Applications to magmas of Augustine Volcano, Alaska. *Am. Mineral.* **100**, 522–535.

Webster J. D. and De Vivo B. (2002) Experimental and modeled solubilities of chlorine in aluminosilicate melts, consequences of magma evolution, and implications for exsolution of hydrous chloride melt at Mt. Somma-Vesuvius. *Am. Mineral.* **87**, 1046–1061.

Wellman T. R. (1969) The vapor pressure of NaCl over decomposing sodalite. *Geochemica Cosmochim. Acta* **33**, 1302–1303.

Wood B. J., Smythe D. J. and Harrison T. (2019) The condensation temperatures of the elements: A reappraisal. *Am. Mineral.* **104**, 844–856.

Zimova M. and Webb S. (2006) The effect of chlorine on the viscosity of Na2O-Fe2O3-Al2O3-SiO2 melts. *Am. Mineral.* **91**, 344–352.

Chapter 3

The effect of composition on chlorine solubility and behaviour in silicate melts

This chapter is currently under review in American Mineralogist, as:

Thomas R. W. and Wood B. J. (In review) The effect of composition on chlorine solubility and behaviour in silicate melts. *American Mineralogist*.

3.1 Abstract

We have performed experiments at 1.5 GPa and 1400 °C on 25 different bulk compositions to determine the effects of major element composition on the Cl contents of silicate melts at known fugacities of Cl_2 and O_2. The experimental method involved mixing a "sliding" chlorine buffer, a mixture of AgCl, AgI and Ag with the silicate and performing the experiment in a graphite capsule together with a source of CO_2 ($AgCO_3$). The graphite capsules were sealed inside welded Pt tubes in order to maintain a CO_2-CO atmosphere with oxygen fugacity fixed at the CCO buffer. During the experiment, the chlorine buffer segregates leaving a Cl-bearing melt which quenches to a glass.

We used the results to define chloride capacity C_{Cl} for each melt at the pressure and temperature of the experiment:

$$C_{Cl} = \frac{Cl\ (wt\%)}{\sqrt{f(Cl_2)}} \times \sqrt[4]{f(O_2)}$$

Chloride capacity was found to correlate positively with optical basicity and NBO/T and negatively with ionic porosity and Larsen Index. We combined our new data with the results of Thomas and Wood (2021) to derive an equation describing the composition, pressure, and temperature dependence of chloride capacity:

$$logC_{Cl} = 1.601 + (4470X_{Ca} - 3430X_{Si} + 2592X_{Fe} - 4092X_{K}\text{-}894P)/T$$

In this equation, X_{Ca}, X_{Si} and so on refer to the oxide mole fractions on a single cation basis, P is in GPa and T in K. The equation reproduces 58 data points with an r^2 of 0.96 and a standard error of 0.089. The addition of literature data on hydrous experiments indicates that the effects of <4.3 weight% H_2O are small enough to be ignored. Within the limits of the data utilised here, water was found to have no detectable effects on chlorine solubility. This suggests that

Cl and OH interactions are negligible, at low water concentrations within the compositional range tests.

We also performed experiments aimed at determining the conditions of NaCl saturation in melts. When combined with literature data we obtained:

$$log(Cl^{-}) = log(a_{NaCl}) + 0.06 - (2431X_{Ca} + 3430X_{Si} - 2592X_{Fe} + 3484X_{Na} + 4092X_{K} - 2417)/T$$

Where (Cl^{-}) is the chlorine content of the melt in weight% a_{NaCl} is the activity of NaCl (liquid) and the other symbols are the same as before. The results indicate that basalt dissolves approximately 8 times more Cl than rhyolite at a given NaCl activity i.e., Cl is approximately 8 times more soluble in basalt than in rhyolite.

3.2 Introduction

The volatile components whose behaviour is best understood in silicate melts are H_2O and CO_2 (Symonds et al., 1994; De Vivo et al., 2005). In the case of H_2O, the reasons are its high abundance, the major effects it has on viscosity, melting and crystallisation temperatures of melts and its importance in hydrothermal ore deposition associated with igneous activity. CO_2 came to be studied experimentally in the 1970's initially because of the observation that carbonatites were magmas with origins in the mantle. More recently concerns about volcanogenic CO_2 as a greenhouse gas has facilitated the establishment of a good database to describe CO_2 solubility in a wide range of melts at a wide range of physical conditions (Brooker et al., 2001; Stanley et al., 2011), allowing for the development of robust models, such as *VolatileCalc* (Newman and Lowenstern, 2002) and *MagmaSat* (Ghiorso and Gualda, 2015). A third group of elements that are geologically and environmentally important and

whose behaviour in melts requires further elucidation are the halogens. Chlorine, the second most abundant of the halogens (after fluorine) in both the primitive, and depleted mantle, and bulk continental crust (Pyle and Mather, 2009), is an important ligand in hydrothermal processes and plays a major role in transporting economically important metals such as Au and Cu in solution (Blundy et al., 2015). The segregation of Cl-rich brines from melts in the later stages of igneous activity can lead to significant metal transport and has resulted in major economic deposits at, for example, Broken Hill, in New South Wales, Australia (Millsteed and Mavrogenes, 2015) and in porphyry copper deposits (Nash, 1976; Fuge et al., 1986). Moore and Nash, (1974) found that halite rich fluid inclusions perfectly outlined the Cu-rich ore zone at Bingham Canyon, Utah, USA and fluid inclusions found in the PGE deposit helped delineate ore at the Stillwater Complex, Montana USA (Hanley et al., 2008); also, the two most economically important iron oxide copper-gold (IOCG) deposits in Chile, Mantoverde and Candelaria-Punta del Cobre, both exhibit high-salinity fluid inclusions (Marschik and Kendrick, 2015).

Halogens released by volcanism act to transport trace metals in gaseous form to the environment (Scholtysik and Canil, 2021) as catalysts for the destruction of stratospheric ozone (von Glasow et al., 2009) and in some cases cause major local environmental degradation. The 1783 eruption of Laki, for example, led to the release of ~8 million tonnes of fluorine causing the deaths by fluorosis of a large fraction of Iceland's sheep and cattle population and about 25% of the population in the ensuing famine.

During igneous differentiation, the halogens behave as highly incompatible elements (Edmonds et al., 2009; Pyle and Mather, 2009) being concentrated in the melts until lost in a gas or fluid phase or incorporated into a quenched glass and minor crystalline phases such as apatite or sodalite (Sharp and Draper, 2013). Thermodynamic equilibrium speciation

calculations and observations of modern volcanic edifices (Symonds et al., 1992; Martin et al., 2006) indicate that the halogens are predominantly degassed in the form of halogen acids (HF, HCl, HBr, and HI; Gerlach, (2004); Martin et al., (2006)). Volcanic gases typically comprise > 90% H_2O plus CO_2, with < 10% SO_2 plus HCl and HF and trace amounts of H_2S, H_2, CO, HBr and HI (Pyle and Mather, 2009; Martin et al., 2012). Estimates of halogen fluxes vary greatly and current volcanic degassing from arc and non-arc eruptions are estimated to vary from 0.3 Tg/Yr to 5.5 Tg/Yr for HCl, 0.15 Tg/Yr to 0.58 Tg/Yr for HF, 0.0001Tg/Yr to 0.016 Tg/Yr for HBr, and 0.00004 Tg/Yr to 0.0017Tg/Yr for HI (Gerlach, 2004; Aiuppa et al., 2009; Pyle and Mather, 2009; Webster et al., 2018).

Given their environmental, geochemical and materials importance, the properties and distribution of halogens in natural and experimentally produced silicate melts and coexisting fluid phases are the subject of broad ongoing interest. They are observed to have profound effects on the phase equilibria and viscosities of melts (Zimova and Webb, 2006; Filiberto and Treiman, 2009b; Baasner et al., 2013) leading, for example to Cl being, on a molar basis, twice as effective at lowering the liquidus of basalt as H_2O (Filiberto and Treiman, 2009b). Experimental determinations under controlled conditions show that Cl solubility tends to increase with decreasing SiO_2 concentration in the melt (Iwasaki and Katsura, 1967; Carroll and Webster, 1994; Webster et al., 1999; Signorelli and Carroll, 2000; Webster and De Vivo, 2002). Decreases in SiO_2 activity generally correlates with increasing activities of network-modifying cations and experiments employing saturation in hydro-saline liquids (Webster et al., 2015) indicate that Cl content, at fixed temperature and pressure increases with CaO, MgO and alkali contents of the coexisting silicate melts. The compositional effects were parameterised as a Cl solubility model (Webster et al., 2015) which provides an important baseline for future work. The model has some uncertainty however because the coexisting hydrosaline liquids change the composition and hence Cl_2 fugacity as silicate melt

composition changes. A method in which chlorine fugacity can be varied independently of silicate melt composition is required to better constrain the compositional effects on chlorine solubility. Thomas and Wood, (2021) developed such a method based on the equilibrium:

$$2AgCl_{(liquid)} \leftrightarrow 2Ag_{(liquid)} + Cl_{2\,(gas)} \qquad (3.1)$$

Coexistence of liquid AgCl and liquid Ag metal at fixed pressure and temperature buffer the fugacity of Cl_2. Since Ag is virtually insoluble in silicate melt except under very oxidising conditions (Thomas and Wood, 2021) the composition of a coexisting silicate melt can be varied almost at will at known, in principle buffered, chlorine fugacity. In practice, we found that chlorine fugacities were so high using the Ag/AgCl buffer that discrete calcium-magnesium chloride liquids segregated from haplobasaltic melts at the experimental conditions of 1.5 GPa/1400^{o}C. In order to suppress the exsolution of chlorides, we therefore, diluted the AgCl with AgI to form a mixed halide of known ratio of Cl to I. This approach enables chlorine fugacity to be calculated from a combination of the thermodynamic data for equilibrium (3.1), the volumes of the liquid Ag and AgCl and the ratio of Cl/(Cl+I) in the "sliding" Ag/AgCl-AgI buffer. We have tested similar approaches with AgF, AgBr, and AgI and can report that all three can be treated in a similar manner to AgCl in order to fix fugacities of fluorine, bromine, and iodine respectively. Given its abundance and importance in hydrothermal fluids and volcanic gases, however, the remainder of this report will be dedicated to the behaviour of chlorine in silicate melts.

3.2.1 Chlorine dissolution in silicate melts

Thomas and Wood, (2021) used the Ag/AgCl buffer method described above to investigate the nature of the initial dissolution of Cl in two silicate melts, an Icelandic basalt and a haplobasalt

of composition $An_{50}Di_{28}Fo_{22}$ (Table 3.1). We found that, at 1.5GPa/1400ºC, dissolution of Cl follows Henry's Law with Cl concentration proportional to the square root of chlorine fugacity and the fourth root of oxygen fugacity up to concentrations of at least 1.6 wt% Cl in the basalt and 2.6 wt% Cl in the haplobasalt. These observations imply that $2Cl^-$ ions in the melt replace O^{2-} according to the reaction:

$$Cl_{2\ gas} + [O^{2-}]_{melt} = 2[Cl^-]_{melt} + \frac{1}{2}O_{2\ gas} \qquad (3.2)$$

As written, the Cl^- ions in the melt are dissociated from one another and it is straightforward to show that, at equilibrium, the concentration of Cl^- in the melt is proportional to $f_{Cl_2}^{0.5}$ and inversely proportional to $f_{O_2}^{0.25}$. At concentrations greater than 2.6 wt% Cl in the haplobasalt and ~1.6 wt% Cl in the natural basalt the relationship between Cl concentration and $f_{Cl_2}^{0.5}$ deviates in a direction consistent with mutual avoidance of the Cl^- ions i.e., the concentration increases less strongly with increasing $f_{Cl_2}^{0.5}$ than in the Henry's Law region (Figure 3.1).

Our observation that a Ca-rich composition ($An_{50}Di_{28}Fo_{22}$) dissolves substantially more Cl at fixed $f(Cl_2)$ than basalt (Thomas and Wood 2021) is qualitatively in agreement with the model of Webster et al (2015) which incorporates strong positive correlations between CaO and MgO concentrations in the melt and its Cl content. These correlations also appear to be reflected in the X-ray absorption (Evans et al., 2008; McKeown et al., 2011) and Nuclear Magnetic Resonance spectra (Stebbins and Du, 2002; Sandland et al., 2004) of Cl in quenched glasses. These authors concluded that Cl nearest-neighbours and hence strongest influences on Cl solubility are predominantly Ca and Mg (Evans et al., 2008; McKeown et al., 2011) or a combination of alkaline Earth and alkali cations (Stebbins and Du, 2002; Sandland et al., 2004).

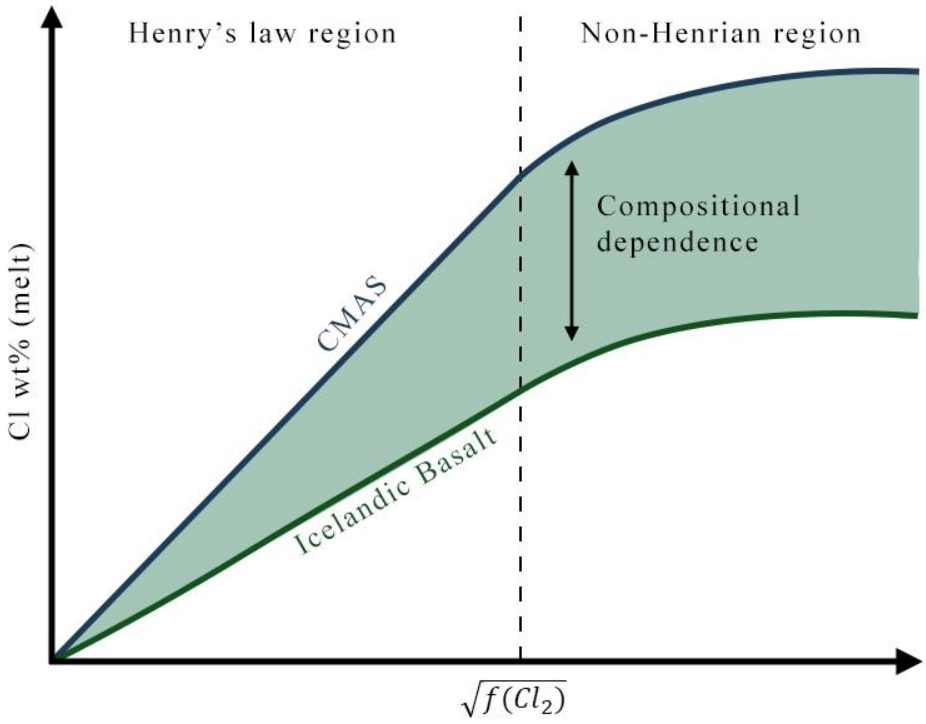


Figure 3.1 A schematic showing the form of the relationship between Cl content and Cl_2 fugacity established by Thomas and Wood (2021). The size of the Henry's Law region depends on major element composition. The end of the Henrian region is inferred from experiment AgI/Cl-036 (Table 2.2, Figure 2.4).

From the preceding discussion and figure 3.1, it is clear that there are strong compositional dependences of Cl solubility in silicate melt and that CaO, MgO and Na_2O concentrations probably play major roles. Our aim here is to quantify these compositional effects at known chlorine fugacity in order to extend the application of our chlorine fugacity buffer and to build on the experimental approach of Webster et al., (2015). A major advantage of the buffer method is that it is applicable to anhydrous melts, which enables us to study compositional effects in the absence of H_2O and a coexisting hydrous fluid. The effect of H_2O on Cl solubility will be treated in a later contribution.

3.3 Experimental methodology

3.3.1 Starting compositions

Since the principal aim of this study was to determine compositional effects on Cl solubility we used a wide range of starting compositions comprising 7 natural samples, and 18 synthetic compositions. (Table 3.1). Synthetic starting compositions were prepared from mixtures of analytical grade oxide powders, (with iron added as Fe_2O_3), and carbonate powders (Na_2CO_3, $CaCO_3$ and K_2CO_3). Powders were ground under ethanol for a minimum of 2.5 hours to ensure homogeneity. The mixtures were subsequently pressed into pellets, decarbonated by incrementally heated overnight from 400 to 800 °C, and the iron reduced overnight in a 1-atmosphere furnace at 1100 °C and at an $f(O_2)$ of IW+1. Once reduced, the pellets were re-ground into powder and then glassed at 1400°C in air at 1 atm to check the starting compositions (Table 3.1).

Table 3.1 Normalised silicate melt compositions used for measuring chlorine solubility

Composition	SiO_2	TiO_2	Al_2O_3	FeO_T	MnO	MgO	CaO	Na_2O	K_2O	P_2O_5	Cr_2O_3	NiO	Total
Icelandic Basalt[a]	50.67	1.02	15.29	9.59	-	9.17	12.24	2.01	-	-	-	-	100
SM-Basalt[b]	41.04	-	10.59	16.36	-	15.20	16.80	-	-	-	-	-	100
MORB[c]	51.17	0.83	15.49	7.91	-	10.52	12.71	1.38	-	-	-	-	100
Low-Mg Basalt[d]	49.66	3.18	15.96	9.13	0.21	4.24	9.46	4.81	2.01	1.33	-	-	100
High-Mg Basalt[e]	43.02	4.15	9.65	13.32	0.18	13.62	11.48	2.82	1.06	0.70	-	-	100
CNMAS ($Fo_5Di_{48}An_{47}$)[f]	48.30	-	16.57	-	-	12.36	21.86	0.90	-	-	-	-	100
CNMAS-2 ($En_{17}An_{43}Di_{40}$)[g]	49.72	-	15.39	-	-	14.30	19.29	1.29	-	-	-	-	100
CMAS ($An_{50}Di_{28}Fo_{22}$)[h]	46.53	-	18.33	-	-	17.82	17.33	-	-	-	-	-	100
Lunar Basalt[i]	41.29	9.06	12.08	18.43	0.40	8.06	10.07	0.60	-	-	-	-	100
Martian Basalt[j]	51.01	1.01	10.15	18.36	0.36	11.94	6.72	-	-	-	-	0.45	100.
HED-Basalt-1[k]	50.93	-	5.21	15.40	0.10	22.53	4.59	0.58	-	-	0.57	0.10	100
HED Basalt-2[k]	53.89	0.02	6.86	15.85	0.08	16.45	6.51	0.02	-	-	0.17	0.13	100
Basanite[l]	46.46	2.54	11.66	12.58	0.20	13.99	10.11	2.22	0.24	-	-	-	100
Andesite[m]	62.49	0.62	18.20	3.99	-	3.47	6.85	3.35	1.03	-	-	-	100
High-Mg Andesite[n]	54.20	0.60	15.60	6.70	-	9.40	9.60	2.60	1.30	-	-	-	100
Dacite[o]	67.23	0.94	15.82	4.47	0.06	1.45	3.40	2.12	4.24	0.27	-	-	100
Obsidian[p]	75.38	-	13.05	1.53	0.07	0.05	0.75	3.98	5.18	-	-	-	100
Picrite[q]	49.38	2.02	9.47	11.37	0.17	17.10	8.13	1.75	0.37	0.22	-	-	100
Nephelinite[r]	44.39	2.45	15.53	10.59	0.31	4.31	11.87	5.46	3.84	1.24	-	-	100
Syn-Nephelinite[s]	40.56	2.80	13.71	11.97	0.28	7.98	13.14	4.61	3.37	1.57	-	-	100
Phonolite[t]	55.96	0.34	21.60	2.88	0.26	0.12	1.84	8.26	8.68	0.05	-	-	100
Syn-phonolite[u]	54.78	1.61	19.17	5.55	0.16	1.77	4.09	9.10	3.66	0.12	-	-	100
Granite[v]	74.75	-	14.92	-	-	-	-	6.61	3.72	-	-	-	100
Albite/Forsterite ($Ab_{95}Fo_5$)[w]	70.61	-	19.14	-	-	2.88	-	7.37	-	-	-	-	100
Syn-Rhyolite-1[o]	75.24	0.29	13.53	1.04	0.05	0.22	0.77	2.18	6.60	0.08	-	-	100
Rhyolite-2[x]	74.80	0.22	13.66	1.27	0.03	0.32	1.15	3.04	5.43	0.07	-	-	100

$FeO_T = FeO + Fe_2O_3$

[a]Natural Icelandic Basalt (Norris and Wood, 2017)

[b]Synthetic Basalt (Sossi et al., 2019)

[c]Synthetic Mid Ocean Ridge Basalt (MORB), by Kiseeva and Wood, (2013) based on Falloon and Green, (1987)

[d]Natural Low-Mg Basalt, El Hierro, Canary Islands, Tephrite, EGT17-01 (Taracsák et al., 2021)

[e]Natural High-Mg Basalt, El Hierro, Canary Islands, Basanite, TNR14-01 (Taracsák et al., 2021)

[f]1 bar eutectic composition (Osborn and Tait, 1952)

[g]1 bar eutectic composition (Hytonen and Schairer, 1960)
[h]1.5 GPa approximate eutectic composition, (Presnall et al., 1978)
[i]Synthetic Lunar Basalt model from Apollo 11
[j]Synthetic Martian Basalt (Matzen et al., 2022)
[k]Synthetic bulk silicate compositions of Vesta (Ashcroft and Wood, 2015)
[l]Synthetic Basanite, modelled from the Nepheline basanite sample UT-70489 (Adam, 1990)
[m]Synthetic Andesite (Carmichael et al., 1974)
[n]Synthetic High-Mg Andesite (Wood and Turner, 2009)
[o]Dacite and Rhyolite compositions based on STXB4y and STXG4y respectively (Muir et al., 2014)
[p]Natural Lipari Obsidian LIP-17714 (Hunt and Hill, 1993)
[q]Natural Picrite, Hawaii, HAW-16095 (Taracsák et al., 2021)
[r]Natural Laacher See Nephelinite, LS-17980 (Taracsák et al., 2021)
[s]Syntheric Nephelinite (Webb and Dingwell, 1990)
[t]Natural Laacher See Phonolite, LS-17985 (Taracsák et al., 2021)
[u]Synthetic Phonolite (Ridley, 1970)
[v]Anhydrous granitic eutectic composition (Ebadi and Johannes, 1991)
[w]Synthetic mixture of 95% Albite and 5% Forsterite
[x]Synthetic Rhyolite made from the compositions of (Nockolds, 1954)

3.3.2 Controlling chlorine and oxygen fugacity

Chlorine fugacity was controlled by intimately mixing AgI and AgCl in a 75:25 ratio. The presence of iodine reduces the chlorine fugacity enough that blobs of $CaCl_2$ and $MgCl_2$ do not segregate from the silicate glass, therefore ensuring that the starting composition remains constant. The chlorine fugacity is then obtained from (Thomas and Wood;2021):

$$logf(Cl_2) = -\frac{11440}{T} + 2.961 + \frac{2150P}{T} - \frac{208P^2}{T} + 2log\left(\frac{Cl}{Cl+I}\right)_{halide} - 2log\left(\frac{Ag}{Ag+Pt}\right)_{metal} \quad (3.3)$$

In equation [3] P is in GPa, T is in Kelvin, and the ratios (Cl/(Cl+I)) and (Ag/(Ag+Pt)) refer respectively to the mole fractions of chlorine in the mixed halide melt and Ag in the coexisting liquid metal. Mixing in both liquids was assumed to obey Raoult's Law, an assumption which can be readily be shown to be reasonable for AgCl-AgI liquids based on the temperature and position of the 1 atmosphere eutectic (Levin et al., 1964), and reasonable for Ag-Pt liquids which are Ag-rich (generally >0.8 mole fraction. Table 3.2).

The starting silicate compositions were ground together with the AgI/AgCl mixture in a ratio of 75:25 (and packed into 2.5mm outside diameter, 1 mm inside diameter graphite capsules. The graphite capsules were placed, with a thin graphite lid, inside 3mm outside diameter platinum capsules with mixtures of graphite and silver carbonate above and below the graphite capsule . The platinum capsule was welded shut. During the experiment, the $AgCO_3$ decomposes to Ag metal, and, by reaction with graphite, CO_2. The coexistence of C and CO_2 buffers oxygen fugacity at CCO (Jakobsson and Oskarsson, (1994)):

$$logf(O_2)_{(CCO)} = 4.325 - \left(\frac{21803}{T}\right) + 0.171\left(\frac{(P-1)}{T}\right) \quad (3.4)$$

At the conditions employed in this study (1400°C and 1.5GPa), the log$f$(O_2) is fixed by this assembly at -7.17 (Thomas and Wood, 2021). The experiments employed a 32 mm long, 12.5

mm outside diameter, 8 mm inside diameter calcium fluoride cylinder as the principal pressure medium. Inside this cylinder was an 8 mm O.D., 6 mm I.D. graphite cylinder which acts as the furnace. The 3 mm outside diameter capsule was placed in the centre of the graphite furnace with crushable MgO pieces above, below and around the capsule. All experiments were then performed with an end-loaded 'Boyd and England'-type ½ inch piston-cylinder apparatus (Boyd and England, 1960) housed at the University of Oxford. The temperature was measured and controlled using an alumina-sheathed C-type ($W_{95}Re_5$–$W_{74}Re_{26}$) thermocouple, introduced through a hole in the upper MgO piece and separated from the capsule by a 0.5 mm thick alumina disc. All experimental assembly pieces were heated to minimise the presence of water as much as possible to ensure anhydrous conditions. This included heating the MgO pieces at 1000 °C overnight. Experiments were performed at a constant temperature and pressure, of 1400 °C and 1.5 GPa respectively (Table 3.2) using the *'hot piston-in'* method and the pressure calibrations of McDade et al., (2002). Experimental durations followed the time series experiments of Thomas and Wood, (2021), in which it was found that 1 hour was several times longer than necessary to reach a constant Cl concentration in the melt. All experiments resulted in a clear segregation of the silicate glass, metal halide and metal. All experiments were quenched by cutting the power to the graphite furnace (cooling at ≈120 °C/s). Once extracted, the recovered capsule was cleaned and weighed to ensure no mass was lost or gained during the experiment.

Two additional experiments were performed with the aim of determining the Cl content of melt at NaCl saturation. For these experiments, we used a natural phonolite (Table 3.1; LS-17985) as the silicate, intimately mixed with 20 wt% NaCl. One experiment was buffered at the CCO oxygen buffer as described above and the other at the Re-ReO_2 buffer using the assembly described by Thomas and Wood, (2021). The experiments were held at 1100°C and 1.0 GPa for 2 hours and quenched in the usual manner.

3.3.3 Analytical techniques

During the experiment, the buffer-silicate mixture segregates into a homogeneous translucent glass, a metal chloride/iodide phase, and an Ag-rich metal alloy. The NaCl-buffered experiments segregated distinctive blobs of NaCl which could be analysed easily with the microprobe. The capsules were mounted in epoxy, ground to expose the charge and polished with water-free diamond paste, using isopropanol as a lubricant to prevent any Cl loss (Mungall and Brenan, 2003).

Product silicate glasses and chlorine fugacity buffers were analysed on the CAMECA SX-Five-FE at the University of Oxford's Department of Earth Sciences. A 20 nA beam current, 15 kV accelerating voltage and a defocused 10 μm beam diameter was used for the glass analyses. To minimise the potential for element migration during analysis, Cl, Na, K, and Si were analysed first. Standards used for silicate glass analysis were natural albite (Si, Al, Na), andradite (Ca, Fe), Thallium-bromide-iodide (I), Titanium dioxide (Ti), Manganese (Mn), Sanidine (K) synthetic periclase (Mg), NaCl crystals (Cl), and pure metals of Ag and Pt. The NaCl standard used is a lab-grown pure, stoichiometric cubic crystal, that remained stable under the beam, and provided consistent results. Furthermore, using NaCl prevented the need of F and P corrections that would be associated in using minerals such as apatites. Counting times were a minimum of 30 s peak and 15 s background for all elements except for Cl for which 80 s peak and 40 s background were used to obtain a detection limit of $\leq$100 ppm. For Na and K 20s peak and 10s background were used to reduce the chance of element migration from the beam and these elements were analysed first on 2 different spectrometers. Replicate analysis on the same spots of glass revealed that Cl counts were stable and consistent at these conditions; with over 20 points on each silicate portion of the charge, and 10–20 points within the remaining buffer and resultant metal phases. Results remained consistent with low (<0.2 wt%) standard deviations (Table 3.2); secondary standards including Durango apatite, containing known

concentrations of Cl of 0.41 wt% (Kusebauch et al., 2015a) were used to ensure accurate Cl analysis, and we obtained an average of 0.412 wt% Cl with a standard deviation of 0.013% for 84 analyses.

3.4 Results

All experiments except those at NaCl saturation were performed at 1400 °C and 15 kbar, using the CCO buffer ($f(O_2)$ = -7.17 log units). All run conditions, the concentrations of chlorine in the resultant glass phases and calculated chlorine fugacities are given in Table 3.2. Complete analyses of the silicate glass products are presented in supplementary Table S2 (Appendix C). In order to compare results obtained at different chlorine fugacities, and, considering that chlorine solubility is proportional to the Henry's Law relationship derived from reaction [2] we define the *chloride capacity* (C_{Cl}; Table 3.2):

$$C_{Cl} = \frac{Cl\ (wt\%)}{\sqrt{f(Cl_2)}} \times \sqrt[4]{f(O_2)} \quad (3.5)$$

We calculated the ferric-ferrous ratio of each experiment using the equation of Kress and Carmichael (1991) and adjusted the FeO and Fe_2O_3 contents of our products accordingly.

Table 3.2 Experimental conditions and compositions

Experiment ID	Silicate composition*	Time (hours)	Pressure (GPa)	Temperature (°C)	Measured Cl^{glass} wt%	Buffer/Silicate by mass	AgI/AgCl	Final Molar *Cl/(Cl+I)*	Molar *Ag/(Ag+Pt)*	*log* $f(O_2)$	$f(Cl_2)$	C_{Cl}	OB	NBO/T	IP	LI
Ab/Fo-1	95% Albite - 5% Forsterite	1	1.5	1400	0.56 (0.02)	75/25	75/25	0.325	0.879	-7.17	8.08E-04	0.32	0.53	0.00	72.56	20.66
Ab/Fo-2	Ab/Fo + $CaCO_3$	1	1.5	1400	1.41 (0.06)	75/25	75/25	0.276	0.943	-7.17	5.05E-04	1.01	0.56	0.27	71.12	8.01
Ab/Fo-3	Ab/Fo + $CaCO_3$	1	1.5	1400	2.75 (0.05)	75/25	75/25	0.183	0.812	-7.17	2.98E-04	2.57	0.58	0.57	69.81	-2.88
Ab/Fo-6	Ab/Fo + $CaCO_3$	1	1.5	1400	0.46 (0.01)	80/20	75/25	0.123	0.892	-7.17	1.12E-04	0.70	0.58	0.38	70.54	5.54
AgI/Cl-27†	Icelandic Basalt	1	1.5	1400	1.6 (0.03)	50/50	75/25	0.209	0.778	-7.17	4.24E-04	1.25	0.58	0.57	69.60	-5.10
AgI/Cl-005†	CMAS	1	1.5	1400	2.55 (0.04)	75/25	75/25	0.198	0.844	-7.17	3.24E-04	2.29	0.60	0.94	67.24	-18.22
AgI/Cl-024†	CMAS+ FeO	1	1.5	1400	2.54 (0.06)	75/25	75/25	0.198	0.887	-7.17	2.94E-04	2.39	0.61	1.09	66.95	-23.01
AgI/Cl-025†	CMAS+ FeO	1	1.5	1400	2.70 (0.19)	75/25	75/25	0.184	0.864	-7.17	2.68E-04	2.66	0.62	1.21	66.86	-25.94
AgI/Cl-026†	CMAS+ FeO	1	1.5	1400	3.49 (0.28)	75/25	75/25	0.120	0.903	-7.17	1.04E-04	5.52	0.64	1.56	65.72	-34.06
CMAS+Na-1	CMAS + Na_2CO_3	2	1.5	1400	2.15 (0.06)	75/25	75/25	0.227	0.800	-7.17	4.76E-04	1.59	0.61	1.03	67.79	-13.33
CMAS+Na+2	CMAS + Na_2CO_3	2	1.5	1400	2.32 (0.1)	75/25	75/25	0.214	0.836	-7.17	3.89E-04	1.90	0.61	0.99	67.33	-17.34
CNMAS	$Fo_5Di_{48}An_{47}$	2	1.5	1400	2.41 (0.14)	75/25	75/25	0.208	0.937	-7.17	2.92E-04	2.28	0.60	0.89	67.66	-16.97
CNMAS-2	$En_{17}An_{43}Di_{40}$	2	1.5	1400	2.60 (0.13)	75/25	75/25	0.194	0.793	-7.17	3.52E-04	2.24	0.60	1.00	67.72	-16.44
Dacite-1	Dacite	2	1.5	1400	0.46 (0.08)	75/25	75/25	0.332	0.854	-7.17	8.90E-04	0.25	0.53	0.01	72.86	22.14
Dacite-2	Dacite	1	1.5	1400	0.17 (0.01)	75/25	90/10	0.142	0.776	-7.17	1.98E-04	0.20	0.53	0.00	73.03	23.44
TNR14-1	High Mg Basalt	1	1.5	1400	2.23 (0.12)	75/25	75/25	0.221	0.913	-7.17	3.47E-04	1.93	0.60	1.14	68.79	-18.68
HA3-2	Basalt	2	1.5	1400	1.62 (0.16)	75/25	75/25	0.265	0.882	-7.17	5.32E-04	0.67	0.59	1.50	67.19	-23.23
HA4-1	Basalt	1	1.5	1400	1.75 (0.2)	75/25	75/25	0.254	0.858	-7.17	5.18E-04	1.24	0.58	0.93	68.71	-9.84
Rhyolite	Rhyolite	1	1.5	1400	0.27 (0.03)	75/25	75/25	0.340	0.812	-7.17	1.04E-03	0.14	0.52	0.00	73.51	30.83
LIP-17714	Lipari Obsidian	1	1.5	1400	0.27 (0.03)	75/25	75/25	0.340	0.832	-7.17	9.85E-04	0.14	0.52	0.00	73.49	29.18
AN-1	Andesite	4	1.5	1400	0.72 (0.03)	25/75	75/25	0.227	0.785	-7.17	4.92E-04	0.52	0.55	0.15	71.76	13.02
AN-2	Andesite	2	1.5	1400	0.90 (0.05)	75/25	75/25	0.306	0.893	-7.17	6.93E-04	0.55	0.55	0.15	71.72	11.17

SM-1	Basalt	2	1.5	1400	3.05 (0.16)	75/25	75/25	0.158	0.938	-7.17	1.67E-04	3.81	0.62	1.51	66.32	-28.16
HiMgAnd	Andesite	1	1.5	1400	1.71 (0.03)	75/25	75/25	0.257	0.916	-7.17	4.65E-04	1.28	0.58	0.58	69.72	-4.45
HAW-16095	Picrite	1	1.5	1400	1.90 (0.14)	75/25	75/25	0.244	0.947	-7.17	3.93E-04	1.55	0.59	0.88	69.27	-12.20
EGT17-1	Low Mg Basalt	1	1.5	1400	1.40 (0.02)	75/25	75/25	0.276	0.837	-7.17	6.43E-04	0.89	0.57	0.28	71.59	5.24
KK3b-1	MORB	1	1.5	1400	1.13 (0.02)	25/75	75/25	0.130	0.707	-7.17	2.00E-04	1.29	0.59	0.72	69.45	-10.45
KK3b-2	MORB	1	1.5	1400	1.70 (0.04)	75/25	75/25	0.257	0.754	-7.17	6.88E-04	1.05	0.58	0.57	69.45	-5.74
Mars-1	Martian Basalt	1	1.5	1400	2.02 (0.2)	75/25	75/25	0.236	0.961	-7.17	3.57E-04	1.73	0.60	1.14	68.09	-20.24
LS-17980	Nephelinite	1	1.5	1400	1.91 (0.03)	75/25	75/25	0.244	0.906	-7.17	4.27E-04	1.49	0.60	0.62	69.64	-9.56
Basanite-1	Basanite	2	1.5	1400	2.06 (0.03)	75/25	75/25	0.234	0.897	-7.17	4.00E-04	1.66	0.59	0.93	68.96	-12.73
Lunar-1	Lunar basalt	2	1.5	1400	2.03 (0.09)	75/25	75/25	0.235	0.935	-7.17	3.75E-04	1.69	0.60	0.78	70.90	-14.80
KK-Rhy	Rhyolite	2	1.5	1400	0.15 (0.02)	75/25	75/25	0.347	0.948	-7.17	7.91E-04	0.09	0.52	0.00	73.28	27.25
Syn-Phono-1	Syn-Phonolite	2	1.5	1400	0.83 (0.02)	75/25	75/25	0.310	0.764	-7.17	9.72E-04	0.43	0.55	0.07	72.20	16.79
LS-17985-1	Phonolite	2	1.5	1400	0.68 (0.07)	75/25	75/25	0.319	0.955	-7.17	6.61E-04	0.43	0.56	0.00	72.06	21.84
LS-17985-2	Phonolite	2	1.5	1400	0.44 (0.03)	75/25	90/10	0.170	0.943	-7.17	1.92E-04	0.51	0.57	0.02	71.93	21.01
Granite-2	Granite	2	1.5	1400	0.31 (0.10)	75/25	75/25	0.339	0.916	-7.17	8.08E-04	0.18	0.52	0.00	73.32	28.08
Gran+Mg-1	Granite + MgO	2	1.5	1400	0.61 (0.10)	75/25	75/25	0.323	0.770	-7.17	1.04E-03	0.31	0.54	0.10	72.34	20.89
Gran+Mg-2	Granite + MgO	2	1.5	1400	0.67 (0.14)	75/25	75/25	0.320	0.918	-7.17	7.16E-04	0.40	0.54	0.15	72.09	19.03
Gran+Mg-3	Granite + MgO	2	1.5	1400	0.78 (0.10)	75/25	75/25	0.313	0.844	-7.17	8.09E-04	0.44	0.54	0.20	71.71	16.31
Phonolite-NaCl-1§	80% LS-17985; 20% NaCl	0.5	1.0	1100	1.09 (0.10)	-	-	-	-	-6.77	2.70E-03	0.42	0.57	0.00	72.67	21.28
Phonolite-NaCl-2§	80% LS-17985; 20% NaCl	2	1.0	1100	1.00 (0.12)	-	-	-	-	-10.31	4.46E-05	0.40	0.57	0.01	72.59	19.39

Cl% error in () is 2 stdev

*Starting silicate melt compositions presented in Table 3.1

† Experiments originally presented in Thomas and Wood, (2021)

§ $f(Cl_2)$ and C_{Cl} calculated using *ChlorCalc_v1* (Spreadsheet available in the supplementary)

C_{Cl} = Chloride capacity, OB = Optical Basicity, IP = Ionic Porosity, LI = Larsen Index (see text)

3.4.1 Henry's Law and melt composition

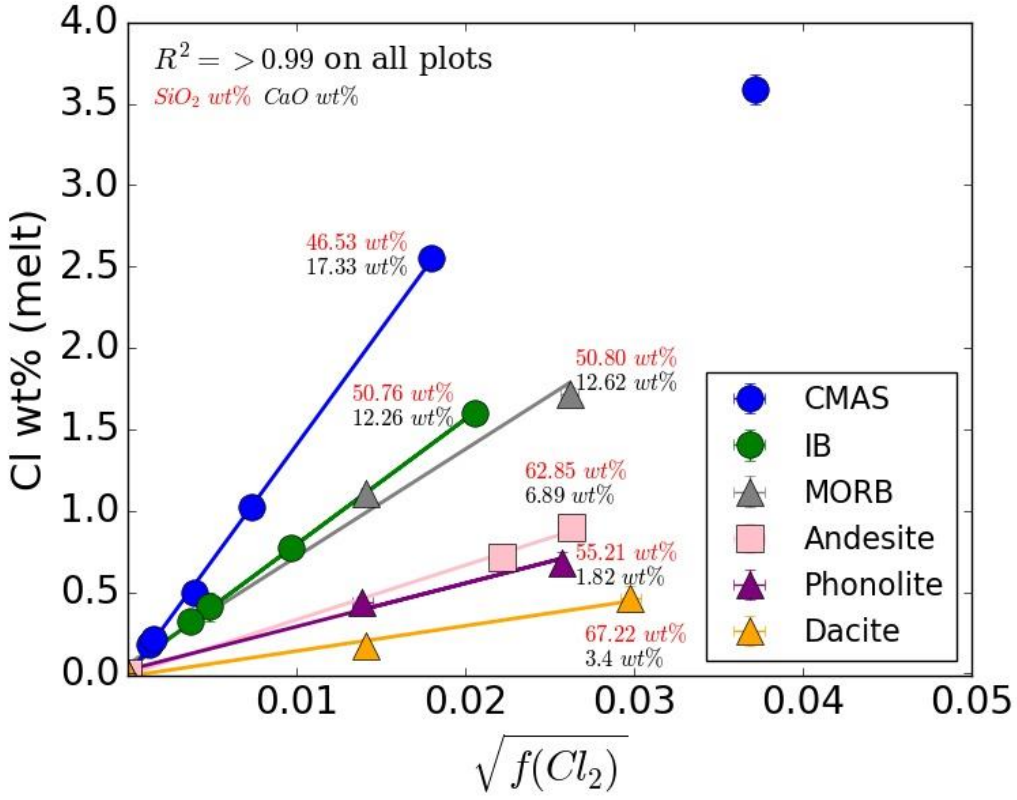


Figure 3.2 This figure illustrates the minimum lengths of the Henry's Law, linear regions for melts of different bulk composition at 1.5 GPa/1400°C. It also implies that SiO_2 and CaO contents are likely important parameters in determining Cl solubility, as reflected in our fit equation (3.12).

Figure 3.2 shows the Cl contents of melts of a wide range of compositions equilibrated at different fugacities of chlorine with oxygen fugacity controlled at the CCO buffer and temperature and pressure of 1400°C and 1.5 GPa respectively. As can be seen, Cl dissolution in all seven melts follows Henry's Law to concentrations of between, depending on major element composition at least 0.5 wt% (dacite) and 2.6 wt % ($An_{50}Di_{28}Fo_{22}$) Cl. The effect of composition is dramatic with more than an order of magnitude difference between Cl contents (under constant $f(O_2)$,$f(Cl_2)$ conditions) of a low SiO_2, high CaO haplobasalt, which is rich in

Cl and a high SiO_2 low CaO dacite, poor in Cl. Specific compositional effects will be discussed further below.

3.4.2 Correlation of empirical compositional parameters with chloride capacity

There are a number of empirical parameters which have been proposed as being simple ways of representing the complexities of silicate melt compositions by a single parameter. These are all basically ways of representing the degree of polymerisation of the melt by assigning different roles to "network-forming" (e.g., SiO_2) and "network-modifying" or depolymerising (e.g., Na_2O) oxide components. Since Cl is observed to replace oxygen in the silicate matrix, it is logical to assume that chloride capacity is a function of the way in which oxygen is bonded in the silicate melt.

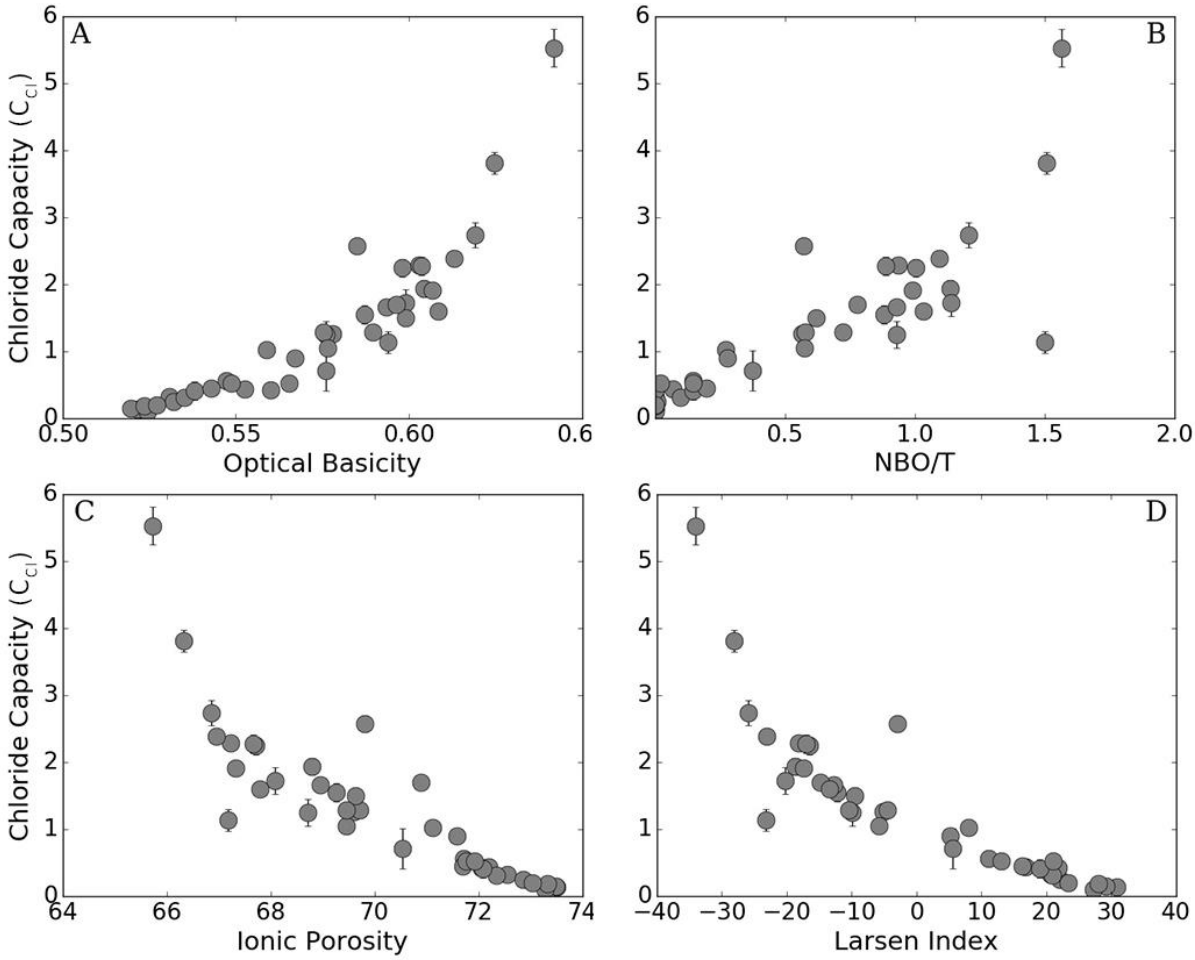


Figure 3.3 Shows our chloride capacity data at 1.5GPa/1400 °C plotted against some of the more relevant empirical parameters which aim to describe degree of polymerisation and acid-base behaviour of silicate melts. See text for definitions and discussion.

Optical basicity: Optical basicity is a parameter which empirically allocates an electron donor power (Lewis basicity) to each individual oxide in a silicate melt matrix (Banin et al., 1997). Optical basicity, denoted, Λ, was proposed as a useful index of melt properties by Duffy and Ingram, (1971) and adapted by Duffy and Ingram, (1976) and Duffy, (2004) as follows:

$$\Lambda = \frac{\sum X_i n_i \Lambda_i}{\sum X_i n_i} \quad (3.6)$$

In equation (3.6) X_i is the mole fraction of oxide i, n_i is the number of oxygen atoms of the oxide, and Λ_i is the optical basicity of oxide i. As expected, optical basicity decreases with increasing SiO_2 and Al_2O_3 contents and increases with CaO, MgO and alkali concentrations. Therefore, as anticipated from Figure 3.2 there is a strong positive correlation of chloride capacity with optical basicity (Figure 3.3a).

NBO/T: A second empirical way of representing the properties of the oxygen atoms in a silicate matrix is through the ratio of non-bridging oxygens to tetrahedrally coordinated cations, NBO/T. The chemical rationale is that oxygen atoms which bridge between tetrahedral Si and Al have different properties from those which terminate silicate chains or are present in isolated tetrahedra. We calculated NBO/T following the approach of Mills, (1993). This derives Y_{NB} and X_T as follows for $Fe^{3+}/(Fe^{2+}+Fe^{3+}) < 0.3$ (Mills, 1993) from the mole fractions x of the different oxides:

$$Y_{NB} = \sum 2[xCaO + xMgO + xFeO + xMnO + xNa_2O + xK_2O] + 6xFe_2O_3 - 2xAl_2O_3 \quad (3.7)$$

$$X_T = \sum xSiO_2 + xTiO_2 + 2xP_2O_5 + 2xAl_2O_3 \quad (3.8)$$

$$\frac{NBO}{T} = \frac{Y_{NB}}{X_T} \quad (3.9)$$

Since Y_{NB} increases with CaO, MgO and alkali contents, NBO/T correlates positively with optical basicity and chloride capacity as shown in Figure 3.3b.

Ionic porosity: This parameter is a calculation of the percentage of the melt volume unoccupied by cations and anions and defined as (Dowty, (1980)):

$$Z = 100(1 - V_{ca}/V_L) \quad (3.10)$$

In equation (3.10) V_{ca} is the total volume occupied by constituent atoms (cations + anions) in one gram of melt, and V_L is the melt volume (cm^3/g) calculated using the oxide partial molar volumes as given by Lange and Carmichael, (1987). We calculated the ionic porosity of each product glass using the calculator presented in Iacono-Marziano et al., (2010). Their model uses the parameters of Carroll and Stolper, (1993) with volumes of individual cations and anions calculated from effective ionic radii given by (Shannon and Prewitt, 1969; Shannon, 1976), assuming spherical geometry. All melt compositions were recalculated to 100% before calculating ionic porosity. Since ionic porosity generally decreases with increasing Ca, Mg and alkalis and decreases with SiO_2, chloride capacity correlates negatively with ionic porosity (Fig 3.3c).

Larsen Index: The Larsen index is a measure of the extent of differentiation of a melt, defined as follows (Larsen, 1938):

$$LI = \left[\left(\frac{1}{3}SiO_2 + K_2O\right) - \left((FeO + \frac{9}{10}Fe_2O_3 + MnO) + CaO + MgO\right)\right] \qquad (3.11)$$

This index (Fig 3.3d) has been used extensively to correlate chlorine solubility with chemical composition (e.g. Webster et al., 2009; Webster et al., 2015; Webster et al., 2018; Webster et al., 2019). Given the positive term in SiO_2 and negative term in CaO, chloride capacity correlates, as expected, negatively with Larsen Index as shown in Figure 3.3d.

Oxide mole fractions: It is clear from Figure 3.3 and the preceding discussion that all of the empirical compositional parameters considered provide reasonable descriptions of the compositional dependence of chloride capacity over the broad compositional range investigated. We were seeking, however, to identify subtle variations in chloride capacity due to different cations of similar, but not identical chemical behaviour. We therefore fitted the logarithm of the chloride capacity using SPSS software to compositional terms for each of the

constituent oxides, with each oxide recalculated as the mole fraction on a single cation basis. We used stepwise linear regression applying the F-test (α=0.05) to determine which compositional parameters are significant. In order to ensure that the compositional terms approach zero at infinite temperature, the oxide mole fractions were divided by temperature. Terms that were not significant at an F of 0.05 were excluded. This approach resulted in the following equation:

$$logC_{Cl} = 1.601 + (4470X_{Ca} - 3430X_{Si} + 2592X_{Fe} - 4092X_{K}\text{-}894\text{P})/\text{T} \quad (3.12)$$

R^2=0.96; standard error = 0.089

In order to take account of pressure and temperature effects on chloride capacity we regressed the data together with the data from Thomas and Wood, (2021) in which the pressure and temperature effects on chloride capacity for the $An_{50}Di_{28}Fo_{22}$ composition and the Icelandic basalt were independently established. As before we found that the term in reciprocal temperature is insignificant, and that the P/T term is required. The value in equation (12) is within error of the same terms previously obtained by regression. Cl content was also explored as a function of the Fe^{3+}/Fe^{2+} ratio in the melt which is thought to play an important role in Cl solubility (Bell and Simon, 2011), but no significant correlation was found. This may be due to 1) performing experiments at limited conditions, 2) using a limited range of Fe, or 3) due to the loss of Fe to the Pt found to occur during the experiment (chapter 2). A spreadsheet enabling the calculation of Cl fugacities and chloride capacities as defined in equations (3.12) and (3.15) is provided as an electronic supplement, *'ChlorCalc_v1'.*

3.5 Discussion

3.5.1 The effects of H_2O on chloride capacity

There are a considerable number of studies of the partitioning of Cl and other elements between silicate melts and aqueous fluids (Shinohara et al., 1989; Métrich and Rutherford, 1992; Webster, 1992; Irina F. Kravchuk and Keppler, 1994; Webster and Rebbert, 1998; Bureau et al., 2000b; Signorelli and Carroll, 2000; Signorelli and Carroll, 2002; Botcharnikov et al., 2007; V. Chevychelov et al., 2008; Stelling et al., 2008a; Alletti et al., 2009; Webster et al., 2009; Zajacz et al., 2012; Alletti et al., 2014; Beermann et al., 2015; Botcharnikov et al., 2015) . In general, however, because of the difficulties of fluid separation and analysis, authors calculate the composition of the fluid by mass balance from the starting composition and the measured melt composition. This approach works reasonably well for Cl, but concentrations of charge-balancing cations in the fluid are difficult to estimate. This is important because, for experiments performed at fixed $f(O_2)$ or fixed $f(H_2)$ the Cl_2 fugacity is related to the HCl fugacity through the equilibria:

$$H_2O = 0.5O_2 + H_2 \qquad (3.13)$$

$$H_2 + Cl_2 = 2HCl \qquad (3.14)$$

If the concentrations of charge balancing cations such as Na, Ca and K are known then any Cl in excess of charge balance can be allocated, approximately, to HCl. If only Cl is known, however, the fugacity of HCl must either be calculated by allocating all Cl to HCl or by arbitrarily subtracting some fraction of the Cl as “bonded with other cations” in the fluid.

Bearing in mind these difficulties we attempted to incorporate the effects of H_2O on chloride capacities using melt-aqueous fluid Cl partitioning data on a phonolite at 1000 ˚C and 10-250 MPa (Alletti et al., 2014) . In this case the authors have calculated the chlorine content of the fluid as HCl. For the experiments of Alletti et al., (2014) we used the Modified Redlich Kwong equation of state for H_2O-H_2-HCl fluids with parameters for H_2O, H_2 (Holloway, 1977b) and HCl (Prausnitz et al., 1999). This enabled us to calculate the Cl_2 fugacity of each experiment

using the equilibrium constant for equilibria (3.13) and (3.14) from the NIST-JANAF thermochemical tables (https://janaf.nist.gov/).

Adding the 23 data from Alletti et al., (2014) to our 62 data and performing stepwise linear regression with the same approach as before we obtained:

$$logC_{Cl} = 0.571 + (4873X_{Ca} - 3803X_{Si} + 2724X_{Fe} + 1891\text{- }943\text{P})/\text{T} \quad (3.15)$$

R^2=0.94; standard error = 0.117

The important points to note are as follows : 1) Although we added the water contents (0.6-4.3 wt%) in mole fractions (0.04-0.26) as a parameter to the regression, the term in H_2O was not significant at the α=0.05 level. 2) The terms in X_{Ca}, X_{Si}, X_{Fe} and P/T are very similar in equations (3.12) and (3.15) implying that they are quite robust. 3) The temperature range of the data has been extended by a further 200 °C which has required the introduction of a term in 1/T. The latter was found not to be significant in our earlier study presumably because of the more restricted temperature range employed in our higher-pressure experiments.

Although other data in the literature have the potential to provide additional compositional constraints we have found it difficult to treat all studies in a consistent way. We therefore present equation (3.15) as an illustration of the extension of our approach to lower temperatures and moderate water contents (up to 4.3%) on the understanding that a systematic addition of H_2O to experiments using our buffering approach is required to better resolve the question of H_2O effects on chloride capacity.

3.6 Implications

3.6.1 H_2O and HCl degassing

Thomas and Wood, (2021) observed that Cl should not degas significantly as HCl during ascent of basalt until pressures are well below 10 MPa, and that most Cl would be degassed below 2 MPa, equivalent to ~ 80 meters depth. In figure 3.4 we illustrate the effect of composition on these estimates made by assuming that the evolved gas is dominantly H_2O. We considered 4 melts, basalt, andesite, dacite and rhyolite (anhydrous compositions in Table 3.1) and estimated their dry liquidi at 50 MPa using *alphaMELTS for Python* (Antoshechkina and Ghiorso, 2018). We then calculated the H_2O content of each melt at 50 MPa and a temperature just above the dry liquidus (1220, 1200, 1080 and 1030 ^oC for basalt, andesite, dacite and rhyolite respectively) using a spreadsheet from (Moore et al., 1998). The latter yields saturated H_2O contents of between 2.13 (andesite) and 2.34 (rhyolite) weight% at 50 MPa (Table 3.3).

Table 3.3 Normalised silicate melt compositions at water saturation

Composition	Temperature (°C)	SiO_2	TiO_2	Al_2O_3	FeO_T	MnO	MgO	CaO	Na_2O	K_2O	P_2O_5	H_2O*	Total
Icelandic basalt	1220	49.57	1.00	14.96	9.38	-	8.97	11.97	1.97	-	-	2.18	100.00
Andesite	1200	61.16	0.61	17.81	3.91	-	3.40	6.70	3.28	1.01	-	2.13	100.00
Dacite	1080	65.72	0.92	15.47	4.37	0.06	1.42	3.32	2.07	4.15	0.26	2.24	100.00
Rhyolite	1030	73.48	0.28	13.21	1.02	0.05	0.21	0.75	2.13	6.45	0.08	2.34	100.00

*H_2O contents are calculated from Moore et al., (1998) at 50 MPa, using anhydrous compositions (Table 3.1)

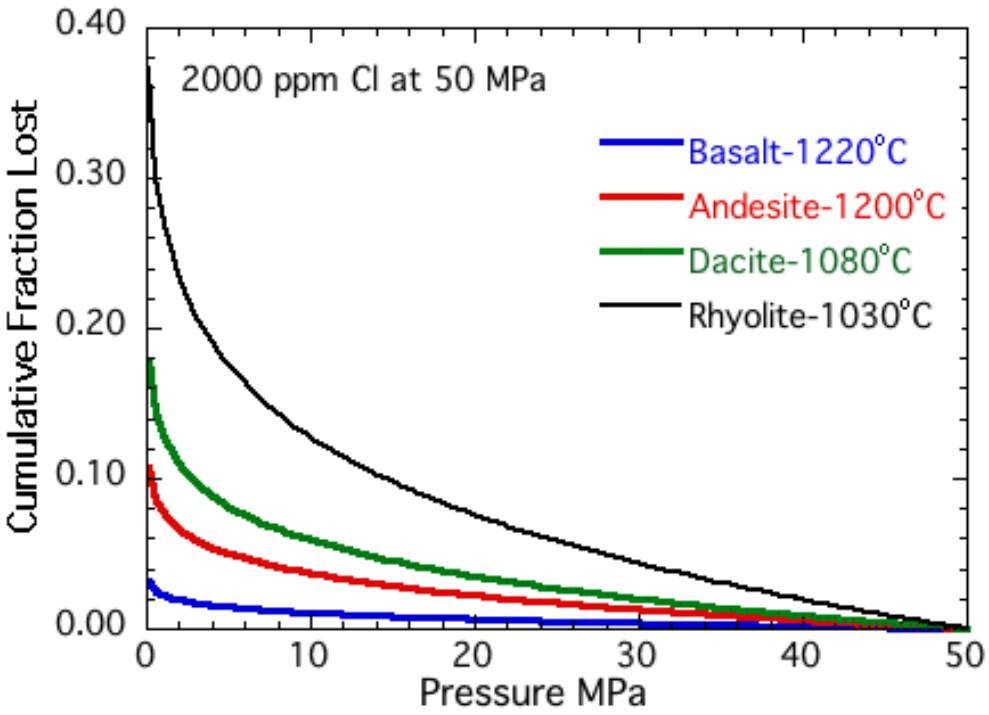


Figure 3.4 Shows the expected losses of chlorine as HCl from ascending magmas of different composition. All 4 melts were assumed to contain 2000 ppm Cl initially and to begin losing HCl at 50 MPa during isothermal ascent. In all 4 cases most loss occurs at pressures below 2 MPa and the fraction lost as the surface is approached varies dramatically with composition as Rhyolite>Dacite>Andesite>Basalt.

In order to calculate the degassing path of Cl from the melts of interest we estimated their chloride capacities from equation (3.15) at an oxygen fugacity corresponding to the fayalite-magnetite–quartz (FMQ) buffer, assumed water saturation at 50 MPa and applied starting concentrations of 0.2 weight% Cl in all 4 melts. We then calculated the amounts of H_2O and HCl degassed in H_2O-HCl fluids from 50 to 0.1 MPa in 0.5 MPa intervals. Although, as before, we adopted the Modified Redlich Kwong (MRK) equation of state for the H_2O-H_2-HCl gas phase, fugacity coefficients for H_2 and HCl in the water-rich gas are so close to 1.0 that they could have been assumed to be perfect gases with little change in result.

It should be noted that, although chloride capacity depends on $f(O_2)$ the degassing of HCl is actually independent of oxygen fugacity. This can be seen by combining the dissolution reaction of Cl in the melt with those for the dissociation of H_2O and formation of HCl:

$$Cl_2 + [O^{2-}]_{melt} = 2[Cl^-]_{melt} + \frac{1}{2}O_2 \qquad \text{(a)}$$

$$H_2O = H_2 + \frac{1}{2}O_2 \qquad (b)$$

$$2HCl = H_2 + Cl_2 \quad (c)$$

If we subtract reaction (b) from (a) and add (c) we eliminate oxygen and chlorine fugacities and obtain:

$$2HCl_{gas} + [O^{2-}]_{melt} = 2[Cl^-]_{melt} + H_2O_{liquid} \qquad (3.16)$$

Thus, the results shown in figure 3.4 are independent of oxygen fugacity provided Cl is dominantly degassed as HCl, which is the case in low pressure, high temperature environments.

As can be seen in Figure 3.4 and anticipated from equation (3.15) the effects of Ca, Fe and Si on chloride capacity result in basaltic melts having much higher Cl solubilities and lower tendences to degas HCl than silica-rich melts poor in Ca and Fe. We calculate that a basaltic melt containing 0.2% Cl at 50 MPa will degas only 0.006% Cl during the ascent to the surface. In contrast, andesitic, dacitic and rhyolitic melts initially containing 0.2% Cl should degas 0.02, 0.035 and 0.074 weight % respectively during ascent. Almost half of the degassing takes place, as before, at pressures below 2 MPa (80 meters depth) conditions under which the gas pressure would be expected to fluctuate substantially due to melt migration and convection. The calculations therefore show that HCl would degas only in the very uppermost parts of a volcanic edifice or during an eruption. This conclusion is consistent with the observations of

Saito et al. (2005) at Miyekejima Volcano, Japan who found that Cl remains in the melt, even after shallow degassing, and thus only degasses at very low pressures, well after H2O and CO2 (Spilliaert et al. 2006). More recently, Edmonds et al. (2009) placed constraints on the depths of Cl degassing at Kilauea and found that Cl degasses at depths of 35 meters or less, pressures below 1MPa, and below pressures of sulphur degassing. This conclusion coincides with the findings of (Lesne et al. 2011) who performed experiments to simulate decompression-driven, closed-system degassing of basaltic magma in equilibrium with an H-C-O-S-Cl fluid. They found that dissolved Cl displayed minimal loss to the fluid over a wide pressure range, remaining in the melt from 400MPa to 25MPa. Finally, the enrichment of Cl in thermal springs is also believed to reflect Cl degassing at very shallow conditions (Li et al. 2015).

3.6.2 Controls on chlorine partitioning

Calculating the chlorine lost to a gas also allows for the determination of the chlorine partition coefficient, between the H_2O-HCl fluid and the silicate melt ($D_{Cl}^{fluid/melt}$). To do this, we first convert the mole fraction of XHCl in the gas to mass % HCl, and then divide by the Cl wt% in the melt:

$$D_{Cl}^{fluid/melt} = \frac{\frac{XHCl \times 36.458}{XHCl \times 36.458 + XH_2O \times 18.015} \times 100}{Cl_{melt}}$$

Where XH_2O is the mole fraction of H_2O (1-XHCl), and values refer to the molar masses of HCl and H_2O. Figure 3.5 presents the partition coefficients derived from these the above calculations and compared against Cl partition coefficients presented from experiments within the literature (Webster and Holloway, 1988; Webster, 1992; Simon et al., 2004; Botcharnikov et al., 2007; Stelling et al., 2008; Webster et al., 2009; Zajacz et al., 2012; Webster et al., 2015; Tattitch et al., 2021), compiled by Tattich et al., (2021). For a given composition, we observe

a decrease in $D_{Cl}^{fluid/melt}$ with pressure from 0-35 MPa reaching a plateau from 50-450 MPa. This is finding is contradictory to the experimentally determined partition coefficients of other authors (such as Tattich et al., 2021; Botcharnikov et al., 2007; Webster, 1998) who found that $D_{Cl}^{fluid/melt}$ increased with pressure, reaching a plateau at approximately 300 MPa in rhyolitic, rhyodacitic and andesitic melts (Figure 3.5A). This disagreement may indicate that the composition of the fluid is a key factor in controlling chlorine partitioning. For example, Tattich et al., (2021) used a starting solution of NaCl–KCl–HCl and, whilst Botcharnikov et al., (2015) only used HCl (and in some cases an addition of AgCl) as the starting fluid composition in their experiments, they concluded that fluid contained between 9 and 64 wt% cations by the end of the experiment. Therefore, the idealised model of HCl-H_2O fluid, presented in this study underrepresents the partition coefficient with a typical, geologically relevant fluid. Additionally, this disparity could be due to 1) the large uncertainties attributed to the experimental data, due to the difficulties involved in determining the Cl content of the fluid by mass balance, and 2) the lack of experimental data at ≤50 MPa, where our model shows the most significant changes. Figure 3.5 however, does show a strong compositional dependence, with rhyolite exhibiting $D^{fl/m}$ values two orders of magnitude greater than that found within the basaltic composition at similar pressures and temperatures. This compositional dependence correlates with the experimental data (Figure 3.5), particularly at pressures greater than 200 MPa. For example, all compositions show, broadly similar, of order of magnitude partition coefficients to those experimentally determined within the literature, with rhyolitic compositions displaying higher partition coefficients than andesitic and basaltic compositions. Figure 3.5B plots $D^{fl/m}$ with temperature, for experiments conducted at 200(±4) MPa. At this pressure, our modelled $D^{fl/m}$, correlates closer to the experimental data, with as before, rhyolitic melts at higher $D^{fl/m}$ values than that of the andesitic and basaltic compositions.

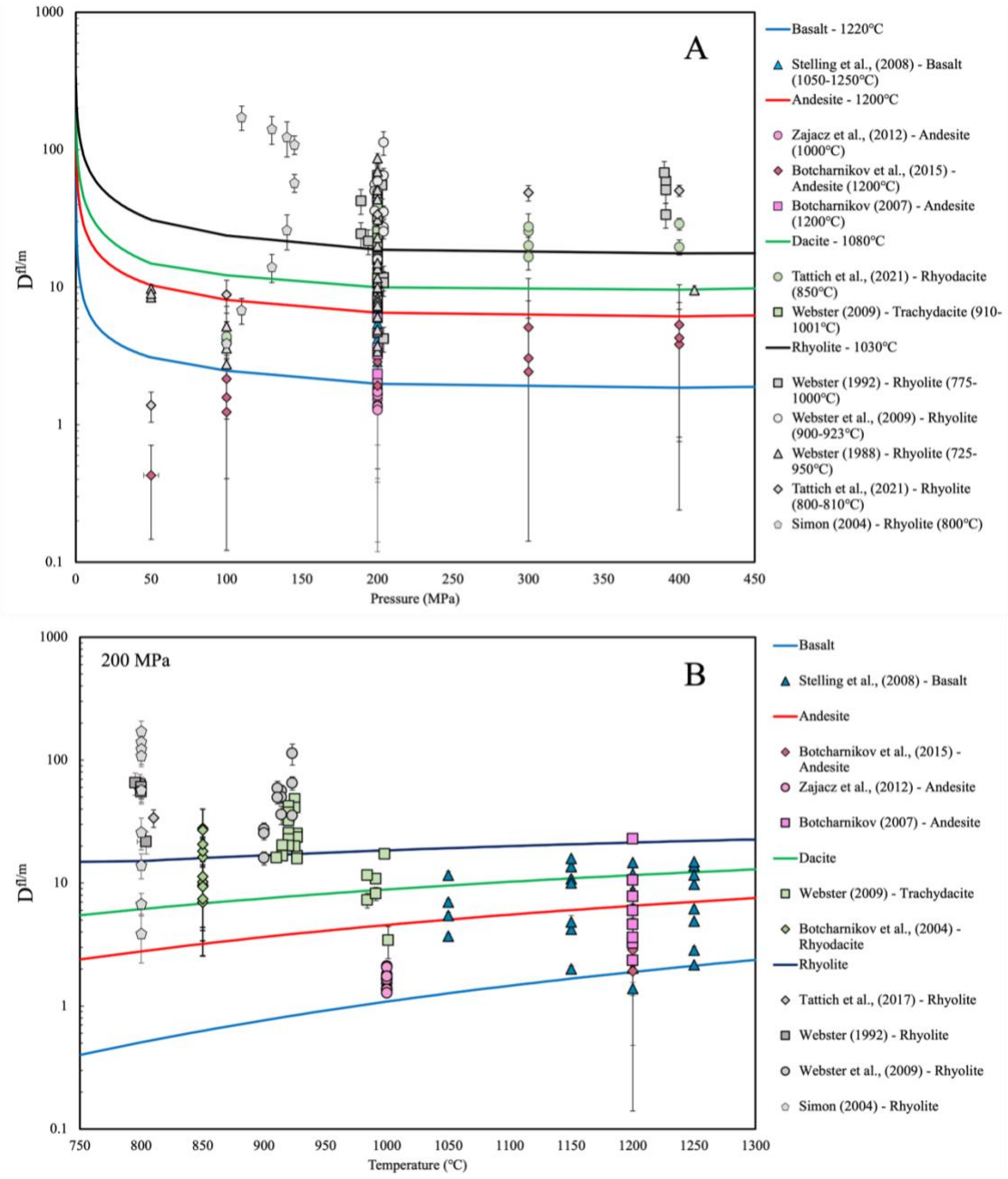


Figure 3.5 Shows the calculated $D^{fl/m}$ of the same 4 compositions as in Fig 3.4 as a function of pressure (A) and temperature (at 200MPa; B). Literature data are colour coded in relation to their rock composition, with Andesite as red or pink colours, rhyolites in shades of grey etc to match the colour of the calculated $D^{fl/m}$ curves.

3.6.3 NaCl activities in Cl-containing silicate melts

Brine separation from melts is an important process in the generation of many economically important ore deposits (Cline and Bodnar, 1994; Bruce et al., 1999; Bortnikov, 2006; Gleeson and Turner, 2007; Wilkinson, 2013; Blundy et al., 2015; Nshimiyimana et al., 2015; Essarraj et al., 2016; Blundy et al., 2021) and understanding of the depths at which saturation occurs is fundamental to the development of an understanding of the process in specific environments.

In order to provide a basis for understanding brine saturation, Webster and De Vivo, (2002) and Webster et al., (2015) performed experiments in which silicate melts of a wide range of compositions were saturated with chloride-rich liquids, the latter being dominated by NaCl and KCl. In some cases, hydrous chlorides such as $FeCl_2.4H_2O$ and $CaCl_2.2H_2O$ were added instead of, or in addition to NaCl and KCl, as were oxalic acid, a source of H_2O and CO_2 and $PtCl_4$. Importantly, the experimental products were very close to chloride saturation and (Webster et al., 2015) used the results to model the solubility of chloride in silicate melts.

In order to connect our chloride capacity measurements to the chloride saturation experiments of Webster and De Vivo, (2002) and Webster et al., (2015), we performed two experiments at 1100 ˚C and 1.0 GPa in which a phonolitic melt was saturated in NaCl at two different oxygen fugacities. In these cases, the activity of NaCl is 1.0 at 1100ºC/1 GPa while the earlier experiments, performed at 1 bar to 0.7 GPa and 700 to 1250 ˚C were saturated in liquids with significantly lower, but unknown, NaCl activities. The important consideration is, however that comparison of our data with the earlier results should be based on NaCl activities as close to 1.0 as possible. We therefore excluded all of the earlier experiments in which Cl was added as $PtCl_4$ and those in which H_2O and/or Ca and Mg chlorides were added. This left 100 experiments of Webster and De Vivo, (2002) and Webster et al., (2015) in which Cl was added as NaCl and KCl and in which NaCl activity was high.

The experimental data were considered in terms of the equilibrium:

$$2NaCl_{solid} + [O^{2-}]_{melt} = 2[Cl^{-}]_{melt} + Na_2O_{solid} \quad (3.17)$$

We rearrange the equilibrium constant for (3.17) to yield:

$$log\left(\frac{a_{Cl^{-}melt}}{a_{O^{2-}melt}{}^{0.5}}\right) = log(a_{NaCl}) + 0.5logK - log\left(a_{Na_2O}\right) \qquad (3.18)$$

The term on the left-hand side is directly related to the chloride capacity through equilibrium (3.2). It must therefore have the same compositional dependence as chloride capacity as derived from equations (3.12) or (3.15). We therefore used the compositional terms from equation (3.12) and calculated an "effective" activity ratio $\left(\frac{a_{Cl^{-}melt}}{a_{O^{2-}melt}{}^{0.5}}\right)$ from Cl concentration (Cl^{-}) in weight % and oxide mole fractions on a single cation basis :

$$log\left(\frac{a_{Cl^{-}melt}}{a_{O^{2-}melt}{}^{0.5}}\right) = log(Cl^{-}) - (4470X_{Ca} - 3430X_{Si} + 2592X_{Fe} - 4092X_{K})/\mathrm{T} \quad (3.19)$$

In equation (3.19) (Cl^{-}) denotes the weight% concentration of chlorine in the melt and the compositional terms on the right-hand side remove the compositional dependence of $\left(\frac{a_{Cl^{-}melt}}{a_{O^{2-}melt}{}^{0.5}}\right)$ as described by equation (3.12). We then had 102 data of known values of pressure, temperature, and the left-hand side of equation (3.18). Using a standard state for NaCl of pure liquid at the pressure and temperature of interest, we assumed that the activity of NaCl in our NaCl-saturated experiments was 1.0 and that the data of Webster and De Vivo, (2002) and Webster et al., (2015) referred to slightly lower values of 0.8. We believe that the latter is a reasonable assumption since NaCl activity values of about 0.5 fitted less well with our data for which the NaCl activity is known. We then regressed $log(a_{NaCl}) - log\left(\frac{a_{Cl^{-}melt}}{a_{O^{2-}melt}{}^{0.5}}\right)$ against 1/T, P/T and oxide mole fractions as before in order to obtain the compositional

dependence of NaCl saturation. Using stepwise linear regression and applying the F-test as before we obtained:

$$log(a_{NaCl}) - log\left(\frac{a_{Cl^-melt}}{a_{O^{2-}melt}^{0.5}}\right) = -0.06 + (6901X_{Ca} + 3484X_{Na} - 2417)/T \quad (3.20)$$

The standard error of the fit is 0.124 and r^2 0.85. We can now put (3.19) and (3.20) together to obtain the Cl content of the melt at any NaCl activity as follows:

$$log(Cl^-) = log(a_{NaCl}) + 0.06 - (2431X_{Ca} + 3430X_{Si} - 2592X_{Fe} + 3484X_{Na} + 4092X_K - 2417)/T \quad (3.21)$$

It is interesting to note that Cl content should not depend on oxygen fugacity $f(O_2)$ at NaCl saturation as indicated by equation (3.17). We confirmed this supposition by performing experiments at both the Re/ReO_2 (4 log $f(O_2)$ units above CCO) and CCO buffers from which Cl contents of 1.09 and 1.00 wt%, respectively were obtained (Table 3.2). Taking activity coefficients for NaCl in a brine from Johnson and Pytowicz (1981) and Raju and Atkinson (1990) across a range of salinities, we can determine the mole fraction of NaCl, and thus infer the salinity of the liquid phase. The relative salinity is plotted on a secondary x-axis in figure 3.6.

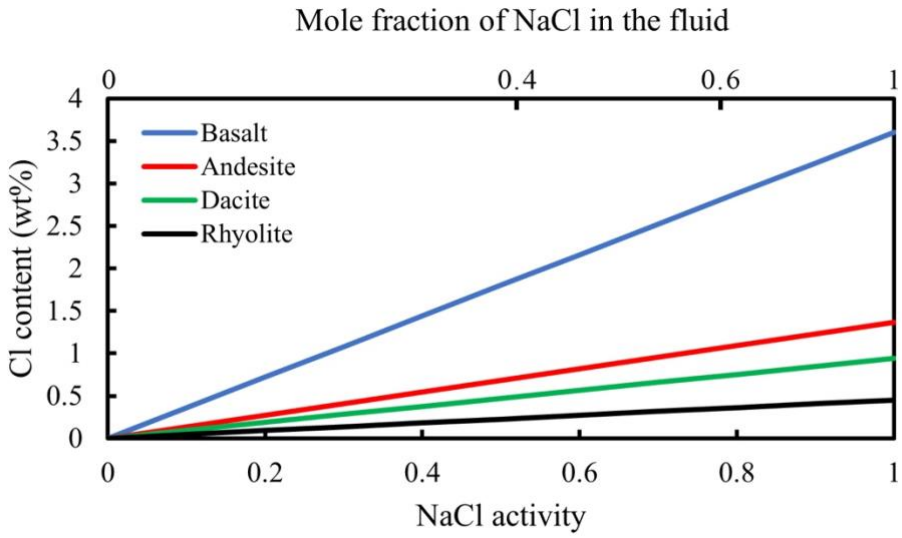


Figure 3.6 Shows the calculated Cl contents of the same 4 compositions as in Fig 3.4 as a function of the NaCl activity at 200 MPa and 900 °C. For fixed NaCl activity the basalt is calculated to contain ~8 times as much Cl as the rhyolite.

Figure 3.6 shows the calculated Cl contents of the same 4 melts as in Figure 3.4 plotted as a function of NaCl activity. The form of equation (3.21) imposes a linear relationship between NaCl activity and Cl content, but as can be seen, the major element composition has an appreciable effect on NaCl solubility and saturation in natural silicate melts. Thus, for example, we calculate that at 200 MPa and 900 °C, the basalt will contain 3.6% Cl (possibly metastably) at NaCl saturation (activity = 1.0) while the rhyolite will reach NaCl saturation at 0.45 weight % Cl. The latter figure is similar to values measured in melt inclusions from some felsic magmas (Webster et al, 2020) indicating that NaCl-rich brines are much more likely to separate from felsic than from basic magmas, which may indicate why ore deposits tend to be associated with felsic melts. Equation (3.21), therefore, leads to a means of using the compositions of melts to estimate the compositions of coexisting fluids, specifically their NaCl contents at the conditions of fluid separation. In this we follow the example of Webster et al (2020) who used

melt inclusion data from a large number of localities to estimate whether or not the melts were in equilibrium with a hydrosaline liquid. To compare our model to Webster et al's (2020) model we find that by using equation 3.21, and assuming an NaCl activity of 1, that our calculated chlorine content is always closer to the observed Cl content of the melt inclusions (derived from the database of Webster et al., 2020) with modelled divided observed Cl contents closer to 1 at all localities tested.

3.7 Conclusions

We find that in the Henry's Law region at 1400 °C and 1.5 GPa, there is a strong dependence of chlorine activity in silicate melts on the concentrations of the major oxide components in the melts. By determining the Cl contents of 25 synthetic and natural compositions, we were able to quantify these compositional effects by deriving for each melt, a chloride capacity C_{Cl} defined as follows:

$$C_{Cl} = \frac{Cl\ (wt\%)}{\sqrt{f(Cl_2)}} \times \sqrt[4]{f(O_2)}$$

We found that chloride capacity correlates very well with commonly used empirical parameters aimed at describing the degree of polymerisation and acid-base properties of the melt, notably Optical Basicity, Ionic Porosity, the Larsen Index and NBO/T. Correlations are positive with optical basicity and NBO/T and negative with ionic porosity and Larsen Index (Fig 3.3). In terms of common igneous rocks, the results indicate that, at fixed Cl_2 fugacity pressure and temperature, basalt will contain approximately 8 times as much Cl as rhyolite (e.g., Fig 3.5). In order to obtain an equation to describe the dependence of chloride capacity on composition, pressure, and temperature, we used stepwise multiple linear regression with a requirement that

additional parameters pass the F-test at $\alpha = 0.05$. This approach resulted in the following best-fit equation for chloride capacity:

$$logC_{Cl} = -1.601 + (4470X_{Ca} - 3430X_{Si} + 2592X_{Fe} - 4092X_{K}\text{-}894P)/T$$

R^2=0.96; standard error = 0.089

In this equation P is pressure in GPa, T is in K and $X_{Si,}$ X_{Ca} X_{Fe} and X_K refer to oxide mole fractions on a single cation basis. By adding 23 results on hydrous experiments in which the silicate melts contained between 0.6 and 4.3 weight % H_2O, we found that the effects of H_2O on chloride capacity could, in this compositional range, be ignored. The fit results indicate that ascending silicate melts that become H_2O-saturated at about 50 MPa will degas very little of their Cl before they reach the surface (Fig 3.4). We calculate, for example, that a basaltic melt containing 0.2% Cl at 50 MPa will degas only 0.006% Cl during the ascent to the surface. In contrast, andesitic, dacitic and rhyolitic melts initially containing 0.2% Cl should degas 0.02, 0.035 and 0.074 weight % respectively during ascent. Almost half of the degassing takes place at pressures below 2 MPa (80 meters depth).

One major question in the context of Cl solubility and activity in silicate melts is the NaCl contents of melts and coexisting brines during brine separation. Brines are regarded as important transporting agents in the development of many ore deposits (Johnson et al., 2000; Fusswinkel et al., 2013; Smith et al., 2013; Blundy et al., 2015; Blundy et al., 2021). The data on saturation of silicate melts in hydrosaline liquids and essentially pure NaCl melts have been combined to generate an equation relating Cl content of the melt to its NaCl activity:

$$log(Cl^-) = log(a_{NaCl}) + 0.06 - (2431X_{Ca} + 3430X_{Si} - 2592X_{Fe} + 3484X_{Na} + 4092X_K - 2417)/T$$

In this equation all parameters are as previously defined (Cl^-) is the weight% concentration of Cl in the melt and a_{NaCl} is the NaCl activity relative to a standard state of pure NaCl at the pressure-temperature conditions of interest.

3.8 Acknowledgements

We acknowledge the stimulation and guidance provided by Jim Webster's numerous papers on halogen behaviour in silicate melts. RWT is grateful to the Natural Environmental Research Council, and the Oxford Doctoral Training Partnership in Environmental Research for studentship and funding (NE/L002612/1). BJW acknowledges funding from Science and Technology Facilities Council grant ST/R000999/1 and the NERC FAMOS project NE/P017452/1. We would like to thank Dr Paula Antoschechkina of Caltech for advice in using AlphaMELTS.

3.9 Supplementary material

Supplementary data tables can be found in Appendix C, and a spreadsheet enabling the calculation of Cl fugacities and chloride capacities is provided as an electronic supplement, *'ChlorCalc_v1'* which has been uploaded alongside this thesis.

3.10 References

Adam J. (1990) The geochemistry and experimental petrology of sodic alkaline basalts from Oatlands, Tasmania. *J. Petrol.* **31**, 1201–1223.

Aiuppa A. (2009) Degassing of halogens from basaltic volcanism: Insights from volcanic gas observations. *Chem. Geol.* **263**, 99–109.

Aiuppa A., Baker D. R. and Webster J. D. (2009) Halogens in volcanic systems. *Chem. Geol.* **263**, 1–18.

Alletti M., Baker D. R., Scaillet B., Aiuppa A., Moretti R. and Ottolini L. (2009) Chlorine partitioning between a basaltic melt and H 2 O–CO 2 fluids at Mount Etna. *Chem. Geol.* **263**, 37–50.

Alletti M., Burgisser A., Scaillet B. and Oppenheimer C. (2014) Chloride partitioning and solubility in hydrous phonolites from Erebus volcano: A contribution towards a multi-component degassing model. *GeoResJ* **3**–**4**, 27–45.

Antoshechkina P. M. and Ghiorso M. S. (2018) MELTS for MATLAB : A new educational and research tool for computational. In American Geophysical Union, Fall Meeting 2018. p. Abstract #ED44B-23.

Ashcroft H. O. and Wood B. J. (2015) An experimental study of partial melting and fractional crystallization on the HED parent body. *Meteorit. Planet. Sci.* **50**, 1912–1924.

Baasner A., Schmidt B. C. and Webb S. L. (2013) The effect of chlorine, fluorine and water on the viscosity of aluminosilicate melts. *Chem. Geol.* **357**, 134–149.

Banin A., Hah F. X., Kan I. and Cieelsky A. (1997) Acidic volatiles and the Mars soil. *J. Geophys. Res.* **102**, 13341–13356.

Beermann O., Botcharnikov R. E. and Nowak M. (2015) Partitioning of sulfur and chlorine between aqueous fluid and basaltic melt at 1050°C, 100 and 200 MPa. *Chem. Geol.* **418**, 132–157.

Bell A. S. and Simon A. (2011) Experimental evidence for the alteration of the Fe3+/ΣFe of silicate melt caused by the degassing of chlorine-bearing aqueous volatiles. *Geology* **39**, 499–502.

Blundy J., Afanasyev A., Tattitch B., Sparks S., Melnik O., Utkin I. and Rust A. (2021) The economic potential of metalliferous sub-volcanic brines. *R. Soc. Open Sci.* **8**.

Blundy J., Mavrogenes J., Tattitch B., Sparks S. and Gilmer A. (2015) Generation of porphyry copper deposits by gas-brine reaction in volcanic arcs. *Nat. Geosci.* **8**, 235–240.

Bortnikov N. S. (2006) Geochemistry and origin of the ore-forming fluids in hydrothermal-magmatic systems in tectonically active zones. *Geol. Ore Depos.* **48**, 3–28.

Botcharnikov R. E., Holtz F. and Beherens H. (2007) The effect of CO2 on the solubility of H2O-Cl fluids in andesitic melt. *Eur. J. Mineral.* **19**, 671–680.

Botcharnikov R. E., Holtz F. and Behrens H. (2015) Solubility and fluid–melt partitioning of H2O and Cl in andesitic magmas as a function of pressure between 50 and 500 MPa. *Chem. Geol.* **418**, 117–131.

Boyd F. R. and England J. L. (1960) Apparatus for phase-equilibrium measurements at pressures up to 50 kilobars and temperatures up to 1750°C. *J. Geophys. Res.* **65**, 741–748.

Brooker R. A., Kohn S. C., Holloway J. R. and McMillan P. F. (2001) Structural controls on the solubility of CO2 in silicate melts part I: Bulk solubility data. *Chem. Geol.* **174**, 225–239.

Bruce S., Yardley B. W. D., Banks D., Boyce A. J., Munoz M., Courjault-Rade P. and Tollon

F. (1999) The genesis of mineralising brines in the South West Massif Central, France. *Miner. Depos. Process. to Process. Vols 1 2* **62A**, 29–32.

Bureau H., Keppler H. and Métrich N. (2000) Volcanic degassing of bromine and iodine: Experimental fluid/melt partitioning data and applications to stratospheric chemistry. *Earth Planet. Sci. Lett.* **183**, 51–60.

Carmichael I. S. E., Turner F. J. and Verhoogen J. (1974) *Igneous Petrology (Earth & Planetary Science)*., New York.

Carroll M. R. and Stolper E. M. (1993) Noble gas solubilities in silicate melts and glasses: New experimental results for argon and the relationship between solubility and ionic porosity. *Geochim. Cosmochim. Acta* **57**, 5039–5051.

Carroll M. R. and Webster J. D. (1994) Solubilities of sulfur, noble gases, nitrogen, chlorine, and fluorine in magmas. *Mineral. Soc. Am. Rev. Mineral.* **30**, 231 –279.

Chevychelov V., Bocharnikov R. E. and Holtz F. (2008) Experimental Study of Chlorine and Fluorine Partitioning between Fluid and Subalkaline Basaltic Melt. *Dokl. Earth Sci.* **422**, 93–97.

Cline J. S. and Bodnar R. J. (1994) Direct evolution of brine from a crystallizing silicic melt at the Questa, New Mexico, Molybdenum deposit. *Econ. Geol.* **89**, 1780–1802.

Dowty E. (1980) Crystal-chemical factors affecting the mobility of ions in minerals. *Am. Mineral.* **65**, 174–182.

Duffy J. A. (2004) Relationship between optical basicity and thermochemistry of silicates. *J. Phys. Chem. B* **108**, 7641–7645.

Duffy J. A. and Ingram M. D. (1976) An interpretation of glass chemistry in terms of the optical basicity concept. *J. Non. Cryst. Solids* **21**, 373–410.

Duffy J. A. and Ingram M. D. (1971) Establishment of an optical scale for Lewis basicity in inorganic oxyacids, molten salts, and glasses. *J. Am. Chem. Soc.* **93**, 6448–6454.

Ebadi A. and Johannes W. (1991) Beginning of melting and composition of first melts in the system Qz-Ab-Or-H2O-CO2. *Contrib. to Mineral. Petrol.* **106**, 286–295.

Edmonds M., Gerlach T. M. and Herd R. A. (2009) Halogen degassing during ascent and eruption of water-poor basaltic magma. *Chem. Geol.* **263**, 122–130.

Edmonds M., Pyle D. and Oppenheimer C. (2001) A model for degassing at the Soufrière Hill Volcano, Montserrat, West Indies, based on geochemical data. *Earth Planet. Sci. Lett.* **186**, 159–173.

Essarraj S., Boiron M.-C., Cathelineau M., Tarantola A., Leisen M., Boulvais P. and Maacha L. (2016) Basinal brines at the origin of the Imiter Ag-Hg deposit (Anti-Atlas, Morocco): Evidence from LA-ICP-MS data on fluid inclusions, halogen signatures, and stable isotopes (H, C, O). *Econ. Geol.* **111**, 1753–1781.

Evans K. A., Mavrogenes J. A., O'Neill H. S., Keller N. S. and Jang L. Y. (2008) A preliminary investigation of chlorine XANES in silicate glasses. *Geochemistry, Geophys. Geosystems* **9**, 1–15.

Falloon T. J. and Green D. H. (1987) Anhydrous partial melting of MORB pyrolite and other peridotite compositions at 10 kbar: Implications for the origin of primitive MORB glasses. *Mineral. Petrol.* **37**, 181–219.

Filiberto J. and Treiman A. H. (2009) The effect of chlorine on the liquidus of basalt: First results and implications for basalt genesis on Mars and Earth. *Chem. Geol.* **263**, 60–68.

Fuge R., Andrews M. J. and Johnson C. C. (1986) Chlorine and iodine, potential pathfinder elements in exploration geochemistry. *Appl. Geochemistry* **1**, 111–116.

Gerlach T. M. (2004) Volcanic sources of tropospheric ozone-depleting trace gases. *Geochemistry, Geophys. Geosystems* **5**, 1–16.

Ghiorso M. S. and Gualda G. A. R. (2015) An H2O–CO2 mixed fluid saturation model compatible with rhyolite-MELTS. *Contrib. to Mineral. Petrol.* **169**, 53.

von Glasow R., Bobrowski N. and Kern C. (2009) The effects of volcanic eruptions on atmospheric chemistry. *Chem. Geol.* **263**, 131–142.

Gleeson S. A. and Turner W. A. (2007) Fluid inclusion constraints on the origin of the brines responsible for Pb-Zn mineralization at Pine Point and coarse non-saddle and saddle dolomite formation in southern Northwest Territories. *Geofluids* **7**, 51–68.

Hanley J. J., Mungall J. E., Pettke T., Spooner E. T. C. and Bray C. J. (2008) Fluid and halide melt Inclusions of magmatic origin in the ultramafic and lower banded series, stillwater complex, Montana, USA. *J. Petrol.* **49**, 1133–1160.

Holloway J. R. (1977) Fugacity and activity of molecular species in supercritical fluids. In *Fraser D.G. (eds) Thermodynamics in Geology. NATO Advanced Study Institutes Series (Series C — Mathematical and Physical Sciences), vol 30* Springer, Dordrecht.

Hunt J. B. and Hill P. G. (1993) Tephra geochemistry: A discussion of some persistent analytical problems. *The Holocene* **3**, 271–278.

Hytonen K. and Schairer J. F. (1960) The plane enstatite-anorthite-diopside and its relation to basalt. *Carnegie Inst. Washingt. Year B.* **60**, 125–141.

Iacono-Marziano G., Paonita A., Rizzo A., Scaillet B. and Gaillard F. (2010) Noble gas solubilities in silicate melts: New experimental results and a comprehensive model of the effects of liquid composition, temperature and pressure. *Chem. Geol.* **279**, 145–157.

Iwasaki B. and Katsura T. (1967) The solubility of hydrogen chloride in volcanic rock melts at

a total pressure of one atmosphere and at temperatures of 1200°C and 1290°C under anhydrous conditions. *Bull. Chem. Soc. Jpn.* **40**, 554–561.

Jakobsson S. and Oskarsson N. (1994) The system C-O in equilibrium with graphite at high pressure and temperature: An experimental study. *Geochim. Cosmochim. Acta* **58**, 9–17.

Johnson K. S. and Pytkowicz R. M. (1981) The activity of NaCl in seawater of 10-40 ‰ salinity and 5-25 °C at 1 atmosphere. *Mar. Chem.* **10**, 85–91.

Kiseeva E. S. and Wood B. J. (2013) A simple model for chalcophile element partitioning between sulphide and silicate liquids with geochemical applications. *Earth Planet. Sci. Lett.* **383**, 68–81.

Kravchuk I. F. and Keppler H. (1994) Distribution of chloride between aqueous fluids and felsic melts at 2 kbar and 800°C. *Eur. J. Mineral.* **6**, 913–924.

Kusebauch C., John T., Whitehouse M. J., Klemme S. and Putnis A. (2015) Distribution of halogens between fluid and apatite during fluid-mediated replacement processes. *Geochim. Cosmochim. Acta* **170**, 225–246.

Lange R. A. and Carmichael I. S. E. (1987) Densities of Na2O-K2O-CaO-MgO-FeO-Fe2O3-Al2O3-TiO2-SiO2 liquids: New measurements and derivated partial molar properties. *Geochim. Cosmochim. Acta* **51**, 2931–2946.

Larsen E. S. (1938) Some new variation diagrams for groups of igneous rocks. *J. Geol.* **46**, 505–520.

Lesne P., Kohn S. C., Blundy J., Witham F., Botcharnikov R. E. and Behrens H. (2011) Experimental simulation of closed-system degassing in the system basalt-H2O-CO2-S-Cl. *J. Petrol.* **52**, 1737–1762.

Li H. and Hermann J. (2015) Apatite as an indicator of fluid salinity: An experimental study of chlorine and fluorine partitioning in subducted sediments. *Geochim. Cosmochim. Acta* **166**, 267–297.

Marschik R. and Kendrick M. A. (2015) Noble gas and halogen constraints on fluid sources in iron oxide-copper-gold mineralization: Mantoverde and La Candelaria, Northern Chile. *Miner. Depos.* **50**, 357–371.

Martin R. S., Mather T. A. and Pyle D. M. (2006) High-temperature mixtures of magmatic and atmospheric gases. *Geochemistry, Geophys. Geosystems* **7**, 1–14.

Martin R. S., Wheeler J. C., Ilyinskaya E., Braban C. F. and Oppenheimer C. (2012) The uptake of halogen (HF, HCl, HBr and HI) and nitric (HNO 3) acids into acidic sulphate particles in quiescent volcanic plumes. *Chem. Geol.* **296**–**297**, 19–25.

Matzen A. K., Woodland A., Beckett J. R. and Wood B. J. (2022) Oxidation state of iron and Fe-Mg partitioning between olivine and basaltic Martian melts. *Am. Mineral.* **In Press**.

McKeown D. A., Gan H., Pegg I. L., Stolte W. C. and Demchenko I. N. (2011) X-ray absorption studies of chlorine valence and local environments in borosilicate waste glasses. *J. Nucl. Mater.* **408**, 236–245.

Métrich N. and Rutherford M. J. (1992) Experimental study of chlorine behavior in hydrous silicic melts. *Geochemica Cosmochim. Acta* **56**, 607–616.

Mills K. (1993) The influence of structure on the physico-chemical properties of slags. *Iron Steel Inst. Japan Int.* **33**, 148–155.

Millsteed P. W. and Mavrogenes J. A. (2015) *The discovery of halogens in the ores at Broken Hill, NSW - Economic implications of sulfide melting*., Canberra.

Moore G., Vennemann T. and Carmichael I. S. E. (1998) An empirical model for the solubility

of H2O in magmas to 3 kilobars. *Am. Mineral.* **83**, 36–42.

Moore W. J. and Nash J. T. (1974) Alteration and fluid inclusion studies of the porphyry copper ore body at Bingham, Utah. *Econ. Geol.* **69**, 631–645.

Muir D. D., Blundy J. D., Rust A. C. and Hickey J. (2014) Experimental constraints on dacite pre-eruptive magma storage conditions beneath Uturuncu volcano. *J. Petrol.* **55**, 749–767.

Mungall J. E. and Brenan J. M. (2003) Experimental evidence for the Chalcophile behavior of the halogens. *Can. Mineral.* **41**, 207–220.

Nash T. J. (1976) Fluid-inclusion petrology - Data from porphyry copper deposits and applications to exploration. *US Geol. Surv. Prof. Pap.*, 1–16.

Newman S. and Lowenstern J. B. (2002) VOLATILECALC: A silicate melt-H2O-CO2 solution model written in Visual Basic for excel. *Comput. Geosci.* **28**, 597–604.

Nockolds S. R. (1954) Average chemical compositions of some igneous rocks. *Bull. Geol. Soc. Am.* **65**, 1007–1032.

Norris C. A. and Wood B. J. (2017) Earth's volatile contents established by melting and vaporization. *Nature* **549**, 507–510.

Nshimiyimana F., Essarraj S. and Mohamed H. (2015) Brines at the Origin of the Silver Mineralization at the Koudia El Hamra Deposit, Central Jebilet, Morocco. In *Brines at the origin of the silver mineralization at the Koudia El Hamra deposit, Central Jebilet, Morocco* pp. 1–5.

Osborn E. F. and Tait D. B. (1952) The system diopside-forsterite - anorthite. *Am. J. Sci.* **Bowen Volu**, 413–433.

Prausnitz J. M., Lichtenthaler R. N. and Gomes De Azevedo E. (1999) *Molecular*

thermodynamics of fluid-phase equilibria. Third. ed. N. R. Amundson, Prentice Hall International series in the physical and chemical engineering sciences, New Jersey.

Presnall D. C., Dixon S. A., Dixon J. R., O'Donnell T. H., Brenner N. L., Schrock R. L. and Dycus D. W. (1978) Liquidus phase relations on the join Diopside-Forsterite-Anorthite from 1 atm to 20 kbar. Their bearing on the generation and crystallization of basaltic magma. *Contrib. to Mineral. Petrol.* **66**, 203–220.

Pyle D. M. and Mather T. A. (2009) Halogens in igneous processes and their fluxes to the atmosphere and oceans from volcanic activity: A review. *Chem. Geol.* **263**, 110–121.

Raju K. U. G. and Atkinson G. (1990) The Thermodynamics of "Scale" Mineral Solubilities. 3. Calcium Sulfate in Aqueous NaCl. *J. Chem. Eng. Data* **35**, 361–367.

Ridley W. I. (1970) The petrology of the Las Canadas volcanoes, Tenerife, Canary islands. *Contrib. to Mineral. Petrol.* **26**, 124–160.

Saito G., Uto K., Kazahaya K., Shinohara H., Kawanabe Y. and Satoh H. (2005) Petrological characteristics and volatile content of magma from the 2000 eruption of Miyakejima Volcano, Japan. *Bull. Volcanol.* **67**, 268–280.

Sandland T. O., Du L.-S., Stebbins J. F. and Webster J. D. (2004) Structure of Cl-containing silicate and aluminosilicate glasses: A 35 Cl MAS-NMR study. *Geochim. Cosmochim. Acta* **68**, 5059–5069.

Scholtysik R. and Canil D. (2021) The effects of S , Cl and oxygen fugacity on the sublimation of volatile trace metals degassed from silicate melts with implications for volcanic emissions. *Geochim. Cosmochim. Acta* **In Press**.

Shannon R. D. (1976) Revised effective ionic radii and systematic studies of interatomie distances in halides and chaleogenides. *Acta Crystallogr.* **32**, 751–767.

Shannon R. D. and Prewitt C. T. (1969) Effective ionic radii in oxides and fluorides. *Acta Crystallogr. Sect. B Struct. Crystallogr. Cryst. Chem.* **25**, 925–946.

Sharp Z. D. and Draper D. S. (2013) The chlorine abundance of Earth: Implications for a habitable planet. *Earth Planet. Sci. Lett.* **369**–**370**, 71–77.

Simon A. C., Pettke T., Candela P. A., Piccoli P. M. and Heinrich C. A. (2004) Magnetite solubility and iron transport in magmatic-hydrothermal environments. *Geochim. Cosmochim. Acta* **68**, 4905–4914.

Shinohara H., Iiyama J. T. and Matsuo S. (1989) Partition of chlorine compounds between silicate melt and hydrothermal solutions: I. Partition of NaCl-KCl. *Geochim. Cosmochim. Acta* **53**, 2617–2630.

Signorelli S. and Carroll M. R. (2002) Experimental study of Cl solubility in hydrous alkaline melts: constraints on the theoretical maximum amount of Cl in trachytic and phonolitic melts. *Contrib. to Miner. Petrol.* **143**, 209–218.

Signorelli S. and Carroll M. R. (2000) Solubility and fluid-melt partitioning of Cl in hydrous phonolitic melts. *Geochim. Cosmochim. Acta* **64**, 2851–2862.

Sossi P. A., Klemme S., O'Neill H. S. C., Berndt J. and Moynier F. (2019) Evaporation of moderately volatile elements from silicate melts: experiments and theory. *Geochim. Cosmochim. Acta* **260**, 204–231.

Spilliaert N., Métrich N. and Allard P. (2006) S-Cl-F degassing pattern of water-rich alkali basalt: Modelling and relationship with eruption styles on Mount Etna volcano. *Earth Planet. Sci. Lett.* **248**, 772–786.

Stanley B. D., Hirschmann M. M. and Withers A. C. (2011) CO2 solubility in Martian basalts and Martian atmospheric evolution. *Geochim. Cosmochim. Acta* **75**, 5987–6003.

Stebbins J. F. and Du L.-S. (2002) Chloride ion sites in silicate and aluminosilicate glasses: A preliminary study by 35Cl solid-state NMR. *Am. Mineral.* **87**, 359–363.

Stelling J., Botcharnikov R. E., Beermann O. and Nowak M. (2008) Solubility of H 2 O-and chlorine-bearing fluids in basaltic melt of Mount Etna at T = 1050-1250 °C and P = 200 MPa. *Chem. Geol.* **256**, 101–109.

Symonds R. B., Reed M. H. and Rose W. I. (1992) Origin, speciation, and fluxes of trace-element gases at Augustine volcano, Alaska: insights into magma degassing and fumarolic processes. *Geochim. Cosmochim. Acta* **56**, 633–657.

Symonds R. B., Rose W. I., Bluth G. J. S. and Gerlach T. M. (1994) Volcanic-gas studies: methods, results and applications. In *Reviews in Mineralogy and Geochemistry* (eds. M. R. Carroll and J. R. Holloway). pp. 1–66.

Taracsák Z., Neave D., Beaudry P., Gunnarson-Robin J., Burgess R., Edmonds M., Halldórsson S. A., Longpré M.-A., Ono S., Ranta E., Stefánsson A., Turchyn A. V and Hartlet M. E. (2021) Instrumental mass fractionation during sulfur isotope analysis by secodary ion mass spectrometry in natural and volcanic glasses. *Chem. Geol.*

Tattitch B., Chelle-Michou C., Blundy J. and Loucks R. R. (2021) Chemical feedbacks during magma degassing control chlorine partitioning and metal extraction in volcanic arcs. *Nat. Commun.* **12**.

Thomas R. W. and Wood B. J. (2021) The chemical behaviour of chlorine in silicate melts. *Geochim. Cosmochim. Acta* **294**, 28–42.

De Vivo B., Lima A. and Webster J. D. (2005) Volatiles in volcanic systems. *Elements* **1**, 19–24.

Webb S. L. and Dingwell D. B. (1990) Non-Newtonian rheology of igneous melts at high

stresses and strain rates: Experimental results for Rhyolite, Andesite, Basalt, and Nephelinite. *J. Geophys. Res.* **95**, 15695–15701.

Webster J. D. (1992) Fluid-melt interactions involving Cl-rich granites: Experimental study from 2 to 8 kbar. *Geochim. Cosmochim. Acta* **56**, 659–678.

Webster J. D. and Holloway J. R. (1988) Experimental constraints on the partitioning of Cl between topaz rhyolite melt and H20 and H20 + CO2 fluids: New implications for granitic differentiation and ore deposition. *Geochim. Cosmochim. Acta* **51**, 2091–2105.

Webster J. D., Baker D. R. and Aiuppa A. (2018) Halogens in Mafic and Intermediate-Silica Content Magmas. In *The Role of Halogens in Terrestrial and Extraterrestrial Geochemical Processes* (eds. D. E. Harlov and L. Aranovich). Springer Geochemistry. pp. 307–430.

Webster J. D., Iveson A. A., Rowe M. C. and Webster P. M. (2020) Chlorine and felsic magma evolution: Modeling the behavior of an under-appreciated volatile component. *Geochim. Cosmochim. Acta*, 248–288.

Webster J. D., Kinzler R. J. and Mathez E. A. (1999) Chloride and water solubility in basalt and andesite melts and implications for magmatic degassing. *Geochim. Cosmochim. Acta* **63**, 729–738.

Webster J. D. and Rebbert C. R. (1998) Experimental investigation of H2O and Cl- solubilities in F-enriched silicate liquids; implications for volatile saturation of topaz rhyolite magmas. *Contrib. to Mineral. Petrol.* **132**, 198–207.

Webster J. D., Sintoni M. F. and De Vivo B. (2009) The partitioning behavior of Cl, S, and H2O in aqueous vapor- ±saline-liquid saturated phonolitic and trachytic melts at 200 MPa. *Chem. Geol.* **263**, 19–36.

Webster J. D., Vetere F., Botcharnikov R. E., Goldoff B., McBirney A. and Doherty A. L. (2015) Experimental and modeled chlorine solubilities in aluminosilicate melts at 1 to 7000 bars and 700 to 1250 °c: Applications to magmas of Augustine Volcano, Alaska. *Am. Mineral.* **100**, 522–535.

Webster J. D. and De Vivo B. (2002) Experimental and modeled solubilities of chlorine in aluminosilicate melts, consequences of magma evolution, and implications for exsolution of hydrous chloride melt at Mt. Somma-Vesuvius. *Am. Mineral.* **87**, 1046–1061.

Wilkinson J. J. (2013) Triggers for the formation of porphyry ore deposits in magmatic arcs. *Nat. Geosci.* **6**, 917–925.

Wood B. J. and Turner S. P. (2009) Origin of primitive high-Mg andesite: Constraints from natural examples and experiments. *Earth Planet. Sci. Lett.* **283**, 59–66.

Zajacz Z., Candela P. A., Piccoli P. M. and Sanchez-Valle C. (2012) The partitioning of sulfur and chlorine between andesite melts and magmatic volatiles and the exchange coefficients of major cations. *Geochim. Cosmochim. Acta* **89**, 81–101.

Zimova M. and Webb S. (2006) The effect of chlorine on the viscosity of Na2O-Fe2O3-Al2O3-SiO2 melts. *Am. Mineral.* **91**, 344–352.

Chapter 4

The bonding behaviour of chlorine in silicate melts

4.1 Abstract

We have examined Cl K-edge X-ray absorption fine structure (XAFS) spectra for 44 silicate glass experiments (from chapters 2 and 3) in both the X-ray absorption near edge structure (XANES) and extended X-ray absorption fine structure (EXAFS) regions. Of the 42 experiments, 35 have distinct compositions and were run at the same conditions, 1400 °C and 15 kbar, and buffered at a known chlorine and oxygen fugacity; this allows us to determine the effect of chemical composition on chlorine bonding. Within the pre-edge region, the presence or absence of a pre-edge feature indicates the extent of covalent bonding of chlorine with silica. Adding divalent cations suppresses the pre-edge feature and shifts to higher energy, as Cl bonding in the glass becomes increasingly ionic. Chlorine is found to predominantly bond to 2^+ cations (Ca, Mg and Fe), confirming the regressions performed in chapter 3. The addition of a 2^+ cation to a Si-rich starting composition exhibits a clear change in bond environment with the small addition of Ca and Mg in the EXAF region. For compositions with significant amounts of Ca and Mg, adding Fe did not change inferred bonding environment until >10 wt% FeO was added. This may indicate that Cl preferentially bonds to Ca and Mg until the activity of Fe is sufficiently high.

Nine further experiments were analysed, all conducted using the same starting silicate composition (Fe-free haplobasalt, $An_{50}Di_{28}Fo_{22}$) across a range of temperatures (1300-1400 °C), pressures (5-20 kbar), chlorine fugacities ($1.38E^{-03}$ to $1.66E^{-06}$), and water contents (expected 0-8 wt% H_2O). The results show that there is little to no change in the spectra across the XANES and EXAFS region, indicating that, at the conditions tested, chlorine bonding is predominantly defined by the chemical composition of the system.

Furthermore, we also demonstrate the problems associated with using crystalline salt standards to determine the bonding environment of chlorine within silicate glasses.

4.2 Introduction

Despite their relatively low abundances in terrestrial rocks (typically < 5000 ppm (Aiuppa et al., 2009)), chlorine has been shown to significantly alter the physio-chemical properties of melts. For example, chlorine is twice as effective as water at lowering the liquidus of Martian basalts (Filiberto and Treiman, 2009). However, the solubility of chlorine in silicate melts and its ability to suppress the silicate liquidus has been shown to be highly dependent on the melt composition, with the most significant liquidus depression being exhibited by basaltic melts enriched in FeO and Al_2O_3 (Filiberto et al., 2014; Farcy et al., 2016). Similarly, the presence of Cl into silicate melts has been shown to affect the melt's viscosity (Dingwell and Hess, 1998; Hess et al., 2004; Zimova and Webb, 2006; Baasner et al., 2013), with Al-free silicate melts being increasingly depolymerised with the addition of Cl Dalou et al., (2015). Conversely, aluminosilicate melts become increasingly polymerised with the addition of chlorine, with the implication that the bonding behaviour of Cl bonds is strongly dependent on the composition of the silicate melt. The aim of this study is to constrain the bonding environment of Cl in a range of synthetic analogues of naturally occurring silicate liquids.

4.2.1 Chlorine incorporation in silicate glasses

Thomas and Wood, (2021) demonstrated that the initial dissolution mechanism of chlorine into a silicate melt involves the replacement of O^{2-} by two dissociated Cl^- ions following the reaction:

$$Cl_{2(gas)} + [O^{2-}]_{(melt)} = 2[Cl^-]_{(melt)} + \tfrac{1}{2}O_{2(gas)} \qquad (4.1)$$

This finding is also supported by studies exploring chlorine dissolution in slag waste deposits (Hirosumi and Morita, 2000) and nuclear waste glasses (Tan and Hand, 2018). However, despite general agreement on the form in which Cl is present in a silicate melt, the bonding environment remains controversial, and there is little consensus as to the nature of the dominant cations involved nor the nature of the chemical bond.

For example, Chmel and Svetlov, (1996) synthesised vitreous silica (x-SiO_2) by vapour deposition and found that chlorine forms Si-Cl complexes, dissolving up to 6 mol% Cl in vitreous silica glasses. Furthermore, in a review of oxyhalide silicate glass synthesis, Kiprianov and Karpukhina, (2006) surmised that chlorine atoms could replace the bridging oxygen atoms at high synthesis temperatures. Conversly, Abramov et al., (1989) examined silica glasses doped with halogens via electron paramagnetic resonance and revealed that both Cl (and F) could preferentially bond with Si by forming two halogen bridges between two silicon atoms, in two mechanisms ≡Si–X X–Si≡ or ≡Si<$(X)_2$>Si≡, where X = F or Cl. The latter mechanism is thought to be energetically more favourable than the ≡Si–O–Si≡ bridge in the silicate network (Dianov et al., 1988; Kiprianov and Karpukhina, 2006).

In contrast, it has been suggested that Cl ions will not bond with network forming ions such as Si (and Al), with the majority of experimental studies within the geological literature documenting that Cl solubility increases with decreasing SiO_2 activities in the melt (Iwasaki and Katsura, 1967; Carroll and Webster, 1994; Webster et al., 1999; Signorelli and Carroll, 2000; Webster and De Vivo, 2002). The proposed reason for this is that decreasing Si activity correlates with increasing activities of network-modifying cations. This is supported in a recent review, where Webster et al., (2018) stated that chlorine dissolution in silicate melts increases strongly with decreasing concentrations of network-forming elements such as Si and P and increases with the concentrations of network-modifying cations, including the alkaline earth

elements and Fe, but less so with those of the alkalis and other constituents. Several studies exploring the effects of Cl on the viscosity of silicate melts observed that the addition of Cl to Fe-bearing melts increases the viscosity of these liquids, this suggests that dissolved Cl bonds with Fe^{2+} in the melt resulting in the disruption of its structural role as a network-modifier. For example, Webb et al., (2014) explored the effect of Cl on the viscosity of mid ocean ridge basalts using micro-penetration. They concluded that addition of Cl reduced the viscosity of the melt, by converting network-forming Fe^{3+} into to a network-modifying Fe^{2+}. This study indicates that a strong chemical interaction exists between Cl and Fe, and that the addition of Cl can also reduce the oxygen fugacity by 3 orders of magnitude.

Preferential bonding of chlorine with alkaline earth elementals is supported spectroscopically. For example, Evans et al., (2008) used X-Ray Absorption Near Edge Structure (XANES) to investigate the local bonding of chlorine in 26 volcanic glasses. They confirmed that Cl does not form bonds with either Si or Al, but rather as a combination of $Ca\text{-}Cl_x$ and $Mg\text{-}Cl_x$ species or, a mixed $Ca\text{-}Mg_y\text{-}Cl_x$ species. They conclude that the short-range structure of the silicate glasses are similar to that of crystalline salts ($CaCl_2$ and $MgCl_2$). Additionally, Sandland et al., (2004) and Stebbins and Du, (2002) spectroscopically explored felsic Cl-bearing silicate and aluminosilicate glasses by solid-state Magic Angle Spinning (MAS) Nuclear Magnetic Resonance (NMR) and found, in agreement with Evans et al., (2008) that 1) there was no evidence of Cl bonding with Si or Al, and that Cl is likely to bond with alkali and alkaline earth elements, with the crucial difference being that these authors did not observe a strong preference between them; and 2) that the environment of Cl is similar in both salts and silicate glasses. Similarly, McKeown et al., (2011) performed Cl K-edge X-ray absorption spectra (XAS) on 15 borosilicate nuclear waste glasses and concluded that the nearest neighbours to Cl-sites were mostly, Ca followed by oxygen, with Na as the second-nearest neighbours, suggesting that the alkali element Na may form a stronger bond with chlorine than with an

alkaline earth element, Mg. The limitation of these studies, however, is the limited compositional range explored, a more thorough investigation across a broader compositional space is required to see if Cl bonds differently with changing cation activities in the silicate melt.

Chlorine solubility is also of great importance to the nuclear waste industry because the pyrochemical reprocessing of spent nuclear fuels leads to the generation of chloride containing wastes, which have limited solubility in the borosilicates currently used for waste vitrification. The goal is therefore to increase chlorine solubility in borosilicate glasses, and limit waste volumes, as such this has been widely documented throughout the nuclear materials literature. For example, Tan and Hand, (2018) made a series of glasses using various alkaline earth bonded chlorides. They that chloride solubility is related to the alkaline earth species as follows Sr > Ba > Ca > Mg, with the strontium aluminosilicate glass accommodating up to 11.97 atomic % Cl, suggesting that chlorine stability increases with bonding to the larger ionic radii alkaline earth elements. In nature, this will correspond to Ca > Mg bond stability with chlorine. Conversely, Veksler et al., (2012) states that alkaline earth cations with smaller ionic radii form more stable, 4-fold coordination, tetrahedral anionic complexes, such as $[MgCl_4]^{2-}$ or $[BeCl_4]^{2-}$, compared to the 6-fold coordination for larger divalent cations in chloride melts, and thus should be more stable.

Given the above discussion, it is predicted that divalent alkaline earth elements are much more efficient at incorporating chlorine within a melt framework compared to that of the monovalent alkali elements (Chevychelov and Suk, 2003). Structurally, this makes sense, as monovalent cations are network disrupters, and so if they formed bonds with Cl^- they must exist separate to the silicate chains. In essence, this would imply measuring the solubility of NaCl, rather than Cl. However, given that the predominant Cl bearing species in geological fluids would either

be HCl at low pressures, or NaCl at high pressures, the main dissolution reaction of Cl might occur with NaCl or HCl, and therefore may not be represented by reaction 4.1.

Further confusion and greater complexity is added when the silicate composition changes from a peraluminous to a more peralkaline, felsic melt. Webster and De Vivo, (2002) state that network-modifying Al, Na, and K have a greater influence over their network-forming counterparts in felsic silicate compositions. It is thought that any Al ions that exceed those that form charge balances with elements such as Na and K in haplogranitic melts effectively behave as 'network-modifying Al ions', and thus significantly enhance Cl solubility comparable to that of the network-forming Al ions (Webster and De Vivo, 2002; Webster et al., 2015). This is supported by the findings of Webster and De Vivo, (2002), who found that chlorine concentrations became proportionally greater for every mole of Al + Ca +Mg that exceeded the mols of the alkali earth elements in more mafic melts. To further explore how Cl bonding changes with the peralkalinity of silicate melts, Baasner et al., (2014) performed MAS NMR spectroscopy in Cl bearing peralkaline and peraluminous melts. They found that Cl forms Na-Ca-Cl bonds in both environments, but that there were more Ca cations present within the peraluminous glasses compared to the peralkaline glasses. The limitations of this study, however, are the relatively low concentrations of Cl in the samples used, and the large distribution of electric field gradients for ^{35}Cl, which reportedly caused a loss of signal in the MAS NMR experiments making large errors of uncertainty, making them unable to define a clear change in bonding environments (Baasner et al., 2014).

Given all this confusion, we aim to determine which elements bond to Cl^- in a silicate liquid, and thus, what controls chlorine solubility in silicate melts. In an attempt to solve these problems, Thomas and Wood, (2021) (chapter 2) developed a methodology to buffer Cl_2 fugacity, allowing the melt composition to remain constant. Chlorine solubility varied linearly

with the square root of chlorine fugacity ($f(Cl_2)$) and the fourth root of oxygen fugacity ($f(O_2)$). Following this methodology, in chapter 3 we were able to define more accurately the compositional dependences on chlorine concentration in silicate melts, at 1400 °C, 1.5 GPa, and at a constant Cl and O fugacity (the latter being buffered to CCO), deriving an equation that described the composition, pressure and temperature dependence of chloride capacity (C_{Cl}):

$$logC_{Cl} = -1.601 + (4470X_{Ca} - 3430X_{Si} + 2592X_{Fe} - 4092X_{K}\text{-}894P)/T \qquad (4.2)$$

X_{Ca}, X_{Si} etc., refer to the oxide mole fractions on a single cation basis, and P and T are in GPa and K, respectively. In order to explore the bonding behaviour of chlorine, we have taken the experiments performed within chapters 2 and 3, (which represent a variety of compositions, temperatures, and pressures) and analysed them by XANES and EXAFS in an effort to determine the nearest neighbour of chlorine.

To date, only three studies have explored chlorine speciation by XAFs in silicate melts, Evans et al., (2008), who examined the XANES region of 26 CMAS (CaO-MgO-Al_2O_3-SiO_2) plus Na_2O, K_2O, or MnO compositions, Mason et al., (2019), who investigated the XANES region of spectra in zirconolite glasses, and examined both the XANES and EXAFS regions in spectra from borosilicate glasses. These studies showed that the applicability and sensitivity of XAFS in identifying the nearest neighbour speciation and bonding environment of chlorine. This work attempts to expand on these efforts and explore a wide variety of silicate melt compositions and experimental conditions.

4.3 Methodology

4.3.1 Starting compositions and experimental conditions

In order to explore how chlorine speciation varies over a range of compositions, we collected X-ray absorption fine structure (XAFS) spectra on 44 silicate glasses. All sample preparation and experimental techniques are detailed within chapters 2 and 3). These experiments were all performed under controlled conditions at 5 and 20 kbar, and 1300-1400 °C and at buffered oxygen fugacity ($f(O_2)$) at the CCO buffer and buffered chlorine fugacity ($f(Cl_2)$) (Table 4.1). As all these conditions are controlled, we can compare all data sets together by calculating the *chloride capacity* ($C_{Cl;}$ Table 4.2), from chapter 3:

$$C_{Cl} = \frac{Cl\ (wt\%)}{\sqrt{f(Cl_2)}} \times \sqrt[4]{f(O_2)} \quad (4.3)$$

The experiments analysed by XAFS were chosen to explore 1) a wide range in compositional space, from granitic to basaltic, utilising 7 natural samples and 18 synthetic compositions, all equilibrated at 15 kbar, 1400°C and at the CCO buffer, with fixed chlorine fugacity ($f Cl_2$). 2) As Fe, Mg and Ca are considered to be the most important cations influencing chlorine solubility (Webster and De Vivo, 2002; Bell and Webster, 2015; Webster et al., 2015; Webster et al., 2018), we have analysed silicate glasses, buffered in Cl with the incremental addition of these cations (Table 4.1). 3) To explore if chlorine bonding behaviour changes with varying intensive variables, at constant composition, we analysed a haplobasaltic CMAS ($An_{50}Di_{28}Fo_{22}$; Presnall et al., 1978) performed at varying pressures (5, 15 and 20 kbar), temperature (1300 and 1400°C) and chlorine fugacity ($f(Cl_2)$; $1.38E^{-03}$ to $1.66E^{-06}$). 4) To investigate how water content influences Cl speciation, we performed additional experiments in which we remade the CMAS composition and incrementally swapped its MgO content for

Brucite ($Mg(OH)_2$), at the temperatures of the experiment it will decompose following the reaction:

$$Mg(OH)_{2\,Solid} \rightarrow MgO_{solid} + H_2O_{liquid} \qquad (4.4)$$

Increasing the proportion of brucite increases the water content whilst leaving the composition otherwise unchanged (Table 4.1). We gravimetrically added 4 and 8 wt% water to the silicate melt, via this method. However only 3.23 and 6.74 wt% was measured in the melt. These experiments were performed in a piston-cylinder apparatus at 1400 °C, 15 kbar, fixed $f(O_2)$ at the CCO buffer, and buffered $f(Cl_2)$ following the methodology described in chapter 2 (Table 4.1).

A series of standards were made from pure (>99.99%) anhydrous powders of $FeCl_2$, $CaCl_2$, $MnCl_2$, $AlCl_3$, $MgCl_2$, KCl, NaCl, and AgCl. Each powder was compressed into 4 mm diameter, approximately 3-5 mm long pellets, using small (<5% of the volume) amounts of pure microcrystalline cellulose as a binding agent. Pure salt standards were chosen following the works of Evans et al., 2008 and McKeown et al., (2011) who both claim to have successfully used pure grade salts to interpret Cl spectra in silicate glasses.

Table 4.1 Silicate melt compositions measured by EPMA

Experiment ID	n	SiO_2	TiO_2	Al_2O_3	FeO_T	MnO	MgO	CaO	Na_2O	K_2O	Cl	I_2O	Ag_2O	P_2O_5	Cr_2O_3	NiO	H_2O	Total
Ab/Fo-1	31	70.47 (0.71)	0.02 (0.02)	19.35 (0.24)	0.13 (0.02)	0.00 (0.01)	2.93 (0.08)	0.15 (0.02)	5.77 (0.23)	0.19 (0.02)	0.56 (0.02)	0.06 (0.07)	0.45 (0.48)	-	-	-	-	100.09
Ab/Fo-2	31	63.51 (0.65)	0.03 (0.02)	15.49 (0.60)	0.10 (0.02)	0.00 (0.02)	2.43 (0.29)	11.06 (0.37)	4.70 (0.21)	0.24 (0.03)	1.41 (0.06)	0.07 (0.03)	0.35 (0.34)	-	-	-	-	99.40
Ab/Fo-3	33	55.97 (0.51)	0.03 (0.02)	12.44 (0.16)	0.11 (0.02)	0.00 (0.01)	1.87 (0.03)	19.69 (0.02)	3.49 (0.12)	0.32 (0.02)	2.75 (0.05)	0.14 (0.03)	0.22 (0.17)	-	-	-	-	97.02
Ab/Fo-5	33	47.44 (0.71)	0.05 (0.04)	10.84 (0.20)	0.06 (0.02)	-	1.52 (0.05)	28.64 (0.42)	2.89 (0.14)	0.09 (0.02)	4.09 (0.14)	0.21 (0.05)	0.12 (0.15)	-	-	-	-	96.03
AgI/Cl-27	20	54.30 (0.82)	0.99 (0.08)	15.84 (0.25)	0.50 (0.13)	-	9.28 (0.12)	13.19 (0.19)	1.86 (0.31)	-	1.60 (0.03)	0.04 (0.02)	0.41 (0.40)	-	-	-	-	98.05
AgI/Cl-024	20	43.05 (0.97)	-	15.92 (0.48)	8.68 (0.19)	-	14.00 (0.34)	13.78 (0.34)	-	-	2.54 (0.06)	0.05 (0.03)	0.31 (0.29)	-	-	-	-	98.75
AgI/Cl-025	20	42.34 (0.38)	-	13.31 (0.21)	15.69 (0.46)	-	11.53 (0.28)	11.39 (0.37)	-	-	2.70 (0.19)	0.11 (0.05)	0.28 (0.42)	-	-	-	-	98.34
AgI/Cl-026	20	37.23 (0.65)	-	12.21 (0.19)	20.88 (0.49)	-	11.50 (0.23)	11.38 (0.18)	-	-	3.49 (0.28)	0.14 (0.10)	0.17 (0.39)	-	-	-	-	97.38
Dacite-1	32	69.65 (1.10)	0.97 (0.08)	15.98 (0.89)	0.69 (0.12)	0.04 (0.02)	1.50 (0.13)	3.49 (0.30)	0.62 (0.13)	4.02 (0.21)	0.46 (0.06)	0.16 (0.14)	1.00 (0.86)	-	-	-	-	97.02
TNR14-1	59	45.44 (1.10)	4.37 (0.46)	10.41 (0.65)	7.15 (0.59)	0.17 (0.03)	14.11 (0.30)	11.43 (0.23)	1.05 (0.09)	0.20 (0.03)	2.23 (0.12)	0.06 (0.03)	0.33 (0.12)	0.69	-	-	-	98.64
HA3_Redo	59	51.75 (0.48)	0.03 (0.04)	7.84 (1.27)	11.61 (0.47)	0.09 (0.03)	22.79 (2.7)	5.72 (0.98)	0.04 (0.06)	0.03 (0.02)	1.62 (0.16)	0.05 (0.02)	0.26 (0.3)	-	0.57	0.10	-	97.63
HA4-1	45	56.30 (0.54)	0.06 (0.04)	8.94 (0.58)	0.54 (0.06)	0.06 (0.02)	15.31 (0.46)	12.07 (0.59)	0.09 (0.03)	0.04 (0.02)	1.75 (0.2)	0.02 (0.03)	0.42 (0.10)	-	0.17	0.13	-	97.53
Rhyolite-1	20	75.44 (1.40)	0.33 (0.05)	13.25 (0.94)	0.13 (0.04)	0.02 (0.03)	0.27 (0.04)	0.92 (0.07)	0.56 (0.20)	6.12 (0.62)	0.27 (0.03)	0.05 (0.10)	0.85 (0.31)	-	-	-	-	95.92
LIP17714	32	77.51 (1.20)	0.08 (0.02)	12.82 (0.77)	0.18 (0.02)	0.03 (0.02)	0.11 (0.02)	0.73 (0.05)	2.73 (0.13)	3.82 (0.46)	0.27 (0.03)	0.02 (0.02)	0.50 (0.42)	-	-	-	-	98.21
AN-2	28	64.50 (0.91)	0.63 (0.05)	17.29 (0.50)	2.04 (0.21)	0.01 (0.02)	3.14 (0.10)	6.22 (0.22)	2.81 (0.11)	0.86 (0.03)	0.90 (0.05)	0.04 (0.02)	0.60 (0.34)	-	-	-	-	98.83
SM_Redo	27	42.82 (0.38)	0.02 (0.02)	10.27 (0.11)	10.26 (0.14)	0.01 (0.02)	14.56 (0.13)	15.44 (0.15)	0.04 (0.02)	0.01 (0.01)	3.05 (0.16)	0.08 (0.02)	0.32 (0.17)	-	-	-	-	99.03
HiMgAnd	29	55.41 (0.47)	0.60 (0.05)	14.26 (0.38)	5.19 (0.12)	0.00 (0.01)	8.85 (0.18)	9.13 (0.16)	1.54 (0.15)	0.61 (0.03)	1.71 (0.03)	0.08 (0.03)	0.35 (0.13)	-	-	-	-	96.88

HAW-16095	28	51.95 (0.75)	2.44 (0.20)	10.97 (0.58)	6.93 (0.26)	0.15 (0.02)	12.39 (1.06)	9.42 (0.46)	0.96 (0.12)	0.14 (0.02)	1.90 (0.14)	0.05 (0.02)	0.40 (0.22)	-	-	-	-	97.73
EGT17-1	35	55.73 (0.60)	3.68 (0.09)	17.43 (0.20)	0.15 (0.04)	0.12 (0.02)	4.49 (0.11)	9.89 (0.21)	3.14 (0.14)	1.10 (0.05)	1.40 (0.02)	0.04 (0.02)	0.38 (0.19)	-	-	-	-	97.69
KK3b-2	27	54.80 (0.60)	0.86 (0.05)	16.34 (0.20)	0.08 (0.02)	0.07 (0.03)	10.54 (0.12)	13.22 (0.13)	1.06 (0.06)	0.07 (0.03)	1.70 (0.04)	0.02 (0.03)	0.48 (0.11)	-	-	-	-	97.49
Mars-1	26	49.32 (1.16)	0.94 (0.15)	9.04 (0.85)	16.11 (0.46)	0.28 (0.04)	12.56 (1.29)	6.35 (0.48)	0.07 (0.02)	0.02 (0.01)	2.02 (0.2)	0.09 (0.06)	0.41 (0.15)	-	-	0.46	-	99.23
Neph-1	20	45.93 (0.44)	2.53 (0.05)	16.45 (0.16)	8.94 (0.09)	0.28 (0.03)	4.33 (0.09)	11.77 (0.07)	2.68 (0.09)	1.19 (0.05)	1.91 (0.03)	0.10 (0.04)	0.43 (0.41)	1.22	-	-	-	97.67
Basanite-1	30	47.42 (0.35)	2.59 (0.05)	12.12 (0.10)	5.46 (0.08)	0.18 (0.04)	12.90 (0.12)	9.72 (0.15)	2.06 (0.03)	0.60 (0.06)	2.06 (0.03)	0.08 (0.04)	0.36 (0.22)	1.50	-	-	-	97.71
Lunar-1	29	45.77 (0.41)	7.54 (0.16)	11.13 (0.14)	12.89 (0.26)	0.47 (0.04)	6.92 (0.11)	8.59 (0.15)	0.47 (0.06)	0.033 (0.02)	2.03 (0.09)	0.10 (0.02)	0.54 (0.31)	-	-	-	-	96.98
KK-Rhy-1	24	75.30 (0.91)	0.07 (0.03)	13.60 (0.84)	0.90 (0.09)	0.08 (0.04)	0.15 (0.02)	0.69 (0.12)	3.59 (0.30)	3.40 (0.13)	0.15 (0.02)	0.20 (0.25)	0.67 (0.69)	-	-	-	-	96.48
JB-Phono-1	36	62.21 (0.84)	1.56 (0.07)	19.79 (0.48)	0.05 (0.02)	0.04 (0.02)	2.02 (0.13)	4.35 (0.20)	5.63 (0.12)	2.15 (0.06)	0.83 (0.02)	0.06 (0.04)	0.36 (0.18)	-	-	-	-	98.81
Phono-1	26	59.17 (0.98)	0.35 (0.03)	24.29 (1.10)	1.21 (0.06)	0.15 (0.03)	0.22 (0.02)	2.20 (0.07)	5.41 (0.17)	5.66 (0.12)	0.68 (0.07)	0.19 (0.20)	0.54 (0.63)	-	-	-	-	99.05
CMAS+Na+2	40	44.93 (0.50)	0.02 (0.03)	16.72 (0.41)	0.07 (0.02)	0.00 (0.02)	15.73 (0.31)	15.62 (0.16)	1.72 (0.13)	0.01 (0.02)	2.32 (0.1)	0.06 (0.03)	0.28 (0.09)	-	-	-	-	100.07
CNMAS-1	36	47.37 (0.45)	0.02 (0.02)	16.17 (0.15)	0.10 (0.02)	0.00 (0.01)	11.28 (0.10)	20.65 (0.14)	0.04 (0.02)	0.02 (0.02)	2.41 (0.14)	0.03 (0.02)	0.34 (0.14)	-	-	-	-	97.49
CNMAS-2	31	50.01 (0.31)	0.02 (0.02)	13.01 (0.26)	0.07 (0.02)	0.00 (0.02)	13.83 (0.20)	18.47 (0.16)	0.03 (0.01)	0.01 (0.02)	2.60 (0.13)	0.05 (0.1)	0.36 (0.17)	-	-	-	-	98.42
Granite-2	36	75.13 (0.76)	0.04 (0.04)	15.94 (0.42)	0.08 (0.02)	0.00 (0.01)	0.06 (0.02)	0.16 (0.03)	4.25 (0.21)	2.96 (0.12)	0.31 (0.10)	0.18 (0.18)	0.44 (0.28)	-	-	-	-	98.46
Gran+Mg-1	41	70.19 (0.98)	0.03 (0.03)	15.79 (0.61)	0.06 (0.02)	0.00 (0.01)	5.11 (0.25)	0.18 (0.03)	4.33 (0.11)	2.47 (0.1)	0.61 (0.10)	0.16 (0.22)	0.63 (0.50)	-	-	-	-	99.56
Gran+Mg-2	43	68.99 (0.72)	0.05 (0.06)	15.48 (0.40)	0.13 (0.02)	0.00 (0.01)	6.30 (0.30)	0.32 (0.13)	4.24 (0.3)	2.40 (0.11)	0.67 (0.14)	0.21 (0.32)	0.56 (0.80)	-	-	-	-	99.59
Gran+Mg-3	43	66.84 (0.51)	0.04 (0.03)	16.08 (0.36)	0.04 (0.02)	0.01 (0.02)	7.930 (0.31)	0.58 (0.04)	4.20 (0.18)	2.2 (0.10)	0.78 (0.10)	0.06 (0.20)	0.49 (0.50)	-	-	-	-	99.36
AgI/Cl-020	15	45.01 (0.42)	-	17.86 (0.19)	-	-	16.53 (0.19)	16.52 (0.24)	-	-	2.41 (0.16)	0.23 (0.40)	0.02 (0.03)	-	-	-	-	98.57

AgI/Cl-032	22	45.63 (0.25)	-	18.10 (0.35)	-	-	16.83 (0.30)	15.69 (0.23)	-	-	3.39 (0.04)	0.15 (0.07)	0.05 (0.05)	-	-	-	-	99.84
AgI/Cl-021	20	45.76 (0.23)	-	17.96 (0.14)	-	-	16.13 (0.20)	16.10 (0.20)	-	-	2.12 (0.03)	0.32 (0.10)	0.01 (0.03)	-	-	-	-	98.40
AgI/Cl-09	22	48.36 (0.48)	-	17.11 (0.13)	-	-	16.76 (0.36)	16.26 (0.14)	-	-	0.50 (0.03)	0.06 (0.03)	0.20 (0.16)	-	-	-	-	99.25
AgI/Cl-013	29	45.94 (0.62)	-	17.87 (0.24)	-	-	16.37 (0.19)	15.73 (0.29)	-	-	3.59 (0.09)	0.00 (0.03)	0.14 (0.07)	-	-	-	-	99.64
AgI/Cl-18	30	47.58 (1.05)	-	17.54 (0.28)	-	-	16.55 (0.16)	16.43 (0.28)	-	-	0.18 (0.01)	0.00 (0.03)	0.05 (0.07)	-	-	-	-	98.33
CMAS-"0"	40	48.49 (0.67)	0.02 (0.02)	14.89 (1.08)	0.05(0.02)	0.01 (0.01)	15.38 (0.45)	15.87 (0.36)	0.04 (0.03)	0.01 (0.02)	2.31 (0.19)	0.04 (0.04)	0.33 (0.11)	-	-	-	-	97.45
CMAS+Brucite-"0.5"	40	47.55 (0.48)	0.02 (0.03)	16.20 (0.24)	0.14 (0.03)	0.01 (0.03)	15.17 (0.18)	15.01 (0.24)	0.00 (0.01)	0.02 (0.01)	2.22 (0.30)	0.04 (0.04)	0.36 (0.20)	-	-	-	3.23*	100.00
CMAS+Brucite-"1"	40	43.84 (0.94)	0.02 (0.04)	16.34 (0.64)	0.12 (0.03)	0.02 (0.03)	15.51 (0.56)	14.51 (0.74)	0.00 (0.01)	0.01 (0.02)	2.52 (0.04)	0.03 (0.03)	0.30 (0.07)	-	-	-	6.74*	100.00

Numbers in parentheses () are analytical uncertainties of two standard deviations of n analysis

*Calculated by difference

4.3.2 Analytical measurement

All experimental silicate glasses and chlorine fugacity buffers, including those measured in chapters 2 and 3 were analysed on the CAMECA SX-Five-FE at the University of Oxford's Department of Earth Sciences. All results are listed in table 4.1.

For the anhydrous experiments, a 20 nA beam current, 15 kV accelerating voltage and a defocused 10 μm beam diameter was used for the glass analyses. To minimise the potential for element migration during analysis, Cl, Na, K, and Si were analysed first. Counting times were a minimum of 30 s peak and 15 s background for all elements except for Cl, for which 80 s peak and 40 s background were used to obtain a detection limit of $\leq$100 ppm. For Na and K 20 s peak and 10 s background were used to reduce any possible element migration during analyses. The hydrous experiments were measured separately using a lower beam current (5 nA) and a larger, 20 μm spot size. The water content was calculated by difference and compared to that predicted from the amount of brucite added (see section 4.3.1).

After microprobe analysis and prior to XAS analyses, samples were re-polished to ensure that the surface was clean and free of carbon coating. 1 μm diamond powder was used, with toluene as a lubricant to prevent the dissolution of any water-soluble components.

4.3.3 XAF measurements

Chlorine K-edge fluorescence XAS spectra were collected on the I18 beamline at the Diamond Light Source Synchrotron, UK, under the supervision of the principal beam scientist Dr Konstantin Ignatyev. All samples analysed were homogenous glasses free of vesicles, with at least >1mm^2 measurable area. Because the Cl K edge is within 385 eV of that of Argon (2822

vs 3207 eV, respectively), the samples were enclosed within a helium-filled bag to minimise X-ray absorption by the atmosphere. Although Ar is often present as a trace component in analytical grade He (Evans et al., 2008), its presence has only a marginal effect on the detection limit of Cl. Spectra were obtained in fluorescence mode using the double crystal Si(111) monochromator and a 4-element silicon drift detector (Vortex ME-4) at a 45° take-off angle. The experimental run products comprised >0.5mm thick glass samples, encased within graphite and Pt capsules (total thickness <2mm; see section 2.1). Thick samples lead to the increased potential for transmission spectra to become distorted by harmonics from the beam, leading to the degradation of the signal-to-noise ratio by increasing background fluorescence (Calvin, 2013). We suppressed the harmonics of the beam by utilising silicon harmonic rejection mirrors (Abe et al., 2018).

For each spectrum collected, the monochromator was scanned from 2700-3200 eV using a defocused (50 × 50 µm square) beam. The scan parameters were set to 5 eV steps in the pre-edge region from 2700 to 2790 eV with a dwell time of 1 s; in the XANES region: 1 eV steps from 2790 to 2800 eV with a dwell time of 2 s; 0.5 eV steps from 2800 to 2850 eV, with a dwell time of 2s; and in the EXAF region:1 eV steps from 2850 to 2950 eV, with a dwell time of 2 s; 2 eV steps from 2950 to 3200 eV with a dwell time of 5 s. The experimental glass samples possessed up to 4wt% Cl, requiring the use of a 2µm Sn filter to minimise sample damage and the detector working distance set to 20mm to maximise detector efficiency. The pure salt standards exhibited pronounced instability when exposed to the same analytical conditions as the glasses, necessitating the use of a 25µm thick Al and 4µm thick V filters to minimise beam damage, and the detector working distance increased to 60 mm to prevent saturation.

Multiple spectra were collected from selected experiments to verify the reproducibility of the instrument. A minimum of 3 spectra were recorded per sample, and up to 6 replicate analyses on the same spot was performed on selected samples periodically to check the stability of the glasses under the beam. Additionally, dwell times were optimised to gain a maximum sensitivity and minimise sample damage.

4.3.4 Post-run analysis and interpretation

All raw XAF spectra were treated using the Larch XAS package (Newville, 2013). Firstly, systematic glitches which arise from alternative diffraction planes (Calvin, 2013) were removed from multiple spectra at 3005 and 3145 eV. Each spectrum was normalised by firstly subtracting a pre-edge linear background over the range -120 to -40 eV from E_0, the energy of the main absorbing edge, which was calculated in Larch (Newville, 2013), where E_0 represents the maximum first derivative which defines the main absorption edge (Figure 4.1). Followed by a polynomial fit to the post-edge points extrapolated back to the absorption edge (120-360 eV from E_0). Multiple spectra taken from the same sample were then checked for repeatability and averaged within Larch. The energy that indicates the position of the first peak of the post edge spectra, E_{Max} was calculated from the position of the peak's maximum intensity, where the first derivative passes through zero immediately after the main absorption edge following Evans et al., (2008), (Figure 4.1b). The elevated Cl contents of the salt standards required an additional correction for self-absorption, which was implemented using the "Fluo" routine of Haskell, (1999), originally developed by Iida and Noma, (1993) and applied through the Larch program (Newville, 2013).

To explore the EXAF region (Figure 4.1), we first applied a spline function to isolate the oscillatory (EXAF) part of the spectrum. Energy values in eV were converted to K-space, $\chi(k)$ ($Å^{-1}$), and weighted to $k^3\chi(k)$, and then converted to R-space, $\chi(R)$ by fourier transform using a *Hanning* function to window the K-space range of 1-6 $Å^{-1}$ following the recommendations of Calvin, (2013). All experimental run summaries and XAF defined properties are listed in Table 4.2.

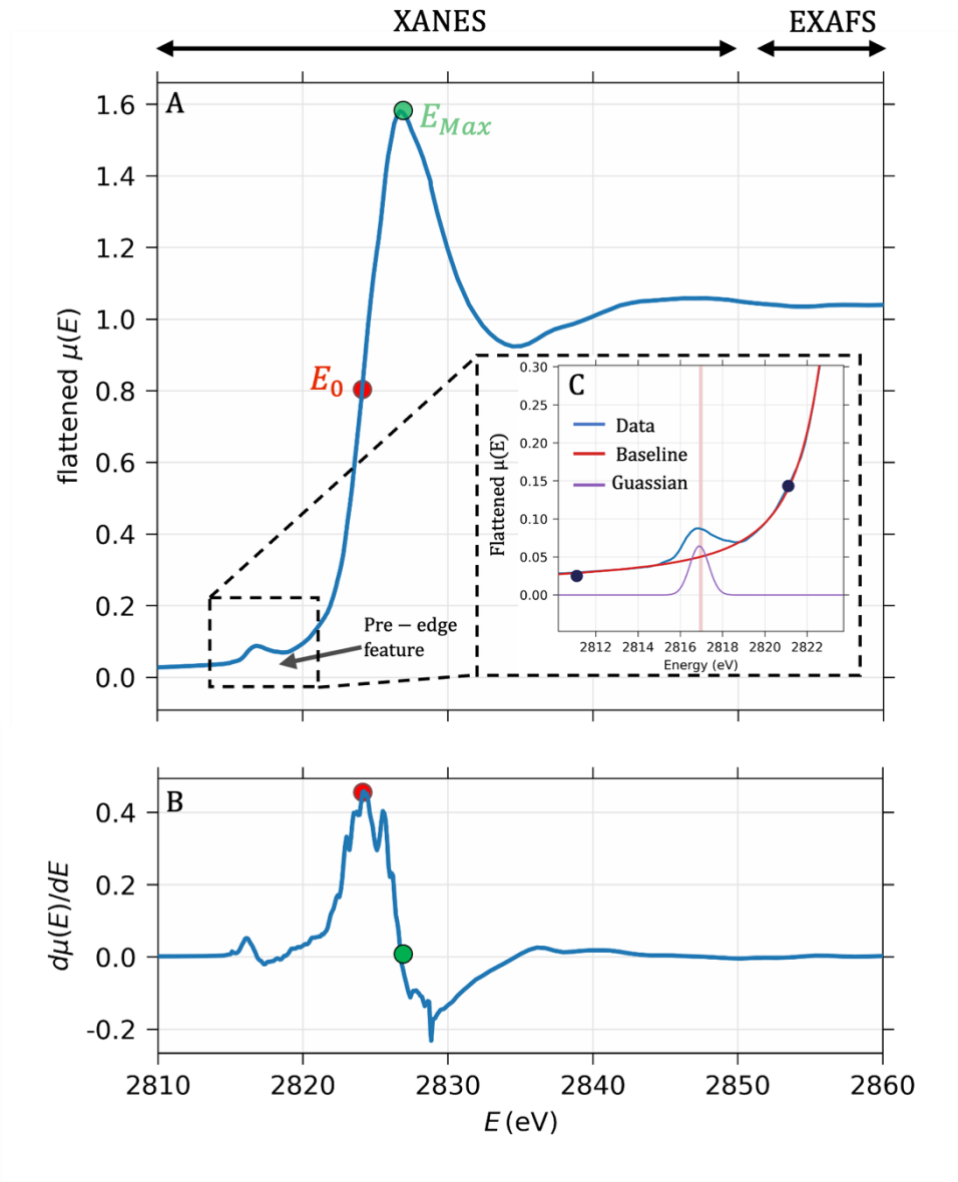


Figure 4.1 A) X-ray absorption fine structure (XAFS), and B) the corresponding first derivatives across the XANES regions. The calculated E_0 and E_{Max} are highlighted by red and green circles, respectively. Pre-edge feature locations and **C)** the pre-edge centroid fitting parameters.

Pre-edge peak fitting

Some spectra displayed pre-edge peaks at approximately 2818 eV (Figure 4.1a and 4.3; Section 3.2.1). To model these peaks, we first fit a 'baseline' curve to the main absorption edge. A

linear function was modelled to the pre-edge and a Lorentzian curve to the main edge. These were then extrapolated to E_0 to determine the edge jump. Pre-edge features were then fit using a simple, single gaussian approach. This provided a good fit to all pre-edge peaks using the same constraints, ensuring that both the amplitude and standard deviation (σ, in eV) remain positive; this then allowed for the calculation of the centroid fit of the pre-edge peak (Figure 4.1c; Table 4.2).

4.4 Results and discussion

All experiments resulted in the segregation of the buffer-silicate mixture into a homogeneous translucent glass, free of vesicles and approximately 0.8 mm across, a metal chloride/iodide phase and an Ag-rich metal alloy (see chapter 2). All experimental run conditions, concentrations of chlorine in the resultant glass phases and XAF defined parameters, E_0, E_{Max}, R (bond distance in Å) and pre-edge centroids are given in Table 4.2. Errors on the values of E_0, E_{Max} were found to be +/- 0.2 eV by determining the differences of each value from the individual spectra (a minimum of three) that were merged to form a spectra per sample. As a result, bond distances, that were calculated using merged spectra and therefore represent an average across each experiment.

Table 4.2 Experimental conditions and measured XAF parameters

Experiment ID	Temperature (°C)	Pressure (Gpa)	Duration (h)	*log f*(O_2)	*log f*(Cl_2)	Chloride capacity (C_{Cl})	Pre-edge centroid (eV)	E_0 (eV)	$E_{max\ (eV)}$	R (Å)
Ab/Fo-1	1400	1.5	1	-7.17	8.08E-04	0.32	2817.20	2824.70	2827.06	2.50
Ab/Fo-2	1400	1.5	1	-7.17	5.05E-04	1.01	2817.90	2824.80	2827.50	2.29
Ab/Fo-3	1400	1.5	2	-7.17	2.98E-04	2.57	2818.10	2824.70	2827.55	2.30
Ab/Fo-5	1400	1.5	1	-7.17	3.69E-05	10.86	2818.19	2824.60	2827.60	2.30
AgI/Cl-27	1400	1.5	1	-7.17	4.24E-04	1.25	-	2824.60	2827.60	2.24
AgI/Cl-024	1400	1.5	1	-7.17	2.94E-04	2.38	-	2825.10	2827.60	2.21
AgI/Cl-025	1400	1.5	1	-7.17	2.68E-04	2.73	-	2824.80	2827.70	2.12
AgI/Cl-026	1400	1.5	1	-7.17	1.04E-04	5.52	-	2824.90	2827.60	2.10
Dacite-1	1400	1.5	2	-7.17	8.90E-04	0.25	2820.17*	2824.50	2827.40	2.21
TNR14-1	1400	1.5	3	-7.17	3.47E-04	1.93	-	2825.10	2827.60	2.23
HA3_Redo	1400	1.5	2	-7.17	5.32E-04	1.13	-	2824.50	2827.50	2.18
HA4-1	1400	1.5	3	-7.17	5.18E-04	1.24	-	2825.10	2827.60	2.24
Rhyolite-1	1400	1.5	2	-7.17	1.04E-03	0.13	2816.81	2824.20	2826.90	2.15
LIP17714	1400	1.5	3	-7.17	9.85E-04	0.14	2816.79	2824.20	2827.04	2.21
AN-2	1400	1.5	1	-7.17	6.93E-04	0.55	-	2824.60	2827.60	2.27
SM_Redo	1400	1.5	2	-7.17	1.67E-04	3.80	-	2825.20	2827.70	2.21
HiMgAnd	1400	1.5	1	-7.17	4.65E-04	1.28	-	2824.80	2827.50	2.15
HAW-16095	1400	1.5	3	-7.17	3.93E-04	1.54	-	2824.60	2827.50	2.18
EGT17-1	1400	1.5	3	-7.17	6.43E-04	0.89	-	2824.70	2827.50	2.27
KK3b-2	1400	1.5	1	-7.17	6.88E-04	1.04	-	2824.80	2827.56	2.26
Mars-1	1400	1.5	2	-7.17	3.57E-04	1.72	-	2825.00	2827.70	2.08
Neph-1	1400	1.5	3	-7.17	4.27E-04	1.49	-	2824.70	2827.60	2.20
Basanite-1	1400	1.5	1	-7.17	4.00E-04	1.66	-	2824.80	2827.60	2.24
Lunar-1	1400	1.5	1	-7.17	3.75E-04	1.69	-	2824.70	2827.70	2.12
KK-Rhy-1	1400	1.5	1	-7.17	7.91E-04	0.09	-	2823.60	2827.29	2.33

JB-Phono-1	1400	1.5	1	-7.17	9.72E-04	0.43	2817.61	2824.40	2827.45	2.33
Phono-1	1400	1.5	1	-7.17	6.61E-04	0.42	2817.59	2824.60	2827.50	2.45
CMAS+Na+2	1400	1.5	2	-7.17	3.89E-04	1.90	-	2824.80	2827.60	2.30
CNMAS-1	1400	1.5	2	-7.17	3.52E-04	2.24	-	2824.80	2827.60	2.28
CNMAS-2	1400	1.5	2	-7.17	2.92E-04	2.27	-	2824.90	2827.60	2.27
Granite-2	1400	1.5	2	-7.17	8.08E-04	0.18	2816.88	2824.20	2826.70	2.24
Gran+Mg-1	1400	1.5	2	-7.17	1.04E-03	0.31	2817.32	2824.70	2827.39	2.38
Gran+Mg-2	1400	1.5	2	-7.17	7.16E-04	0.41	2817.38	2824.80	2827.20	2.34
Gran+Mg-3	1400	1.5	2	-7.17	8.09E-04	0.44	2817.49	2824.70	2827.40	2.36
AgI/Cl-020	1300	1.5	1	-7.90	1.38E-04	2.17	-	2824.60	2827.60	2.25
AgI/Cl-032	1400	0.5	1	-8.20	1.09E-05	10.87	-	2824.90	2827.60	2.27
AgI/Cl-021	1400	2	1	-6.66	1.20E-03	0.65	-	2825.00	2827.70	2.27
AgI/Cl-09	1400	1.5	1	-7.17	1.59E-05	2.02	-	2825.10	2827.65	2.23
AgI/Cl-013	1400	1.5	1	-7.17	1.38E-03	1.56	-	2824.50	2827.60	2.27
AgI/Cl-18	1400	1.5	1	-7.17	1.66E-06	2.25	-	2824.60	2827.50	2.22
CMAS-"0"	1400	1.5	2	-7.17	4.88E-04	1.69	-	2825.00	2827.60	2.24
CMAS+Brucite-"0.5"	1400	1.5	2	-7.17	4.39E-04	1.71	-	2824.90	2827.60	2.27
CMAS+Brucite-"1"	1400	1.5	2	-7.17	3.54E-04	2.16	-	2824.80	2827.50	2.27
Compressed salt standards:										*Shannon (1976):*
$CaCl_2$								2824.7	2827.24	2.81
$MgCl_2$								2824.50	2827.16	2.38
$FeCl_2$								2825.30	2827.35	2.42
$MnCl_2$								2824.50	2825.36	2.47
$AlCl_3$								2825.00	2826.01	2.35
KCl								2824.80	2825.82	2.83
NaCl								2824.90	2825.94	2.80
AgCl								2823.40	2823.99	2.48

*pre-edge present as a shoulder on the main edge and so wasn't used in interpretation

4.4.1 Interpreting salt standard spectra

Compressed, pure, nominally anhydrous ("ultra-dry") analytical grade crystalline salts (each greater than 99.99% purity sourced from Alpha Aesar) were measured across the full energy range (2700-3200 eV). The standards were chosen to encompass the valance range of cations (Na, K, Ca, Mg, Mn, Si, and Al,) in a silicate melt. In the XANES region, we find in agreement with Evans et al., (2008) that the salt standards are distinguishable from each other due to differences in the edge position and the primary peak, and also the complexity of the near-edge features (Figure 4.2). The divalent cation salts typically form a double-first peak, present immediately after the main absorption edge (e.g., $MnCl_2$ and $FeCl_2$), with <3 eV between the peaks, with the second peak exhibiting greater intensity at higher eV. Additionally, this may be present as a shoulder on the flank of the main absorption edge (e.g., $CaCl_2$). All divalent cations share a relatively featureless EXAFS region. The monovalent cation salts display a single peak and a more complex post-edge region.

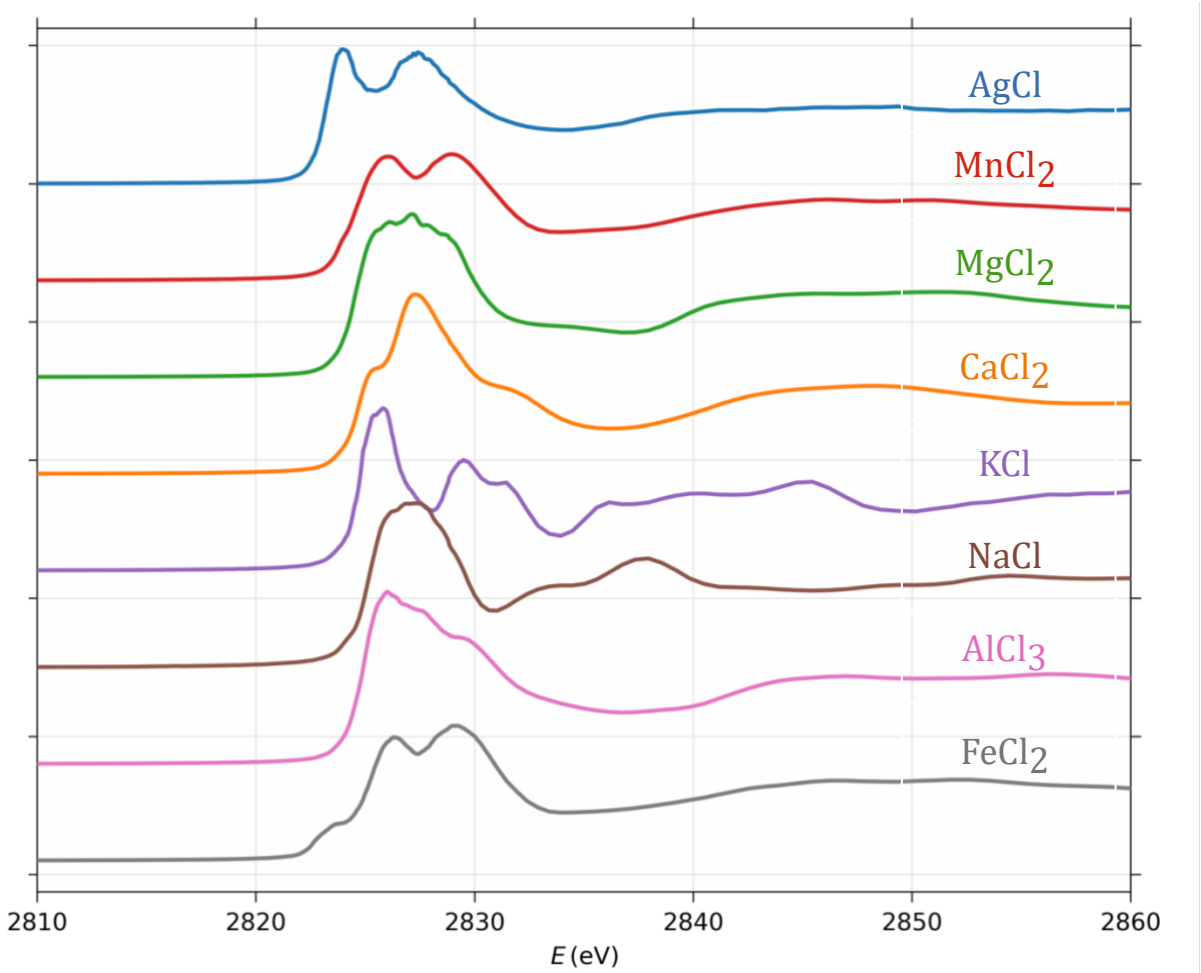


Figure 4.2 Stacked, normalised X-ray absorption fine structure (XAFS) of compressed salt standards, corrected for self-absorption and glitches removed. Standards can be distinguished from each other by peak positions, shape, and complexity of the post edge region.

The salt standards chosen (Table 4.2) cover a range of bonding geometries (Jain et al., 2013), and bond distances (calculated from the ionic radius from Shannon, (1976)) including NaCl and KCl, which form a cubic structure with Cl surrounded by six alkali cations, forming Cl−Na bonds with bond distances of 2.80 Å and Cl−K is 2.83 Å respectively. AgCl forms orthorhombic crystals in a 5-coordinate geometry, forming Ag-Cl bond distances of 2.48 Å. In $CaCl_2$, Cl^- is bonded to three Ca^{2+} atoms, within a distorted trigonal planar geometry at Cl−Ca

bond distances of 2.81 Å. In $MgCl_2$, $FeCl_2$, and $MnCl_2$, Cl^- is bonded to three Mg, Fe, or Mn^{2+} atoms in a distorted T-shaped geometry, forming bonds Mg-Cl at 2.38 Å, Fe-Cl at 2.42 Å and Mn-Cl at 2.47 Å. In $AlCl_3$ Cl^- is bonded to two Al^{3+} atoms in an L-shaped geometry at bond lengths of 2.35 Å (Shannon, 1976; Jain et al., 2013).

Potential problems in using compressed salt as standards to interpret the bonding of Cl in a silicate glass include: 1) the salts exhibited pronounced instability at the same analytical conditions as the glasses, requiring additional filters to be applied (section 4.2.3). 2) The salt standards take the form of cubic crystals, and 3) Cl contents an order of magnitude above the most Cl rich experimental glass. This poses a potential problem when attempting comparison with our non-cubic, more complex silicate glass structure. The differences between the standard and experimental spectra, after normalisation, still do not allow for the reliable use of linear combination fitting to determine the proportionality of Cl bonding to each standard.

4.4.2 Determining the effect of chemical composition on chlorine bonding

The spectra show distinct changes across five chosen compositions, covering a compositional range from rhyolite to basalt (Figure 4.3), including 1) the presence or otherwise of pre-edge features. 2) shifting E_0 and E_{Max}, and 3) increasing features within the post-edge region. As such, these features will be the focus of the proceeding discussion.

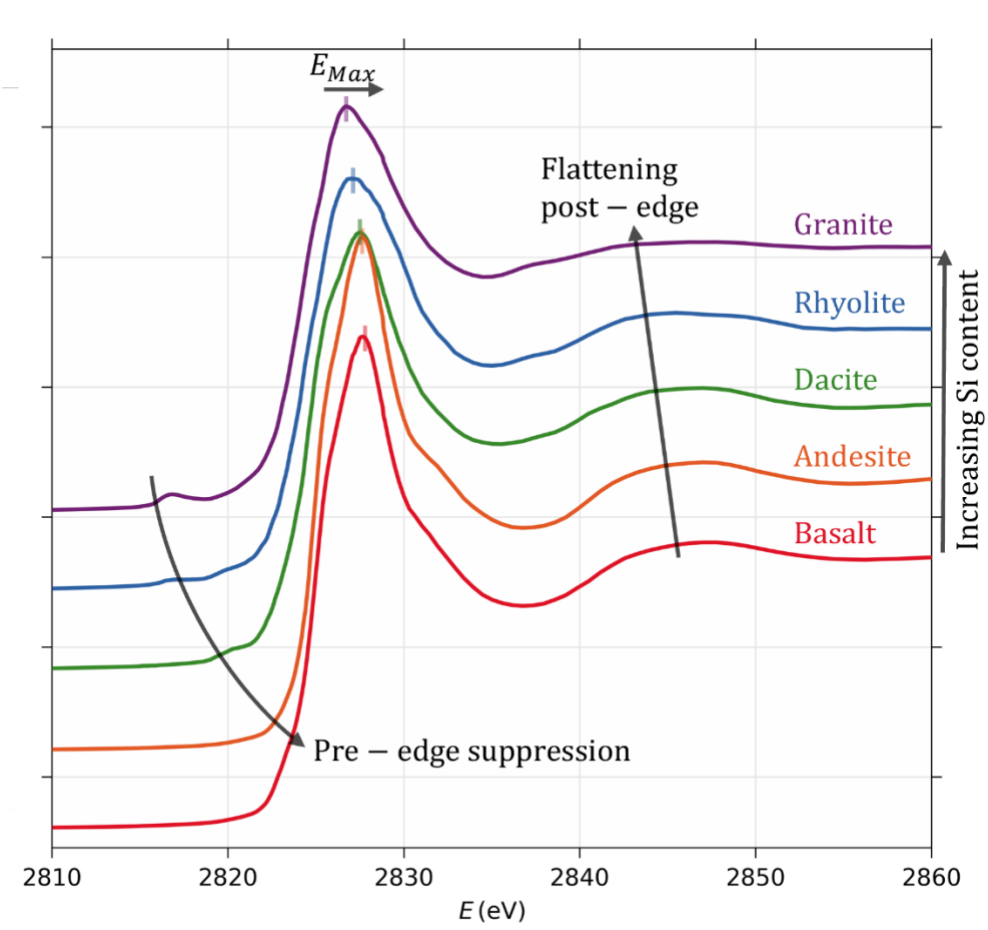


Figure 4.3 XAF spectra, covering a range of compositions from granite to basalt. Key features that change with composition are i) Presence and suppression of a pre-edge peak. ii) shifting of E_0 and E_{Max}, and ii) changing shape within the post-edge region.

Interpreting pre-edge features

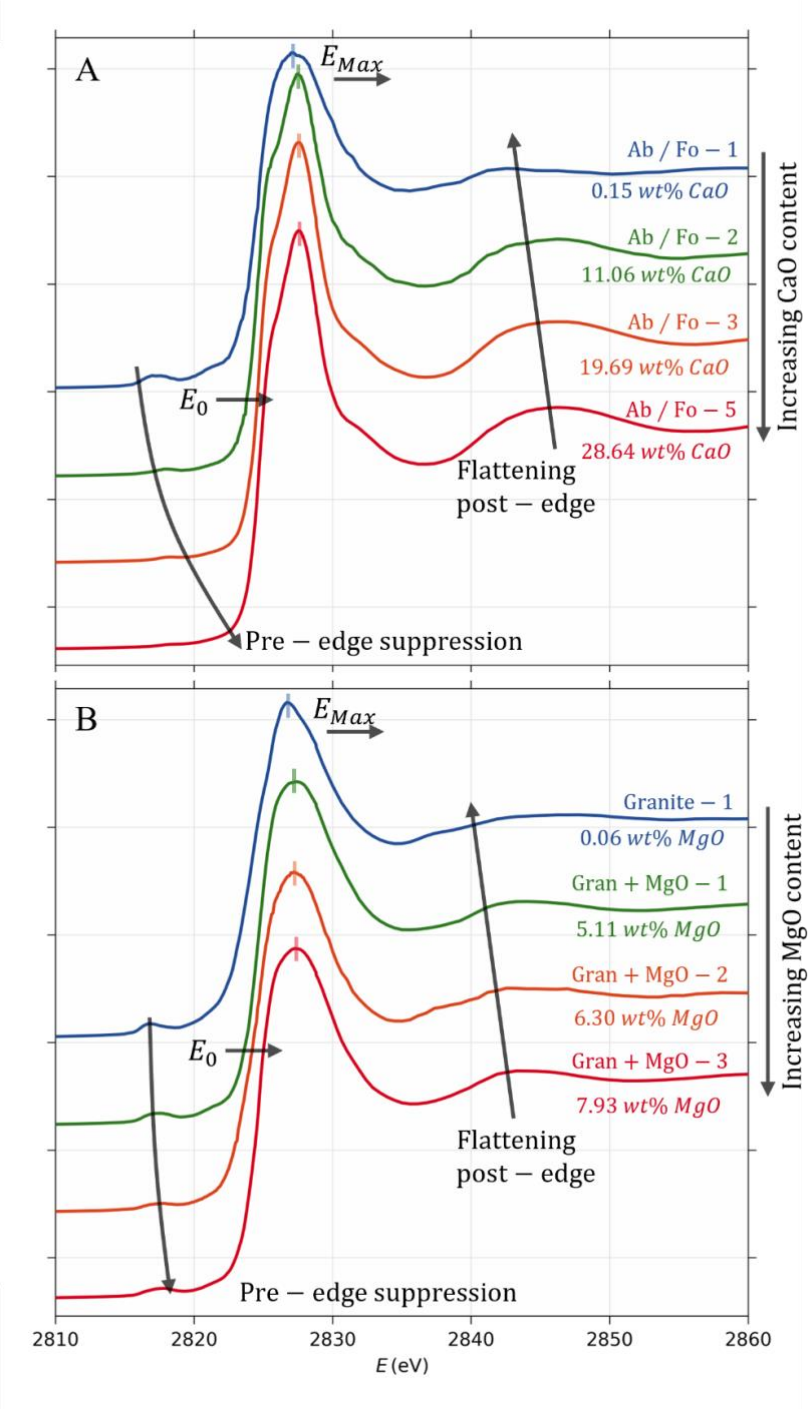


Figure 4.4 XAF Spectra showing a series of experiments with the addition of CaO (A), MgO (B), each show a change in E_0, E_{Max} with addition of the 2^+ cation. A pre-edge feature is only observed in the MgO and CaO series, becoming suppressed upon addition of $\sum \mathbf{2}^+$ cation content.

Pre-edge features (Figure 4.1, 4.3 and 4.4) were only present in 13 out of the 44 samples analysed (Table 4.2), corresponding to experiments low in 2^+ cation and low chlorine concentrations. The presence of these pre-edge features is due to the bonding of Cl with an open shell transition metal (Rompel et al., 1997), and so, is absent in metal systems with a full d-manifold (Shadle et al., 1994). The pre-edge represents a forbidden 1s → 3d transition as a result of mixing ligand p-orbitals with metal d-orbitals. (Rompel et al., 1997; Calvin, 2013). This is supported by Shadle et al., (1994), who explored the bonding behaviour of Cl and Cu and found that pre-edge features were the result of a significant component of Cl 3p bonding covalently with half-occupied Cu 3d orbitals.

The amplitude of the pre-edge feature exhibited by Si-rich granites and albite-forsterite become smaller as the MgO, or CaO increases, respectively (Figure 4.4). Furthermore, the pre-edge peak centroids shift to higher energy with increasing 2^+ cation and chlorine concentrations (Figure 4.5). Therefore, the nature of Cl bonding depends on both Cl solubility and the 2^+ cation concentrations (especially, CaO, MgO and FeO).

Pre-edge features are ascribed to transitions from 1s → 3d orbitals, with the magnitude of the features representing the degree of bond covalency between a transition element and Cl. This means that they cannot be due to bonding of Cl with alkali or alkaline earth metals, which lack the 3d orbitals required; this leaves Fe and Si as the possible cause of these pre-edge features. The pre-edge features were observed in experiments that were nominally Fe free and was absent in experiments that contained more than 1.2 wt% FeO. In an additional compositional series, where FeO was added to a CMAS composition (Figure 4.8c), no pre-edges were observed, presumably due to the concentrations of Mg and Ca being present in the starting silicate CMAS mix (Table 4.1). Therefore, we suggest that the pre-edge feature arises from the covalent bonding of Cl with Si, which has available 3d orbitals (Esro et al., 2017). Suppression

of pre-edge features with increasing 2^+ cation concentrations is the result of an increasing ionic bonding environment (figure 4.4), and the shifting of the centroid to higher energies in figure 4.5. This also correlates with the regressions of equation 4.2 (and the findings of chapter 3).

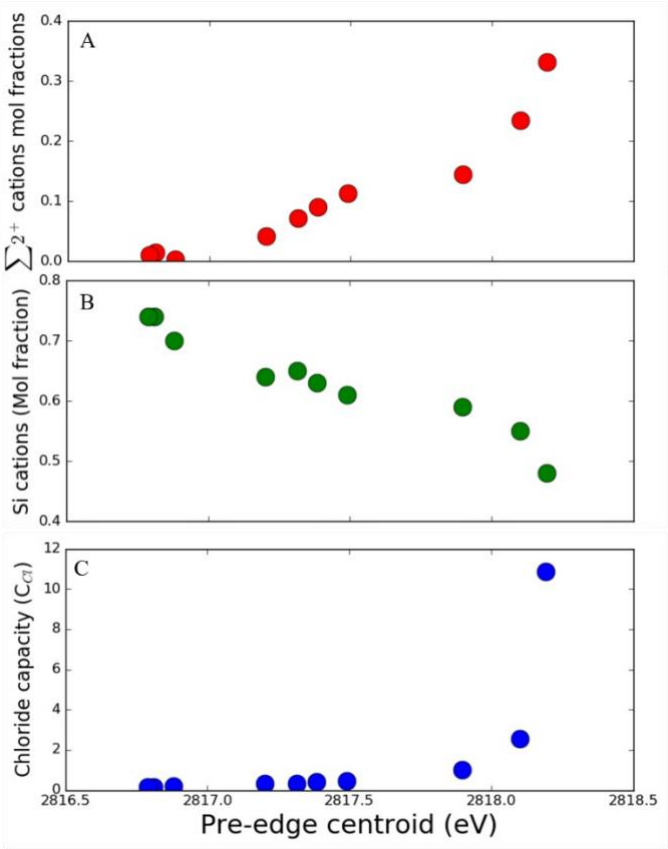


Figure 4.5 Pre-edge centroid positions shift towards higher eV with increasing 2^+ cation concentration and chloride capacity (C_{Cl}), and also with the subsequent decrease in Si concentration. Note the rapid increase in Cl solubility with increasing 2^+ cation concentrations

Determining the compositional effects of Cl bonding by edge characteristics

E_0 and E_{Max}, has been shown to be linearly related to the charge of the absorber (Shadle et al., 1994). As such, we began by following the work of Evans et al., (2008), and plotted E_0 against E_{Max} for both the standards and the experiments in (Figure 4.6). Firstly, it is apparent that

standards vary from one another in both E_0 and E_{Max}, with the 2^+ cations occupying the highest E_{Max} values compared to the 1^+ cations. The majority of the experiments plot at higher E_{Max} values than the standards and closest to the $CaCl_2$, $MgCl_2$, and $MnCl_2$ salt standards. However, as the latter is found in concentrations of less than 0.15 wt% in the compositions tested it can be deemed to not be the significant control over Cl bonding in these glasses. Two samples with 4.24 and 5.77 wt% NaCl plot closer to the NaCl standard; and experiments that contain samples enriched in FeO, appropriately plot closer towards the $FeCl_2$ standards (Figure 4.6). With the exception of a few anomalous samples, glasses that contain the highest amounts of Si, and therefore, lowest concentrations of Ca, Mg, and Fe, have relatively lower E_0 and E_{Max} values, as demonstrated by the colour scale of the experimental points in Figure 4.6.

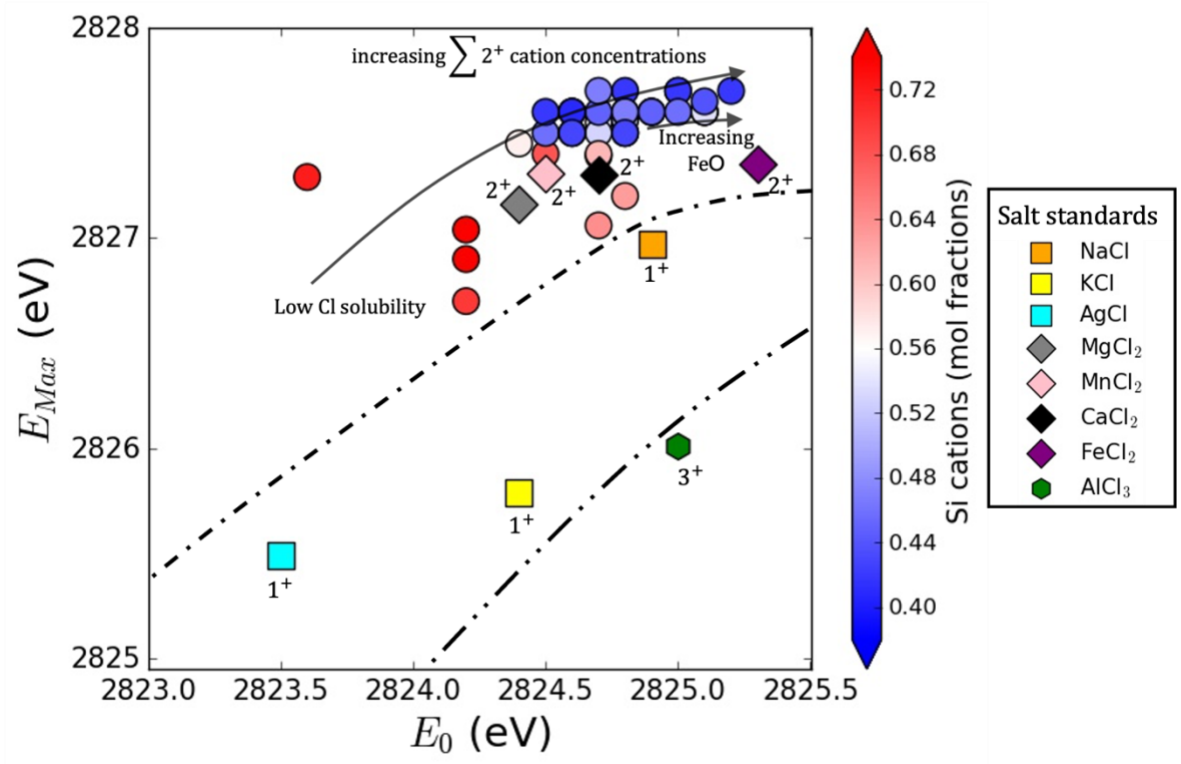


Figure 4.6 Experimental spectra plotting in E_0 vs E_{Max} space, colour graded, depicting a decrease in Si content and subsequent increase in the concentrations of 2^+ cations towards higher E_0 and E_{Max} values. Standard salt standards were overlain, and despite the potential for errors in comparison (see text) show that most experiments plot closest to standards with a 2^+ charge.

Given the uncertainties obtained when using crystalline salt standards to explore silicate glasses (section 4.1), the potential error means the above findings can only be used to demonstrate a general relation between the salt standards and the silicate glasses. To more accurately define the relations of E_0 and E_{Max} with the absorbing element, we fitted both E_0 and E_{Max} to the compositional terms for each of the constituent oxides, with each oxide recalculated as the mole fraction on a single cation basis. We then applied a stepwise linear regression using the F-test (α=0.05) to determine which compositional parameters are the most significant using

the *SPSS software*. The Si content was found to be the only significant term in each test performed using both E_0 or E_{Max}, as the dependent variable.

Figure 4.7 shows that E_{Max} increases with Cl solubility and also Ca, Mg and Fe content ($\sum 2^+$cations), and subsequently decreases with Si concentration. However, changes in E_0 and E_{Max} relate only to the bonding environment; hence changes in 2^+ concentration would not change the E_{Max}. It only represents the change in Cl solubility. This is demonstrated in Figure 4.7, where the sum of 2^+ cations display a spread of E_{Max} at similar concentrations. This range represents the change in bonding from Mg to Ca to Fe with each of the experiments enriched in each cation plotting at these energies (Figure 4.7). To further illustrate this, the Ab-Fo + Ca series (Table 4.1 and Figure 4.4) is highlighted in green in figure 4.7. As Ca content is increased, there is an increase in E_{Max} until approximately 2827.5 eV. Subsequent addition of Ca (and therefore decrease in Si) does not change the E_{Max} further. This might reflect a saturation point in which Cl is clustered by 2^+ cations. This would indicate that Cl only replaces selective oxygen atoms in the silicate melt and that the length of the Henry's law region is dependent upon the 2^+ cations present. However, given the findings from chapters two and three, Henry's Law is obeyed in a range of compositions up to 2.6 wt% Cl (figures 2.4 and 3.2). Therefore, clustering is unlikely to occur within the melt and may represent a result of quenching. This would suggest a strong temperature effect on Cl-species in the melt, and therefore also on solubility.

The propensity of chlorine bonding to 2^+ cations might explain the formation of $CaCl_2$ and $MgCl_2$ blobs that sequestered from the melt in the high $f(Cl_2)$ experiments of chapter 2 (also discussed in chapter 1). Additionally, this may justify why basaltic melts that contain high concentrations of Ca and Fe have lower tendencies to degas HCl than silica-rich melts poor in Ca and Fe, as discussed in chapter 3.

Given the thermodynamic expression of chlorine solubility (4.1), it is expected that chlorine joins the melt as 2 dissociated Cl^- ions. Chlorine might be expected therefore to bond with monovalent metals such as Na and K. The presence of a pre-edge (discussed above) is evidence of such covalency, but this pre-edge feature is absent from the majority of the spectra, and as discussed above is not found in samples containing >1.2% FeO. The apparent bonding of $MeCl_2$ complexes may therefore indicate that Cl is associated within the melt. This may result from 1) as chlorine replaces an O^{2-} in the melt, the presence of 2^+ cations may change the availability of oxygen in the silicate melt, which is more favourable for Cl bonding and thus solubility. 2) In the melt, the Cl may form O-Ca-Cl silicate chains. Structurally, this appears logical, as monovalent cations are network disrupters, and so if they formed bonds with Cl^-, this would terminate the Si-polymeric chains and thus must exist separate to the silicate chains. 3) Alternatively, this could represent a transition in bonding upon quench, whereby the Cl atoms join the melt as 2 unassociated Cl^- ions but form associated bonds in the resultant glass.

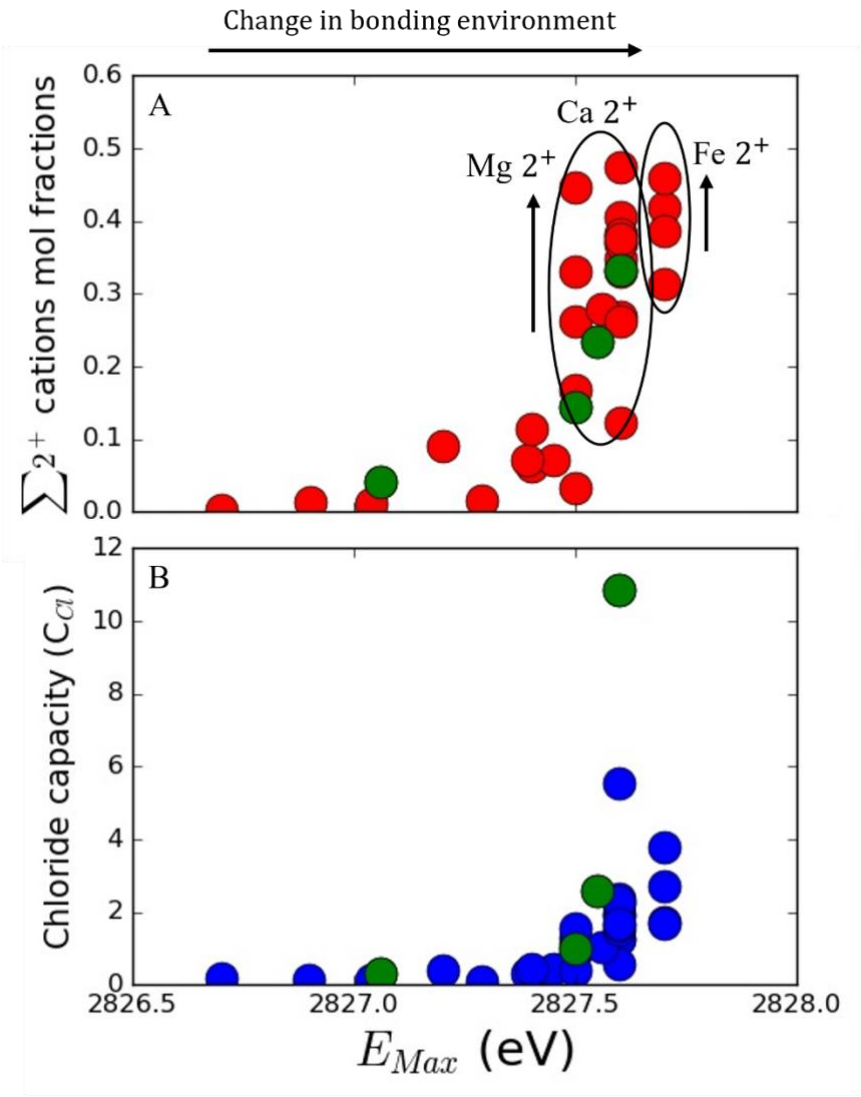


Figure 4.7 E_{Max} increasing with A) $\sum 2^+$ cation and B) chloride capacity (C_{Cl}). E_{Max} represents a change in Cl-bonding. As the Cl solubility rapidly increases with increasing 2^+ cation concentrations, it can infer a preference in bonding. The series of experiments in which Ca was added to an albite-forsterite composition is highlighted in green. Perceived errors are smaller than the symbols (see text).

.

Determining the compositional effects of Cl bonding by EXAFS

As R-space (the bonding distance, measured in angstroms, Å), corresponds to the shells of atoms surrounding the Cl atom. We can also explore the bonding environment of Cl by EXAFS. Given the above discussion, it is likely that Cl bonds with the 2^+ cations present in the melt. To examine this, we focused on the series of experiments in which Ca, Mg and Fe were sequentially added to a silicate melt (Figure 4.8).

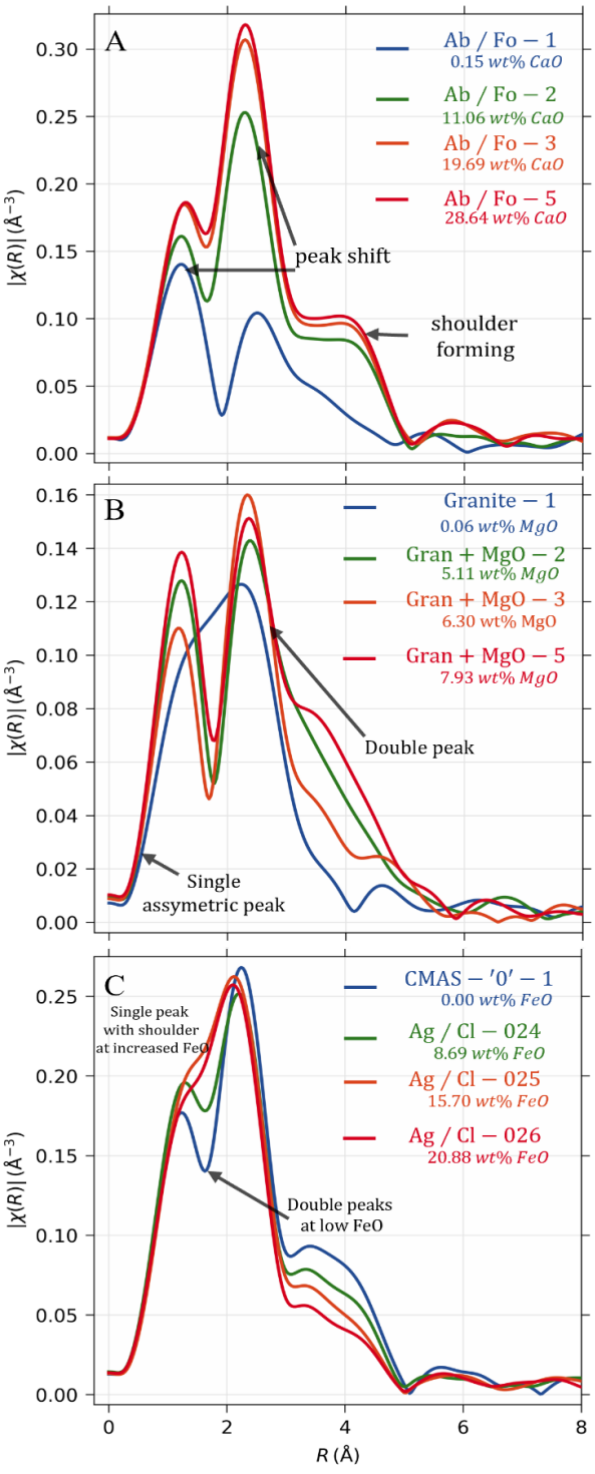


Figure 4.8 Bonding distances (Å) with the addition of A) CaO to Albite/Forsterite, B) MgO addition to granite, and C) FeO addition to CMAS. Each plot shows a change in R number and the shape of and position of the peaks with increasing divalent cation concentration.

The calcium-free, albite-forsterite composition (table 4.1; Figure 4.8a), shows a primary peak at 1.19 Å, and a secondary peak at 2.50 Å. With the addition of 11 wt% CaO, the primary peak shifts from 1.19 to 2.29 Å and the development of a shoulder on the flank of the peak. The following additions of Ca produce the same peaks but with increasing amplitude, reflecting the increase in Cl content.

In the granite, free of MgO, there is a clear singular, broad peak at 2.23 Å with a shoulder at 1.40 Å. On the addition of 5.11 wt% MgO, the R-space peaks display two distinct peaks at 1.23 and 2.32 Å, with the highest intensity at the latter peak (Figure 8b). This indicates that small addition of MgO can change the bonding environment of Cl; this is reflected in the change in Cl content, rising from 0.31 to 0.61 wt% Cl upon the addition of MgO.

The FeO free CMAS ($An_{50}Di_{28}Fo_{22}$) glass composition forms two R-space peaks, at 1.24 and 2.27 Å (Figure 8c). These two peaks are preserved with the addition of 8.69 wt% FeO, although the peaks have shifted to 1.31 and 2.22 Å. Upon further addition of FeO, the double peak becomes a single peak at 2.13 Å, with a shoulder at 1.40 Å. This may indicate a gradual change in the primary bonding environment of Cl from Ca and Mg, which are both present at concentrations greater than 15 wt% in the initial haplobasaltic composition. This is supported by the findings of (Thomas and Wood, 2021), who showed that FeO contents in the range of 0-10 wt% did not generate measurables differences in Cl content of a silicate melt. However, further work here is required to explore the Fe^{2+}/Fe^{3+} ratio, which has been shown to influence Cl solubility (e.g Simon and Bell, 2011).

To further examine the EXAFS region, we generated atom clusters to simulate the structures of potential bonds, including CaCl to represent Ca-Cl, and chloromagnesite ($MgCl_2$) to represent Mg-Cl bonds, and Lawrencite ($FeCl_2$) to represent Fe-Cl bonds. We set a maximum radial distance of 5 Å, following McKeown et al., (2011). The simulated EXAFS of these

crystals were then calculated using the FEFF fitting functions embedded into Larch (Newville, 2013), calculating the theoretical distances of Ca-Cl, Mg-Cl, and Fe-Cl. These could then be fit to our data series to provide confirmation of a proposed bonding environment. Fitting Ca-Cl was shown to match all samples of the series that contained CaO (Figure 4.8a), with increasing fit, at higher Ca contents. The same was found in MgO, where all samples that contained MgO (Figure 4.8b) fitted to the theoretical Mg-Cl bond distances. A close fit of the theoretical Fe-Cl bond distances was only observed, as predicted in the compositions, which exceeded 10 wt% FeO (Figure 4.8c). No fit was achievable in the sample containing 8.69 wt% FeO. However, these theoretical fits represent crystalline structures and as discussed in section 3.1, are also un-reliable in predicting the bonding of a complex silicate framework. For this reason, further FEFF fittings were not performed for the remainder of the experiments.

4.4.3 The effect of temperature, pressure, chlorine fugacity ($f(Cl_2)$) and water content on the bonding environment of Cl

XAF spectra were taken for a series of experimental glasses, all using the same haplobasaltic composition (CMAS; Table 4.1), performed at a range of temperatures, pressures, chlorine fugacities and water contents (Table 4.2). All glasses produced nearly identical spectra (Figure 4.9a), with E_0 and E_{Max} in the range 2824.6 to 2825.1 and 2827.5 to 2827.7 eV, respectively. They also display similar calculated bond distances (R) at values of approximately 2.22-2.27 Å and a smaller peak at 1.28 Å (Figure 4.9b). This similarity in all experimental spectra suggests the bonding environment does not change as a function of temperature, pressure, chlorine fugacity or water content, at least over the conditions investigated.

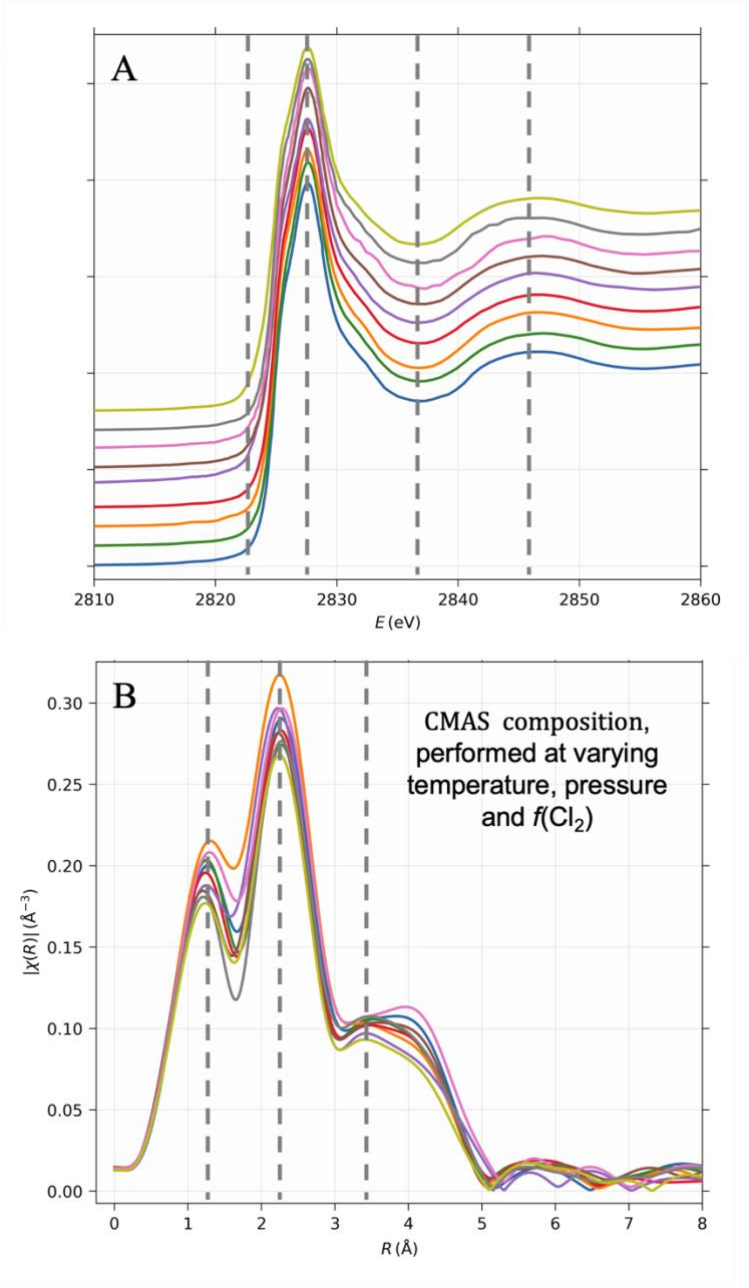


Figure 4.9 Compiled XAFS measurements of a series of experiments performed using a constant chemical composition (CMAS), at a variety of temperatures, pressures, chlorine fugacities, and water contents (Table 4.1). All spectra show similar features in both, A) the XANES region spectra and B) the EXAF region sharing similar bond distances.

The series of experiments in which water was added to a CMAS composition (by replacing brucite ($Mg(OH)_2$) with MgO) to create expected concentrations of 0, 4 and 8 wt% water), all display nearly identical spectra and R numbers Table 4.2, Figure 4.9. Additionally, Cl content shows little change and lies within 2 standard deviations of error from 2.31 to 2.22 wt% with an increase from 0 to 4 wt% H_2O and increasing slightly to 2.52 wt% Cl at an expected 8 wt% H_2O content. This supports the finding of chapter 3, where it was determined that water contents of ≤4.3 wt% H_2O content does not cause a change in chlorine solubility.

4.5 Conclusions

Chlorine XAF data was collected for 35 compositionally different silicate glasses. The XAF spectra vary systematically with increasing 2^+ cation concentrations in both the XANES and EXAF regions. The presence, or otherwise of a pre-edge feature, indicates that Cl must covalently bond with Si, contrary to the findings of (Stebbins and Du, 2002; Sandland et al., 2004; Evans et al., 2008). This finding also suggests that Cl will preferentially bond with Si rather than 1^+ cations, including Na and K, which are present in concentrations up to 5.77 and 6.12 wt%, respectively, in samples that experience a pre-edge. Structurally, this means that Cl must interact with a silicate chain instead of forming monovalent chlorides that act as network modifiers, which would first exist separate from the silicate chain before being dissolved as monovalent chlorides. With the addition of 2^+ cations to a silicate melt, Cl bonding transitions to increasingly ionic, predominantly forming bonds with Ca, Mg and Fe.

Within the EXAF region, there is a clear bonding change with the small addition of both Ca and Mg (Figure 4.8). However, this is not the case for Fe, which did not show a bonding change until more than 10 wt% FeO was added to melt. This may indicate that Fe is less efficient at

forming bonds with Cl than Ca and Mg, which were also present in the haplobasaltic composition used, and only becomes a dominant bond-forming cation when Fe concentrations exceed that of Ca and Mg, which is demonstrated by the increasing chloride capacity with FeO (Table 4.1). Coupled with the absence of a pre-edge in Fe-rich samples, would indicate that Cl bonds preferentially with Ca and Mg over Fe in the silicate melt.

Despite the errors involved in using the salt standards (see section 4.4.1), the 2^+ cation standards were found to be closest in E_0 and E_{Max} space with the experimental glasses (Figure 4.6), including Mn, which has been neglected from solubility models due to its limited variabilities in experimental glasses (e.g. Chapter the model developed in chapter 3, Webster and De Vivo, 2002; Webster et al., 2015). Mn has been shown to form a strong covalent bond with Cl (Rompel et al., 1997), and so the effect of Mn on chlorine solubility should be investigated further.

Further chlorine XAF data was collected for 9 haplobasaltic experiments, produced at a range of temperatures (1300-1400 °C), pressures (5-20 kbar), chlorine fugacity ($1.38E^{-03}$ to $1.66E^{-06}$), and water content (0- 7 wt% calculated by difference). No systematic variations were observed in either the XANES or EXAF regions across these experiments (Figure 4.9). This implies that Cl bonding is primarily controlled by the chemical composition of the silicate melt. Therefore, processes such as fractionation and assimilation, which are most likely to alter the contents of the 2^+ cations, are likely to be critical in determining the chlorine contents of silicate melts; this is also supported from the findings of (Evans et al., 2008).

4.6 Acknowledgements

RWT is grateful to the Natural Environmental Research Council and the Oxford Doctoral Training Partnership in Environmental Research for studentship and funding (NE/L002612/1). This project could not have been achieved without the help and support of our beamline scientist, Dr Konstantin Ignatyev. We would also like to thank Matthew Newville for his bountiful resources in how to use his LARCH software.

4.7 References

Abe H., Aquilanti G., Boada R., Bunker B., Glatzel P., Nachtegaal M. and Pascarelli S. (2018) Improving the quality of XAFS data. *J. Synchrotron Radiat.* **25**, 972–980.

Abramov A. V, V A. E. and Dianov E. M. (1989) Effect of halogen (chlorine, flourine) impurity on the formation of colour centers in pure silicate glasses. In *Proceedings of the XV internal congress on glass* (ed. O. V Mazurin). Leningrad. pp. 164–166.

Aiuppa A., Baker D. R. and Webster J. D. (2009) Halogens in volcanic systems. *Chem. Geol.* **263**, 1–18.

Baasner A., Schmidt B. C. and Webb S. L. (2013) The effect of chlorine, fluorine and water on the viscosity of aluminosilicate melts. *Chem. Geol.* **357**, 134–149.

Baasner A., Hung I., Kemp T. F., Dupree R., Schmidt B. C. and Webb S. L. (2014) Constraints on the incorporation mechanism of chlorine in peralkaline and peraluminous. *Am. Mineral.* **99**, 1713–1723.

Bell A. S. and Webster J. D. (2015) Dissolved Cl, oxygen fugacity, and their effects on Fe behavior in a hydrous rhyodacitic melt. *Am. Mineral.* **100**, 1595–1599.

Calvin S. (2013) *XAFS for everyone*. 1st ed., Taylor and Francis, Boca Raton, Florida.

Carroll M. R. and Webster J. D. (1994) Solubilities of sulfur, noble gases, nitrogen, chlorine, and fluorine in magmas. *Mineral. Soc. Am. Rev. Mineral.* **30**, 231 –279.

Chevychelov V. Y. and Suk N. I. (2003) Influence of the composition of magmatic melt on the solubility of metal chlorides at pressures of 0.1-3.0 kbar. *Petrology* **11**, 62–74.

Chmel A. and Svetlov V. N. (1996) Si-Cl groups in chlorine-impregnated silica. *J. Non. Cryst. Solids* **195**, 176–179.

Dalou C., Le Losq C., Mysen B. O. and Cody G. D. (2015) Solubility and solution mechanisms of chlorine and fluorine in aluminosilicate melts at high pressure and high temperature. *Am. Mineral.* **100**, 2272–2283.

Dianov E. M., Sokolov V. O. and Sulimov V. B. (1988) Interaction of atomic chlorine with bridging oxygen atoms in vitreous silicon dioxide. *Fiz. i Chim. stekla* **14**, 119–121.

Dingwell D. B. and Hess K. U. (1998) Melt viscosities in the system Na-Fe-Si-O-F-Cl: Contrasting effects of F and Cl in alkaline melts. *Am. Mineral.* **83**, 1016–1021.

Esro M., Kolosov O., Jones P. J., Milne W. I. and Adamopoulos G. (2017) Structural and electrical characterization of SiO2 gate dielectrics deposited from solutions at moderate temperatures in air. *ACS Appl. Mater. Interfaces* **9**, 529–536.

Evans K. A., Mavrogenes J. A., O'Neill H. S., Keller N. S. and Jang L. Y. (2008) A preliminary investigation of chlorine XANES in silicate glasses. *Geochemistry, Geophys. Geosystems*

9, 1–15.

Farcy B. J., Gross J., Carpenter P., Hicks J. and Filiberto J. (2016) Effect of chlorine on near-liquidus crystallization of olivine-phyric shergottite NWA 6234 at 1 GPa: Implication for volatile-induced melting of the Martian mantle. *Meteorit. Planet. Sci.* **51**, 1–12.

Filiberto J., Dasgupta R., Gross J. and Treiman A. H. (2014) Effect of chlorine on near-liquidus phase equilibria of an Fe–Mg-rich tholeiitic basalt. *Contrib. to Mineral. Petrol.* **168**, 1027.

Filiberto J. and Treiman A. H. (2009) The effect of chlorine on the liquidus of basalt: First results and implications for basalt genesis on Mars and Earth. *Chem. Geol.* **263**, 60–68.

Haskell D. (1999) *Computer program FLUO: Correcting XANES for self absorption in fluorescence data*.,

Hess K. U., Dingwell D. B., Potuzak M. and Courtial P. (2004) The effect of halogens (F, Cl, Br, I) on the viscosity-temperature behaviour of a silicate melt. In *Lithos* p. S50.

Hirosumi T. and Morita K. (2000) Solubility of chlorine in aluminosilicate slag systems. *ISIJ Int.* **40**, 943–948.

Iida A. and Noma T. (1993) Correction of the self-absorption effect in fluorescence x-ray absorption fine structure. *Jpn. J. Appl. Phys.* **32**, 2899–2902.

Iwasaki B. and Katsura T. (1967) The solubility of hydrogen chloride in volcanic rock melts at a total pressure of one atmosphere and at temperatures of 1200°C and 1290°C under anhydrous conditions. *Bull. Chem. Soc. Jpn.* **40**, 554–561.

Jain A., Ong S. P., Hautier G., Chen W., Richards W. D., Dacek S., Cholia S., Gunter D., Skinner D., Ceder G. and Persson K. A. (2013) The materials project: A materials genome

approach to accelerating materials innovation. *APL Mater.* **1**.

Kiprianov A. A. and Karpukhina N. G. (2006) Oxyhalide silicate glasses. *Glas. Phys. Chem.* **32**, 1–27.

Mason A. R., Thornber S. M., Stennett M. C., Gardner L. J., Lützenkirchen-Hecht D. and Hyatt N. C. (2019) Preliminary investigation of chlorine speciation in zirconolite glass-ceramics for plutonium residues by analysis of Cl K-edge XANES. *MRS Adv.* **5**, 37–43.

McKeown D. A., Gan H., Pegg I. L., Stolte W. C. and Demchenko I. N. (2011) X-ray absorption studies of chlorine valence and local environments in borosilicate waste glasses. *J. Nucl. Mater.* **408**, 236–245.

Newville M. (2013) Larch: An analysis package for XAFS and related spectroscopies. *J. Phys. Conf. Ser.* **430**, 1–7.

Presnall D. C., Dixon S. A., Dixon J. R., O'Donnell T. H., Brenner N. L., Schrock R. L. and Dycus D. W. (1978) Liquidus phase relations on the join Diopside-Forsterite-Anorthite from 1 atm to 20 kbar. Their bearing on the generation and crystallization of basaltic magma. *Contrib. to Mineral. Petrol.* **66**, 203–220.

Rompel A., Andrews J. C., Cinco R. M., Wemple M. W., Christou G., Law N. A., Pecoraro V. L., Sauer K., Yachandra V. K. and Klein M. P. (1997) Chlorine K-edge X-ray absorption spectroscopy as a probe of chlorine- manganese bonding: Model systems with relevance to the oxygen evolving complex in photosystem II. *J. Am. Chem. Soc.* **119**, 4465–4470.

Sandland T. O., Du L.-S., Stebbins J. F. and Webster J. D. (2004) Structure of Cl-containing silicate and aluminosilicate glasses: A 35 Cl MAS-NMR study. *Geochim. Cosmochim. Acta* **68**, 5059–5069.

Shadle S. E., Hedman B., Hodgson K. and Solomon E. I. (1994) Ligand K-Edge X-ray Absorption Spectroscopy as a Probe of Ligand-Metal Bonding: Charge Donation and Covalency in Copper-Chloride Systems. *Inorg. Chem.* **33**, 4235–4244.

Shannon R. D. (1976) Revised effective ionic radii and systematic studies of interatomie distances in halides and chaleogenides. *Acta Crystallogr.* **32**, 751–767.

Signorelli S. and Carroll M. R. (2000) Solubility and fluid-melt partitioning of Cl in hydrous phonolitic melts. *Geochim. Cosmochim. Acta* **64**, 2851–2862.

Bell A. S. and Simon A. (2011) Experimental evidence for the alteration of the Fe3+/ΣFe of silicate melt caused by the degassing of chlorine-bearing aqueous volatiles. *Geology* **39**, 499–502.

Stebbins J. F. and Du L.-S. (2002) Chloride ion sites in silicate and aluminosilicate glasses: A preliminary study by 35Cl solid-state NMR. *Am. Mineral.* **87**, 359–363.

Tan S. and Hand R. J. (2018) Incorporation and phase separation of Cl in alkaline earth aluminosilicate glasses. *J. Nucl. Mater.* **507**, 135–144.

Thomas R. W. and Wood B. J. (2021) The chemical behaviour of chlorine in silicate melts. *Geochim. Cosmochim. Acta* **294**, 28–42.

Thomas R. W. and Wood B. J. The effect of composition on chlorine solubility and behaviour in silicate melts. *Am. Mineral.*

Veksler I. V, Dorfman A. M., Dulski P., Kamenetsky V. S., Danyushevsky L. V, Jeffries T. and Dingwell D. B. (2012) Partitioning of elements between silicate melt and immiscible fluoride, chloride, carbonate, phosphate and sulfate melts, with implications to the origin

of natrocarbonatite. *Geochim. Cosmochim. Acta* **79**, 20–40.

Webb S. L., Murton B. J. and Wheeler A. J. (2014) Rheology and the Fe 3 +-chlorine reaction in basaltic melts. *Chem. Geol.* **366**, 24–31.

Webster J. D., Baker D. R. and Aiuppa A. (2018) Halogens in Mafic and Intermediate-Silica Content Magmas. In *The Role of Halogens in Terrestrial and Extraterrestrial Geochemical Processes* (eds. D. E. Harlov and L. Aranovich). Springer Geochemistry. pp. 307–430.

Webster J. D., Kinzler R. J. and Mathez E. A. (1999) Chloride and water solubility in basalt and andesite melts and implications for magmatic degassing. *Geochim. Cosmochim. Acta* **63**, 729–738.

Webster J. D., Vetere F., Botcharnikov R. E., Goldoff B., McBirney A. and Doherty A. L. (2015) Experimental and modeled chlorine solubilities in aluminosilicate melts at 1 to 7000 bars and 700 to 1250 °c: Applications to magmas of Augustine Volcano, Alaska. *Am. Mineral.* **100**, 522–535.

Webster J. D. and De Vivo B. (2002) Experimental and modeled solubilities of chlorine in aluminosilicate melts, consequences of magma evolution, and implications for exsolution of hydrous chloride melt at Mt. Somma-Vesuvius. *Am. Mineral.* **87**, 1046–1061.

Zimova M. and Webb S. (2006) The effect of chlorine on the viscosity of Na2O-Fe2O3-Al2O3-SiO2 melts. *Am. Mineral.* **91**, 344–352.

Chapter 5

Conclusions and future directions

5.1 Conclusions

Chapter 2 outlined a new methodology that provided a means of buffering both the chlorine and oxygen fugacity. The chlorine fugacity buffer was based on the equilibrium between Ag and AgCl:

$$2AgCl_{(liquid)} \leftrightarrow 2Ag_{(liquid)} + Cl_{2\,(gas)} \quad (5.1)$$

The addition of pure Ag metal and AgCl buffers the fugacity of chlorine at values given by the equilibrium constant for reaction (1). Silver is virtually insoluble in silicate melt, except under very oxidising conditions, and so the composition of a coexisting silicate melt can be varied almost at will at known chlorine fugacity. In practice, however, we added AgI to the AgCl to lower the chlorine fugacity and suppress the formation of immiscible chloride "blobs" (Figure 2.2b). The Ag(I,Cl) mixture forms a melt at high temperatures and becomes a "sliding buffer" or $f(Cl_2)$ sensor whose composition reacts to the change in Cl content of the melt. Oxygen fugacities were also controlled within the charge at the C-CO-CO_2 (CCO) buffer and the Re-ReO_2 buffer using the capsule assemblies of figure 2.1. This buffering methodology has the potential to be adapted and used to determine the solubility of a range of elements, including the remaining halogens (F, Br and I) and sulphur.

The chlorine buffer methodology was applied to a natural Icelandic basalt and a synthetic haplobasalt ($Anorthite_{50}$-$Diopside_{28}$-$Forsterite_{22}$) as a starting silicate composition. The results demonstrated that the Cl concentrations in silicate melts follow a linear dependence on $f(Cl_2)^{0.5}$ at 1.5GPa and 1400 °C (Figure 2.4) to concentrations beyond the values typically observed in nature (~0.8 wt%). The Henry's Law behaviour indicates that the initial dissolution mechanism for chlorine involves the replacement of O^{2-} in the silicate melt by two dissociated Cl^- ions according to the reaction:

$$Cl_2 + [O^{2-}]_{melt} = 2[Cl^-]_{melt} + 0.5O_2 \qquad (5.2)$$

The observed dependence of Cl content on $f(O_2)^{0.25}$ confirmed this hypothesis (Figure 2.5).

Reaction (5.2) was then used to correct the effects of pressure and temperature on chlorine and oxygen fugacity to determine the true effect of pressure and temperature on chlorine solubility. It was found that Cl concentrations increase with temperature and strongly decrease with pressure. From the pressure dependence, it was found that the difference in volume between $1Cl^-$ ion and $0.5O^{2-}$ in silicate melt agrees well with half the volume difference between crystalline $CaCl_2$ and CaO.

Our experimental measurements enabled us to calculate the fugacity of chlorine in basalt as a function of P, T $f(O_2)$ and Cl concentration. This was used to calculate the HCl contents of gases released from basaltic eruptions as a function of pressure (Figure 2.8), showing that chlorine was largely retained until pressures fell below 5 MPa.

Chapter 3 applied the experimental methodology developed in chapter two to explore chlorine solubility as a function of composition (Figure 3.3). 44 experiments covering a range of compositions from granite to Fe-rich basalt were investigated at 1.5 GPa and 1400 °C under anhydrous conditions and controlled fugacities of chlorine and oxygen. The results show that chlorine solubility increases with CaO and FeO content and decreases with SiO_2 content.

Knowing the compositional effects at fixed conditions allowed for the quantification of a chloride capacity (C_{Cl}) defined as follows:

$$C_{Cl} = \frac{Cl\,(wt\%)}{\sqrt{f(Cl_2)}} \times \sqrt[4]{f(O_2)} \qquad (5.3)$$

The chloride capacity allows for the comparison of various experimental data sets obtained at known temperatures, pressure, and $f(O_2)$. The results of this chapter were then combined with

the experiments of chapter 2 and regressed to derive an equation describing the composition, pressure, and temperature dependence of chloride capacity. This was further extrapolated to compare my own data with those present in the literature, covering more extensive P-T ranges and also water content, all regressed together, gave the equation:

$$logC_{Cl} = 0.571 + (4873X_{Ca} - 3803X_{Si} + 2724X_{Fe} + 1891\text{- }943\text{P})/\text{T} \quad (5.4)$$

Ca, Fe, Si and were found to be the most significant in controlling the chloride capacity. Water was found to be insignificant in controlling chlorine solubility at concentrations less than 4.3 wt%. Equation (5.4) was then used to determine the conditions that HCl would degas, expanding upon calculations performed in chapter 2. The results indicate that, at fixed Cl_2 fugacity, pressure, and temperature, most HCl loss occurs at pressures below 2 MPa. Additionally, the fraction lost as the surface is approached varies dramatically with composition as rhyolite>dacite>andesite>basalt (e.g., Fig 3.4).

To investigate the conditions in which brines may segregate from a melt, additional experiments were conducted to determine the conditions of NaCl saturation. These were then combined with literature data to generate an equation relating chlorine concentration in a melt to NaCl activity. Results indicate 1) that Cl concentration increases linearly with NaCl activity; and 2) at a given NaCl activity, Cl is approximately eight times more soluble in basalt than in rhyolite (Figure 3.6).

In **chapter 4**, the experiments of chapters 2 and 3 were analysed by X-ray absorption spectroscopy. The aim was to determine the bonding environment of chlorine in silicate melts across a range of compositions, temperatures, pressures, water content and chlorine fugacity.

Pre-edge features were observed in 2^+ cation poor, Si-rich compositions, such as granite. Upon addition of a 2^+ cation, the pre-edge features became suppressed and shifted to higher eV,

eventually forming a shoulder of the main absorbing edge. The presence of a pre-edge indicates a 1s→3d orbital transition and so could only be formed by a covalent bond of Cl with Si. This is contrary to previous studies (Evans et al., 2008; McKeown et al., 2011). With the addition of 2^+ cations, bonding shifts to increasingly ionic. In the XANES region, Cl was found to most likely bond with the 2^+ cations, Ca, Mg, Fe, and Mn. The last of these is currently underexamined in the literature and is neglected from chlorine solubility models (including in chapter 3) because of its low concentration in natural melts. Within the EXAF region, there is an apparent change of bonding with the small addition of both Ca and Mg (e.g., <5.11 wt% FeO; Figure 4.8). However, this is not the case for Fe, which did not show a bonding change until more than 10 wt% FeO was added to melt. Results suggest that Cl is most likely bonded to 2^+ cations, which might explain the findings of chapter 3, where basalts containing higher 2+ cation concentrations degas less Cl than 2^+ cation poor rhyolites at similar conditions.

Experiments using a constant haplobasaltic composition, performed at various temperatures (1300 – 1400 °C), pressures (5 – 20 kbar), chlorine fugacities ($1.38E^{-03}$ to $1.66E^{-06}$) and water contents (expected to be 0 – 8 wt%), display no systematic variations in either the XANES or EXAF regions across these experimental ranges (Figure 4.9). This indicates that these variables do not control chlorine bonding at the conditions tested.

5.2 Future directions

The methodologies developed as part of this thesis allows for the determination of the thermodynamic properties of chlorine in silicate melt. This is necessary to calculate the conditions of chlorine degassing and mineral formation. Further work would involve using this buffering method to help resolve additional unanswered questions.

5.2.1 Composition, temperature, and pressure effects on Cl solubility in silicate melts

In chapter 3, I utilised the experiments from the literature to determine the effect of water on chloride capacity. Additional experiments should be conducted using the chlorine buffering methodology outlined in chapter 2 to improve our understanding of the effects of water on chlorine behaviour. This can be achieved by using brucite to add water to a silicate melt, as described in chapter 4, but extended up to the point of saturation. Covering a compositional range including granitic, dacitic, basaltic and andesitic melts at 0.3-0.8 GPa and 800-1200 °C with known and buffered fugacities of Cl_2 and O_2. This will provide the thermodynamic properties under conditions appropriate to fluid separation in large-scale magmatic systems. The observed H_2O-dependence of Cl concentration at known $f(O_2)$ and $f(Cl_2)$ leads directly to the relative volatilities of Cl_2 in the anhydrous system and HCl in the hydrous system from the equilibria:

$$2[Cl^-]_{melt} + 0.5O_{2\ fluid} = Cl_{2\ fluid} + [O^{2-}]_{melt} \quad (5.5)$$

$$2[Cl^-]_{melt} + H_2O_{\ fluid} = 2HCl_{\ fluid} + [O^{2-}]_{melt} \quad (5.6)$$

These experiments, with the addition of the thermodynamic data for the formation of H_2O and HCl from the elements (Barin et al., 1989), will enable the calculation of the conditions of pressure and temperature of HCl release. The intention would be to use the Re/ReO_2 oxygen buffer since this, unlike the CCO buffer (Figure 1.1), does not rely on the presence and additional complexity of a mixed C-H-O fluid. The data will provide a direct link between melt chlorine activities and Cl partitioning between melts and fluids. This should enable us to

resolve any contradictions present in previous partitioning studies. To do this, experiments should focus on more silicic compositions that will allow for the connection of the results to experimental determinations under lower temperature-pressure conditions at the H_2O contents required.

In addition, as can be seen from the EPMA analyses in tables S1 and S2, totals for the silicate melt are consistently low, typically around 97-98%, with some as low as 96%. This is inferred to be due to the addition of CO_2 which has dissolved into the melt introduced by the $f(O_2)$ buffer (CCO) used throughout this thesis. Eguchi and Dasgupta (2018) developed a model based on a thermodynamic framework for CO_2 concentrations and speciation in natural silicate melts at graphite/diamond-saturated to fluid-saturated conditions. Using their model, it is calculated that CO_2 can be dissolved Icelandic basalt up to 1.3 wt%, and 2.4 wt% in the CMAS mixture at 1400°C and 15 Kbar. However, there is also potential for a small amount of water to be present. Both H_2O and CO_2 are thought to influence Cl solubility (Botcharnikov et al. 2007; Webster et al. 2018, and references therein). Therefore, further work should include measuring CO_2 and H_2O via Secondary Ion Mass Spectrometry (SIMS). The measured concentrations can then be used as additional variables within the regressions as performed in chapter 3, to assess the effects of CO_2 and H_2O on chlorine solubility.

5.2.2 Chlorine fugacities and the properties of fluids and brines

Performing experiments at controlled Cl_2 fugacity will enable the comparison of available data on the partitioning of Cl between silicate melts and fluids, including brines, in an internally consistent framework. There have been many partitioning studies at moderate pressures and temperatures, e.g. (Webster and Holloway, 1988; Webster, 1992; Signorelli and Carroll, 2000,

2002; Botcharnikov et al., 2004, 2007. 2015; Chevychelov et al., 2008; Webster et al., 2017) and the principal difficulty in generalising the results is the lack of an adequate description of Cl_2 fugacity (or activity) in either of the phases. Therefore, although there are many available data on Cl partitioning between melts and fluids with different contents of NaCl (and KCl, $CaCl_2$ etc.), the fact that Cl activity is unknown means that it is difficult to compare datasets except in an empirical fashion. There is no need to repeat any of these experiments. Instead, as outlined above, adding H_2O to granitic, dacitic, basaltic and andesitic melts up to the point of saturation at fixed oxygen fugacity (Re-ReO_2) and known Cl_2 fugacity will allow for these comparisons to be made. Additionally, because the outer Pt capsules of figure 2.1 are permeable to H_2 it may be required to change the outer capsule for hydrous experiments in order not to gain (under oxidising conditions) or lose (under reducing conditions) hydrogen. Relatively impermeable AuPd alloys make viable alternatives to Pt in the temperature range of interest (up to 1200 °C). It will then be known (in the P-T range of 0.3-0.8 GPa and 800-1200 °C) what exact Cl_2 fugacity is represented by each partitioning experiment, based on the measured Cl content of the hydrous melt. This means that all data can be corrected for the effects of different melt compositions and interactions in the fluids separated from those in the melts. Given recent thermodynamic expressions for component activities in fluids in the systems H_2O-NaCl-CO_2 (Dubacq et al., 2013; Ivanov and Bushmin, 2021) and H_2O-$CaCl_2$-CO_2 (Ivanov and Bushmin, 2019), my data on Cl activities in melts will allow for the calculation of Cl_2 activities in fluids, from compositions of coexisting melts. Measurements of Cl_2 activities leads directly, for example, given the H_2O-NaCl- CO_2 model and known $f(O_2)$ to the activity of Na_2O and the fugacity of HCl from the equilibria:

$$2Na_2O_{(melt)} + 2Cl_{2\,(fluid)} = 4NaCl_{(fluid)} + O_2 \qquad (5.7)$$

$$2H_2O_{(fluid)} + 2Cl_{2(fluid)} = 4HCl_{(fluid)} + O_2 \qquad (5.8)$$

5.2.3 Determining the NaCl activity of silicate melts by chlorine solubility

Brine separation from melts is an important process in the generation of many economically significant ore deposits (Cline and Bodnar, 1994; Bruce et al., 1999; Bortnikov, 2006; Gleeson and Turner, 2007; Wilkinson, 2013; Blundy et al., 2015; Nshimiyimana et al., 2015; Essarraj et al., 2016; Blundy et al., 2021). To determine the depths at which NaCl saturation occurs is fundamental to determine the conditions that brine separation occurs in specific environments. This was explored in chapter 3 but should be extended further to include lower temperatures (800-1200 °C) and pressures (0.3-0.8 GPa). As was shown in chapter 3, chlorine content should not depend on oxygen fugacity. So, all that is required to explore NaCl saturation are experiments performed at a range of compositions, temperatures, and pressures. The dataset will then allow us to determine the conditions that fluid separation occurred from the NaCl contents of the fluids. Additionally, performing NaCl saturated experiments at known chlorine fugacity will allow us to create a model to calculate the activity of NaCl in fluid by measuring the contents of the silicate melt by rearranging equation 3.21. As shown in section 3.6, this method accurately determined the Cl contents of melt inclusions measured from multiple localities and across range of compositions and conditions. However, a constraining the effects of T, P and composition will improve the accuracy.

To examine the change of activity of NaCl in the fluid as a function of T, P and composition, we can also reduce the activity of NaCl in our experiments by mixing NaCl with Ag+AgCl, which should, mix completely resulting in a homogenous Na-Ag-Cl phase. This would allow us to calculate the activities of Cl_2 and NaCl simultaneously and allow us to explore how the activity of NaCl varies as a function of both Na and Cl in the silicate melt.

5.2.4 Determining the fugacities of F, Br and I using the AgX/Ag buffer approach

This thesis has focused on understanding the chemical behaviour of chlorine. However, the thermodynamic properties of the other halogens (F, Br, and I) in silicate melts are yet to be addressed by the buffered activity approach outlined in chapter 2. However, there are an appreciable number of studies in which the partitioning of different halogens between melts and fluids and between crystals and melts has been determined. There is an increase in partitioning into melt from aqueous fluid and hence an implied increase in compatibility with decreasing ionic radius in the order F>Cl>Br>I (Bureau et al., 2000b; Bureau et al., 2016). As might be expected from the similar sizes of F^- and O^{2-} fluorine partitions more readily into mantle phases than does chlorine but is much less compatible in these phases than is oxygen (Dalou et al., 2012; Joachim et al., 2015).

Additionally, both HBr and HF are important ozone-reactive gases. Their relative volatilities in halogen and hydrogen-bearing melts are unknown, although empirical observation suggests that HBr is more volatile than HCl and HF is the least volatile (Bureau et al., 2000b; Aiuppa et al., 2009). In order to quantitatively establish the dissolution mechanisms of F and Br in silicate melts, experiments should be performed using Ag(I,F) and Ag(I,Br) together with Ag to buffer their fugacities, using the methodology developed in chapter 2. Presently, data on the Br and I solubility in magmas remain much more scarce than Cl and F, in part due to the analytical challenges posed by their low concentration levels, potentially due to their larger ionic radii relative to O and hydroxyl (Bureau et al., 2000b; Dolejš and Zajacz, 2018). Therefore, conducting a range of halogen buffered experiments can shed much-needed light on their physiochemical properties and phase equilibria.

I expect that concentrations of F, Cl, Br will decrease respectively within the silicate melt due to the increase in ionic radius (Bureau et al., 2000b), where the radii of halide anions decrease from 2.20 (I-) to 1.33 Å (F-), the latter being very close to O and hydroxyl radii (1.40 and 1.37 Å, respectively; Shannon, 1976). Therefore, F will readily substitute for O on the vertices of aluminate or silicate tetrahedra, which promotes its solubility in the melt. In contrast, incorporation of I will be restricted to interstitial or network-modifier sites, limiting their solubility in the melt (Dolejš and Zajacz, 2018). However, general observations of the differences in viscosity caused by the addition of F to silicate melts (Dingwell and Scarfe, 1985) as opposed to those induced by the addition of Cl (Dingwell and Hess, 1998; Hess et al., 2004) indicate that the substitution mechanism is different for F from that which I have determined for Cl (chapter 2).

In preliminary experiments, I have found that AgBr/Ag mixtures buffer the Br contents of melts at measurable levels (up to 1.6 weight% Br); and that F is, as expected, highly soluble in silicate melts at F_2 fugacities several orders of magnitude below those employed in the study of chlorine dissolution under anhydrous conditions.

Once we understand the chemical behaviour of each of the halogens, we can then explore the relative effects halogens have on the solubility of one another at known activities. Currently, it is thought that Cl solubility increases with increasing F contents in silicate melts (Webster and Holloway, 1988). Currently, too few data on Br and I solubility is present in literature to postulate how they may influence each other.

5.3 References

Aiuppa A., Baker D. R. and Webster J. D. (2009) Halogens in volcanic systems. *Chem. Geol.*

263, 1–18.

Barin I., Sauert F., Schultze-Rhonhof E. and Sheng W. S. (1989) *Thermochemical data of pure substances: Part II*., Weinheim, New York, Basel, Cambridge.

Blundy J., Afanasyev A., Tattitch B., Sparks S., Melnik O., Utkin I. and Rust A. (2021) The economic potential of metalliferous sub-volcanic brines. *R. Soc. Open Sci.* **8**.

Blundy J., Mavrogenes J., Tattitch B., Sparks S. and Gilmer A. (2015) Generation of porphyry copper deposits by gas-brine reaction in volcanic arcs. *Nat. Geosci.* **8**, 235–240.

Bortnikov N. S. (2006) Geochemistry and origin of the ore-forming fluids in hydrothermal-magmatic systems in tectonically active zones. *Geol. Ore Depos.* **48**, 3–28.

Botcharnikov R. E., Behrens H., Holtz F., Koepke J. and Sato H. (2004) Sulfur and chlorine solubility in Mt. Unzen rhyodacitic melt at 850 °C and 200 MPa. *Chem. Geol.* **213**, 207–225.

Botcharnikov R. E., Holtz F. and Beherens H. (2007) The effect of CO2 on the solubility of H2O-Cl fluids in andesitic melt. *Eur. J. Mineral.* **19**, 671–680.

Botcharnikov R. E., Holtz F. and Behrens H. (2015) Solubility and fluid–melt partitioning of H2O and Cl in andesitic magmas as a function of pressure between 50 and 500 MPa. *Chem. Geol.* **418**, 117–131.

Brown G. C. and Fyfe W. S. (1970) The production of granitic melts during ultrametamorphism. *Contrib. to Mineral. Petrol.* **28**, 310–318.

Bruce S., Yardley B. W. D., Banks D., Boyce A. J., Munoz M., Courjault-Rade P. and Tollon F. (1999) The genesis of mineralising brines in the South West Massif Central, France. *Miner. Depos. Process. to Process. Vols 1 2* **62A**, 29–32.

Bureau H., Auzende A.-L., Marocchi M., Raepsaet C., Munsch P., Testemale D., Mézouar M., Kubsky S., Carrière M., Ricolleau A. and Fiquet G. (2016) Modern and past volcanic degassing of iodine. *Geochim. Cosmochim. Acta* **173**, 114–125.

Bureau H., Keppler H. and Métrich N. (2000) Volcanic degassing of bromine and iodine: Experimental fluid/melt partitioning data and applications to stratospheric chemistry. *Earth Planet. Sci. Lett.* **183**, 51–60.

Chevychelov V. Y., Botcharnikov R. E. and Holtz F. (2008) Experimental Study of Fluorine and Chlorine Contents in Mica (Biotite) and Their Partitioning between Mica, Phonolite Melt, and Fluid. *Geochemistry Int.* **46**, 1081–1089.

Cline J. S. and Bodnar R. J. (1994) Direct evolution of brine from a crystallising silicic melt at the Questa, New Mexico, Molybdenum deposit. *Econ. Geol.* **89**, 1780–1802.

Dalou C., Koga K. T., Nobumichi S., Boulon J. and Devidal J.-L. (2012) Experimental determination of F and Cl partitioning between lherzolite and basaltic melt. *Contrib. to Mineral. Petrol.* **163**, 591–609.

Dingwell D. B. and Hess K. U. (1998) Melt viscosities in the system Na-Fe-Si-O-F-Cl: Contrasting effects of F and Cl in alkaline melts. *Am. Mineral.* **83**, 1016–1021.

Dingwell D. B. and Scarfe C. M. (1985) Chemical diffusion of fluorine in melts in the system Na2O-Al2O3-SiO2. *Earth Planet. Sci. Lett.* **73**, 377–384.

Dolejš D. and Zajacz Z. (2018) Chapter 7 Halogens in Silicic Magmas and Their Hydrothermal Systems. In *The Role of Halogens in Terrestrial and Extraterrestrial Geochemical Processes* pp. 431–543.

Dubacq B., Bickle M. J. and Evans K. A. (2013) An activity model for phase equilibria in the H2O-CO2-NaCl system. *Geochim. Cosmochim. Acta* **110**, 229–252.

Eguchi J. and Dasgupta R. (2018) A CO2 solubility model for silicate melts from fluid saturation to graphite or diamond saturation. *Chem. Geol.* **487**, 23–38.

Essarraj S., Boiron M.-C., Cathelineau M., Tarantola A., Leisen M., Boulvais P. and Maacha L. (2016) Basinal brines at the origin of the Imiter Ag-Hg deposit (Anti-Atlas, Morocco):

Evidence from LA-ICP-MS data on fluid inclusions, halogen signatures, and stable isotopes (H, C, O). *Econ. Geol.* **111**, 1753–1781.

Evans K. A., Mavrogenes J. A., O'Neill H. S., Keller N. S. and Jang L. Y. (2008) A preliminary investigation of chlorine XANES in silicate glasses. *Geochemistry, Geophys. Geosystems* **9**, 1–15.

Filiberto J. and Treiman A. H. (2009) The effect of chlorine on the liquidus of basalt: First results and implications for basalt genesis on Mars and Earth. *Chem. Geol.* **263**, 60–68.

Gleeson S. A. and Turner W. A. (2007) Fluid inclusion constraints on the origin of the brines responsible for Pb-Zn mineralisation at Pine Point and coarse non-saddle and saddle dolomite formation in southern Northwest Territories. *Geofluids* **7**, 51–68.

Hess K. U., Dingwell D. B., Potuzak M. and Courtial P. (2004) The effect of halogens (F, Cl, Br, I) on the viscosity-temperature behaviour of a silicate melt. In *Lithos* p. S50.

Ivanov M. V. and Bushmin S. A. (2019) Equation of state of the H2O–CO2–CaCl2 fluid system and properties of fluid phases at P-T parameters of the middle and lower crust. *Petrology* **27**, 395–406.

Ivanov M. V and Bushmin S. A. (2021) Thermodynamic model of the fluid system H2O–CO2–NaCl at P-T parameters of the middle and lower crust. *Petrology* **29**, 77–88.

Joachim B., Pawley A., Lyon I. C., Marquardt K., Henkel T., Clay P. L., Ruzié L., Burgess R. and Ballentine C. J. (2015) Experimental partitioning of F and Cl between olivine, orthopyroxene and silicate melt at Earth's mantle conditions. *Chem. Geol.* **416**, 65–78.

Makhluf A. R., Newton R. C. and Manning C. E. (2017) Experimental determination of liquidus -H2O contents of haplogranite at deep-crustal conditions. *Contrib. to Mineral. Petrol.* **172**, 1–18.

McKeown D. A., Gan H., Pegg I. L., Stolte W. C. and Demchenko I. N. (2011) X-ray absorption studies of chlorine valence and local environments in borosilicate waste

glasses. *J. Nucl. Mater.* **408**, 236–245.

Nshimiyimana F., Essarraj S. and Mohamed H. (2015) Brines at the Origin of the Silver Mineralization at the Koudia El Hamra Deposit, Central Jebilet, Morocco. In *Brines at the origin of the silver mineralisation at the Koudia El Hamra deposit, Central Jebilet, Morocco* pp. 1–5.

Shannon R. D. (1976) Revised effective ionic radii and systematic studies of interatomie distances in halides and chaleogenides. *Acta Crystallogr.* **32**, 751–767.

Signorelli S. and Carroll M. R. (2002) Experimental study of Cl solubility in hydrous alkaline melts: constraints on the theoretical maximum amount of Cl in trachytic and phonolitic melts. *Contrib. to Miner. Petrol.* **143**, 209–218.

Signorelli S. and Carroll M. R. (2000) Solubility and fluid-melt partitioning of Cl in hydrous phonolitic melts. *Geochim. Cosmochim. Acta* **64**, 2851–2862.

Webster J. D. (1992) Fluid-melt interactions involving Cl-rich granites: Experimental study from 2 to 8 kbar. *Geochim. Cosmochim. Acta* **56**, 659–678.

Webster J. D., Goldoff B. A., Flesch R. N., Nadeau P. A. and Silbert Z. W. (2017) Hydroxyl, Cl, and F partitioning between high-silica rhyolitic melts-apatite-fluid(s) at 50–200 MPa and 700–1000 °C. *Am. Mineral.* **102**, 61–74.

Webster J. D. and Holloway J. R. (1988) Experimental constraints on the partitioning of Cl between topaz rhyolite melt and H20 and H20 + CO2 fluids: New implications for granitic differentiation and ore deposition. *Geochim. Cosmochim. Acta* **51**, 2091–2105.

Webster J. D. and Rebbert C. R. (1998) Experimental investigation of H2O and Cl- solubilities in F-enriched silicate liquids; implications for volatile saturation of topaz rhyolite magmas. *Contrib. to Mineral. Petrol.* **132**, 198–207.

Webster J., Thomas R., Förster H. J., Seltmann R. and Tappen C. (2004) Geochemical evolution of halogen-enriched granite magmas and mineralizing fluids of the Zinnwald

tin-tungsten mining district, Erzgebirge, Germany. *Miner. Depos.* **39**, 452–472.

Wilkinson J. J. (2013) Triggers for the formation of porphyry ore deposits in magmatic arcs. *Nat. Geosci.* **6**, 917–925.

Appendix A

A.1 Piston cylinder apparatus

All experiments performed and discussed within this thesis were performed using a ½" *'Boyd and England'* type piston-cylinder apparatus (Boyd and England, 1960), modified by Bernard Wood, and John Holloway, and is now known as a *'Bristol (or Clifton)-style'* press (Figure A.1).

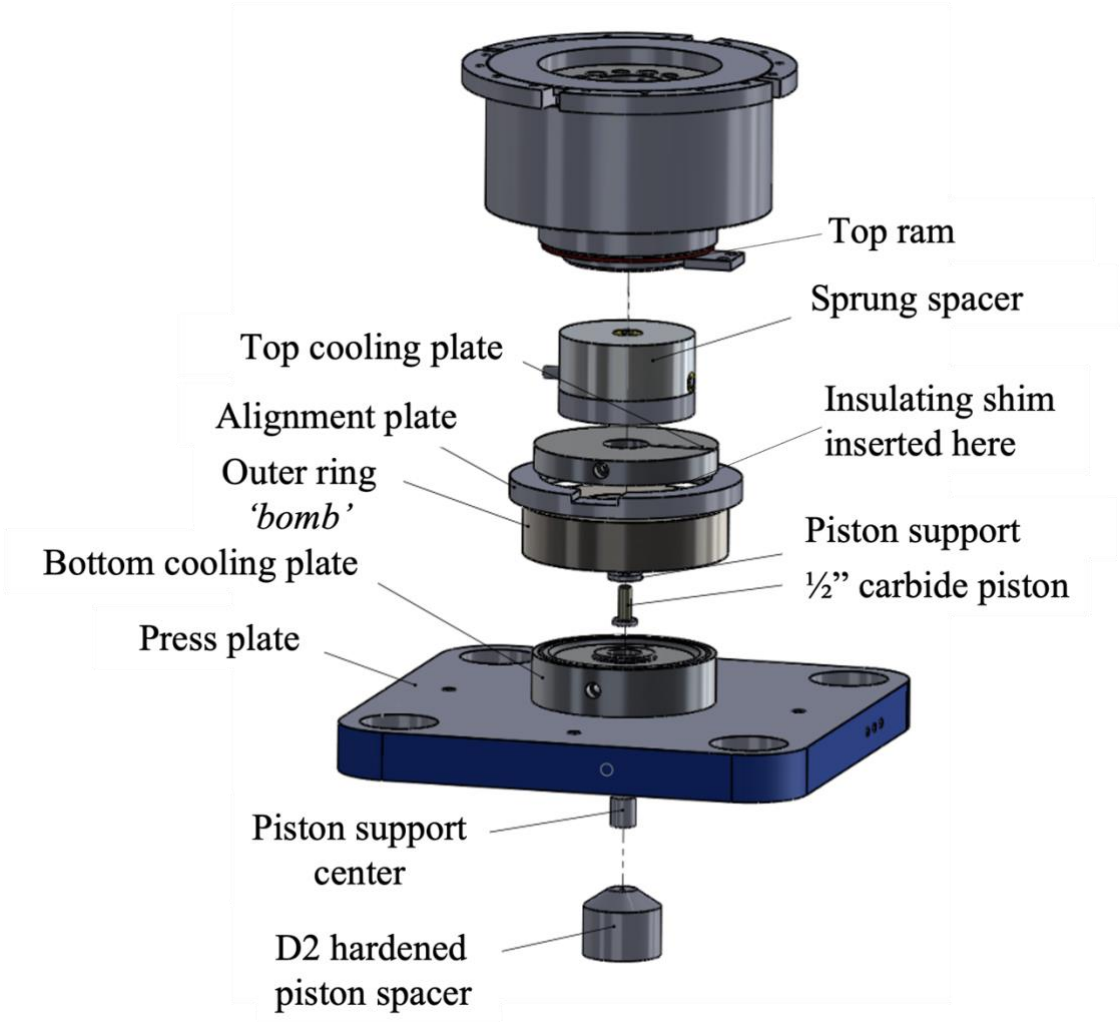


Figure A.1 Exploded schematic section of the *'Bristol-type'* piston cylinder used throughout this thesis. CAD image is courtesy of Jamie Long, University of Oxford.

A.2 Choice of capsule material

Inner capsules

Graphite capsules have been widely used in high-pressure, high-temperature experiments to prevent iron loss from iron-bearing samples. However, a key problem found during my experimental runs was the alloying of Pt from the outer capsule with the pure Ag metal from the chlorine buffer. This had two negative effects on the experiment: 1) Pt-Ag alloying increases the chlorine fugacity and 2) Fe was found to complex with the Pt that was hosted within the Ag metal, thus reducing the iron within the silicate melt, distorting the silicate composition. In some instances, there was a clear dyke of metal from the outer capsule, through the graphite capsule and into the silicate melt. In an attempt to limit this, experiments were performed using different graphite specifications for the capsule. A softer graphite capsule was trialled with the hope that it would be more ductile and less likely to fracture. However, the soft graphite was also very porous, and showed Pt and some silicate blobs within pore spaces. Instead, we resorted to using the harder, less porous graphite, but placing it at approximately 1/3 of the experiments total pressure for approximately an hour before any temperature was applied. This limited the formation of metal dykes and seems to produce a consistent amount of Pt in the resultant Ag metal phase.

Outer capsules

All capsule assemblies detailed in this thesis employed a noble metal outer capsule to ensure that no halogen loss occurred through volatilisation during the experiment (Figure A.2). Initially, trials were conducted using gold-palladium (AuPd) capsules, which has been widely used for retaining volatiles such as halogens (e.g Dalou et al., 2014), and also for imposing an

oxygen fugacity with mineral buffers (e.g Matjuschkin et al., 2015). However, it was found that in experiments using graphite inner capsules, and AuPd outer capsules, that Au readily alloyed with the Ag utilised in the *f*(Cl_2) buffer (≈36% Au in the Ag metal), raising the chlorine fugacity sufficiently enough that alkaline earth exsolution occurred even at low chorine fugacities, where the buffer was diluted by the addition of AgI (see Section 1.6). Any alloying with the Ag metal from the chlorine buffer reduces the concentration of available Ag in the system and thus reduces its activity, in turn increasing the *f*(Cl_2). This can be shown, from the reaction :

$$2AgCl_{(liquid)} \leftrightarrow 2Ag_{(liquid)} + Cl_{2\,(gas)} \qquad \text{(A.1)}$$

Where the equilibrium constant, and fugacity can be represented as:

$$K = \frac{a^2 AgCl}{a^2 Ag + f(Cl_2)} \quad and \quad f(Cl_2) = \frac{a^2 AgCl}{a^2 Ag\, K} \qquad \text{(A.2)}$$

Instead, Pt capsules were employed. Despite some Ag-Pt alloying (≈80:20), no exsolution of alkaline earth metals were observed, and so it was assumed that Pt did not raise the fugacity enough to cause exsolution. Therefore, Pt used for all experiments employed in this thesis. Pt capsules were first annealed at 1300°C, and then crimped into three-points with pliers (although the *"milk carton"* design (Sneeringer and Watson, 1985) was also successfully used) plasma welded across the seams, and then flattened in a hand press. Capsules were weighed before and after the experimental run to ensure no Cl had been lost, or any components introduced into the experiment as a result of any holes within the Pt.

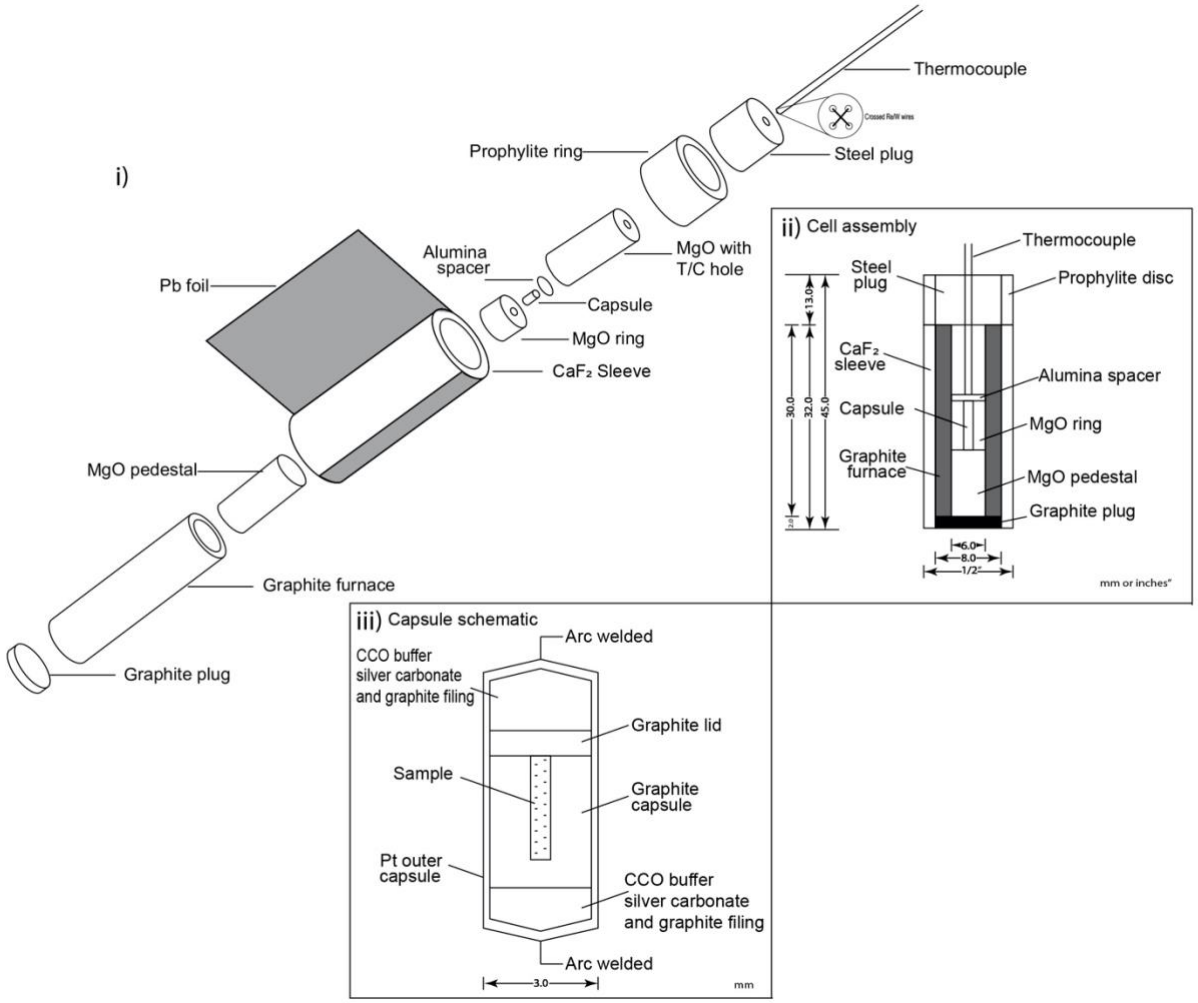


Figure A.2: i) Schematic of the experimental assembly used in piston-cylinder experiments. ii) a cross section of a cell assembly with the outer diameters and lengths of each component labelled. iii) a cross section of a capsule used for the majority of experiments.

A.3 Pressure calibration

In principle, the piston-cylinder apparatus (Figure A.1) is applicable for phase equilibrium measurements over a wide range of pressures and temperatures, typically from 0.8 to 4 GPa and 600 to 2000ºC (McDade et al., 2002). However, to perform experiments at different pressures requires the use of different cell assemblies, optimised in terms of the mechanical and thermal properties for some parts of the experimental range. To examine chlorine solubility

as a function of pressure (Chapter 2), I first needed to calibrate the piston-cylinder to ensure that all experiments were conducted at reliable and accurate pressures. To calibrate the piston cylinder, I started by calculating the amplification factor (AF), from the ratio of the areas of the top ram and the piston (Figure A.1), this could then be used to calculate an effective pressure on the sample (in GPa) at a given hydraulic pressure, measured in psi. The nominal hydraulic pressure in the piston-cylinder press is controlled by an oil medium and measured using an EN 839-1 precision manometer (produced by SM Gauge Co, UK), with measurement subdivisions marked at 20 psi (≈ 0.14 MPa) intervals, allowing for reliable precision to approximately 10 psi (Vlach et al., 2019). To test the accuracy of the effective pressure on the capsule, I followed the methodology outlined by Vlach et al., (2019). This involved filling a Pt capsule, with reagent-grade NaCl, the liquidus of which is known, and calculable at a given pressure using the calculations of (Bohlen, 1984). A small Pt bead (0.2-0.4 mm) was then added to the top of the salt within the capsule, which was subsequently dried at 110°C before being welded shut. The idea follows that if the salt melts during the experiment, then the Pt bead will fall to the bottom of the capsule. In practice, I found putting a Pt bead at the top and bottom of the capsule was the best way to prevent the human error of inserting the capsule into the assembly upside down, or by confusing its orientation when removing the capsule from the assembly post experiment. Therefore, the NaCl was determined to have melted if the two Pt beads were together at the end of the experiment. Several repeat experiments were performed at a given pressure, at different temperature intervals to determine the liquidus temperature of the NaCl. Any difference in temperature from that calculated from Bohlen, (1984) to that of the experimental temperature, is assumed to be an error in pressure.

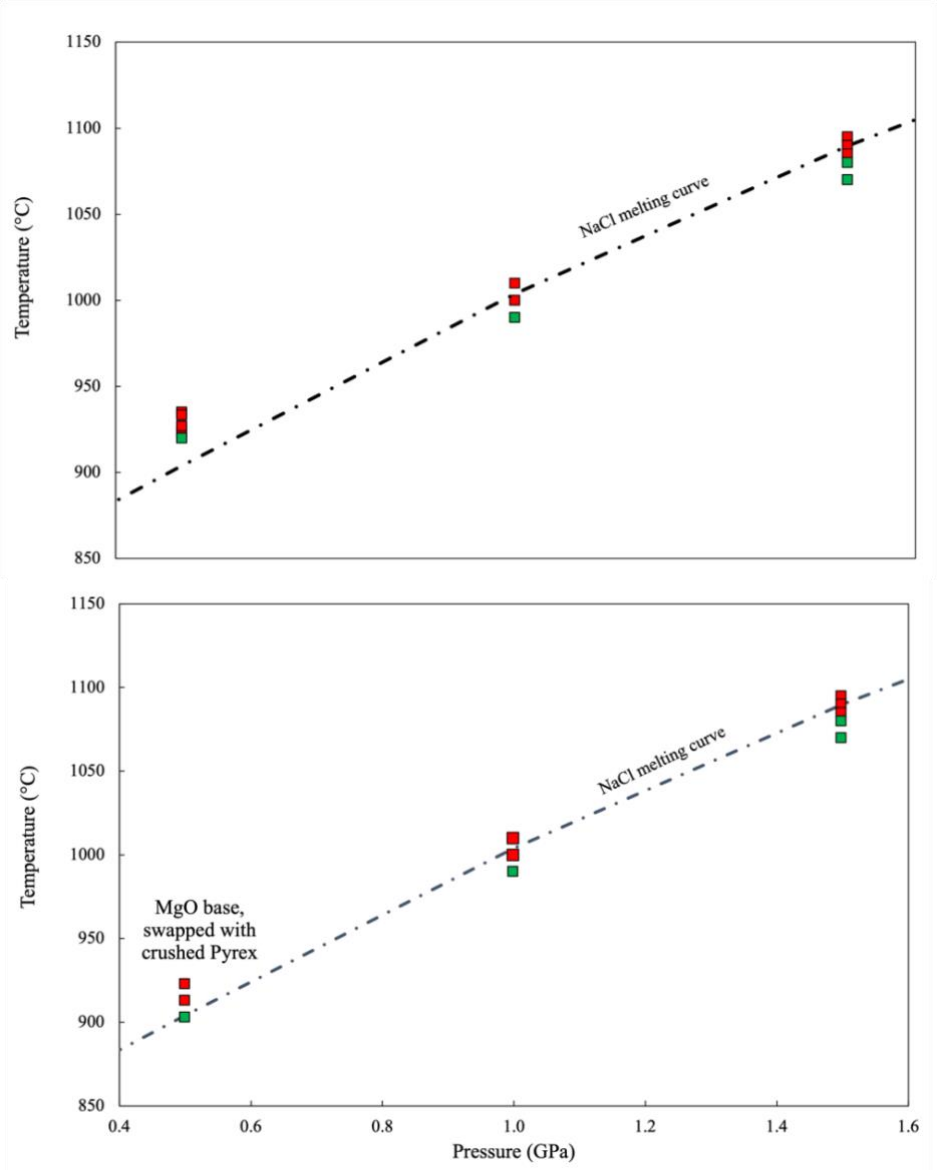


Figure A.3 Pressure calibrations, NaCl melting curve is defined by Bohlen, (1984), Red symbols represent experiments that resulted in molten NaCl (Pt beads together), and the green represent experiments in which NaCl was still solid. A) Experiments were performed using MgO pieces above and below the capsule, whereas in B) the MgO pedestals (Figure A.2) were replaced by crushed pyrex for experiments performed at 0.5 GPa.

All experiments in this pressure calibration series were conducted using CaF_2 pressure mediums, and using the assembly illustrated in Figure A.2. Experiments performed ≥1 GPa are close to the predicted melting curve and require only minimal corrections. However, as can be seen in Figure A.3A, the experiments performed at 0.5 GPa show that salt was still solid at temperatures much higher than that predicted by Bohlen, (1984). This indicates a positive *'anvil-effect'* has occurred, magnifying the pressure on the sample by reducing the piston area, and thus increasing the true pressure. This arises if the column of material which encloses the sample is more rigid and less compressible than its surroundings (Johannes et al., 1971). In this instance it appeared be most likely to result from the crushable MgO pieces used above and below the capsule (Figure A.2). To resolve this issue, I replaced the MgO pedestal (Figure A.2) with crushed pyrex following the methodology of Vlach et al., (2019), and repeated the experiments at 0.5 GPa. The results show that this resolved the issue and matched the predicted NaCl melting curve (Figure A.3B), and so this assembly could be used with minimal corrections required.

During the pressure calibration series, experimental durations were short, ≤25 minutes, but long enough to determine if the NaCl had melted (or not). When conducting the experiments outlined in chapter 2, however, experimental durations were ≥1 hour. It was discovered that experiments performed at low pressure (<1 GPa), and high temperature (1400°C) resulted in the oxidation of the thermocouple, which, subsequently increased the operating power throughout the run, and in some cases, even break the thermocouple. To prevent this, the steel plugs (Figure A.2) were replaced with softer brass plugs, which deform more easily than steel, and compress around the thermocouple sheath tighter, limiting air ingress. In addition, a stream of argon gas was passed over the thermocouple, where they exit the alignment plate (Figure A.1) to further eliminate the potential for oxidation of the thermocouple.

A.4 Improving the quench rate of an experiment

All experimental runs presented in this thesis were quenched by turning the power off to the heating element, without adjusting the end-load or piston load pressures. This allows the charge to be cooled rapidly by chilled water that circulates through the top and bottom cooling plates (Figure A.1). All quench rates were measured on a hand operated stopwatch, measuring the time between turning the power off, and the temperature, as measured by the Eurotherm, dropping below 500°C. The quench rates of each experiment performed were consistent, with minimal variation from experiments performed at the same conditions (<0.5 seconds, well within any error produced by delayed reactions). To increase the quench rate and reduce the potential of quench textures developing in silicate glass, several methods were trialled. I began by releasing the sample pressure by '*dropping the pin'* immediately after turning off the power – this reduces the pressure quickly, and provides a quench rate of >150°C. However, this damages the piston and is difficult to precisely reproduce each time. I found instead, that punching holes in the insulative mylar shim (Figure A.1) allowed water to circulate between the bomb and the cooling plates more efficiently, whilst leaving the insulation where it is required. This method did inflict any damage to the apparatus, and provided quicker, consistent quench rates. This method was then employed for all experiments.

A.5 Further details for calculating chlorine fugacity ($f(Cl_2)$)

The fugacity of Cl_2 in the Ag + AgCl buffer is defined by the equilibrium reaction:

$$2AgCl_{(liquid)} \leftrightarrow 2Ag_{(liquid)} + Cl_{2\,(gas)} \qquad \text{(A.1)}$$

The log of the equilibrium constant (K') for this reaction is obtained from thermodynamic data of Barin et al., (1989). At temperatures explored in this study (1573 and 1673 K), both Ag and AgCl are in the liquid state at 1 bar so we use liquid as the reference state. Barin et al., (1989) give:

logK' = 4.32 at 1573K and, logK' = 3.88 at 1673K

Extrapolating from Barin et al., (1989) over 1000-1800 K and 1 bar, we get:

LogK' = 11440/T - 2.961 (A.3)

Displayed graphically in figure A.4:

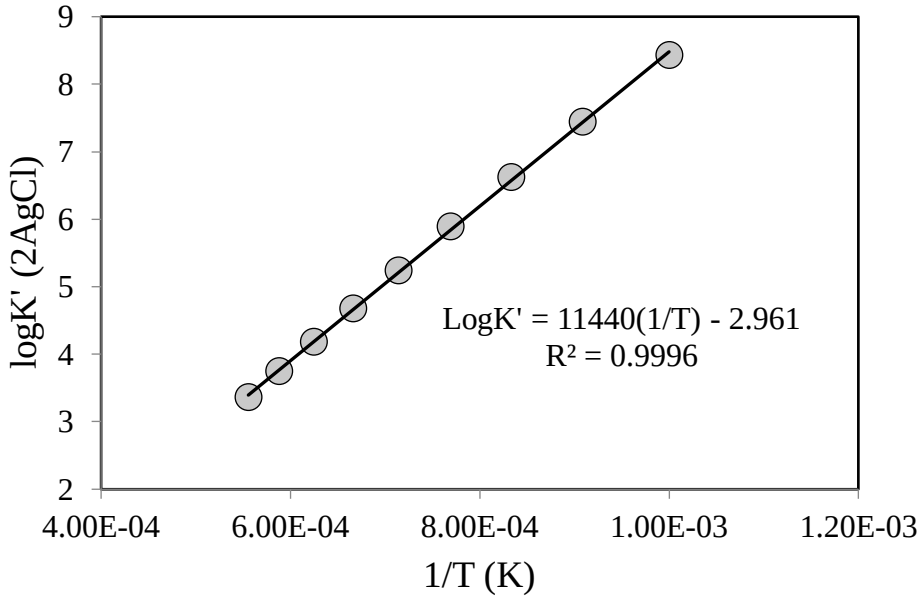


Figure A.4 The equilibrium constant (Log K') of 2AgCl as a function of temperature (K) at 1 bar.

The negative of the log of the equilibrium constant (K'), provides the log of the chlorine fugacity ($\log f(Cl_2)$) at equilibrium with liquid Ag and AgCl at 1 bar:

Log$f(Cl_2)$= -11440/T + 2.961 (A.4)

However, several corrections need to be made for experiments performed at varying temperatures (1473-1673K) and pressures (5-20 Kbar). Firstly, to resolve the effect of pressure, normally we could use volumes at 1 bar and integrate up pressure assuming constant volume. However, AgCl has high coefficient of thermal expansion and high compressibility which needs to be considered. Unfortunately, densities of AgCl liquid in the literature are not well known beyond 1123K so we choose to integrate at this temperature. To a good approximation we can express volume (V) as a function of pressure (P) by:

$V_{PT} = V_{1T}(1 - bP)$ (A.5)

where *b* is the compressibility, of 0.101per GPa at 801 K (Marcus, 2013) and V is the volume. Taking account of the temperature dependence of the adiabatic compressibility from Takeda et al., (2007) means an isothermal compressibility of about 0.13/GPa at 1123 K. The V of AgCl liquid at 1123K is 31.95 cm^3 or 3.195 J/GPa. Integrating VdP between 0 and P at constant temperature gives the free energy change of AgCl liquid between atmospheric pressure and P. From (A.5) above:

$\int VdP = V(P-0.5bP^2)$ (A.6)

At 1.5 GPa and 1123K, $V(P-0.5bP^2)$ is 43252 J for 1 mole of AgCl. At 1GPa the integral is 29873 J. For Ag liquid, the volume at the 1 atm melting point of 1233K is 11.49 cm^3. Taking thermal expansion, volume and compressibility from Tsu et al., (1982) provides a volume of 11.37 cm^3, and *b* of 0.0146/GPa at 1123K by metastable extrapolation. Equation (A.6) provides

the free energy change of pure Ag liquid between atmospheric pressure and P. Once both states are calculated, we can define the free energy difference between 1 bar and 1 GPa of reaction (A.1) can be calculated by:

$$\int_{1\ Gpa}^{atm} VdP_{buffer} = 2\int_{1Gpa}^{atm} VdP_{AgCl} - 2\int_{1Gpa}^{atm} VdP_{Ag} \qquad (A.7)$$

So, to calculate the chlorine fugacity in the experiments we simply divide these numbers by 2.303*R*T and add them to the 1 bar values calculated above. In practice however, the AgCl is mixed with AgI or AgBr in the buffer and Ag also complexes with Pt from the outer capsule. Therefore, we assume ideal mixing and calculate X_{Cl} = Cl/(Cl+I) and X_{Ag} = Ag/(Ag+Pt) on a molar basis. Then for mixed Ag-Pt and AgI-AgCl we have:

$$logf(Cl_2) = logf\left(Cl_2^{Pure\ AgCl}\right) + logf(X_{Cl}) - 2logf\left(X_{Ag}\right) \qquad (A.8)$$

A.6 Reducing *f*(Cl_2)

A key aspect of this research was to determine how chlorine solubility varied as a function of chlorine fugacity. This was achieved by adding various ratios of iodine into the buffer in the form of AgI. Thus, reducing the overall concentration and fugacity of the silver chlorides. The effect of varying the concentration of Cl can be shown by the following reaction the reaction of A.1, and investigating the equilibrium constant of the reaction:

$$K = \frac{a^2 AgCl}{a^2\ Ag + f(Cl_2)} \qquad (A.9)$$

Where K is the equilibrium constant, *a* is the activity of phase *i*, and *f* is the fugacity,

Which can be written as:

$$f(Cl_2) = \frac{a^2 AgCl}{a^2\ Ag\ K} \qquad (A.10)$$

If the Ag metal remains pure, then $aAg = 1$, and so (A.10) becomes:

$$f(Cl_2) = \frac{a^2 AgCl}{K} \qquad \text{(A.11)}$$

If the AgCl also remains pure, then $aAgCl = 1$ and thus:

$$f(Cl_2) = \frac{1}{K} \quad \text{(A.12)}$$

Now, given an assumption that $aAgCl = XAgCl$, then we can see that reducing the concentration of Cl (the numerator of equation A.11) by the addition of AgI, will reduce the fugacity of Cl appropriately. In our experiments we only had the interaction of Ag and Pt from the outer capsule material. No iodine was measured within the metal blobs, under the conditions tested, all I remained as a AgI salt, with the exception of <0.1 wt% I which was frequently measured in the silicate melt.

A.7 Mass balancing for low *f*(Cl_2) – Keeping enough glass to analyse

To attain increasingly lower chlorine fugacities, smaller quantities of AgCl are mixed into the buffer with AgI. To produce a buffered system, excess metal chloride is required in the experimental charge, and therefore, the ratio of buffer to silicate melt must also be increased. To fulfil this, experiments utilising 90% buffer to 10% silicate melt were employed. This however resulted in several problems: 1) only small silicate glass blobs were formed, making micro-analysis increasingly difficult, which resulted in smaller spot sizes, and fewer points being analysed during microprobe analysis; 2) The measurable results of low glass fraction experiments were un-reliable, with disappointingly low totals ≈95 wt%. These low totals are perceived to depict any CO_2 or water in the nominally dry experiments being isolated within the small glass blobs that result, thus impairing results. 3) For the lowest fugacity experiments, the silicate glass was either not found upon polishing, or insufficient for statistically reliable microprobe analysis. To overcome this problem, a simple mass balance was computed to attain

lower fugacities, whilst retaining enough glass for analysis. This was achieved by the following:

$$C_{Cl}^{M} X^{M} + C_{Cl}^{B} X^{B} = C_{Cl}^{Bulk} \qquad \text{(A.13)}$$

$$C_{I}^{M} X^{M} + C_{I}^{B} X^{B} = C_{I}^{Bulk} \qquad \text{(A.14)}$$

Where X^{i} is the fraction of the buffer (B) or melt (M) in percent, and C_{i}^{j} is the concentration of component *i* (Cl = Chlorine, I = Iodine), in phase *j*. The interaction of chlorine between the buffer and the melt will vary as a function of its partition coefficient, D_{Cl}:

$$D_{Cl} = \frac{C_{Cl}^{B}}{C_{Cl}^{M}} : C_{Cl}^{M} D_{Cl} = C_{Cl}^{B} : C_{Cl}^{M} = \frac{C_{Cl}^{B}}{DCl} \qquad \text{(A.15)}$$

If, $X^{M} + X^{B} = 1$ (the *bulk* composition), then, $1 - X^{M} = X^{B}$, therefore:

$$C_{Cl}^{B} X^{M} + C_{Cl}^{B} X^{B} = Bulk \qquad \text{(A.16)}$$

$$\frac{C_{Cl}^{B}}{D_{Cl}} X^{M} + C_{Cl}^{B} - C_{Cl}^{B} X^{B} = Bulk \qquad \text{(A.17)}$$

$$C_{Cl}^{B} \left(\frac{X^{M}}{D_{Cl}} + 1 - X^{M} \right) = Bulk \qquad \text{(A.18)}$$

$$C_{Cl}^{B} = \frac{Bulk}{\left(\left(\frac{X^{M}}{D_{Cl}} \right) + 1 - X^{M} \right)} \qquad \text{(A.19)}$$

$$Bulk = C_{Cl}^{B^{0}} X^{B} + C_{Cl}^{M^{0}} X^{M} = C^{B^{0}} (1 - X^{M}) \qquad \text{(A.20)}$$

Where, B^{0} is the initial starting buffer. The remaining Cl content in the remaining buffer can thus be calculated by:

$$C_{Cl}^{B} = \frac{C_{Cl}^{B^{0}} (1 - X^{M})}{\left(\left(\frac{X^{M}}{D_{Cl}} \right) + 1 - X^{M} \right)} \qquad \text{(A.21)}$$

These calculations are dependent upon the partition coefficient (D_{Cl}) which vary with *f*(Cl_2) and are determined by extrapolation from successful experiments attained at higher fugacities, with enough glass present for analysis. The result is a means of attaining the desired chlorine fugacity, whilst retaining sufficient silicate melt for accurate and reliable data analysis (Figure A.5).

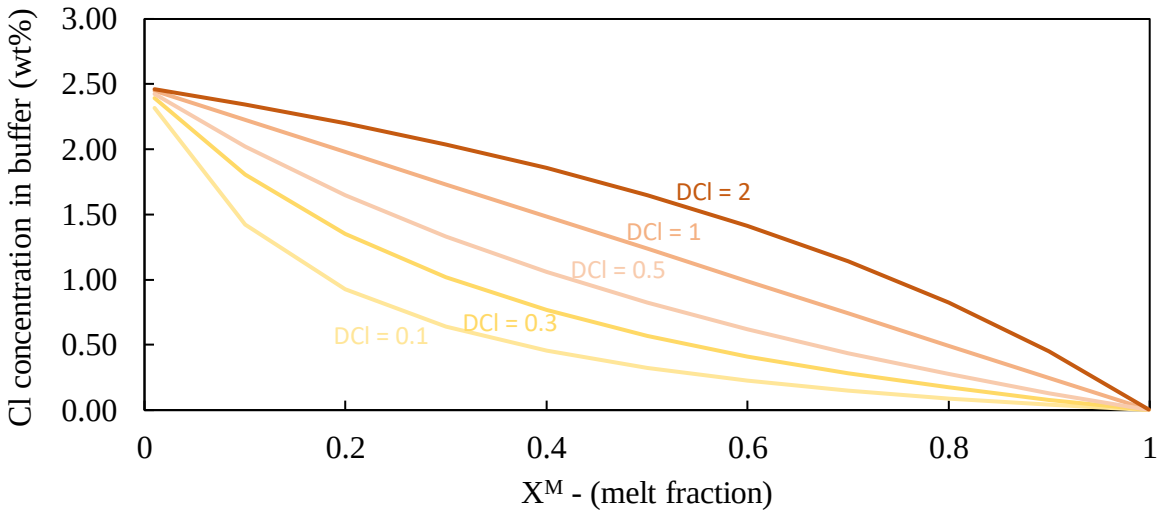


Figure A.5 Melt fraction vs Cl concentration in the buffer – a means of providing low chlorine fugacity experiments whilst maintaining a sufficient melt fraction to allow for accurate analysis.

A.8 Derivations for calculating HCl degassing

To determine how Cl degasses as HCl, we start with the reaction:

$$H_2O_{gas} + Cl_{2\,gas} = 2HCl_{gas} + \frac{1}{2}O_{2\,gas} \qquad \text{(A.22)}$$

Then the equilibrium constant logK for this reaction can be expressed as:

$$logK_{(A.22)} = 2logf(HCl) + \frac{1}{2}logf(O2) - logf(Cl_2) - logf(H_2O) \qquad \text{(A.23)}$$

Finding the equilibrium constant for equilibria A.22 from the NIST-JANAF thermodynamic tables (https://janaf.nist.gov/; one could equally use Barin (1989) as before), between 800-1800K, provides logK as a function of temperature at 1 bar:

$$logK_{(A2.22)1\,bar} = -3102.6/T + 3.575 \quad \text{(A.24)}$$

Oxygen fugacity ($f(O_2)$) can be calculated from the equations of Frost, (1991), and $f(Cl_2)$ can be calculated from rearranging equation 2.17, or by calculating the chloride capacity from equation 3.15, and then solving for $f(Cl_2)$ by rearranging equation 3.5. The fugacity of water ($f(H_2O)$) can be expressed as:

$$logf(H_2O) = P\Gamma_{H_2O}X_{H_2O} \quad \text{(A.25)}$$

Where P is pressure (in bars), Γ_{H_2O} is the fugacity coefficient, which is calculated from the Modified Redlich Kwong (MRK) equation of state, and X_{H_2O} is the mole fraction of water, which we assume to be equal to 1. We can then put all our knowns into equation A.23 and solve for $f(HCl)$:

$$2logf(HCl) = logK_{(A.22)} - \frac{1}{2}logf(O2) + logf(H_2O) + logf(Cl_2) \text{ (A.26)}$$

$$logf(HCl) = P\,\Gamma_{HCl}X_{HCl} \quad \text{(A.27)}$$

Again, taking the fugacity coefficient, Γ_{HCl} from the MRK equation, we can rearrange A.26 to attain X_{HCl}, the mole fraction of HCl in the gas. Then, to simulate degassing I calculated the solubility of H_2O in the melt from the spreadsheet of Moore et al., (1998) and then calculated the mass of chlorine lost with decreasing pressures in a series of steps, adjusting to account for the chlorine that has already been released at each step, and the change in water solubility between each step, with the cumulative fraction of Cl lost, defined as the sum of the Cl lost at all subsequent steps. Furthermore, inspection of A.26 shows that the fugacity of HCl will always be greater than the fugacity of Cl_2, and therefore dominates, as the primary mode of

degassing, and so this simplified model can be used with a degree of accuracy to simulate the complex degassing of Cl in volcanic systems. As a further examination of the mixtures of HCl and Cl_2 in the gas, we can calculate the XCl_2, following the calculation presented in A.27, and find the ratio of $XHCl/XCl_2$ at a range of temperatures and pressures. Doing this we find that at 10 bars, and temperatures from 20 to 2000 °C that XHCl is 48 to 6 orders of magnitude greater than XCl_2; and at 1100°C and pressures ranging from 1 bar to 3 GPa, that XHCl is 8-9 orders of magnitude greater than XCl_2. Therefore, under all volcanic conditions, Cl would predominantly degas as HCl.

A.9 Attainment of equilibrium

To accurately measure the solubility of halogens in silicate melts it is vital that all experiments reached chemical equilibrium. This has been determined through a batch of time-series experiments, where, equilibrium is determined to have been reached if there is no observable variation in concentration of the experiment after a duration of time. The time it takes to experience no change in concentration signifies the minimum time required for equilibrium to be obtained (Blaine et al., 2005). The time-series experiments were conducted in both a haplobasalt composition and a dacitic composition (sections 2.4.1 and 3.3.2 respectively). These compositions were chosen to ensure equilibrium was attained in all compositions including compositions with high viscosities, such as dacite. Both time-series were performed at a fixed temperature (1400°C), pressure (1.5 GPa) and chlorine buffer (75:25 buffer:silicate) for 5 minutes, 30 minutes, 1 hour, and 2 hours. The concentration of Cl was consistent with within-error variation between experiments performed at 0.5-2hours (Figure 2.3).

An additional method to assess the timescale for chlorine chemical equilibrium can also be calculated by the estimation of chlorine diffusion in silicate melts. This can be attained by the simple relationship:

$$x = 2\sqrt{Dt} \quad \text{(A.22)}$$

where x is the distance, D is the diffusion coefficient, and *t* is time. Using the diffusion coefficient from Alletti et al., (2007) of 1.3×10^{-10} m^2/s^{-1} which they determined for Hawaiitic melts at 1450°C (close to that of my experiment at 1400°C) indicates that Cl would diffuse 0.97 mm in 30 minutes. Therefore, chemical equilibrium of chlorine partitioning between buffer and silicate glass, would take less than 1 hour in a capsule that is <1.5mm long when under pressure. This is comparable to the findings of Kuwahara et al., (2017) who performed Cl partition experiments, and demonstrated that chorine could diffuse 1.5-3.8mm in 30 minutes at 1600 °C.

As a further test, the equilibration of chlorine between the buffering metal-metal chloride phase and the silicate glass can be indicated petrographically. 1) by the lack of zoning at the buffer-silicate boundary, and 2) the homogeneity of Cl within the glass phase, with 2 standard deviations ≤0.2%., and 3) clear segregations of the silicate glass, pure metal phase, and remnant chloride/iodide buffer is further evidence that equilibrium was attained. As a result of the above tests, all experiments were conducted at 1 hour to ensure equilibrium was attained. This appears to me sufficient to qualify that the equilibrium was achieved in my experiments.

A.10 Fundamentals of X-Ray Absorption Spectroscopy (XAFS)

The intricacies of how x-rays are absorbed by an atom at energies near and above the core-level binding energies of an atom are referred to as X-ray absorption fine structure (XAFS). XAFS is the change in an atom's x-ray absorption probability as a result of the chemical and

physical state of the atom of interest (Newville, 2014). XAFS spectra are particularly sensitive to the formal oxidation state, coordination chemistry, and species of the atoms which immediately surround an element. Because of this dependence, XAFS provides a practical and straightforward method for determining the chemical state and local atomic structure of a given atomic species (Newville, 2014). In this study, we performed all our synchrotron experiments at the Diamond light source in Oxfordshire, UK (outlined in Chapter 4). Diamond light source generates light at wavelengths ranging from X-rays to infrared by electromagnetic radiation, that is emitted by charged particles travelling near the speed of light.

The basic principle is that a sample of interest is bombarded with X-rays of definite, known energy. Some of these X-rays are absorbed by the atoms in the sample, causing a core electron to become excited or ejected. This absorption can be measured by 1) comparing the incident and transmitted beam intensities, 2) by measuring the fluorescence given off by the excited atoms as an electron fills the now-vacant core orbital (the core hole), or 3) by measuring the ejected electrons as the core hole is filled (Auger electrons) (Calvin, 2013). Once the absorption is determined for one energy of incident x-rays, the energy is changed slightly, and incrementally the process is repeated. By stepping through a range of energies in this way, a spectrum is created (Calvin, 2013) (Figure 4.1).

The X-ray absorption spectrum is divided into two key regions: 1) X-ray absorption near-edge spectroscopy (XANES) and 2) extended X-ray absorption fine-structure spectroscopy (EXAFS) as shown in Figure 4.1. Though the two have the same physical origin, the XANES region is strongly sensitive to the oxidation state and coordination chemistry of the absorbing atom, while the EXAFS region is used to determine the distances, coordination number, and species of the neighbours of the absorbing atom.

A.11 References

Alletti M., Baker D. R. and Freda C. (2007) Halogen diffusion in a basaltic melt. *Geochemica Cosmochim. Acta* **71**.

Barin I., Sauert F., Schultze-Rhonhof E. and Sheng W. S. (1989) *Thermochemical data of pure substances: Part I.*,

Blaine F. A., Linnen R. L., Holtz F. and Brügmann G. E. (2005) Platinum solubility in a haplobasaltic melt at 1250°C and 0.2 GPa: The effect of water content and oxygen fugacity. *Geochim. Cosmochim. Acta* **69**, 1265–1273.

Bohlen S. R. (1984) Equilibria for precise pressure calibration and a frictionless furnace assembly for the piston-cylinder apparatus. *Neues Jahrb. für Mineral. Monatshefte* **9**, 404–412.

Boyd F. R. and England J. L. (1960) Apparatus for phase-equilibrium measurements at pressures up to 50 kilobars and temperatures up to 1750°C. *J. Geophys. Res.* **65**, 741–748.

Calvin S. (2013) *XAFS for everyone*. 1st ed., Taylor and Francis, Boca Raton, Florida.

Dalou C., Koga K. T., Le Voyer M. and Shimizu N. (2014) Contrasting partition behavior of F and Cl during hydrous mantle melting: implications for Cl/F signature in arc magmas. *Prog. Earth Planet. Sci.* **1**, 1–17.

Frost R. B. (1991) Introduction to oxygen fugacity and its petrologic importance. *Rev. Mineral. Geochemistry* **25**, 1–9.

Johannes W., Bell P. M., Mao H. K., Washington N. W., Boettcher A. L., Chipman D. W., Hays J. F., Newton R. C. and Seifert F. (1971) *An interlaboratory comparison of piston-cylinder pressure calibration using the albite-breakdown reaction.*, Springer-Verlag.

Kuwahara H., Gotou H., Shinmei T., Ogawa N., Yamaguchi A., Takahata N., Sano Y., Yagi

T. and Sugita S. (2017) High pressure experiments on metal-silicate partitioning of chlorine in a magma ocean: Implications for terrestrial chlorine depletion. *Geochemistry, Geophys. Geosystems* **18**, 1–17.

Marcus Y. (2013) The compressibility of molten salts. *J. Chem. Thermodyn.* **61**, 7–10.

Matjuschkin V., Brooker R. A., Tattitch B., Blundy J. D. and Stamper C. C. (2015) Control and monitoring of oxygen fugacity in piston cylinder experiments. *Contrib Miner. Pet.* **169**, 1–16.

McDade P., Wood B. J., Van Westrenen W., Brooker R., Gudmundsson G., Soulard H., Najorka J. and Blundy J. (2002) Pressure corrections for a selection of piston-cylinder cell assemblies. *Mineral. Mag.* **66**, 1021–1028.

Moore G., Vennemann T. and Carmichael I. S. E. (1998) An empirical model for the solubility of H2O in magmas to 3 kilobars. *Am. Mineral.* **83**, 36–42.

Newville M. (2014) Fundamentals of XAFS. *Rev. Mineral. Geochemistry* **78**, 33–74.

Sneeringer M. A. and Watson E. B. (1985) Milk cartons and ash cans: two unconventional welding techniques. *Am. Mineral.* **70**, 200–201.

Takeda S., Nagata Y. and Kawakita Y. (2007) Slow dynamic properties of molten silver halides. *J. Non. Cryst. Solids* **353**, 3169–3173.

Tsu Y., Suenaga H., Katsutoshi T. and Yutaka S. (1982) The velocity of ultrasound in molten bismuth, aluminium, silver and copper. *Trans. Japan Inst. Met.* **23**, 1–7.

Vlach S. R. F., Salazar-Naranjo A. F., Torres-Corredor J. S., De Carvalho P. R. and Mallmann G. (2019) Calibration of high-temperature furnace assemblies for experiments between 200 and 600 MPa with end-loaded piston-cylinder apparatuses. *Brazilian J. Geol.* **49**.

Appendix B

Table S1 Compositions of silicate glass in wt% measured by EPMA, which accompanies chapter 2.

Experiment	n	SiO_2	TiO_2	Al_2O_3	FeO	MgO	CaO	Na_2O	Cl	I	Ag	Re	Total
AgI/Cl-001	20	45.69 (0.48)	-	18.35 (0.60)	-	17.05 (0.44)	17.34 (0.35)	-	-	-	-	-	98.43
AgI/Cl-002	45	45.27 (0.36)	-	17.82 (0.09)	-	16.33 (0.12)	16.26 (0.15)	-	2.74 (0.14)	0.05 (0.02)	0.23 (0.08)	-	98.71
AgI/Cl-005	55	45.35 (0.51)	-	17.95 (0.22)	-	16.34 (0.16)	16.24 (0.19)	-	2.55 (0.04)	0.04 (0.02)	0.27 (0.27)	-	98.75
AgI/Cl-006	15	44.88 (0.35)	-	17.70 (0.13)	-	16.41 (0.20)	16.19 (0.25)	-	2.56 (0.07)	0.03 (0.03)	0.26 (0.08)	-	98.02
AgI/Cl-007	41	45.33 (0.33)	-	17.98 (0.38)	-	16.25 (0.33)	16.48 (0.34)	-	2.24 (0.05)	0.04 (0.05)	0.25 (0.21)	-	98.57
AgI/Cl-008	41	46.74 (0.42)	-	17.63 (0.32)	-	16.57 (0.20)	16.54 (0.27)	-	1.02 (0.03)	0.06 (0.07)	0.20 (0.36)	-	98.75
AgI/Cl-009	22	48.36 (0.48)	-	17.11 (0.13)	-	16.76 (0.36)	16.26 (0.14)	-	0.50 (0.03)	0.06 (0.03)	0.20 (0.16)	-	99.25
AgI/Cl-010	30	48.76 (0.58)	-	17.06 (0.28)	-	16.65 (0.23)	16.45 (0.12)	-	0.21 (0.01)	0.08 (0.16)	0.20 (0.16)	-	99.41
AgI/Cl-013	29	45.94 (0.62)	-	17.87 (0.24)	-	16.37 (0.19)	15.73 (0.29)	-	3.59 (0.09)	0.00 (0.03)	0.14 (0.07)	-	99.64
AgI/Cl-018	30	47.58 (1.05)	-	17.54 (0.28)	-	16.55 (0.16)	16.43 (0.28)	-	0.18 (0.01)	0.00 (0.03)	0.05 (0.07)	-	98.33
AgI/Cl-019	28	45.76 (0.56)	-	18.56 (0.23)	-	16.42 (0.17)	15.85 (0.23)	-	2.93 (0.04)	0.01 (0.02)	0.11 (0.05)	-	99.63
AgI/Cl-020	15	45.01 (0.42)	-	17.86 (0.19)	-	16.53 (0.19)	16.52 (0.24)	-	2.41 (0.16)	0.02 (0.03)	0.23 (0.40)	-	98.36
AgI/Cl-021	20	45.76 (0.23)	-	17.96 (0.14)	-	16.13 (0.20)	16.10 (0.20)	-	2.12 (0.03)	0.01 (0.03)	0.32 (0.10)	-	98.40
AgI/Cl-023	13	54.94 (0.94)	0.95 (0.05)	15.11 (0.56)	3.24 (0.89)	8.86 (0.36)	12.30 (0.45)	1.42 (0.13)	0.77 (0.06)	0.08 (0.03)	0.32 (0.15)	-	98.26
AgI/Cl-024	20	43.05 (0.97)	-	15.92 (0.48)	8.68 (0.19)	14.00 (0.34)	13.78 (0.34)	-	2.54 (0.06)	0.05 (0.03)	0.31 (0.29)	-	98.34
AgI/Cl-025	20	42.34 (0.38)	-	13.31 (0.21)	15.69 (0.46)	11.53 (0.28)	11.39 (0.37)	-	2.70 (0.19)	0.11 (0.05)	0.28 (0.42)	-	97.38
AgI/Cl-026	20	37.23 (0.65)	-	12.21 (0.19)	20.88 (0.49)	11.50 (0.23)	11.38 (0.18)	-	3.49 (0.28)	0.14 (0.10)	0.17 (0.39)	-	97.02

AgI/Cl-027	20	54.30 (0.82)	0.99 (0.08)	15.84 (0.25)	0.50 (0.13)	9.28 (0.12)	13.19 (0.19)	1.86 (0.31)	1.60 (0.03)	0.04 (0.02)	0.41 (0.40)	-	98.05
AgI/Cl-028	60	45.22 (0.41)	-	17.79 (0.18)	-	16.34 (0.15)	16.24 (0.16)	-	2.66 (0.07)	0.05 (0.05)	0.28 (0.38)	-	98.58
AgI/Cl-029	22	44.31 (0.43)	-	17.11 (0.23)	-	15.90 (0.17)	15.95 (0.14)	-	0.69 (0.04)	0.04 (0.03)	0.66 (0.11)	4.36 (0.25)	99.02
AgI/Cl-031	36	51.09 (0.93)	1.01 (0.07)	15.15 (0.25)	3.48 (0.10)	8.64 (0.08)	11.25 (0.11)	1.68 (0.16)	0.33 (0.02)	0.07 (0.03)	0.83 (0.12)	4.32 (0.38)	97.85
AgI/Cl-032	22	45.63 (0.25)	-	18.10 (0.35)	-	16.83 (0.30)	15.69 (0.23)	-	3.39 (0.04)	0.05 (0.05)	0.15 (0.07)	-	99.84
AgI/Cl-037	10	54.39 (1.30)	0.93 (0.11)	15.95 (0.84)	1.67 (0.17)	8.79 (0.38)	12.58 (1.04)	1.85 (0.50)	0.41 (0.09)	0.08 (0.06)	0.33 (0.08)	-	96.97
AgI/Cl-039	25	54.20 (0.47)	0.99 (0.05)	16.05 (0.16)	2.60 (0.18)	8.99 (0.08)	13.05 (0.15)	1.88 (0.10)	0.32 (0.01)	0.07 (0.03)	0.25 (0.13)	-	98.40
AgI/Cl-043	70	49.51 (0.35)	0.94 (0.05)	14.94 (0.21)	8.85 (0.13)	8.15 (0.17)	11.97 (0.23)	1.59 (0.09)	1.77 (0.09)	0.06 (0.05)	0.34 (0.19)	-	97.74
AgI/Cl-044	55	54.24 (0.50)	1.01 (0.16)	15.98 (0.28)	1.11 (0.16)	9.22 (0.47)	12.96 (0.20)	1.71 (0.05)	1.52 (0.06)	0.05 (0.03)	0.43 (0.17)	-	98.23
AgI/Cl-045	66	50.84 (0.51)	1.05 (0.19)	16.00 (0.80)	8.20 (0.31)	8.15 (0.79)	11.98 (0.75)	1.92 (0.15)	1.48 (0.17)	0.04 (0.07)	0.28 (0.17)	-	99.94
AgI/Cl-048	40	50.08 (0.69)	0.93 (0.05)	14.55 (0.32)	7.58 (0.17)	8.59 (0.12)	11.93 (0.12)	1.61 (0.09)	2.05 (0.12)	0.12 (0.04)	0.3 (0.30)	-	97.74
AgI/Cl-049	45	50.28 (0.74)	0.96 (0.05)	14.66 (0.56)	8.22 (0.19)	8.60 (0.16)	11.88 (0.17)	1.72 (0.20)	1.62 (0.13)	0.00 (0.04)	0.28 (0.42)	-	98.22
AgI/Cl-050	30	50.52 (0.61)	1.01 (0.07)	14.63 (0.28)	8.24 (0.15)	8.67 (0.15)	12.02 (0.18)	1.17 (0.06)	2.19 (0.11)	0.22 (0.06)	0.17 (0.29)	-	98.59
AgI/Cl-051	30	48.68 (0.9)	-	17.13 (0.41)	-	17.43 (0.26)	15.91 (0.20)	-	1.23 (0.03)	0.06 (0.03)	0.16 (0.13)	-	100.41
AgI/Cl-052	20	47.61 (0.59)	-	17.03 (0.20)	-	15.44 (0.20)	15.83 (0.19)	-	0.81 (0.02)	0.03 (0.03)	0.27 (0.11)	-	97.02
f(O_2) sensor	42	51.19 (0.42)	0.94 (0.05)	12.75 (0.15)	5.22 (0.12)	9.00 (0.10)	12.75 (0.15)	2.11 (0.10)	-	-	-	-	96.16

Numbers in parentheses () are analytical uncertainties of two standard deviations of n analysis

CO_2 solubility is expected to account for 1.3wt% in IB to 2.4 wt% in CMAS using the calculator of Eguchi and Dasgupta (2018)

Appendix C

Table S2 Compositions of silicate glass in wt% measured by EPMA, which accompanies chapter 3.

Experiment ID	n	SiO_2	TiO_2	Al_2O_3	FeO_T	MnO	MgO	CaO	Na_2O	K_2O	Cl	I_2O	Ag_2O	PtO_2	P_2O_5*	Cr_2O_3*	NiO*	Re	Total
Ab/Fo-1	31	70.47 (0.71)	0.02 (0.02)	19.35 (0.24)	0.13 (0.02)	0.00 (0.01)	2.93 (0.08)	0.15 (0.02)	5.77 (0.23)	0.19 (0.02)	0.56 (0.02)	0.06 (0.07)	0.45 (0.48)	0.01 (0.06)	-	-	-	-	100.09
Ab/Fo-2	31	63.51 (0.65)	0.03 (0.02)	15.49 (0.60)	0.10 (0.02)	0.00 (0.02)	2.43 (0.29)	11.06 (0.37)	4.70 (0.21)	0.24 (0.03)	1.41 (0.06)	0.07 (0.03)	0.35 (0.34)	0.00 (0.03)	-	-	-	-	99.40
Ab/Fo-3	33	55.97 (0.51)	0.03 (0.02)	12.44 (0.16)	0.11 (0.02)	0.00 (0.01)	1.87 (0.03)	19.69 (0.02)	3.49 (0.12)	0.32 (0.02)	2.75 (0.05)	0.14 (0.03)	0.22 (0.17)	0.00 (0.05)	-	-	-	-	97.02
Ab/Fo-6	33	57.87 (0.76)	0.04 (0.02)	15.88 (0.24)	0.00 (0.01)	0.08 (0.02)	2.43 (0.06)	11.54 (0.40)	7.89 (0.20)	0.07 (0.02)	0.46 (0.01)	0.22 (0.02)	0.12 (0.15)	0.00 (0.03)	-	-	-	-	96.61
AgI/Cl-27	20	54.30 (0.82)	0.99 (0.08)	15.84 (0.25)	0.50 (0.13)	-	9.28 (0.12)	13.19 (0.19)	1.86 (0.31)	-	1.60 (0.03)	0.04 (0.02)	0.41 (0.40)	-	-	-	-	-	98.05
AgI/Cl-005	47	45.35 (0.51)	-	17.95 (0.22)	-	-	16.34 (0.16)	16.24 (0.19)	-	-	2.55 (0.04)	0.04 (0.02)	0.27 (0.27)	-	-	-	-	-	98.75
AgI/Cl-024	20	43.05 (0.97)	-	15.92 (0.48)	8.68 (0.19)	-	14.00 (0.34)	13.78 (0.34)	-	-	2.54 (0.06)	0.05 (0.03)	0.31 (0.29)	-	-	-	-	-	98.34
AgI/Cl-025	20	42.34 (0.38)	-	13.31 (0.21)	15.69 (0.46)	-	11.53 (0.28)	11.39 (0.37)	-	-	2.70 (0.19)	0.11 (0.05)	0.28 (0.42)	-	-	-	-	-	97.38
AgI/Cl-026	20	37.23 (0.65)	-	12.21 (0.19)	20.88 (0.49)	-	11.50 (0.23)	11.38 (0.18)	-	-	3.49 (0.28)	0.14 (0.10)	0.17 (0.39)	-	-	-	-	-	97.02
Dacite-1	32	69.65 (1.10)	0.97 (0.08)	15.98 (0.89)	0.69 (0.12)	0.04 (0.02)	1.50 (0.13)	3.49 (0.30)	0.62 (0.13)	4.02 (0.21)	0.46 (0.06)	0.16 (0.14)	1.00 (0.86)	-0.01 (0.04)	-	-	-	-	98.64
TNR14-1	59	45.44 (1.10)	4.37 (0.46)	10.41 (0.65)	7.15 (0.59)	0.17 (0.03)	14.11 (0.30)	11.43 (0.23)	1.05 (0.09)	0.20 (0.03)	2.23 (0.12)	0.06 (0.03)	0.33 (0.12)	-0.03 (0.05)	0.69	-	-	-	97.63
HA3_2	59	51.75 (0.48)	0.03 (0.04)	7.84 (1.27)	11.61 (0.47)	0.09 (0.03)	22.79 (2.7)	5.72 (0.98)	0.04 (0.06)	0.03 (0.02)	1.62 (0.16)	0.05 (0.02)	0.26 (0.3)	0.00 (0.06)	-	0.57	0.10	-	97.53
HA4-1	45	56.30 (0.54)	0.06 (0.04)	8.94 (0.58)	0.54 (0.06)	0.06 (0.02)	15.31 (0.46)	12.07 (0.59)	0.09 (0.03)	0.04 (0.02)	1.75 (0.2)	0.02 (0.03)	0.42 (0.10)	0.01 (0.03)	-	0.17	0.13	-	95.92
Rhyolite	20	75.44 (1.40)	0.33 (0.05)	13.25 (0.94)	0.13 (0.04)	0.02 (0.03)	0.27 (0.04)	0.92 (0.07)	0.56 (0.20)	6.12 (0.62)	0.27 (0.03)	0.05 (0.10)	0.85 (0.31)	0.00 (0.04)	-	-	-	-	98.21
LIP17714	32	77.51 (1.20)	0.08 (0.02)	12.82 (0.77)	0.18 (0.02)	0.03 (0.02)	0.11 (0.02)	0.73 (0.05)	2.73 (0.13)	3.82 (0.46)	0.27 (0.03)	0.02 (0.02)	0.50 (0.42)	0.00 (0.05)	-	-	-	-	98.83
AN-2	28	64.50 (0.91)	0.63 (0.05)	17.29 (0.50)	2.04 (0.21)	0.01 (0.02)	3.14 (0.10)	6.22 (0.22)	2.81 (0.11)	0.86 (0.03)	0.90 (0.05)	0.04 (0.02)	0.60 (0.34)	0.00 (0.03)	-	-	-	-	99.03
SM-1	27	42.82 (0.38)	0.02 (0.02)	10.27 (0.11)	10.26 (0.14)	0.01 (0.02)	14.56 (0.13)	15.44 (0.15)	0.04 (0.02)	0.01 (0.01)	3.05 (0.16)	0.08 (0.02)	0.32 (0.17)	0.00 (0.07)	-	-	-	-	96.88

HiMgAnd	29	55.41 (0.47)	0.60 (0.05)	14.26 (0.38)	5.19 (0.12)	0.00 (0.01)	8.85 (0.18)	9.13 (0.16)	1.54 (0.15)	0.61 (0.03)	1.71 (0.03)	0.08 (0.03)	0.35 (0.13)	0.00 (0.03)	-	-	-	-	97.73
HAW-16095	28	51.95 (0.75)	2.44 (0.20)	10.97 (0.58)	6.93 (0.26)	0.15 (0.02)	12.39 (1.06)	9.42 (0.46)	0.96 (0.12)	0.14 (0.02)	1.90 (0.14)	0.05 (0.02)	0.40 (0.22)	-0.01 (0.06)	-	-	-	-	97.69
EGT17-1	35	55.73 (0.60)	3.68 (0.09)	17.43 (0.20)	0.15 (0.04)	0.12 (0.02)	4.49 (0.11)	9.89 (0.21)	3.14 (0.14)	1.10 (0.05)	1.40 (0.02)	0.04 (0.02)	0.38 (0.19)	-0.06 (0.06)	-	-	-	-	97.49
KK3b-2	27	54.80 (0.60)	0.86 (0.05)	16.34 (0.20)	0.08 (0.02)	0.07 (0.03)	10.54 (0.12)	13.22 (0.13)	1.06 (0.06)	0.07 (0.03)	1.70 (0.04)	0.02 (0.03)	0.48 (0.11)	0.00 (0.03)	-	-	-	-	99.23
Mars-1	26	49.32 (1.16)	0.94 (0.15)	9.04 (0.85)	16.11 (0.46)	0.28 (0.04)	12.56 (1.29)	6.35 (0.48)	0.07 (0.02)	0.02 (0.01)	2.02 (0.2)	0.09 (0.06)	0.41 (0.15)	0.00 (0.01)	-	-	0.46	-	97.67
Neph-1	20	45.93 (0.44)	2.53 (0.05)	16.45 (0.16)	8.94 (0.09)	0.28 (0.03)	4.33 (0.09)	11.77 (0.07)	2.68 (0.09)	1.19 (0.05)	1.91 (0.03)	0.10 (0.04)	0.43 (0.41)	-0.06 (0.04)	1.22	-	-	-	97.71
Basanite-1	30	47.42 (0.35)	2.59 (0.05)	12.12 (0.10)	5.46 (0.08)	0.18 (0.04)	12.90 (0.12)	9.72 (0.15)	2.06 (0.03)	0.60 (0.06)	2.06 (0.03)	0.08 (0.04)	0.36 (0.22)	-0.06 (0.08)	1.50	-	-	-	96.98
Lunar-1	29	45.77 (0.41)	7.54 (0.16)	11.13 (0.14)	12.89 (0.26)	0.47 (0.04)	6.92 (0.11)	8.59 (0.15)	0.47 (0.06)	0.033 (0.02)	2.03 (0.09)	0.10 (0.02)	0.54 (0.31)	0.00 (0.02)	-	-	-	-	96.48
KK-Rhy	24	75.30 (0.91)	0.07 (0.03)	13.60 (0.84)	0.90 (0.09)	0.08 (0.04)	0.15 (0.02)	0.69 (0.12)	3.59 (0.30)	3.40 (0.13)	0.15 (0.02)	0.20 (0.25)	0.67 (0.69)	0.01 (0.05)	-	-	-	-	98.81
Syn-Phono-1	36	62.21 (0.84)	1.56 (0.07)	19.79 (0.48)	0.05 (0.02)	0.04 (0.02)	2.02 (0.13)	4.35 (0.20)	5.63 (0.12)	2.15 (0.06)	0.83 (0.02)	0.06 (0.04)	0.36 (0.18)	0.00 (0.02)	-	-	-	-	99.05
Phono-1	26	59.17 (0.98)	0.35 (0.03)	24.29 (1.10)	1.21 (0.06)	0.15 (0.03)	0.22 (0.02)	2.20 (0.07)	5.41 (0.17)	5.66 (0.12)	0.68 (0.07)	0.19 (0.20)	0.54 (0.63)	0.01 (0.03)	-	-	-	-	100.07
CMAS+Na-1	28	45.91 (0.70)	0.04 (0.03)	13.99 (0.49)	0.18 (0.03)	0.01 (0.01)	14.03 (0.36)	13.46 (0.28)	5.17 (0.60)	0.01 (0.01)	2.15 (0.06)	0.14 (0.03)	0.20 (0.08)	0.00 (0.03)	-	-	-	-	95.29
CMAS+Na-2	40	44.93 (0.50)	0.02 (0.03)	16.72 (0.41)	0.07 (0.02)	0.00 (0.02)	15.73 (0.31)	15.62 (0.16)	1.72 (0.13)	0.01 (0.02)	2.32 (0.1)	0.06 (0.03)	0.28 (0.09)	0.00 (0.03)	-	-	-	-	97.49
$En_{17}An_{43}Di_{40}$	31	50.01 (0.31)	0.02 (0.02)	13.01 (0.26)	0.07 (0.02)	0.00 (0.02)	13.83 (0.20)	18.47 (0.16)	0.03 (0.01)	0.01 (0.02)	2.60 (0.13)	0.05 (0.1)	0.36 (0.17)	0.00 (0.03)	-	-	-	-	98.46
$Fo_5Di_{48}An_{47}$	36	47.37 (0.45)	0.02 (0.02)	16.17 (0.15)	0.10 (0.02)	0.00 (0.01)	11.28 (0.10)	20.65 (0.14)	0.04 (0.02)	0.02 (0.02)	2.41 (0.14)	0.03 (0.02)	0.34 (0.14)	0.00 (0.06)	-	-	-	-	98.42
Granite-2	36	75.13 (0.76)	0.04 (0.04)	15.94 (0.42)	0.08 (0.02)	0.00 (0.01)	0.06 (0.02)	0.16 (0.03)	4.25 (0.21)	2.96 (0.12)	0.31 (0.10)	0.18 (0.18)	0.44 (0.28)	0.00 (0.04)	-	-	-	-	99.56
Gran+Mg-1	41	70.19 (0.98)	0.03 (0.03)	15.79 (0.61)	0.06 (0.02)	0.00 (0.01)	5.11 (0.25)	0.18 (0.03)	4.33 (0.11)	2.47 (0.1)	0.61 (0.10)	0.16 (0.22)	0.63 (0.5)	0.00 (0.04)	-	-	-	-	99.59
Gran+Mg-2	43	68.99 (0.72)	0.05 (0.06)	15.48 (0.40)	0.13 (0.02)	0.00 (0.01)	6.30 (0.30)	0.32 (0.13)	4.24 (0.3)	2.40 (0.11)	0.67 (0.14)	0.21 (0.32)	0.56 (0.8)	0.00 (0.04)	-	-	-	-	99.36
Gran+Mg-3	43	66.84 (0.51)	0.04 (0.03)	16.08 (0.36)	0.04 (0.02)	0.01 (0.02)	7.930 (0.31)	0.58 (0.04)	4.20 (0.18)	2.2 (0.1)	0.78 (0.10)	0.06 (0.20)	0.49 (0.5)	0.00 (0.07)	-	-	-	-	99.28
AN-1	25	64.44 (0.88)	0.62 (0.06)	17.48 (0.73)	0.00 (0.01)	0.07 (0.04)	3.31 (0.13)	6.59 (0.21)	3.84 (0.14)	1.18 (0.07)	0.72 (0.03)	0.05 (0.04)	0.43 (0.13)	0.01 (0.03)	-	-	-	-	98.74
KK3b-1	35	51.42 (1.08)	0.82 (0.06)	15.33 (0.42)	4.19 (0.32)	0.15 (0.03)	10.21 (0.12)	12.68 (0.31)	1.73 (0.14)	0.13 (0.02)	1.13 (0.02)	0.05 (0.03)	0.34 (0.29)	0.00 (0.03)	-	-	-	-	98.16

Phono-2	29	58.30 (0.46)	0.34 (0.07)	22.91 (0.41)	2.22 (0.11)	0.22 (0.03)	0.19 (0.03)	1.87 (0.08)	6.36 (0.33)	5.80 (0.12)	0.44 (0.03)	0.32 (0.61)	0.37 (0.37)	0.02 (0.05)	-	-	-	-	99.37
Dacite-2	29	71.78 (0.57)	0.91 (0.07)	15.38 (0.81)	0.08 (0.05)	0.03 (0.02)	1.56 (0.16)	3.23 (0.41)	0.50 (0.10)	3.78 (0.22)	0.17 (0.01)	0.04 (0.06)	0.78 (0.16)	0.01 (0.05)	-	-	-	-	98.26
Phonolite-NaCl-1	70	54.67 (0.78)	0.31 (0.06)	25.13 (0.57)	2.14 (0.24)	0.15 (0.03)	0.14 (0.06)	1.53 (0.12)	8.57 (0.21)	5.10 (0.11)	1.09 (0.10)	-	-	-	-	-	-	-	99.69
Phonolite-NaCl-2	50	56.56 (0.90)	0.31 (0.03)	26.02 (0.44)	1.38 (0.41)	0.10 (0.04)	0.08 (0.04)	1.17 (0.11)	9.46 (0.47)	5.57 (0.14)	1.00 (0.10)	-	-	-	-	-	-	-	101.65
From Thomas and Wood 2021:																			
AgI/Cl-005	55	45.35 (0.51)	-	17.95 (0.22)	-	-	16.34 (0.16)	16.24 (0.19)	-	-	2.55 (0.04)	0.27 (0.27)	0.04 (0.02)	-	-	-	-	-	98.75
AgI/Cl-008	41	46.74 (0.42)	-	17.63 (0.32)	-	-	16.57 (0.20)	16.54 (0.27)	-	-	1.02 (0.03)	0.20 (0.36)	0.06 (0.07)	-	-	-	-	-	98.75
AgI/Cl-019	28	45.76 (0.56)	-	18.56 (0.23)	-	-	16.42 (0.17)	15.85 (0.23)	-	-	2.93 (0.04)	0.11 (0.05)	0.01 (0.02)	-	-	-	-	-	99.63
AgI/Cl-020	15	45.01 (0.42)	-	17.86 (0.19)	-	-	16.53 (0.19)	16.52 (0.24)	-	-	2.41 (0.16)	0.23 (0.40)	0.02 (0.03)	-	-	-	-	-	98.36
AgI/Cl-021	20	45.76 (0.23)	-	17.96 (0.14)	-	-	16.13 (0.20)	16.10 (0.20)	-	-	2.12 (0.03)	0.32 (0.10)	0.01 (0.03)	-	-	-	-	-	98.40
AgI/Cl-027	20	54.30 (0.82)	0.99 (0.08)	15.84 (0.25)	0.50 (0.13)	-	9.28 (0.12)	13.19 (0.19)	1.86 (0.31)	-	1.60 (0.03)	0.41 (0.40)	0.04 (0.02)	-	-	-	-	-	98.05
AgI/Cl-028	60	45.22 (0.41)	-	17.79 (0.18)	-	-	16.34 (0.15)	16.24 (0.16)	-	-	2.66 (0.07)	0.28 (0.38)	0.05 (0.05)	-	-	-	-	-	98.58
AgI/Cl-029	22	44.31 (0.43)	-	17.11 (0.23)	-	-	15.90 (0.17)	15.95 (0.14)	-	-	0.69 (0.04)	0.66 (0.11)	0.04 (0.03)	-	-	-	-	4.36 (0.25)	99.02
AgI/Cl-031	36	51.09 (0.93)	1.01 (0.07)	15.15 (0.25)	3.48 (0.10)	-	8.64 (0.08)	11.25 (0.11)	1.68 (0.16)	-	0.33 (0.02)	0.83 (0.12)	0.07 (0.03)	-	-	-	-	4.32 (0.38)	97.85
AgI/Cl-032	22	45.63 (0.25)	-	18.10 (0.35)	-	-	16.83 (0.30)	15.69 (0.23)	-	-	3.39 (0.04)	0.15 (0.07)	0.05 (0.05)	-	-	-	-	-	99.84
AgI/Cl-043	70	49.51 (0.35)	0.94 (0.05)	14.94 (0.21)	8.85 (0.13)	-	8.15 (0.17)	11.97 (0.23)	1.59 (0.09)	-	1.77 (0.09)	0.34 (0.19)	0.06 (0.05)	-	-	-	-	-	97.74
AgI/Cl-044	55	54.24 (0.50)	1.01 (0.16)	15.98 (0.28)	1.11 (0.16)	-	9.22 (0.47)	12.96 (0.20)	1.71 (0.05)	-	1.52 (0.06)	0.43 (0.17)	0.05 (0.03)	-	-	-	-	-	98.23
AgI/Cl-045	66	50.84 (0.51)	1.05 (0.19)	16.00 (0.80)	8.20 (0.31)	-	8.15 (0.79)	11.98 (0.75)	1.92 (0.15)	-	1.48 (0.17)	0.28 (0.17)	0.04 (0.07)	-	-	-	-	-	99.94
AgI/Cl-048	40	50.08 (0.69)	0.93 (0.05)	14.55 (0.32)	7.58 (0.17)	-	8.59 (0.12)	11.93 (0.12)	1.61 (0.09)	-	2.05 (0.12)	0.3 (0.30)	0.12 (0.04)	-	-	-	-	-	97.74
AgI/Cl-049	45	50.28 (0.74)	0.96 (0.05)	14.66 (0.56)	8.22 (0.19)	-	8.60 (0.16)	11.88 (0.17)	1.72 (0.20)	-	1.62 (0.13)	0.28 (0.42)	0.00 (0.04)	-	-	-	-	-	98.22
AgI/Cl-050	30	50.52 (0.61)	1.01 (0.07)	14.63 (0.28)	8.24 (0.15)	-	8.67 (0.15)	12.02 (0.18)	1.17 (0.06)	-	2.19 (0.11)	0.17 (0.29)	0.22 (0.06)	-	-	-	-	-	98.59

AgI/Cl-051	30	48.68 (0.9)	-	17.13 (0.41)	-	-	17.43 (0.26)	15.91 (0.20)	-	-	1.23 (0.03)	0.16 (0.13)	0.06 (0.03)	-	-	-	-	-	100.41
AgI/Cl-052	20	47.61 (0.59)	-	17.03 (0.20)	-	-	15.44 (0.20)	15.83 (0.19)	-	-	0.81 (0.02)	0.27 (0.11)	0.03 (0.03)	-	-	-	-	-	97.02

Numbers in parentheses () are analytical uncertainties of two standard deviations of n analysis
* Measured via LA-ICPMS